SHIGELLA FLEXNERI REQUIRES THE HOST SCAFFOLD PROTEIN RACK1 TO MODULATE ACTIN POLYMERIZATION, PROMOTING INFECTION

by

Karla Valenzuela

Submitted in partial fulfilment of the requirements
for the degree of Doctor of Philosophy

at

Dalhousie University
Halifax, Nova Scotia
April 2022

TABLE OF CONTENTS

LIST OF TABLES ..... **vi**

LIST OF FIGURES ..... **vii**

ABSTRACT ..... **x**

LIST OF ABBREVIATIONS USED ..... **xi**

ACKNOWLEDGEMENTS ..... **xiv**

CHAPTER 1 INTRODUCTION **1**

1.1 Overview 1

1.2 *Shigella* and shigellosis 2

1.3 *Shigella flexneri* pathogenesis 4

1.4 *Shigella* life cycle within the epithelial cell 6

1.4.1 The making of an invasive pathogen 6

1.4.2 Invasion of the epithelial cell 8

1.4.3 Vacuolar escape 13

1.4.4 Establishment of a replicative niche within the epithelial cell 16

1.4.5 Actin-based motility and cell-to-cell spreading 24

1.5 Receptor for activated C kinase 1, a scaffolding protein involved in diverse functions 30

1.5.1 Cell signalling and ribosome interaction 30

1.5.2 RACK1's role in autophagy 31

1.5.3 RACK1's role in apoptosis 33

1.6 RACK1 and cytoskeleton dynamics 34

1.6.1 RACK1 and cell migration 34

1.6.2 RACK1's interactions with the cytoskeleton 36

1.7 RACK1's roles in pathogenesis 37

1.8 Rationale, hypothesis, and objectives 42

CHAPTER 2 MATERIALS AND METHODS 44

2.1 Bacterial strains and growth conditions 44

2.1.1 *Shigella flexneri* 44

2.1.2 *Escherichia coli* 45

2.2 Mammalian cell lines and growth conditions 50

2.3 Molecular biology techniques 51

2.3.1 Polymerase chain reaction (PCR) 51

2.3.2 Agarose gel electrophoresis 51

2.3.3 Nucleic acid purification 52

2.3.4 Competent *E. coli* and heat shock transformation 52

2.3.5 Competent *Shigella* and transformation by electroporation 53

2.3.6 Plasmid construction 53

2.4 Protein techniques 58

2.4.1 Preparation of whole-cell lysates 58

2.4.2 Protein quantification and sample preparation 58

2.4.3 SDS-polyacrylamide gel electrophoresis (SDS-PAGE) 58

2.4.4 Western blotting and relative protein expression quantification 59

2.4.5 Co-immunoprecipitation for mass spectrometry 60

2.4.6 Coomassie and silver stain 61

2.5 RACK1 knockdown and stable/transient reporter cell lines 64

2.5.1 Lentiviral production 64

2.5.2 Lentiviral transduction of target cells 64

2.5.3 Transient expression of fluorescently tagged proteins 66

2.6 Proliferation assay (MTT) 66

2.7 Gentamycin protection assay 67

2.8 *Shigella* infection of *Drosophila melanogaster* 67

2.9 Cell death evaluation....68
2.9.1 Annexin V apoptosis assay using flow cytometry....68
2.9.2 Cytotoxicity detection assay....69
2.10 Immunofluorescence of fixed samples and data analysis....70
2.10.1 Immunofluorescence....70
2.10.2 Analysis of intracellular replication in fixed samples....72
2.10.3 Targeting of *Shigella* by guanylate-binding proteins (GBPs)....73
2.10.4 Analysis of actin tails in fixed samples....74
2.10.5 Quantification of Arp2 recruitment to *Shigella*....74
2.11 Live-cell imaging and data analysis....75
2.11.1 Live-cell imaging of *Shigella* entry and vacuolar escape in HeLa cells....76
2.11.2 Evaluation of Δ*icsA Shigella* entry to HeLa cells....77
2.11.3 Evaluation of entry foci dynamics....78
2.11.4 Evaluation of *Shigella*'s intracellular motility....79
2.11.5 RACK1 localization during *Shigella* infection....80
2.11.6 LC3 targeting of *Shigella*....81
2.11.7 Aqueous two-phase (ATP) infection system....82
2.11.8 Modified plaque assay....83
2.11.9 Real-time monitoring of *Shigella* cell-to-cell spreading....84
2.12 Characterizations of the role of RACK1 in actin cytoskeleton dynamics....85
2.12.1 Analysis of actin polymerization and depolymerization using actin-binding drugs....85
2.12.2 Fluorescence Recovery After Photobleaching (FRAP)....86
CHAPTER 3 RESULTS....91
3.1 RACK1 silencing and characterization....91
3.2 RACK1 modulates Shigella infection of HeLa cells and *Drosophila melanogaster*....98
3.2.1 Silencing RACK1 impairs *Shigella* growth in HeLa cells....98
3.2.2 RACK1 silencing protects *Drosophila* melanogaster from *Shigella* infection....110

3.2.3 Steps of *Shigella* intracellular life cycle studied in this project. 113

3.3 RACK1 silencing reduces *Shigella* invasion of HeLa cells 115

3.4 Study of the role of RACK1 in vacuolar escape 126

3.5 Study of RACK1 functions during *Shigella* intracellular replication and cell death induction 133

3.6 RACK1 silencing affects actin tail polymerization 142

3.7 RACK1 silencing inhibits *Shigella* cell-to-cell spreading 151

3.8 RACK1's role in actin cytoskeleton dynamics 159

CHAPTER 4 DISCUSSION 170

4.1 RACK1 promotes *Shigella* infection in vitro and in vivo 171

4.2 *Shigella* requires RACK1 to manipulate the host actin cytoskeleton 175

4.2.1 RACK1 promotes *Shigella* invasion of HeLa cells 175

4.2.2 RACK1 is not involved in *Shigella* vacuolar escape 179

4.2.3 RACK1 silencing does not impact *Shigella* intracellular replication or apoptosis inhibition 182

4.2.4 RACK1 promotes *Shigella* actin tail polymerization, actin-mediated motility and cell-to-cell spreading 184

4.3 RACK1 plays a role in actin filament turnover 191

4.4 Model of RACK1 function in *Shigella* infection 195

4.5 Concluding remarks and further work 199

APPENDIX A Media, buffers, and other solutions 201

APPENDIX B Fiji macros and R scripts 203

APPENDIX C Supplementary figures 228

BIBLIOGRAPHY 231

LIST OF TABLES

Table 2.1. Bacterial strains used in this study.....46

Table 2.2. Plasmids used in this study 47

Table 2.3. Oligonucleotides used in this study 56

Table 2.4. Antibodies and fluorescent dyes used in this study 63

Table 2.5. Microscopes used in this study and its specifications.....88

Table 3.1. Percentage of *Shigella* targeted by GBP1 in control (NS) and RACK1-KD (KD-92) HeLa cells treated with IFN-γ or Ruxolitinib (RUX). 136

Table 3.2. Cytoskeleton related proteins identified as RACK1 binding partners by Co-IP-MS 164

LIST OF FIGURES

Figure 1.1. *Shigella* secretes T3SS effectors that trigger profuse actin polymerization leading to epithelial cell invasion. 12

Figure 1.2. *Shigella* escapes the endocytic vacuole generating membrane remnants that trigger xenophagy. 19

Figure 1.3. *Shigella* induces actin polymerization to form an actin tail which mediates intracellular motility. 28

Figure 3.1.1. RACK1 expression silencing using shRNAs delivered by lentiviruses. 94

Figure 3.1.2. HeLa cells differentially maintain RACK1 silencing efficiency. 95

Figure 3.1.3. RACK1 silencing affects cell proliferation but not cell size. 96

Figure 3.1.4. RACK1 expression was silenced in CaCo-2 but not in HT-29 cells. 97

Figure 3.2.1. Standardization of HeLa cells infected by *Shigella flexneri*. 103

Figure 3.2.2. RACK1 silencing inhibits *Shigella* growth in HeLa cells. 105

Figure 3.2.3. *Shigella* growth impairment was confirmed in RACK1-KD cells using an aqueous two-phase (ATP) infection system. 107

Figure 3.2.4. Stable RACK1 overexpression promotes *Shigella* growth in HeLa cells. 108

Figure 3.2.5. Transient RACK1 overexpression promotes *Shigella* growth in HeLa cells. 109

Figure 3.2.6 RACK1 silencing protects *Drosophila melanogaster* from *Shigella* infection. 111

Figure 3.2.7. Critical steps of *Shigella* intracellular life cycle studied in this project. 114

Figure 3.3.1. RACK1 is recruited to *Shigella*'s entry focus in HeLa cells. 119

Figure 3.3.2. RACK1 silencing increases entry foci duration but does not affect foci area or fluorescence intensity. 121

Figure 3.3.3. Silencing RACK1 reduces the actin polymerization rate to *Shigella*'s entry focus. 123

Figure 3.3.4. Knocking down RACK1 expression reduces *Shigella* entry into HeLa cells. 124

Figure 3.4.1. RACK1 does not localize to the *Shigella* containing vacuole, and it is not required for vacuolar escape. 129

Figure 3.4.2. Evaluation of endocytic markers and LC3 recruitment to *Shigella*..... 131

Figure 3.5.1. RACK1 does not play a role in *Shigella*'s intracellular replication. 137

Figure 3.5.2. Silencing of RACK1 expression does not affect *Shigella*-induced cell death. 139

Figure 3.5.3. Targeting of *Shigella* by guanylate-binding protein (GBP) 1 and 4 is not affected by RACK1 silencing. 141

Figure 3.6.1. RACK1 does not localize to *Shigella*'s actin tail, but it is required for efficient actin tail polymerization. 146

Figure 3.6.2. RACK1 silencing impairs actin tail elongation. 148

Figure 3.6.3. Knocking down RACK1 expression reduces *Shigella*'s actin-mediated motility. 149

Figure 3.7.1. Plaque assay procedure and data analysis. 154

Figure 3.7.2. Methocel efficiently restricts *Shigella* diffusion through the media reducing secondary plaque formation. 155

Figure 3.7.3. RACK1 silencing reduces the plaque area formed by *Shigella* in HeLa and CaCo-2 cells. 156

Figure 3.7.4. *Shigella* requires RACK1 for efficient cell-to-cell spreading in HeLa cells. 157

Figure 3.8.1. Study of RACK1 interactome in *Shigella*-infected HeLa cells. 163

Figure 3.8.2. RACK1 is not required for Arp-2 recruitment to *Shigella*. 165

Figure 3.8.3. Filamentous-actin (F-actin) aggregate formation is reduced in RACK1-KD cells treated with jasplakinolide. 166

Figure 3.8.4. Cytochalasin D (CytoD) mediated disruption of filamentous actin (F-actin) is not affected by RACK1 silencing. 167

Figure 3.8.5. RACK1 silencing affects actin turnover in membrane ruffles but not in stress fibres. 168

Figure 4.1. Model of RACK1 function in *Shigella* infection. 197

ABSTRACT

Shigella flexneri, the causative agent of the acute diarrheal disease shigellosis, manipulates the host actin cytoskeleton to infect intestinal epithelial cells (ECs). *Shigella* secretes bacterial effectors into the EC cytoplasm, inducing actin polymerization at the entry site. After cell invasion, *Shigella* escapes the endocytic vacuole accessing the cytoplasm, where the pathogen polymerizes an actin tail acquiring actin-mediated motility. Propelled by the actin tail, *Shigella* generates a bacterium-containing membrane protrusion that infects neighbouring cells. The receptor for activated C kinase 1 (RACK1) is a scaffolding protein that provides a platform for protein-protein interactions playing pivotal roles in host cell homeostasis. However, the role of RACK1 in bacterial pathogenesis is unclear. RACK1 binds to the focal adhesion kinase and actin-binding proteins, allowing proper focal adhesion assembly and cell migration; thus, I hypothesized that RACK1 promotes *Shigella*-mediated induction of actin polymerization. Live-cell microscopy and automated image data analysis were used to characterize the role of RACK1 in *Shigella* infection. I found that RACK1 silencing in HeLa cells reduced the yield of *Shigella* recovered from within ECs, due to cell invasion impairment and cell-to-cell spreading inhibition. RACK1 was recruited to the entry focus promoting *Shigella*-mediated induction of actin polymerization and internalization. RACK1 also promoted actin tail polymerization and actin-mediated motility, resulting in effective cell-to-cell spreading. In contrast, RACK1 silencing did not affect *Shigella*'s escape from the vacuole or intracellular replication. Moreover, RACK1 depletion in *Drosophila melanogaster* enterocytes reduced mortality of *Shigella*-fed flies. Furthermore, RACK1 silencing inhibited jasplakinolide-induced actin polymerization and reduced actin turnover in membrane ruffles but not in stress fibres. In conclusion, I report a novel function of RACK1 promoting *Shigella* invasion and spreading in ECs and colonization of *Drosophila*'s intestine. My findings also suggest RACK1 function in actin polymerization is not restricted to *Shigella* infection.

LIST OF ABBREVIATIONS USED

°C	Degrees Celsius
A	Amperes
Abl	Abelson Murine Leukemia Kinase
AfaI	Afimbrial Adhesin From *E. coli*
ANOVA	Analysis Of Variance
Arp2/3	Actin-Related Protein 2/3 Complex
ATP	Aqueous Two-Phase Infection System
Blast	Blasticidin
Cdc42	Cell Division Control Protein 42
CFU	Colony-Forming Units
Co-IP	Co-Immunoprecipitation
CytoD	Cytochalasin D
DAPI	4',6-Diamidino-2-Phenylindole, Dihydrochloride
dsRED	*Discosoma* sp. Red Fluorescent Protein
EC	Epithelial Cell
EEA1	Early Endosome Antigen
F-actin	Filamentous Actin
FAK	Focal Adhesion Kinase
FBS	Fetal Bovine Serum
FI	Fluorescence Intensity
FRAP	Fluorescence Recovery After Photobleaching
G-actin	Globular Actin
Gal-3	Galectin-3
GAPs	GTPase-Activating Proteins
GBPs	Guanylate-Binding Proteins
GEFs	Guanine Nucleotide Exchange Factors
GFP	Green Fluorescent Protein
GTPase	Guanosine Triphosphatase
h	Hours

HEPES	4-(2-Hydroxyethyl)-1-Piperazineethanesulfonic Acid
HRP	Horseradish Peroxidase
IcsA	Intracellular Spread A
IF	Immunofluorescence
IFN-γ	Interferon-Gamma
Jasp	Jasplakinolide
KD	Knock Down
LB	Lysogeny Broth
LC3	Microtubule-Associated Protein 1A/1B-Light Chain 3
LDH	Lactate Dehydrogenase
LSM	Laser Scanning Microscopy
MAPK	Mitogen-Activated Protein Kinase
mCherry	Monomeric Cherry
min	Minutes
MOI	Multiplicity Of Infection
MS	Mass Spectrometry
MTT	3-[4,5-Dimethylthiazol-2-Yl]-2,5-Diphenyltetrazolium Bromide
N-WASP	Neuronal-Wiskott Aldrich Syndrome Protein
ns	Not Significant
OD	Optical Density
PBS	Phosphate-Buffered Saline
PEI	Polyethyleneimine
PMN	Polymorphonuclear Leukocyte
pOrange	Orange Fluorescent Protein
Puro	Puromycin
PVDF	Polyvinylidene Difluoride
Rab11	Ras-Associated Binding
Rac1	Ras-Related C3 Botulinum Toxin Substrate 1
RACK1	Receptor for Activated C Kinase 1
ROI	Region of Interest
SCV	*Shigella* Containing Vacuole

SD	Standard Deviation
SDS-PAGE	Sodium Dodecyl Sulfate-Polyacrylamide Gel Electrophoresis
sec	Seconds
SFs	Stress Fibres
shRNA	Short Hairpin RNA
Src	Sarcoma Tyrosine Kinase
T3SS	Type 3 Secretion System
TSB	Tryptic Soy Broth
V	Volts
WB	Western Blot
WT	Wild Type
X	Times
Δ	Delta

ACKNOWLEDGEMENTS

During my Ph.D., I have been fortunate to be surrounded by friends and mentors who supported me and made my learning journey very enjoyable and fulfilling. I want to thank my supervisor, Dr. Zhenyu Cheng and co-supervisor, Dr. John Rohde, for their constant support and guidance. To my committee members, Dr. John Archibald, Dr. Song Lee, and Dr. James Fawcett thank you for sharing your expertise with me and helping me focus my research efforts. Special mention to Dr. Rohde and Dr. Lee for always having a door open for a quick chat. Your experience and insight were very helpful to my thesis project and my career development.

To past and present members of the Cheng Lab, thank you for your friendship and support through the highs and lows of completing my Ph.D. I could not have asked for better lab mates. I also want to thank my family for their endless encouragement and love. Thank you for believing in me.

Lastly, I would like to acknowledge the funding agency Agencia Nacional de Investigación y Desarrollo, for providing a four-year scholarship (folio 72160538). I also like to acknowledge MITACS for providing a scholarship to go to Pasteur Institute (Paris) and learn the live-cell imaging used throughout this study.

CHAPTER 1 INTRODUCTION

1.1 Overview

Infectious diseases are caused by pathogenic microorganisms, from which bacterial infections remain a substantial cause of morbidity and mortality. These infections are commonly transient in a healthy host or are treated with antibiotics. The host's innate immune system recognizes the invading pathogen, triggering antimicrobial and inflammatory responses upon bacterial colonization. Innate immune cells, such as macrophages and neutrophils, perform the clearing of most intruders. However, some bacterial pathogens have evolved mechanisms to survive and even replicate inside these cells.

Intracellular bacteria can cause acute or persistent infections characterized by immune evasion and sophisticated modulation of the host cell machinery. For example, *Shigella flexneri*, the causative agent of the acute diarrheal disease shigellosis, thrives inside macrophages and epithelial cells [1]. To invade and replicate intracellularly, *Shigella* extensively manipulates host functions. This pathogen targets the host cytoskeleton, exploiting actin polymerization to invade cells [2]. After cell invasion, *Shigella* escapes the containment of the phagocytic vacuole, accessing the cytoplasm where nutrients are readily available [3]. However, in the cytoplasm, *Shigella* faces immune surveillance mechanisms that trigger autophagy and apoptosis [1]. Thus, *Shigella* must replicate without disturbing host cell function and actively inhibit cytoplasmic surveillance. Nevertheless, the most surprising mechanism of *Shigella* pathogenesis is the ability to induce polymerization of an actin tail that confers intracellular motility and mediates cell-to-cell spreading [4].

Despite extensive study of *Shigella* pathogenesis, the puzzle of *Shigella*-host interactions is far from complete. Most studies have been restricted to characterizing how *Shigella* escapes immune recognition. However, there is a lack of understanding regarding *Shigella*'s reliance on the host factors that maintain cell homeostasis. One such host factor is the Receptor for Activated C Kinase 1 (RACK1). As a scaffold protein, RACK1

participates in numerous aspects of cellular function in eukaryotic organisms, such as protein shuttling, protein activity stabilization, and signalling [5]. In mammals, RACK1 has been shown to promote hepatitis C viral translation [6]. Protein-protein interaction screenings have shown secreted effectors of the intracellular bacteria *Yersinia*, *Mycobacterium,* and *Helicobacter* bind to RACK1 [7–97], exerting various functions. Moreover, RACK1 is required for innate immune pathway activation in *Caenorhabditis elegans* infected with *Shigella* [10].

Shigella's fine-tuning of cellular function results from millions of years of adaptation to humans. In the present study, I seek to understand the role of the highly conserved host scaffold protein RACK1 in *Shigella* infection. In the introductory chapter, I describe in detail the intracellular life cycle of *Shigella* and how this pathogen modulates the host actin cytoskeleton. Then, I provide a brief review of the known RACK1 functions, highlighting the importance of RACK1 in cytoskeleton homeostasis, followed by a summary of RACK1's functions in host-pathogen interactions. Finally, I state my hypothesis and specific objectives of this project.

1.2 *Shigella* and shigellosis

Members of the genus *Shigella* are the causative agents of shigellosis, an acute intestinal infection [11]. Shigellosis is a self-limited disease, the symptoms of which can range from mild watery diarrhea to severe inflammatory dysentery characterized by intense abdominal cramps, fever, blood and mucus in the stools (dysentery) [12]. However, shigellosis may become life-threatening for patients with a weakened immune system or if adequate medical care is unavailable, causing high mortalities [11]. According to global disease burden estimates, *Shigella* is the second leading cause of diarrhea mortality in all age groups [13]. Children younger than five years and adults older than 70 years are at a higher risk of dying from shigellosis [13]. Increased shigellosis morbidity among men who have sex with men has been reported [14,15]. Morbidity is also common among travellers returning from developing countries [16] (traveller's diarrhea).

Lack of sanitation and hygiene systems in developing countries and natural disaster areas create optimal conditions for *Shigella* spreading. Most shigellosis cases are sporadic in industrialized countries. Outbreaks are often caused by asymptomatic carriers with poor personal hygiene handling food [17]. Shigellosis is transmitted through the fecal-oral route and contaminated water or food consumption. The infection dose of *Shigella* is as low as ten bacteria [18]; thus, transmission in crowded or poor sanitation settings is highly effective. The fact that humans are the only natural reservoir for *Shigella* implies that an asymptomatic percentage of the population maintains the global burden of shigellosis [19,20].

The genus *Shigella*, composed of non-motile, non-sporulating Gram-negative rods, is part of the large Enterobacteriaceae family. There are four *Shigella* species divided into serotypes based on their O-antigen: *S. flexneri* and *S. boydii* with 19 serotypes each, *S. dysenteriae* with 15 serotypes, and *S. sonnei* with one serotype [21]. *S. flexneri* is the most prevalent species in developing countries, whereas *S. sonnei* is predominant in industrialized countries [17,22]. Although *S. dysenteriae* is rarely isolated nowadays [23,24], this species caused epidemics characterized by severe disease and high mortalities[25,26]. *S. dysenteriae* serotype 1 produces Shiga toxin, a potent virulence factor that halts protein synthesis, leading to the destruction of endothelial cells and subsequent dysentery [27]. A further complication caused by Shiga toxin-producing *S. dysenteriae* is the development of Haemolytic-Uremic Syndrome (HUS), characterized by hemolysis and renal failure with about a 36% mortality rate [28]. Post-reactive arthritis is another complication of shigellosis, occurring in 2 to 7% of people infected with *S. flexneri*. Joint inflammation can last for months or years and, in some cases, lead to chronic arthritis [29,30].

Shigella species are becoming alarmingly more resistant to the first and second-line treatments of ciprofloxacin and azithromycin, respectively [31]. Resistance genes from other enteropathogens have been found in *Shigella* species, suggesting horizontal transfer in the human gut [32,33]. In particular, *S. sonnei* has been shown to rapidly acquire and disseminate resistance genes through mobile genetic elements [22,34]. The emergence of multidrug-resistant *Shigella* strains presents a significant public health challenge and underpins the growing need for vaccines against *Shigella* infections. Unfortunately, despite multiple

trials, no vaccine against shigellosis has been approved yet [35]. The wide variety of *Shigella* serotypes and their differential geographical distribution complicates vaccine development. In this regard, *S. flexneri*, *S. sonnei* and the potentially epidemic *S. dysenteriae* type 1 strains should most critically be included in a polyvalent formulation [23,24]. Delivery of effective and cheap *Shigella* vaccines could control shigellosis independently of health infrastructure improvements in developing countries, halting the spread of multidrug resistance among enteropathogens.

1.3 *Shigella flexneri* pathogenesis

Most of what is known regarding *Shigella* pathogenesis mechanisms is derived from studies of *S. flexneri*. This species was the second member of the *Shigella* genus described, initially reported by Simon Flexner in 1900 [36]. More than 100 years later, *S. flexneri* continues to be a primary etiological agent of foodborne diarrhea [23]. The pathogenicity of *S. flexneri* (hereafter referred to as *Shigella*) is driven by its ability to invade the colonic epithelium. But first, *Shigella* circumvents host barriers such as stomach acid, the microbiota, and the mucus layer of the intestine. Acid resistance is given by the regulator *rpoS* [37]. Evidence shows that *Shigella* species produce colicins, antibacterial proteins that reduce *E. coli* competition in the gut [38]. Secretion of mucinase and neuraminidase could alter mucus integrity, although the role of these enzymes in *Shigella* virulence is not well characterized [39].

After crossing the mucus layer, *Shigella* targets specialized epithelial cells (ECs) called microfold (M) cells. The primary function of M cells is to sample and transport antigens by transcytosis (vesicular transport) from the intestine lumen to the lymphoid cells underneath the epithelium [40]. *Shigella* exploits the transcytosis function of M cells to access the subepithelial space and invade colonic ECs through the basolateral end [41–43]. It was recently confirmed that *Shigella* also invades the cytoplasm of M cells, spreading directly from their cytosol to neighbouring enterocytes [44]. In the subepithelial space, resident macrophages phagocytose *Shigella.* Yet, instead of degrading the incoming pathogen, infected macrophages become factories for *Shigella* replication because *Shigella* exits the

phagosome to replicate in the macrophage's cytoplasm, triggering rapid lytic cell death releasing *Shigella* to infect colonic ECs [45].

In macrophages, *Shigella* triggers a newly characterized form of cell death denominated pyroptosis [46–48]. This inflammatory cell death mechanism involves inflammasome-mediated activation of the protease caspase-1 [48,49]. Cytoplasmic *Shigella* is recognized by the NLRC4/NLRP3-inflammasomes, leading to caspase-1 activation and subsequent processing of Gasdermin D (GSDMD), interleukin-1β (IL-1β) and interleukin-18 (pro-IL-18) [50–52]. Cleaved GSDMD targets the cellular membrane, assembling into a permeability pore and causing cell lysis [53]. When macrophages lyse, *Shigella* and the pro-inflammatory cytokines IL-1β and IL-18 are released. Both cytokines contribute to the acute inflammatory response characteristic of Shigellosis [54,55]. IL-18 promotes the production of interferon-gamma (IFN-*γ)* from natural killer (NK) lymphocytes. IFN-*γ* is essential for the control of *Shigella* infection in mice [56]. Whereas IL-1β facilitates *Shigella* infection progression as shown in rabbits treated with an IL-1 receptor antagonist [55]. Moreover, *IL-1β*$^{-/-}$ mice infected with *Shigella* present less inflammation and minor *Shigella* invasion of tissue [54]. These findings suggest that inflammation in response to *Shigella* infection initially promotes further bacterial spreading in the colonic epithelium.

Profuse polymorphonuclear leukocyte (PMN) recruitment to the site of infection is one of the hallmarks of Shigellosis [57]. Macrophage-released IL-1β starts the PMN influx [55]. However, most PMN infiltration is triggered by IL-8 released from *Shigella*-infected epithelial cells [58,59]. PMNs arrive at the basolateral side of the epithelium and migrate into the intestine lumen, where they ingest and destroy bacteria [60,61]. Paradoxically, PMNs arrest further *Shigella* translocation into the subepithelial space while simultaneously enabling bacterial translocation without the need for M cells [62,63]. This is due to PMN releasing proteolytic enzymes, such as myeloperoxidases, that actively destroy tissue [64]. *Shigella* exploits the damage induced by PMNs to further invade the epithelium [63]. It has been reported that *Shigella* finely tunes PMN recruitment by secreting a serine protease that functions as a PMN chemoattractant and the effector proteins OspB, OspC1 and OspZ to promote PMN migration [65–68]. On the other hand, *Shigella* represses PMN recruitment by

dampening transcription of IL-8 and other genes involved in immune responses by the action of the bacterial effector OspF [69]. *Shigella* cannot escape the phagosome within PMNs, and PMN extracts effectively kill *Shigella in vitro* [62,70]. Therefore, PMNs not only contribute initially to the severe tissue damage characteristic of shigellosis but eventually, PMNs tilt the balance towards *Shigella* elimination, resolving the infection in healthy individuals [23].

In summary, macrophage inflammatory cell death (pyroptosis), the release of pro-inflammatory cytokines (IL-1β, IL-18, IL-8), and concomitant PMN-mediated epithelium damage are essential for the establishment of infection. Moreover, the severe tissue destruction observed in *Shigella*-infected patients results mainly from the damage to the epithelium caused by the acute inflammatory response [57].

1.4 *Shigella* life cycle within the epithelial cell

1.4.1 The making of an invasive pathogen

Shigella species are traditionally classified by their biochemical properties and serological reactivity [71]. However, comparative genomics shows that *Shigella* species are specialized lineages derived from the gut commensal *Escherichia coli* [72], perhaps the species classification is obsolete. It was estimated by phylogenetic analysis of eight housekeeping genes that three major clusters of *Shigella* evolved separately within the last 35,000 to 270,000 years [73]. *S. sonnei* belongs to a newer group outside of the major three clusters that diverged in the 17th century and rapidly adapted to humans living in the developed world [74,75]. What makes *Shigella* an invasive pathogen is also answered by comparative genomics. Consecutive genetic events where *Shigella* acquired a large virulence plasmid and chromosomal pathogenicity islands led to the evolution of invasive *Shigella* species [76]. In the process, *Shigella* also disposed of genetic loci that attenuated virulence or were no longer needed for intracellular life, such as *cadA* and *ompT* [77,78]. The surface protease OmpT attenuates virulence by interfering with the expression of the motility protein IcsA, and *cadA* encodes a lysine decarboxylase that inhibits *Shigella*'s

enterotoxic activity [77,78]. In this manner, *Shigella* species became highly specialized, human-specific pathogens tailored to interact with the host intestinal mucosa.

Shigella's ability to invade ECs is mainly determined by its virulence plasmid pWR100 [79,80]. The genes necessary for invasion are within a 31-kb region of the plasmid, which encodes all the components required to assemble a type III secretion system (T3SS) and most of the proteins secreted by this machinery [81,82]. T3SSs are needle-like apparatuses spanning the membranes of pathogenic Gram-negative bacteria that allow injection of effector proteins into the host cell cytosol [83]. *Shigella*'s T3SS protein components are encoded in the pWR100 by the *mxi/spa* (membrane expression of *ipa*/surface presentation of *ipa*) operon [84,85]. Significantly, assembly and activation of the T3SS are tightly regulated by a repressor histone-like nucleoid structure (H-NS), and three transcription factors named virulence gene F (VirF), VirB, and MxiE. Temperatures above 32 °C trigger the release of H-NS from *virF* permitting VirF expression [3,86]. VirF controls the expression of VirB which subsequently activates the expression of the *mxi/spa* operon and the invasion plasmid antigen (*ipa*) genes *ipaABCD* [87,88]. The protein products of the mentioned operons are the building blocks of the T3SS. The *mxi-spa* T3SS structure consists of a cytoplasmic C-ring, a basal body (MxiD/G/J) crossing inner and outer membranes, the rod (MxiI) and the needle (MxiH) [89]. The translocator proteins IpaB and IpaD assemble at the tip of the needle [3,90,91]. Regulation of T3SS protein synthesis ensures the apparatus is not assembled before encountering the host.

Once the T33SS is assembled, host membrane sensing is the cue that triggers secretion. Transcriptional reporters of T3SS secretion demonstrated that the T3SS is under on-off regulation during the various stages of *Shigella*'s intracellular life cycle. Upon membrane sensing by IpaB at the tip of the T3SS, IpaB inserts its C-terminus domain in the host cell membrane triggering the secretion of IpaC, which is also inserted forming the translocon [92–94]. After the invasion of the EC, *Shigella* continuously secret effectors while within the vacuole. The T3SS becomes inactive after vacuolar escape until *Shigella* reencounters the host membrane due to intracellular motility.

Through the active T3SS, *Shigella* injects approximately 30 effector proteins into the host cytosol that trigger bacterial uptake by the EC and interfere with many other cell signalling pathways [81,95,96]. The T3SS effectors can be classified according to the timing of gene expression [1,97]. The first group of effectors is produced independently of the T3SS activation and includes IpaA/B/C/D, IcsB, invasion plasmid gene (Ipg)B1/2, IpgD, outer *Shigella* protein (Osp)C2-4, OspD1/2 [86]. The second group of effectors is expressed under non-secreting conditions and upregulated after T3SS activation. These genes encode OspB, OspC1, OspF, and VirA effectors [86]. The expression of a third group is triggered by T3SS activation and comprises OspD3, OspE1/2, OspG, IpaH1/2, IpaH4.5, IpaH7.8 and IpaH9.8 [86]. VirB is the central transcription regulator of the first group of secreted effectors, while the second and third group expression is MxiE dependent [86]. Functionally, the first set of effectors mainly induces actin cytoskeleton reorganization to promote bacterial invasion of ECs. They are followed by the second and third group, which modulate cell death and dampen innate immune responses [1].

1.4.2 Invasion of the epithelial cell

Shigella invades colonic ECs from their basolateral side, but contrary to most invasive pathogens, *Shigella* lacks any classical adhesin [98]. The absence of dedicated bacterial attachment proteins most likely accounts for *Shigella*'s moderate capacity to invade cultured cells *in vitro* [99]. However, *Shigella* is a highly efficient invasive pathogen *in vivo*. Hence, *Shigella* must deploy alternative strategies to attach to ECs. The outer membrane protein intracellular spread A (IcsA), whose primary role is to confer actin-mediated motility, has been shown to react to bile salts and become adhesive in a T3SS dependent manner [100,101]. Recently, a specific adhesion domain that binds to an unidentified host receptor was found in IcsA; deletion of this region reduced *Shigella* invasion [102]. Moreover, cholesterol-rich areas of the EC membrane, where the two receptors Cluster of Differentiation 44 (CD44) and $\alpha_5\beta_1$ integrin are found, serve as sites for *Shigella* binding [103,104]. IpaB, IpaC, and IpaD, located at the tip of the T3SS, directly bind to $\alpha_5\beta_1$, and IpaB interacts with CD44 [104,105]. Antibody-mediated blocking of the IpaB-CD44 interaction inhibits *Shigella* entry into HeLa cells [105]. Sensing the host membrane by the tip complex

activates the T3SS, leading to IpaB-IpaC insertion into the host membrane forming a pore, denominated translocon, through which bacterial effectors are secreted into the host cytoplasm [93,97,106].

Shigella extensively manipulates the host cytoskeleton as part of its strategy to invade cells. Translocation of pre-formed bacterial effectors triggers actin polymerization, resulting in filamentous (F-) actin accumulation and extensive membrane ruffling at the entry site (entry foci, Figure 1.1). To achieve this, *Shigella* effectors hijack the function of Rho (Ras homologous) small GTPases, tyrosine kinases, and actin-binding proteins [107–109]. The Rho family of small GTPases are core regulators of actin cytoskeleton rearrangements and are tightly regulated. Small GTPases function as molecular switches that alternate between the GTP-bound active and GDP-bound inactive forms. Guanine nucleotide exchange factors (GEFs) activate small GTPases, whereas GTPase-activating proteins (GAPs) inactivate them [110]. Activation of the Cell division control protein 42 (Cdc42), Rac1 (Ras-related C3 botulinum toxin substrate 1) and RhoA small GTPases trigger the assembly of cytoskeletal structures, such as filopodia, lamellipodia and stress fibres [111]. Upon translocon assembly in the host cell membrane, the C-terminus of IpaC indirectly activates Cdc42 and Rac1, triggering actin polymerization [112–114]. In addition, IpaC binds to and activates the sarcoma (Src) tyrosine kinase, which phosphorylates the actin-binding protein cortactin (Figure 1.1). Active cortactin forms a complex with the adapter protein Crk (chicken tumour virus number 10 regulator of kinase), triggering binding and activation of the Actin-related protein 2/3 (Arp2/3) complex [115,116]. The Arp2/3 complex is an actin nucleator that promotes actin filament branching, creating actin networks underneath the cell membrane (Figure 1.1) [117].

The Abelson murine leukemia (Abl) kinase, another host tyrosine kinase involved in actin dynamics, is activated during the initial stages of *Shigella* infection, although no bacterial effector has been found to directly target Abl [118]. Activated Abl phosphorylates Crk, possibly facilitating cortactin-mediated actin polymerization (Figure 1.1) [115,118]. Moreover, the T3SS effectors IpgB1 and IpgB2 mimic the function of GEFs to further induce actin polymerization by maintaining Rac1, Cdc42 and RhoA in their active state

(Figure 1.1) [119–121]. VirA, described initially as a cysteine protease that severs microtubules, has also been linked to *Shigella* entry [122,123]. VirA induces membrane ruffles in a Rac1 dependent manner, promoting invasion [122,124]. However, instead of a protease, VirA functions as a GAP to inactivate Rab1, although how Rab1 inactivation promotes *Shigella* invasion is unclear [125–127].

Besides GTPases and kinases, *Shigella* also targets the membrane phospholipid phosphatidylinositol 4,5-bisphosphate (PIP_2) via the secreted effector IpgD [128,129]. PIP_2 is one of seven phosphoinositides. These phospholipids regulate remodelling of the actin cytoskeleton and other cellular functions by acting as a platform for protein recruitment to intracellular membranes [130]. IpgD is an inositol 4-phosphatase that hydrolyzes PIP_2 to produce phosphatidyl-inositol 5-phosphate (PI5P) [129]. Accumulation of PI5P disconnects the subcortical actin cytoskeleton from the membrane, thereby promoting membrane ruffling (Figure 1.1) [129]. *Shigella* also regulates Ca^{2+} signalling through the function of IpgD [131,132]. PIP_2 is the precursor of inositol 1,4,5-trisphosphate (IP_3), regulating cytoplasmic Ca^{2+} levels [133]. IpgD-mediated depletion of PIP_2 results in a decrease of IP_3 production, leading to inhibition of Ca^{2+} release from the endoplasmic reticulum [132]. Additionally, *Shigella* restricts diffusion of preformed IP_3 by enrichment of IP_3 receptors at the entry site, triggering long-lasting local Ca^{2+} responses [134]. These local Ca^{2+} signals are involved in *Shigella* entry as demonstrated by impaired *Shigella* actin foci formation in cells treated with a Ca^{2+} chelator [131,135].

F-actin polymerization is a highly dynamic process correlated with actin disassembly [136]. *Shigella*-induced entry foci rely on rapid polymerization and depolymerization of actin. Therefore, *Shigella* uses one more tool from its repertoire to regulate actin depolymerization. The T3SS effector IpaA binds to vinculin, an actin-binding protein enriched at cell-matrix adhesion complexes called focal adhesions [137,138]. Active vinculin binds to the actin filament barbed end, preventing actin polymerization (capping activity, Figure 1.1) [139]. IpaA possesses three regions that strongly bind to vinculin, activating its caping function as demonstrated by increased F-actin depolymerization *in vitro* and *in vivo* [138,140–142]. IpaA deletion reduces *Shigella* invasion ten times compared to the wild-type

bacterium, confirming actin depolymerization's critical role in regulating membrane protrusions during *Shigella* entry [137].

The focal adhesion protein, talin, is also targeted by IpaA [143]. Talin binds to integrins and vinculin, connecting the two to strengthen focal adhesions [144]. One of the three vinculin-binding domains of IpaA also binds talin suggesting a competitive interaction between IpaA, talin and vinculin [145]. Talin is enriched around *Shigella* at the entry site in an IpaA dependent manner, and silencing talin reduces *Shigella* invasion [145]. Interestingly, talin is predominantly found at the filopodial tip during *Shigella* infection [145]. This observation supports previous findings that suggest *Shigella* invades cells from the apical side [146]. Filopodial capture has been observed *in vitro*. Polarized intestinal epithelial cells initially capture *Shigella* through filopodia, which then retract, bringing *Shigella* close to the cell body, where invasion proceeds [146]. Taken together, *Shigella* promotes F-actin foci formation and membrane remodelling, forcing uptake by epithelial cells through complex and coordinated processes involving numerous effectors.

Figure 1.1. *Shigella* secretes T3SS effectors that trigger profuse actin polymerization leading to epithelial cell invasion.
Sensing the host membrane by the translocon tip activates the T3SS, leading to IpaB-IpaC insertion into the host membrane forming a pore, through which bacterial effectors are secreted into the cytoplasm. These effectors trigger actin polymerization, resulting in filamentous (F-) actin accumulation (magenta) and extensive membrane ruffling at the entry focus. Actin polymerization is initiated by the T3SS effector IpaC, indirectly activating the small GTPases Cdc42 and Rac1. These GTPases activate N-WASP leading to Arp2/3 complex recruitment and polymerization of branched actin filaments. The T3SS effectors IpgB1 and IpgB2 maintain Rac1 and Cdc42 in a GTP-bound active state, enhancing actin polymerization. IpaC also interacts with the kinase Src which phosphorylates (P) the actin-binding protein cortactin. Active cortactin forms a complex with the adapter protein Crk following Crk activation by the kinase Abl. The cortactin-Crk complex recruits and activates Arp2/3. Actin turnover during invasion is regulated by the effector IpaA which binds to the actin-binding protein vinculin. Active vinculin binds to the actin filament barbed end (capping activity), promoting actin depolymerization and maintaining the globular (G) actin pool. The bacterial inositol 4-phosphatase IpgD hydrolyzes phosphatidylinositol 4,5-bisphosphate (PIP2) to produce phosphatidyl-inositol 5-phosphate (PI5P). Accumulation of PI5P in the cell membrane promotes membrane ruffling.

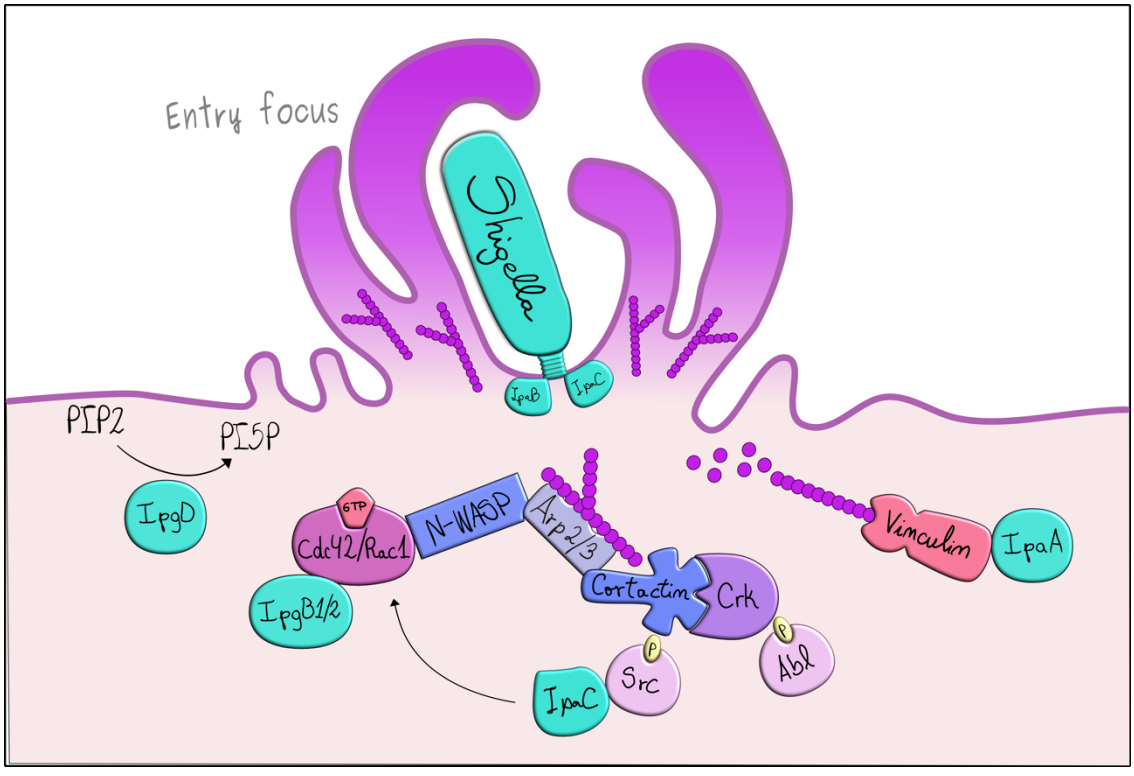

1.4.3 Vacuolar escape

In contrast to most intracellular bacterial pathogens, *Shigella* escapes the vacuole shortly (less than 10 min) after cell invasion to replicate in the cytoplasm [147]. Despite the substantial study of *Shigella*'s mechanisms of pathogenesis, the vacuolar rupture process remains poorly understood. Insertion of the T3SS translocon, formed by IpaB and IpaC, into the vacuolar membrane has been suggested as a mechanism of vacuolar damage (Figure 1.2). Indeed, insertion of the translocon proteins in the membrane of red blood cells exposed to *Shigella* induces hemolysis [92]. Given that IpaB and IpaC are absolutely required for invasion, their role in vacuolar escape is hard to dissect from the entry process. Nevertheless, *in vitro* studies demonstrated that purified IpaB and IpaC disrupt lipid vesicles [148,149].

Evidence supports a decisive role of IpaC in membrane lysis, as the heterologous expression of IpaC in the normally membrane-bound intracellular pathogen *Salmonella* leads to lysis of the vacuole [150]. Since macrophages phagocytose bacteria, infection of macrophages permits evaluation of bacterial vacuolar escape of the otherwise invasion deficient Δ*ipaB* mutant. Surprisingly, Δ*ipaB Shigella* remains trapped inside the phagosome, but it can still replicate inside it [151]. Macrophage infection could also be used to study Δ*ipaC Shigella*, but this mutant shows reduced macrophage invasiveness, suggesting that IpaC directs *Shigella* entry into macrophages [152]. A newer study demonstrated that the Δ*ipaB* mutant vacuolar exit is not entirely abrogated but delayed [45]. Similar results were found with a Δ*ipaH7.8 Shigella* strain [45]. IpaH7.8 is a ubiquitin ligase secreted through the T3SS with a significant role in macrophage cell death induction [50].

Innovative techniques such as time-lapse microscopy, small interfering RNA (siRNA) screens, and fluorescent reporters have shed light on *Shigella*'s vacuolar escape mechanisms [153]. The fact that no specific *Shigella* effector mutation completely abolishes vacuolar escape suggests this process is multifactorial, and perhaps host mechanisms are involved. Indeed, the knockdown of 32 host factors decelerates vacuolar rupture [154]. The most remarkable are endocytic markers Ras-associated binding (Rab) 5, Rab11 and early endosome antigen (EEA1), revealing a pivotal role of endocytic pathways in vacuolar

escape [154]. Rab5 and Rab11 belong to the Rab family of small GTPases, which bind and control most intracellular vesicle trafficking [155]. Rab5 tags early endosomes (EEs), phagosomes, and macropinosomes mediating the maturation of these compartments, whereas Rab11 regulates vesicular trafficking from EEs to the endocytic recycling compartment (ERC) [155,156]. Massive accumulation of Rab11 positive vesicles follows *Shigella* entry into epithelial cells along with transient recruitment of Rab5 EEs [154].

Descriptions of galectin-3 (Gal-3) as a novel tool to spot vacuolar lysis helped decipher the dynamics of Rabs recruitment to *Shigella* [147,157,158]. Gal-3 is a cytosolic protein, constitutively expressed in myeloid and ECs, that binds to exposed glycans in damaged membranes such as those induced by *Shigella*'s vacuolar escape (Figure 1.2) [159]. Time-lapse microscopy experiments confirmed Rab5 and Rab11 positive vesicles are found in the vicinity of the *Shigella*-containing vacuole (SCV) before Gal-3 recruitment [154,160]. Since phosphoinositides recruit Rab11 to vesicular membranes, the inositol 4-phosphatase IpgD was hypothesized as the *Shigella* effector modulating Rab11 positive vacuoles [161]. An IpgD deletion mutant and a phosphatase inactive IpgD mutant failed to recruit Rab11 positive vesicles [154]. Furthermore, both mutants showed delayed Gal-3 recruitment, demonstrating that the IpgD dependent Rab11 recruitment is required for efficient rupture of the SCV (Figure 1.2) [154,162]. Later reports identified the Rab11 positive vesicles as macropinosomes formed due to *Shigella*'s massive membrane ruffle induction that fuse back into the membrane, taking up extracellular fluid (Figure 1.2) [160,162].

A study using large volume correlative focused ion beam imaging coupled to scanning electron tomography (C-FIB/SET) revealed the ultrastructure of the invasion site microenvironment [162]. Initially, the vacuolar membrane tightly encloses *Shigella* in a compartment separated from the surrounding Rab11-tagged macropinosomes [162]. Subsequently, *Shigella* damages the vacuolar membrane, triggering Gal-3 recruitment accompanied by macropinosome binding to the damaged SCV [160,162]. Macropinosome attachment to the SCV membrane is facilitated by the exocyst complex, a multi-protein complex directing secretory vesicle transport [163]. Rab11 relocates the exocyst complex to the macropinosomes to tether them to the SCV proximity [160]. The macropinosomes then

assist *Shigella* exit from the SCV, followed by vacuole fragmentation into membrane remnants that quickly lose Gal-3 signal [158,160].

A newly identified *Shigella*-induced structure was recently characterized in detail. Rapid time-lapse imaging revealed that a thick actin-rich cage, coined as a cocoon, assembles around the SCV after internalization by ECs (Figure 1.2) [154,162]. *Shigella* actively induces actin polymerization of the cocoon, and its disassembly precedes vacuolar escape [158,164]. The actin cocoon is found in only 20% of WT *Shigella*, whereas > 80% of Δ*ipgD Shigella* are trapped inside the cocoon and show vacuolar escape impairment [154]. This finding supported the idea that actin cocoon polymerization was a host-induced event to restrict vacuolar escape. However, it was later shown that cocoon assembly-disassembly around the SCV is induced by *Shigella* and a crucial step required for efficient vacuolar escape [164].

The T3SS effector IcsB, a fatty acyltransferase, was identified as the primary regulator of cocoon assembly (Figure 1.2) [165,164]. IcsB mediates Cdc42 recruitment to the SCV. Subsequently, Cdc42 activates the Neuronal-Wiskott Aldrich syndrome protein (N-WASP) coupled to the Transducer of Cdc42-dependent actin assembly (Toca-1) protein. Then the Cdc42-N-WASP-Toca-1 complex triggers actin nucleation through the Arp2/3 complex (Figure 1.2) [164]. The cocoon then disassembles right before Gal-3 recruitment [158,164]. Although bacteria associated with cocoons take longer to escape the vacuole, they are more efficient in disentangling from the vacuole's membrane remnants and becoming motile afterwards [164]. Conversely, similar to Δ*ipgD*, the Δ*icsB* mutant shows more cocoon-positive bacteria along with delayed vacuolar escape [164]. Thus, other bacterial effectors and possibly host proteins are involved in actin cocoon polymerization. Furthermore, ectopic expression of IcsB promotes actin cytoskeleton disassembly in HeLa cells, suggesting that deletion of IcsB and possibly IpgD likely interferes with actin cocoon turnover [165]. The role of the actin cocoon in *Shigella* pathogenesis and the precise mechanisms involved in its polymerization-depolymerization remain to be fully characterized.

Consequently, these findings expose a complex mechanism underlying *Shigella* vacuolar escape that implicates mechanical damage of the membrane by insertion of the IpaB-IpaC translocon followed by IpgD-mediated subversion of the vesicular trafficking regulators Rab11 and exocyst to gain access to the host cytosol efficiently. Furthermore, a newly described mechanism of vacuolar escape regulation, the actin cocoon, facilitates recycling and removal of the SCV membrane remnants from *Shigella*.

1.4.4 Establishment of a replicative niche within the epithelial cell

Shigella establishes its replicative niche in the cytoplasm of ECs, where they are out of sight from the innate immune system (e.g., PMNs). However, ECs are armed with defence mechanisms against intracellular pathogens, such as endocytic degradation, autophagy recognition, pathogen-induced inflammatory responses, and the last resource, cell death. *Shigella* has evolved mechanisms to escape or counteract these antimicrobial defences and keep its replicative niche from cell death long enough to ensure replication.

As detailed in the previous section, *Shigella* stays inside the SCV for a short time, during which, *Shigella* actively blocks the endocytic maturation process (Figure 1.2). IpgD produces PI5P at the entry site, which accumulates in endosomal membranes [154,166], blocking the binding of late markers such as the Lysosomal-Associated Membrane Protein 1/2 (LAMP-1/2) [166]. SCV targeting by the early marker EEA-1 has not been reported suggesting *Shigella* halts maturation early after uptake. The ultimate escape from endocytic degradation is to exit the vacuole. However, SCV rupture and release of membrane remnants generate danger signals that trigger autophagy responses (Figure 1.2) [167,168]. A selective form of autophagy denominated xenophagy sequesters invading pathogens inside membranous compartments called autophagosomes that later fuse with lysosomes to degrade their content [169]. Xenophagy senses the damaged SCV and membrane remnants as they become ubiquitinated by the ubiquitin-ligase Leucine-Rich Repeat and Sterile Alpha Motif Containing 1 (LRSAM1, Figure 1.2) [168,170]. The autophagy receptors sequestosome 1 (p62) and nuclear dot protein 52 (NDP52) then bind to the ubiquitinated membranes and recruit the canonical autophagy markers microtubule-associated protein 1 light chain 3

(LC3) and autophagy-related 5 (Atg5) to initiate autophagosome formation (Figure 1.2) [167,168,171,172]. Likewise, the recruitment of galectins to damaged membranes triggers autophagy [159]. Galectin-3, -8 and -9 bind to damaged SCVs, from which galectin-8 recruits NDP52 and LC3 [157,173]. Although the role of galectin-3 and -9 in host defence against *Shigella* is not clear, it has been shown that galectin-3 accumulation to damaged phagosomes containing the foodborne pathogen *Listeria monocytogenes* suppresses galectin-8 recruitment and autophagy activation [174].

Shigella has developed strategies to escape xenophagy recognition. The secreted effectors VirA and IcsB act synergistically to antagonize this process (Figure 1.2), as demonstrated by the increased number of LC3-positive SCVs found in single and double mutants of VirA and IcsB [167,172]. Also, SCVs formed in these mutants are less likely to be targeted by galectin-3 and more often associated with the lysosomal marker LAMP-2 than the WT strain [172]. VirA functions as a GAP for Rab1 and IcsB is a fatty acyltransferase that inactivates Rho-GTPases. Therefore, these two effectors likely impair LC3 recruitment by blocking actin-based processes regulated by Rho-GTPases. Indeed, Leu *et al.* showed that IcsB modifies the Charged Multivesicular Body Protein 5 (CHMP5) involved in the sorting of endosomal cargo (Figure 1.2). Fatty acylation of CHMP5 by IcsB blocked LC3 recruitment to the SCV [165]. LC3 recruitment occurs exclusively on the SCV but not in cytosolic bacteria; thus, IcsB localization to the SCV membrane could modify membrane identity by inactivating RhoGTPase. [172]. The Δ*virA* and Δ*icsB* mutants seem to be trapped for a more extended period within the SCV, probably due to a lack of RhoGTPase inactivation leading to LC3 accumulation and increased susceptibility to lysosomal degradation. Toca-1 recruitment to the SCV is IcsB dependent and associated with less LC3 targeting (Figure 1.2), although the mechanism of LC3 displacement is not known [175]. It is thought that polymerization of an actin cocoon around the SCV, a process that relies on IcsB-mediated Toca-1 recruitment, physically blocks LC3 targeting [164]. Furthermore, deletion of the canonical autophagy-related protein Atg16L1 enhances *Shigella* killing by macrophages. The mechanism behind this phenotype is that non-selective autophagy, mediated by Atg16L1, reduces antibacterial oxidative stress in the cytoplasm of macrophages, decreasing microbicidal capacity [176].

It is plausible that Rab1 promotes the targeting of SCVs by xenophagy in epithelial cells since Rab1 is required for autophagosome assembly upon autophagy induction [177]. Therefore, the inactivation of Rab1 by VirA through its GAP activity could allow *Shigella* to escape xenophagy recognition [127]. This possibility is supported by the recently described global inhibition of trafficking pathways exerted by VirA and IpaJ [178]. Like VirA, IpaJ also modifies small-GTPases, with the difference that IpaJ removes the myristoyl group of the ADP-ribosylation factor (ARF1) thus inhibiting the myristoyl-mediated association of ARF1 with ER and Golgi membranes. Releases ARF1 from the Golgi membranes result in Golgi fragmentation and inhibition of the general secretory pathway [179,180]. Through inactivating ARF1 and Rab small GTPases families, VirA and IpaJ freeze vesicular trafficking (Figure 1.2) [178].

Once in the cytosol, *Shigella* starts replicating and hijacks the host actin polymerization machinery to enable actin-based motility. However, the host can recognize the curvature of replicating bacteria via septins and trap them inside septin cages blocking actin tail polymerization (Figure 1.2) [181,182]. Septins are cytoskeleton proteins that assemble to form filaments, bundles and rings implicated in cell division [183]. Although septin cage entrapment of *Shigella* correlates with LC3 binding, it is unclear whether these LC3-positive cages are formed before or after vacuolar rupture [181,182]. Moreover, in the absence of IcsB, *Shigella* appears more frequently associated with septin structures, whereas the outer membrane IcsA promotes septin binding [181,184]. Likewise, IcsA is recognized by Atg5, potentially triggering xenophagy, but IcsB masks the Atg5 binding site on IcsA, thereby inhibiting recognition (Figure 1.2) [167]. IcsA mediates the polymerization of an actin tail at one pole of the bacterium, allowing intracellular motility [185]. It was shown that septins reduce the number of tailed *Shigella* possibly by binding and blocking the function of IcsA [181,184]. Septins also reduce inflammation and are required for neutrophil-mediated immunity in a zebrafish model of *Shigella* infection [186]. Nevertheless, the role of septin-mediated restriction of *Shigella*'s intracellular growth and motility requires further study.

Figure 1.2. *Shigella* escapes the endocytic vacuole generating membrane remnants that trigger LC3 recruitment.
Upon entry, *Shigella* remains within the *Shigella*-containing vacuole (SCV) for a short time before exiting into the cytoplasm. Massive accumulation of Rab11 positive macropinosomes follows *Shigella* entry into epithelial cells. IpgD hydrolyzes phosphatidylinositol 4,5-bisphosphate (PIP2) to produce phosphatidyl-inositol 5-phosphate (PI5P), promoting macropinosome formation and Rab11 recruitment. IpgD-mediated accumulation of PI5P also blocks binding of the endosomal markers EEA1 and LAMP 1/2. After internalization, an actin cocoon (magenta) assembles around some of the SCVs. Cocoon formation is IcsB-dependant, resulting in Cdc42-N-WASP-Toca-1 recruitment and subsequent Arp2/3 mediated actin polymerization. The cocoon then disassembles before *Shigella* damages the SCV possibly by IcsB mediated inactivation of Cdc42. The T3SS translocon, formed by IpaB and IpaC, is the primary mechanism used by *Shigella* to damage the SCV. Galectin-3 (Gal3) binds to exposed glycans in damaged SCVs and membrane remnants hence its use as a vacuolar escape reporter. As *Shigella* exits the SVC, membrane remnants are generated triggering LC3 recruitment. The ubiquitin-ligase LRSAM1 ubiquitinates membrane remnants. Then the xenophagy receptors p62 and NDP52 bind to the ubiquitinated membranes and recruit the LC3. *Shigella* blocks LC3 recruitment to the damaged SVC using the effectors VirA and IpaJ. These effectors inactivate several Rab small GTPases, including Rab1, freezing vesicular trafficking and reducing LC3 targeting. IcsB localizes to the SCV membrane where it modifies CHMP5, a host protein involved endosomal cargo sorting, thereby blocking LC3 targeting of the SCV. Cytoplasmic *Shigella* is recognized by the cytoskeleton proteins septins, which bind to dividing bacteria blocking actin mediated motility. The outer membrane protein IcsA, which mediates actin-tail polymerization, promotes septin binding to dividing bacteria in the host's cytosol. The canonical autophagy marker Atg5 also binds to IcsA. *Shigella* counteracts septin and autophagy recognition by masking IcsA with IcsB.

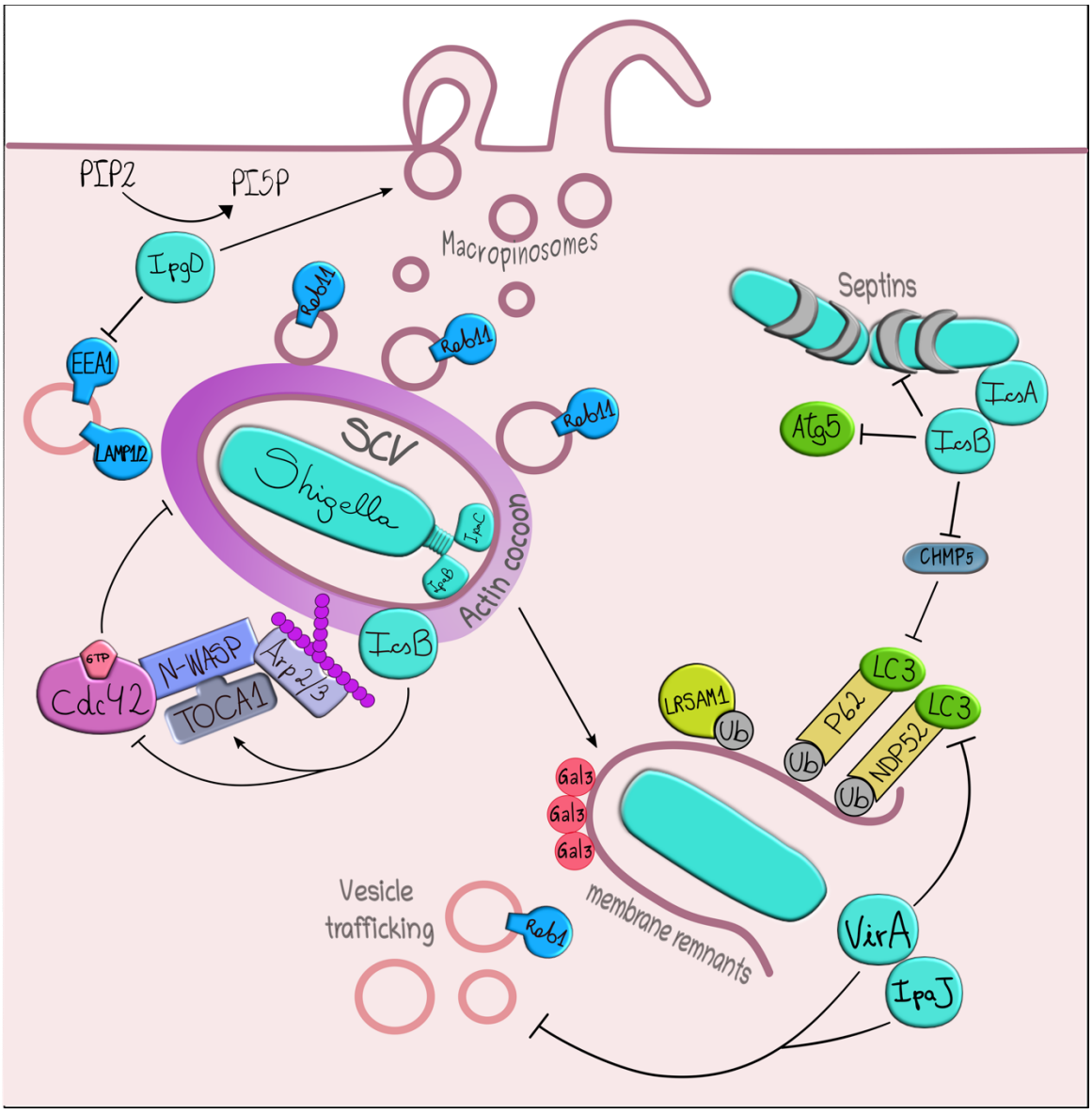
PIP2
PI5P
IpgD
Macropinosomes
Rab11
Rab11
Rab11
EEA1
LAMP1/2
SCV
Shigella
IpaC
IpaB
Actin cocoon
IcsB
GTP
Cdc42
N-WASP
TOCA1
Arp2/3
Septins
IcsA
Atg5
IcsB
CHMP5
LRSAM1
Ub
LC3
P62
Ub
LC3
NDP52
Ub
Gal3
Gal3
Gal3
membrane remnants
Vesicle
trafficking
Rab1
VirA
IpaJ

In contrast to the rapid cell death induced in macrophages, *Shigella* strives to protect its replicative niche inside ECs. Bacteria-induced cell death can be classified into apoptosis, necrosis, necroptosis (programmed necrosis) and pyroptosis [187]. Apoptosis is defined as a non-lytic non-inflammatory process mediated by caspase activation. Morphologically, apoptosis is characterized by membrane blebbing, nucleus fragmentation and the formation of apoptotic bodies that are cleared by phagocytic cells [188]. On the other hand, necrosis, necroptosis and pyroptosis are pro-inflammatory lytic processes characterized by cell membrane rupture and cytoplasm leakage. Thus, their progression can be assessed utilizing cell-impermeable DNA binding dyes and the release of cellular contents, including lactate dehydrogenase (LDH) [189]. Necrosis and necroptosis are caspase-independent forms of cell death triggered by toxins, hypoxia, and other cell-damaging insults. In contrast, pyroptosis is mainly induced by pathogens that activate inflammasome assembly and caspase activity [188].

Shigella infection damages the host-cell DNA, activating the transcriptional factor proto-oncogene p53, inducing apoptosis [135]. This cell death pathway is mediated by the initiator caspases 2, 8, and 9, which cleave and activate the executioner caspases 3, 6, and 7 [190]. Moreover, the lipopolysaccharide (LPS) of *Shigella* binds to caspases-3 and-7 via O-antigen moiety, blocking apoptosis [191]. *Shigella* delivers the effector OspC1 to further inhibit apoptosis by blocking caspase-8 activation [192]. Indirectly, IpgD inhibits apoptosis as demonstrated by the less caspase-3 activation found in cells overexpressing IpgD and treated with the apoptosis inducer staurosporine [193].

A programmed form of necrosis denominated necroptosis is triggered when the first-line apoptotic cell death responses fail. The key regulators of necroptosis are the serine/threonine kinase receptor-interacting protein (RIPK)1 and RIPK3. They phosphorylate the mixed lineage kinase domain-like protein (MLKL), which oligomerizes, forming a pore in the cellular membrane [194]. Active caspase-8 not only activates downstream caspase-3/7 but also cleaves RIPK1 and RIPK3, blocking necroptosis [195]. OspC1 mediated inactivation of caspase-8 thus also relieves the blockade of necroptosis.

Shigella subsequently delivers the protease OspD3 to antagonize necroptosis activation by RIPK1/RIPK3 degradation [192].

Pyroptosis can be dependent (canonical) or independent (non-canonical) of inflammasome activation. Inflammasomes are multimolecular complexes activated by pattern recognition receptors (PRRs) in response to pathogen-associated molecular patterns (PAMPs) detection [196]. Inflammasome activation leads to caspase-1 activation, which cleaves pro-IL-1β or pro-IL-18, resulting in the secretion of the mature cytokines. Active caspase-1 also cleaves the executor protein GSDMD, which oligomerizes to form pores in the cell membrane, inducing cell lysis [196]. Inflammasome independent pyroptosis is mediated by caspase-4/5. IFN-γ–induced guanylate-binding proteins (GBPs) act as PRRs targeting the LPS of intracellular bacteria [197]. GBP coating of bacterial surface triggers recruitment and activation caspase-4/5, which subsequently cleave GSDMD but not pro-IL-1β/pro-IL-18 [196,197]. The T3SS rod component MxiI induces inflammasome-caspase-1 activation and rapid lysis of macrophages [198]. Remarkably, *Shigella* further promotes macrophage pyroptosis by inducing the formation of IpaB channels in the cell membrane, suggesting macrophage lysis is desirable for infection [199]. In contrast, *Shigella* actively safeguards its replicative niche within ECs. *Shigella* antagonizes the non-canonical pathway by delivering the T3SS effector OspC3 [200,201]. This effector inactivates caspase-4 by ADP-riboxanation [202]. Moreover, the E3 ubiquitin ligase IpaH7.8 ubiquitylates GSDMD, targeting it for degradation, thus impairing both canonical and non-canonical pathways [203]. *Shigella* secretes IpaH9.8, another ubiquitin ligase that targets the pyroptosis upstream ligand GBP1 for degradation via Lys48-linked ubiquitination [204,205].

Other *Shigella* effectors involved in maintaining epithelial niche integrity include OspF, OspG, OspZ, OspI and IpaH1.4/2.5. These effectors interfere with nuclear factor kappaB (NF-κB)-dependent production of IL-8, a potent PMN chemoattractant, thus dampening intestinal inflammation and EC damage. OspF is a phosphothreonine lyase, which irreversibly dephosphorylates mitogen-activated protein kinases (MAPKs) p38 and ERK, preventing access of NF-κB to the IL-8 promoter [69,206]. The ubiquitin ligases IpaH1.4/2.5 target the Linear Ubiquitin chain Assembly Complex (LUBAC) enzymatic

center HOIP for proteasomal degradation. Reduced LUBAC activity results in a lack of RIPK1 and NEMO (IKKγ) ubiquitination, thereby interfering with NF-κB activation [207]. De Jong et. al also found that IpaH1.4 cooperates with OspI, a glutamine deamidase, to inhibit the activity of the E2 ubiquitin-conjugating enzume UBC13 to further suppress NF-κB activation [207,208]. Moreover, the methyltransferase OspZ inhibits NF-κB activation and nuclear translocation by modifying upstream regulators [209]. Lastly, the effector OspG inhibits ubiquitylation and proteasomal degradation of the inhibitor of NF-κB type α (IκBα), thereby dampening NF-κB responses [210,211]. The multiple effectors that *Shigella* employs to subvert the NF-κB pathway demonstrate the central role of NF-κB in innate immune responses against intracellular pathogens.

To summarize, *Shigella* escapes LC3-mediated xenophagy by exiting SCV and quickly peeling off vacuolar membrane remnants. The secreted effectors VirA, IpaJ and IcsB are critical for efficient escape and vesicular trafficking modulation. Cytoplasmic *Shigella* faces entrapment by septins and Atg5-dependent xenophagy, but IcsB antagonizes Atg5 binding to IcsA. *Shigella* safeguards its cytosolic niche by counteracting cell death mechanisms triggered by the presence of PAMPs in the cytosol. *Shigella* antagonizes apoptosis, necrosis-necroptosis, and pyroptosis in ECs, while pyroptosis is actively induced in macrophages. *Shigella* uses a myriad of effectors to modulate these processes. IpgD, VirA, OspC1 and *Shigella's* LPS inhibit apoptosis. OspD2 inhibits VirA-mediated necrosis, and OspD3 antagonizes OspC1's indirect induction of necroptosis. Pyroptosis is differentially regulated depending on the cell type. The T3SS components MxiI and IpaB promote rapid pyroptosis in macrophages. In contrast, OspC3 and the ubiquitin ligases IpaH7.8 and IpaH9.8 impair pyroptosis to maintain ECs integrity. Furthermore, *Shigella* uses the effectors OspF, OspG, OspZ and IpaH9.8 to circumvent the activation of pro-inflammatory responses-mediated through the NF-κB and MAPKs pathways. The multiple mechanisms that *Shigella* uses to target various host functions during its life cycle in the cytoplasm demonstrate a long coevolutionary process, where *Shigella* adapted to escape host recognition to allow for unnoticed replication and spread to other cells.

1.4.5 Actin-based motility and cell-to-cell spreading

After cell invasion, *Shigella* rapidly escapes from the phagocytic vacuole into the cytosol, inducing actin polymerization to form an actin tail that confers intracellular motility. The adhesin IcsA, which localizes to one pole of the bacterium, mediates actin tail formation by recruitment and activation of N-WASP and the Arp2/3 complex (Figure 1.3) [212,185,213]. The actin tail allows bacteria to engage the host cell membrane, forming *Shigella*-containing protrusions [100]. These protrusions are endocytosed by neighbouring cells [214,215]. After the invasion of a second cell, *Shigella* escapes a double-membrane vacuole in a T3SS dependent manner to reach the cytoplasm [216,217]. Following these events, *Shigella* starts a new replication cycle, actin-based motility and cell-to-cell spread [217].

The molecular mechanisms enabling actin tail polymerization of *Shigella* and other intracellular pathogens have been studied extensively [4]. Ogawa *et al.* reported in the 1960s that when *Shigella* entered cells, it exhibited vigorous directional movements; this observation was surprising at the time, given that *Shigella* is described as non-motile [218]. It was not until the 1980s that genetic studies identified *Shigella*'s outer membrane protein IcsA, also known as VirG, as the central mediator of actin tail polymerization and bacterial motility [100,219].

The *icsA* gene is located on the *Shigella* virulence plasmid [191]. It encodes a 120-kDa outer membrane protein composed of three domains: a secretion signal peptide, a passenger domain located on the cell surface and the β-domain that anchors the protein to the outer membrane [220–222]. The T3SS does not mediate IcsA translocation across the membrane. Instead, IcsA is an autotransporter protein secreted by the Sec-pathway into the periplasm [221]. From there, the β-domain inserts into the outer membrane, mediating translocation of the passenger domain to the bacterial surface [220,221]. Interestingly, IcsA preferentially localizes to the old pole of the bacterium; as *Shigella* divides, IcsA is expressed in opposite poles of the daughter cells [223]. Cleavage and release of the passenger domain, mediated by the protease IcsP (SopA), determine the unipolar localization of IcsA and proper intracellular motility [224,223,225]. When exposed to the host cell cytosol, surface-bound IcsA

recruits and activates the actin polymerization machinery and catalyzes the directed elongation of an actin tail.

Shigella utilizes pre-existing host cell pathways of actin nucleation, polymerization, and cross-linking to induce actin-based motility. Knowing the essential components that mediate actin filament polymerization helps better understand how bacteria hijack this process. Actin exists in two forms, monomeric globular (G-) actin polymerizes into filamentous (F-) actin. Actin nuclei are trimers of G-actin, from which actin nucleation starts *de novo* to form a filament. F-actin filaments are polar; they have a fast-growing barbed end where ATP-bound G-actin monomers are added and a slow-growing pointed end from which ADP-bound G-actin is dissociated [226,227]. Thus, actin filaments are maintained in a dynamic equilibrium of polymerization and depolymerization. Regulatory proteins are required to retain this equilibrium. For example, profilin prevents actin monomer self-nucleation, and cofilin stimulates ADP-actin dissociation at the pointed end of the filament, promoting depolymerization [228].

Actin filaments are stabilized by capping proteins that bind either the barbed or pointed end [229]. *De novo* actin polymerization is unfavourable and inhibited by profilin. Therefore, actin polymerization must be stimulated by actin-nucleating proteins. The best-characterized actin-nucleator is the Arp2/3 complex composed of seven subunits, among which the Arp2 and Arp3 subunits are structurally similar to actin [117]. Arp2/3 activity is regulated by nucleation-promoting factors such as N-WASP [230]. Under nonpolymerizing conditions, N-WASP is maintained in an autoinhibited conformation stabilized by intramolecular contacts [231]. Rho family GTPases, such as Cdc42, relieve N-WASP autoinhibition [231]. Active N-WASP then recruits and activates the Arp2/3 complex, which binds to the side of a filament, initiating nucleation of branched filaments to form networks [117].

In vitro reconstitution of actin polymerization using purified proteins determined the essential proteins for *Shigella* motility. Globular (G-) actin, N-WASP, Arp2/3, cofilin and capping protein are the minimum requirement for actin-tail polymerization and movement

of an *E. coli* strain expressing IcsA [232]. However, other host proteins are required for more efficient actin tail polymerization and intracellular motility. For example, it was thought that IcsA binding to N-WASP was sufficient for its activation [233,234]. It was later demonstrated that IcsA mainly mediates the recruitment of N-WASP to one pole of the bacterium, and it is Toca-1 that relieves N-WASP autoinhibition (Figure 1.3) [235].

Toca-1's recruitment to *Shigella* is IcsA independent, while an unknown T3SS effector mediates Toca-1 recruitment to the bacterium's surface before bacterial motility starts [235]. Given that IcsB recruits Cdc42, which activates N-WASP with the help of Toca-1, to induce the polymerization of actin cocoons around the SCV, IcsB may be the effector that recruits Toca-1 to IcsA [164]. This is very likely since IcsB directly binds Toca-1 *in vitro,* and both proteins colocalize around *Shigella* early during infection [175]. Given that IcsB is not required for actin tail polymerization but interacts with IcsA, IcsB may have a role in the process that leads to N-WASP recruitment and activation [167,175]. After N-WASP-Arp2/3-mediated actin polymerization, Toca-1 is no longer required for the subsequent maintenance of active N-WASP or actin tail elongation [235]. The importance of Toca-1 for efficient actin tail polymerization was demonstrated in Toca-1-depleted cells, where the percentage of *Shigella* that forms normal-appearing actin tails was markedly reduced [235].

Furthermore, the activity of Bruton's tyrosine kinase (Btk) and Abelson tyrosine kinase (Abl) is required to phosphorylate N-WASP (Figure 1.3), promoting its recruitment to *Shigella*. Depleting these two host kinases reduces the percentage of bacteria with actin tails [118,236]. Similarly, the expression of an N-WASP mutant lacking its profilin binding leads to an 80% reduction in actin tail formation by *Shigella* [237,213]. As mentioned, profilin is an actin monomer-binding protein that delivers G-actin to the site of actin polymerization (Figure 1.3). Thus, the functional interactions of profilin with N-WASP and G-actin are critical for *Shigella* actin-based motility. In addition, the T3SS-secreted effector VirA was shown to destabilize the dense microtubule network in the cytoplasm, promoting *Shigella* motility (Figure 1.3). It was initially reported that VirA was a cysteine protease that directly degraded α-tubulin [123]. Later reports challenged this assumption, demonstrating that

purified VirA does not cleave tubulin [126]. The mechanism by which VirA contributes to *Shigella* spreading remains to be identified.

Motile *Shigella* reaches the cell periphery, deforming the plasma membrane to form bacteria containing protrusions (Figure 1.3). These protrusions project into neighbouring cells, collapsing into a membrane-bound compartment endocytosed by the target cell [238]. Although protrusion formation is a critical step in cell-to-cell spread and a key mechanism to escape immune recognition, this process is not as well characterized as other steps in *Shigella*'s life cycle. Membrane protrusion formation seems to result solely from the force developed by the actin tail that deforms the plasma membrane [217]. However, it has been shown that the Diaphanous-related formins Dia1 and Dia2 are required for efficient protrusion development but not for actin tail polymerization [239]. These formins are effectors for Rho small GTPases and stimulate polymerization of unbranched actin filaments [240]. Dia1/Dia2 may promote *Shigella* protrusions by mediating parallel nucleation of several unbranched actin filaments, similar to the process that initiates filopodia, thereby increasing pushing efficiency [241].

Myosin-X, an unconventional myosin that promotes filopodia formation, is recruited to *Shigella* containing protrusions [242,243]. Silencing of Myosin-X reduces the length but not the number of protrusions. Moreover, cell-to-cell spreading is impaired, but cell invasion was not affected, indicating that shorter protrusions are less likely to infect neighbouring cells [243]. For efficient cell-to-cell spreading, *Shigella* also relies on myosin IIA and its specific kinase, myosin light chain kinase (MLCK). Interestingly, myosin IIA filaments are found at the bases of myosin X-induced filopodia, where they mediate filopodia stability [244]. Collectively, these observations suggest that *Shigella* hijacks the filopodia machinery to induce long and stable protrusions.

Figure 1.3. *Shigella* induces actin polymerization to form an actin tail which mediates intracellular motility.
Shigella's outer membrane protein, IcsA, localizes to one pole of the bacterium, mediating actin tail (magenta) formation. IcsA recruits N-WASP, which is activated by Toca-1. The host kinases Btk and Abl phosphorylate (P) N-WASP, enhancing its activation. Active N-WASP then recruits and activates the Arp2/3 complex mediating polymerization of branched actin filaments (magenta). The newly formed actin filaments are stabilized by capping proteins. Cofilin severs filaments and stimulates globular (G) actin dissociation promoting filament depolymerization. G-actin is stabilized by profilin, which binds to N-WASP, delivering actin monomers to the site of actin polymerization. The T3SS-secreted effector VirA promotes *Shigella* motility by an unknown mechanism resulting in microtubules destabilization. The actin tail allows bacteria to engage the host cell membrane, forming *Shigella*-containing protrusions.

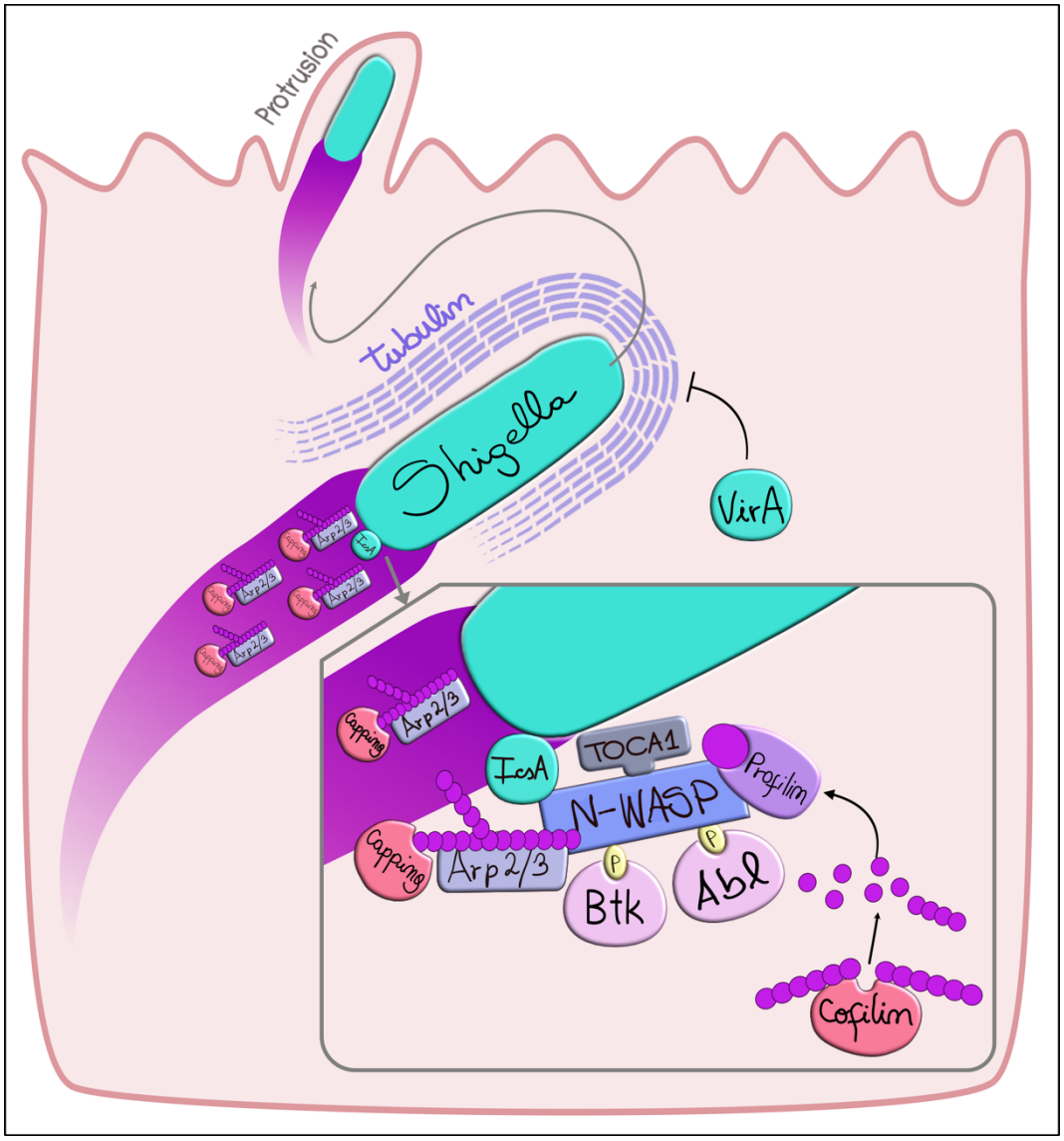

Shigella manipulates cortical tension at cell junctions, preferentially generating protrusions in areas where three or four cells join [215]. An early study showed that E-cadherin, a significant component of the intermediate cellular junctions, is involved in *Shigella* cell-to-cell spreading [245]. Other junction proteins, such as connexin 26, play essential roles in *Shigella* invasion and movement into adjacent epithelial cells [246]. *Shigella* uses the secreted effector IpaC to destabilize cell junctions and facilitate spreading. IpaC interacts with β-catenin, a protein that interacts with cadherin to form tight adherent junctions, leading to β-catenin phosphorylation by an unknown kinase. β-catenin phosphorylation destabilizes the functional cadherin complex, perturbing cell-to-cell adhesion [247]. Moreover, *Shigella* expressing an IpaC mutant that cannot interact with β-catenin is defective in protrusion formation and cell-to-cell spread [248].

T3SS activity is absolutely required for cell invasion and vacuolar escape. Studies have shown that the T3SS is also necessary for efficient protrusion formation [216]. T3SS function is triggered by membrane contact; thus, *Shigella*'s actin-mediated motility facilitates close interaction between the bacterium and the cell membrane to activate secretion [97]. Subsequently, *Shigella* containing protrusions recruit and activate tyrosine kinase signalling in a T3SS dependent manner [216]. The activity of the kinases STK11 and PIK3C2A then mediate the resolution of protrusions into a vacuole-like structure [249,250]. For this, protrusion "stems" collapse most likely due to actin tail polymerization termination. The specific T3SS effectors involved in tyrosine kinase signalling during protrusion progression have yet to be elucidated.

The uptake of *Shigella* containing vacuole-like structures is mediated by clathrin-dependent endocytosis [215]. The canonical function of clathrin is to mediate the uptake of small particles in the cell [251]. Although it is recruited to other bacteria, it remains unclear how clathrin function assists the uptake of *Shigella* containing protrusions [252]. The membrane remodelling protein epsin-1 and the GTPase Dynamin2 also facilitate uptake of *Shigella* by an undefined mechanism [215,253]. Notably, actin tail independent infections (primary infections) are different from actin tail mediated infections (secondary infections). The SCV formed in primary infected cells is composed of a single membrane derived from

the host plasma membrane, while in secondary infections, *Shigella* must break through a two-membrane SCV. One membrane is derived from the primary infected cell, and the second membrane derives from the secondary infected cell. The same effectors involved in escaping a single membrane SCV participate in *Shigella* escape from double-membrane compartments [254]. However, IcsB and VirA seem to play a more prominent role in escaping from membrane compartments formed during cell-to-cell spread [172,255].

1.5 Receptor for activated C kinase 1, a scaffolding protein involved in diverse functions

1.5.1 Cell signalling and ribosome interaction

The Receptor for Activated C Kinase 1 (RACK1) belongs to the tryptophan-aspartate repeat (WD-repeat) family of proteins [256,257]. These proteins comprise polypeptide domains of 40–60 amino acids, in which each repeat folds into a four-stranded antiparallel β-blade [256]. The seven-bladed β-propeller conformation that RACK1 adopts facilitates interactions with various protein partners concurrently [258]. As a scaffold protein, RACK1 participates in numerous aspects of cellular function in eukaryotic organisms [5]. RACK1 was initially described as a PKC anchoring protein, from which it acquired its name [259]. The interaction between these two proteins stabilizes PKC in its active conformation [260,261]. RACK1 acts as a shuttling protein, moving PKC to where its substrates are located [260]. Similarly, RACK1's scaffolding function integrates many other kinase signalling pathways critical for fundamental cellular activities. For example, RACK1 binds several MAPKs, including the extracellular signal-regulated kinase 1 (ERK1), P38 and c-Jun N-terminal kinase (JNK) [262–264]. These kinases are activated upon stress, cytokines, and growth factors [265]. Modulation of MAPK by RACK1, including their stabilization, subcellular localization, and association with their substrates, makes this scaffold protein a pivotal regulator of cellular homeostasis [5].

RACK1 interacts with cytoplasmic tails of several membrane receptors, facilitating signal transduction pathways. For example, RACK1 functions as an adaptor for growth factor receptor I (IGF-1R) signalling. RACK1 is associated with the signal transducer and

activator of transcription factor 3 (STAT3) and IGF-1R upon insulin activation [266,267]. Active STAT3 mediates the expression of genes related to cell growth [268]. RACK1 also binds the β integrin receptor, bridging signalling between IGF-1R and integrins, thereby influencing cell migration [269–271]. The RACK1-integrin interaction also promotes cell survival pathways, the recruitment of several PKC isoforms and MAPK activation [272,262,273]. More details about the role of RACK1 in integrin-mediated signalling will be discussed in the following sections.

The best characterized RACK1 partnership is with the ribosome. Structural studies identified RACK1 as a component of the ribosome, demonstrating that RACK1 integrates to the 40S ribosomal subunit [274,275]. Blades 1–4 of RACK1 bind to the ribosomal protein S17 and 18S ribosomal RNA (rRNA) [275]. RACK1 does not mediate ribosome stability or integrity; instead, RACK1 recruits different translation control factors to the ribosome [276]. For example, the recruitment of activated PKC leads to increased translation, because PKC phosphorylates the anti-association factor eIF6, relieving translational repression [277]. Likewise, RACK1 binding to the ribosome leads to efficient recruitment of the eukaryotic initiation factor 4E (eIF4E), which mediates cap-dependent translation initiation [278,279]. The interaction of RACK1 with the ribosome also regulates ribosome subcellular localization. RACK1 binding to β-integrins has been suggested to relocate ribosomes to focal adhesions [269,280]. Another crucial regulatory role of RACK1-ribosome interaction is demonstrated by the expression of a RACK1 mutant unable to bind the ribosome, resulting in selective translation of mRNAs of genes that induce autophagy [281].

1.5.2 RACK1's role in autophagy

Autophagy is an evolutionarily conserved cellular process that degrades long-lived proteins and damaged organelles collected within double-membraned vacuoles fused with lysosomes [282]. The first step in autophagy is the formation of a phagophore, a small vacuole that subsequently expands and surrounds a portion of the cytoplasm and cellular organelles. The phagophore then closes, forming a double-membraned structure denominated autophagosome, which then fuses with lysosomes to degrade the cargo [282]. The progression

of these steps is regulated by autophagy (Atg) related proteins that function in an organized sequential manner [283]. Autophagy is induced by various stressors, such as nutrient starvation, hypoxia, oxidative stress, and pathogen infection [282].

The role of RACK1 in autophagy signalling is only beginning to be understood. The first indication that RACK1 function could be related to autophagy came from the finding that RACK1 deficiency in hepatocytes leads to lipid accumulation in the liver. RACK1 is essential for development; therefore, studying the various functions of this protein in animal models is challenging [284]. An alternative is to create conditional knockouts targeting RACK1 expression in specific organs. RACK1 knockout in the liver results in increased accumulation of lipids in the cytoplasm of hepatocytes and tumorigenesis [285]. This phenotype is consistent with that observed in autophagy-deficient Vps34−/− livers [286]. Lipid accumulation was associated with an increment in polyubiquitinated proteins and p62. Moreover, co-immunoprecipitation analysis identified various Atg proteins, Beclin-1 and Vps34, as RACK1 interactors [285]. The adenylate-activated protein kinase (AMPK) is an autophagy regulator that mediates ULK activation [287]. It was discovered that RACK1 is a substrate of AMPK. RACK1 phosphorylation by AMPK promotes its binding to Beclin-1, resulting in the assembly of the autophagy-initiation complex [285]. RACK1 also interacts with Atg proteins downstream of the Beclin-1/Vps34 complex. RACK1 is recruited to the Atg12-Atg5-Atg16 complex by interacting with Atg5 upon starvation [288]. Cells expressing a RACK1 mutant that could no longer bind to Atg5 display less LC3 positive puncta under starvation, confirming the RACK1-Atg5 interaction is necessary for starvation-induced autophagy [288].

Abnormal expression of RACK1 has been linked to cancer development [289]. Since RACK1 depletion leads to autophagy inhibition, the expected outcome is an accumulation of damaged organelles and protein aggregates, which are known to create an environment for cancer initiation. Moreover, accumulation of p62 and deletion of Beclin-1 are related to cancer development [290]. Conversely, RACK1 overexpression is also linked to malignancy. Analysis of RACK1 expression in colon cancer patients showed progressive RACK1 overexpression, which correlated with significantly poorer overall survival. The study

demonstrated that RACK1-induced autophagy increases colon cancer cell proliferation, suggesting that RACK1 acts as an oncogene in colonic cells. Autophagy alterations have been found in many cancers; the impact of RACK1 regulation in these alterations remains to be revealed [291].

1.5.3 RACK1's role in apoptosis

Apoptosis is a crucial process for tissue homeostasis, triggered by many insults, such as DNA damage, γ-irradiation, oncogene activation and growth factor withdrawal. Activation of the apoptotic program leads to caspase-mediated proteolysis, nuclear condensation, cell shrinkage and membrane blebbing. The dying cell becomes fragmented into apoptotic bodies quickly phagocytosed by surrounding macrophages. There are two major apoptosis programs in the cells denominated extrinsic and intrinsic pathways. The extrinsic pathway is triggered by events outside the cell and is mediated by death-promoting receptors. Fas, death receptor 4 (DR4) and DR5, and TNF receptor (TNF-R1) are the primary receptors involved in the extrinsic pathway. Activation of these receptors leads to the processing of pro-caspases-8/-10 into the initiator caspases-8/-10. The initiator caspases then activate the effector caspases-3/-6/-7, triggering apoptosis. In contrast, the intrinsic pathway is triggered by intracellular events and is controlled by a series of specific death-promoting molecules released from damaged mitochondria. Mitochondrial permeability is regulated by members of the Bcl-2 family of proteins composed of pro- and anti-apoptotic members. These proteins regulate the release of cytochrome-c, a component of the mitochondrial inner membrane. Cytochrome-c associates with the apoptosis-protease activating factor 1 (Apaf-1) in the cytoplasm, which leads to initiator caspase-9 activation. Caspase-9 subsequently activates the effector caspases-3/-6/-7.

RACK1 exerts pro- and anti-apoptosis effects, depending on cellular conditions, tissue type or interacting partner. For example, RACK1 induces apoptosis of human colon cells by regulating members of the Bcl-2 family of proteins. RACK1 inhibits the expression of anti-apoptotic Bcl-2 and Bcl-XL and upregulates pro-apoptotic Bim. RACK1 also mediates translocation of Bax, another pro-apoptotic Bcl-2 family member, to the

mitochondria [292]. Bim induces the oligomerization of Bax at the mitochondria, destabilizing its membrane [293]. Additionally, Bcl-XL sequesters Bax to prevent its oligomerization, but RACK1 disrupts this association and releases Bax [294]. Thus, RACK1 promotes apoptosis by downregulating Bcl-XL, blocking Bax/Bcl-XL association and upregulating Bim. RACK1-mediated Bax oligomerization is required to activate the intrinsic pathway in staurosporine-treated cells [292]. RACK1 was shown to promote apoptosis in intestinal epithelia after irradiation and in breast cancer [295,296].

Conversely, another group demonstrated that RACK1 forms a complex with dynein light chain 1 (DLC1), sequestering BimEL, a Bim isomer, in the presence of apoptosis-inducing agents. RACK1 also promotes proteasome-mediated degradation of BimEL, inhibiting apoptosis in breast cancer cells [297]. More evidence of the anti-apoptotic role of RACK1 was found by Subauste et al. [298]. The protease activating factor-1 (Fem1b) is a pro-apoptotic protein that interacts with the death receptors Fas and TNF-R1, activating the extrinsic pathway [299]. RACK1 binds to Fem1b, promoting its ubiquitination and concomitant degradation by the proteasome. Accordingly, RACK1 downregulation leads to Fem1b-mediated apoptosis in colon cancer cells [298]. Furthermore, RACK1 counteracts the apoptotic effect of the adenoviral E1A protein [300]. Although RACK1 directly interacts with E1A, the mechanism of how RACK1 interferes with E1A-mediated apoptosis is unknown. Other reports link RACK1 downregulation to apoptosis induction in different contexts [301,302]. Taken together, RACK1 plays differential roles in apoptosis, manipulating the intrinsic and extrinsic pathways. Hence, the outcome of RACK1 activity depends on the cellular context and the proteins targeted.

1.6 RACK1 and cytoskeleton dynamics

1.6.1 RACK1 and cell migration

RACK1 scaffolding of signalling proteins and membrane receptors is crucial for cell migration, adhesion, and proliferation. RACK1 regulation of these processes has been extensively studied in cancer development. RACK1 is upregulated in many cancers, promoting cell proliferation by diverse mechanisms that involve MAPK signalling

modulation, preferential translation of factors involved in growth, enhancement of GSK3β, among others [303–306]. One of the hallmarks of cancer cells is that they have the potential to metastasize. This process requires loss of matrix adhesion and cell-cell contacts, allowing cells to leave their original tissue. Cell migration is also a physiological process essential for development and tissue homeostasis.

The cell migration process involves dynamic reorganization of the cytoskeleton to form leading-edge protrusions that firmly attach to the substrate as the cell tail detaches from the extracellular matrix and retracts [307]. Protrusion of a leading-edge is driven by actin polymerization of branched filaments catalyzed by the ARP2/3 complex under the regulation of the Rho GTPases Rac1 and Cdc42 [307]. As the cell senses the extracellular matrix (EM), nascent focal adhesions (FAs) assemble. FAs are the mechanical link between the cell and the EM, and integrins initiate their assembly. Attachment of the integrins' extracellular domain to EM ligands triggers integrin clustering on the cell surface. Subsequently, the integrins' cytoplasmic domains recruit the scaffold paxillin, the actin-binding proteins talin, α-actinin and vinculin, and signalling kinases [308]. Talin and vinculin link the cytoplasmic domain of the integrins to thick bundles of F-actin called stress fibres, and α-actinin stabilizes this interaction by cross-linking actin filaments [309,310]. Paxillin functions as a platform for Src family kinases (Src and Fyn) and the focal adhesion kinase (FAK) [311]. These kinases regulate the assembly of FAs by phosphorylating multiple integrin-associated proteins [312]. FAs are active sites for actin polymerization controlled by Rac1, Rho and Cdc42 [313]. Mature FAs generate forces to pull the cell forward; as the leading edge protrudes, FAs at the rear must disassemble to continue cell movement [307].

RACK1 is a crucial regulator of FA assembly mainly by interacting with FAK and Src. RACK1 is recruited to the cell's membrane upon IGF-IR activation, where it binds to integrins, facilitating downstream signalling that culminates in FA assembly. FAK docks to the nascent FA by binding to blades I and III of RACK1's seven-blade β-propeller [271]. RACK1 binding to FAK is required for FAK phosphorylation, suggesting that RACK1 facilitates the interaction between FAK and its regulators. For example, phosphorylated Erb-B2 receptor tyrosine kinase 2 (pErbB2) binds to RACK1 to activate FAK and promote

cell migration in non-small cell lung cancer cells [314]. Similarly, RACK1 binds to FAK upon PKC activation and recruits the cyclic AMP phosphodiesterase 4D5 (PDE4D5) [272,315,316]. The FAK/RACK1/PDE4D5 complex keeps cAMP levels low in the nascent FA periphery, promoting FA stabilization and cell polarization [317]. RACK1, vimentin, and FAK form an intermolecular complex required for endothelial cell invasion in response to growth factors [318]. Vimentin is a member of the intermediate filament family that strengthens the FA by forming physical links [319]. Vimentin is also required to recruit and activate Rac1 for actin polymerization [320]. Furthermore, RACK1 regulates FA assembly by shuttling Src kinases to their site of action. Src and Fyn kinase's activity is inhibited by RACK1 binding [266,321–323]. Src release from RACK1 sequestration is mediated by IGF-IR and results in Src activation [266]. Active Src phosphorylates and fully activates FAK, promoting FA assembly [312]. Taken together, the ability of RACK1 to interact with many members of the FA complex enables the regulation of cell adhesion and migration.

1.6.2 RACK1's interactions with the cytoskeleton

Although RACK1 has been shown to interact with cytoskeleton-related proteins, RACK1's modulation of cytoskeleton dynamics is not well understood [324–326]. Up or down-regulation of RACK1 expression alters cell morphology and the cytoskeleton. Transient overexpression of RACK1 in Chinese hamster ovary (CHO) cells increases the number of stress fibres and FAs, leading to inhibition of cell migration on fibrinogen-coated coverslips [327]. Moreover, the expression of a C-terminus truncated version of RACK1 missing the Src/integrin-binding domain induces loss of central focal adhesions and stress fibres [328]. Likewise, the interaction between RACK1 and Src is required for actin ring formation in osteoclasts [329]. Other members of the Src kinase family are regulated by RACK1 activity. For example, the Lck kinase, which regulates cytoskeletal rearrangement in response to T-cell activation, is an interacting partner of RACK1 [330]. Lck kinase binds to RACK1 regardless of its activation state, but only in the presence of active Lck does the F-actin bundling protein α-actinin binds to the RACK1-Lck complex [330]. The implications of this interaction in cytoskeleton rearrangements are unknown.

It has been shown that RACK1 maintains the integrity of cortical F-actin in mast cells [326]. RACK1 silencing in these cells causes changes in cell morphology, which appear more rounded. Also, F-actin forms large aggregates throughout the cell cortex in response to antigen stimulation. Silencing RACK1 in mast cells increases the G-actin/F-actin ratio in response to antigen, suggesting RACK1 regulates actin polymerization or depolymerization [326]. RACK1 localizes with F-actin bundles in neuronal cells, and axon extension relies on RACK1 activity [331]. Furthermore, RACK1 has been found to colocalize or interact with other cytoskeleton-related proteins, such as vinculin, plectin and kindlin-3 [328,331–333]. Still, the physiological significance of these findings is not well understood, although most of these proteins are involved in cell adhesion [334].

1.7 RACK1's roles in pathogenesis

Like in the other cellular processes discussed in the previous sections, RACK1 plays differential roles in pathogenesis. RACK1 displays pro- or anti-pathogen functions depending on the cellular context and pathogen nature. The RACK1 protein of eukaryotic pathogens generally contributes to virulence. Asc1, a RACK1 homolog of the opportunistic pathogen *Candida albicans*, is required for adhesion, growth, and hyphal development *in vitro* [335,336]. Pseudohyphae are crucial for tissue invasion, thus not surprisingly, deletion of the Asc1 gene abolishes *C. albicans* pathogenicity in a mouse model [335]. In the yeast-like pathogen *Cryptococcus neoformans*, RACK1 homolog Gib2 is required for growth and full virulence in mice [337,338]. Like its mammalian counterpart, Gib2 interacts with proteins that regulate cAMP signalling, such as PKC, the adenylyl cyclase Cac1 and the small GTPase Ras1 [338]. The cAMP pathway is critical for synthesizing *C. neoformans* virulence factors melanin and capsule [339]. In *Plasmodium falciparum*, the causal agent of malaria, RACK1 is required for asexual replication within erythrocytes [340]. It was shown that ectopic expression of *Plasmodium*'s RACK1 (PfRACK1) in human embryonic kidney (HEK-293) cells impairs Ca^{2+} signalling, suggesting secretion of PfRACK1 could be a virulence strategy to modulate host functions [341]. Although *Plasmodium* possesses an apical secretory apparatus, secretion of PfRACK1 was not confirmed [342]. The parasite *Leishmania major* encodes four copies of the *Leishmania* RACK1 (LACK) gene. A minimum of two copies

are required for robust virulence *in vivo* [343]. LACK is essential for efficient cytochrome-c oxidase activity and ATP synthesis when these parasites are exposed to the host's temperature [344]. Conversely, LACK is highly immunogenic, inducing the production of protective cytokines in patients with active leishmaniasis. Therefore, LACK1 has been proposed as a vaccine candidate [345].

On the other hand, viruses have a reduced genome that compels them to an exclusively intracellular replication cycle as they are unable to synthesize proteins. Since RACK1 is a ribosomal protein required to regulate translation, it is not surprising that viruses target RACK1 to facilitate the translation of viral mRNAs. RACK1 is necessary for cap-independent Internal Ribosome Entry Site (IRES)-mediated translation by some RNA viruses, although RACK1 participates in cap-dependent translation in the host [278,346]. During infection, viruses impair the host cell cap-dependent translation and promote viral RNAs translation using IRES elements [347]. The first report linking RACK1 to viral replication came from the study of picorna-like *Drosophila* C virus (DCV) and hepatitis C virus (HCV) [348]. Infection of RACK1-depleted flies by DCV is impaired, and viral loads are reduced. Likewise, RACK1 silencing in Huh7.5.1 liver cells strongly impairs HCV replication [348]. The effect of RACK1 on IRES-mediated translation of HCV mRNAs was confirmed using an IRES luciferase reporter [348]. Similar findings were reported in other IRESs-containing viruses, such as poliovirus (PV) and encephalomyocarditis virus (EMCV), suggesting that the need for RACK1 is broadly conserved among these viruses [346]. Another ingenious strategy used by viruses to exploit the host translation machinery was found in the Vaccinia virus (VacV), a dsDNA virus that replicates exclusively in the cytoplasm. VacV mRNAs contain a 5'-poly(A) leader that confers translational advantage not mediated by IRES [349]. An undetermined VacV kinase phosphorylates the flexible loop domain of RACK1, modifying its charge to mimic plant RACK1 [350]. In plants, this RACK1 loop is negatively charged and acts as a natural translation enhancer for mRNAs with 5'-poly(A) leaders. Therefore, VacV modifies mammalian RACK1 to mimic its plant counterpart, biasing ribosome selectivity towards viral mRNAs [350].

The role of RACK1 in viral infection is not restricted to translation. Many viral proteins bind to RACK1 to exploit various host functions. For example, RACK1 interacts with the influenza A virus (IAV) matrix protein M1 [351]. This viral protein is required for IAV budding from the plasma membrane of infected cells [352]. RACK1 interaction with M1 is required for M1 phosphorylation putatively by PKC or other host kinases [351]. Moreover, mutation of residue 16 of M1 prevents its interaction with RACK1 impairing the release of IAV particles [353]. RACK1 is also a pro-viral factor for insect-borne viruses, including Zika virus (ZIKV), West Nile Virus (WNV), Dengue Virus (DENV), Powassan Virus (POWV) and Langat Virus (LGTV). Silencing of RACK1 drastically reduces infective viral particle release in cells infected with these viruses. Likewise, RACK1 is required for SARS-CoV-2 replication, demonstrating that RACK1 functions are hijacked by a wide range of RNA viruses [354]. Furthermore, it was found that RACK1 interacts with the non-structural protein 1 (NS1) of ZIKV and DENV [355]. NS1 remodels the endoplasmic reticulum membrane to form the viral replication complex, a membranous structure where the viral genome replicates [356]. RACK1 silencing markedly reduces the number of viral replication complexes formed. This effect is not related to viral protein translation, suggesting the interaction of RACK1 with N1 regulates assembly of the replication complex [354].

Less is known about the role of RACK1 in bacterial infections. A few reports described RACK1 interactions with secreted bacterial effectors found by yeast two-hybrid screenings. The enteropathogen *Yersinia pseudotuberculosis* can replicate within macrophages and epithelial cells. However, after a few rounds of intracellular replication *Y. pseudotuberculosis* replicates extracellularly. This pathogen uses a T3SS to translocate *Yersinia* outer proteins (Yops) into the cytoplasm of macrophages to avoid phagocytosis [357]. Among these effectors, YopK was found to interact with RACK1 [7]. YopK finely regulates the translocation of other effectors to the right amount [358]. Overexpression of this effector causes secretion inhibition, whereas deletion results in uncontrolled secretion, causing cell cytotoxicity [358]. Interestingly, RACK1 silencing promotes bacteria internalization. The authors hypothesized that in the absence of RACK1, YopK is unable to control effector translocation into the host cell to antagonize internalization. However, this hypothesis was not confirmed [7]. Similarly, the vacuolating toxin VacA secreted by

Helicobacter pylori, the causal agent of stomach ulcers, binds to RACK1 [9]. VacA enhances the pathogenicity of this pathogen and contributes to the development of gastric adenocarcinoma [359]. Although the biological significance of VacA-RACK1 interaction has not been explored, *H. pylori* downregulate RACK1 expression by an unknown mechanism. RACK1 downregulation leads to activation of the NF-κB pathway, which is crucial for *H. pylori*-induced inflammation and carcinogenesis [360].

Recent findings suggest that mammalian RACK1 participates in innate immune responses against bacterial pathogens. Qu et al. reported that RACK1 acts as an endogenous host sensor for *Mycobacterium tuberculosis* [8]. This pathogen targets macrophages to establish its replicative niche. However, RACK1 binds to *M. tuberculosis* secreted effector EST12, triggering cell death by pyroptosis, thereby halting intracellular replication [8]. The EST12-RACK1 complex triggers NLRP3 inflammasome assembly and activation, which leads to caspase-1/GSDMD-mediated cell death and interleukin-1β releasing. Importantly, activation of this pathway results in mycobacterial clearance in mice [8]. Another report supports these findings, showing that RACK1 is required for NLRP3 assembly in response to LPS stimulation in macrophages [361].

Of interest for this thesis, RACK1 has been linked to *Shigella* infection before. It was demonstrated that RACK1 is required for *Caenorhabditis elegans* innate immunity against *Shigella*. *C. elegans* worms succumb to *Shigella* infection after 6 days of exposure, and death occurs regardless of the presence of an alternative food source [362]. Moreover, *Shigella* proliferates in the guts of infected worms. RACK1 deletion significantly increases the bacterial load in the gut, and the mutant worms die earlier than control worms [10]. The immune response in *C. elegans* is mainly mediated by MAPKs. Interestingly, RACK1 deletion leads to downregulation of MAPK expression in *Shigella*-infected worms. Also, activation of the MAPK pathway and expression of the antimicrobial peptide NLP-29 are inhibited [10]. P38 MAPK regulates the expression of NLP-29. Therefore, RACK1 regulates MAPK expression and activation, resulting in the expression of downstream mediators that establish an immune response against *Shigella* infection [10]. RACK1's function in plants supports these findings. *Arabidopsis* contains three copies of RACK1, all of which function

as a scaffold for the MAPK pathway [363]. Secreted protease IV of *Pseudomonas aeruginosa* activates host sensors in the surface of *Arabidopsis* leaves, triggering a G protein complex-MAPK cascade that culminates in immune responses such as oxidative burst. The G protein complex, composed of Gα, Gβ, and Gγ subunits, assemblies at the membrane after sensor activation [364]. RACK1 forms a complex with the Gβ subunit and the MAPKKK/MAPKK/MAPK downstream kinases. RACK1 communicates the G complex signal to the first kinase upon protease IV exposure. As the kinases become active, they are released from RACK1 binding to execute downstream functions [363]. Furthermore, RACK1 binds to Rac1, RAR1 and SGT1, assembling into a complex located at the plasma membrane [365]. This complex regulates innate immunity in rice, triggering ROS production to fight invading pathogens. In agreement, rice and maize plants overexpressing RACK1 show fewer symptoms caused by fungal pathogens demonstrating the protective role of RACK1 [365,366].

To conclude, RACK1 is a crucial mediator of virulence in pathogenic fungi and parasites. While RNA viruses exploit RACK1 translational function to promote viral replication, the role of RACK1 in bacterial pathogenesis is more complex. *Yersinia* and *Helicobacter* target RACK1 to promote pathogenesis, unlike *Mycobacterium*, which triggers immune responses through RACK1-mediated recognition. RACK1's function as a defence molecule against pathogens has been well described in plants. It seems that RACK1 might have a similar role in mammalian organisms as it is involved in inflammasome assembly. However, the functions of RACK1 in host-pathogen interactions remain poorly understood.

1.8 Rationale, hypothesis, and objectives

Despite extensive study of *Shigella* pathogenesis mechanisms, shigellosis is still a significant contributor to the global diarrhoeal disease burden. There are no approved vaccines against *Shigella*, and antibiotic resistance is rising. The myriad of strategies used by this pathogen to invade the colonic epithelia, subvert immune surveillance, and replicate intracellularly is astonishing. However, many gaps in the mechanisms *Shigella* uses to exploit host pathways remain unaddressed. Most research on *Shigella* pathogenesis has focused on bacterial factors involved in invading epithelial cells. However, the host factors and pathways *Shigella* hijacks to invade and spread in epithelial cells are not fully understood.

The role of scaffold proteins in coordinating cellular signalling events makes them a target for invasive pathogens. Given that RACK1 participates in numerous aspects of cellular function in eukaryotic organisms, we thought to evaluate its role in *Shigella* infection. RACK1 has been linked to pro- and anti-pathogenic responses. For example, mammalian RACK1 promotes viral replication, while RACK1 enables immune responses against bacterial pathogens in plants. Moreover, RACK1 has been linked to immune responses against *Shigella* infection in *C. elegans*. As explained in previous sections, *Shigella* exploits the host's actin cytoskeleton, targeting many actin polymerization regulators to invade the cell. Polymerization of an actin tail is pivotal for bacterial intracellular motility and cell-to-cell spread. The fact that RACK1 is an essential player in focal adhesion assembly and actin cytoskeleton dynamics makes this protein an excellent candidate to be targeted by *Shigella*. Understanding the strategies *Shigella* uses to modify the cytoskeleton is crucial for developing treatments that halt invasion and cell-to-cell spreading.

Hypothesis

RACK1 promotes *Shigella*-mediated induction of actin polymerization leading to efficient invasion and cell-to-cell spreading.

Objectives

1. Characterize the effect of RACK1 silencing on *Shigella* infection in HeLa cells and the model organism *Drosophila melanogaster*.
2. Evaluate the role of RACK1 in the main steps of *Shigella*'s intracellular life cycle, including cell invasion, vacuolar escape, intracellular replication, actin tail polymerization and cell-to-cell spreading.
3. Evaluate the impact of RACK1 silencing on actin polymerization dynamics.

CHAPTER 2 MATERIALS AND METHODS

2.1 Bacterial strains and growth conditions

2.1.1 *Shigella flexneri*

Shigella flexneri M90T and its derivatives (Table 2.1) harbouring the pWR100 virulence plasmid were used in this thesis [367]. M90T was collected by Dr. Samuel Formal and first described by Dr. Philippe Sansonetti [79]. The *Shigella* mutant Δ*icsA* is derived from M90T where *icsA* was replaced by a tetracycline resistance cassette (Table 2.1). This mutant cannot spread in epithelial cells [185]. Thus, Δ*icsA Shigella* was used to evaluate bacterial invasion and intracellular replication. M90T and Δ*icsA Shigella* harboured the afimbrial adhesin gene (*afaI*) from *E. coli* [368]. The *afaI* gene confers *Shigella* with much higher invasion abilities in epithelial cells [103]. A faster invasion was desirable to facilitate time-lapse experiments. AfaI was expressed alone (pBR322-AfaI plasmid, Table 2.2) or fused to dsRED (pBR322-AfaI-dsRED plasmid, Table 2.2) to make the strains fluorescent (Table 2.1). *S. flexneri* strains were grown in TSA (BD Bacto™ Tryptic Soy Broth, Cat. No. 21182) supplemented with 15 g/L agar (BioShop, Cat. No. AGR003), 100 µg/mL ampicillin (Sigma Cat. no. A9393, Appendix A) and 0.02% (w/v) congo red (Sigma Cat. No. C6277) to select for functional T3SS system (red colonies). TSA plates were incubated for 15 to 20 h at 37 °C.

For infections, one to three congo red positive *Shigella* colonies were inoculated into 5 mL of TSB (BD Bacto™ Tryptic Soy Broth, Cat. No. 21182) supplemented with 100 µg/mL ampicillin and grown for 15 to 20 h (overnight) with shaking (200 rpm). The next day, a subculture was prepared by inoculating 200 µL of overnight culture into 5 mL of fresh TSB supplemented with ampicillin (100 µg/mL) and grown at 37 °C with shaking until an optical density (OD) of 0.4-0.6 was reached (measured at the wavelength 600 nm, OD_{600}). To prepare the inoculum, 1 mL of *Shigella* subculture was washed once by centrifugation at 5000 x g for 1 min (Hettich Mikro 20) with prewarmed (37 °C) PBS (Phosphate-Buffered Saline, Appendix A). Afterward, the culture was diluted in

prewarmed (37 °C) Dulbecco's Modified Eagle Medium (DMEM, Wisent, Cat. No. 319-005-CL) to the desired multiplicity of infection (MOI) per cell. It is estimated that a culture of *E. coli* that has reached an OD_{600} = 0.5 has approximately 5 x10^8 bacteria/mL [369]. Thus, to infect 1x10^6 cells with an MOI of 10, an inoculum containing 1x10^7 bacteria was prepared.

2.1.2 *Escherichia coli*

The *E. coli* strains used in this study were DH5α and Stbl3™. DH5α was used for general cloning and plasmid storage. Stbl3 was used for cloning, and lentiviral plasmid production as this strain reduces the frequency of homologous recombination of unstable regions such as the long terminal repeats found in lentiviral plasmids. Both bacterial strains were grown at 37 °C on Lysogeny broth (LB, BioShop, Cat. No. LBL407) or LB solidified with 15 g/L agar. Ampicillin (100 µg/mL) or kanamycin (Sigma, Cat. No. K1377-5G, 50 µg/mL) was added to the medium for plasmid selection. Carbenicillin (Thermo Fisher Scientific, Cat. No. BP26485, 100 µg/mL) was used instead of ampicillin when growing Stbl3 transformed with lentiviral plasmids because this antibiotic is more stable and allows higher plasmid yield. Frozen stocks of all strains were maintained at -80 °C in TSB or LB supplemented with 25% glycerol (Sigma, Cat. No. G5516).

Table 2.1. Bacterial strains used in this study

Bacterial strain	Characteristics	Source	In this study referred as
Shigella flexneri M90T	M90T-Sm serotype 5a (GenBank #CM001474.1) carrying the pWR100 plasmid (GenBank #AL391753.1)	Onodera *et al.* [367]	M90T *Shigella*
Shigella flexneri M90T AfaI	Harbours pBR322-AfaI plasmid	Labigne-Roussel *et al.* [368]	WT *Shigella* or *Shigella*
Shigella flexneri M90T AfaI-dsRED	Harbours pBR322-AfaI-dsRED plasmid	This study	dsRED-WT *Shigella*
Shigella flexneri M90T Δ*icsA*	Derivative from M90T. *icsA* was replaced with a tetracycline resistance gene *tetRA* (*icsA*::*tetRA*)	Sidik *et. al.* [370]	Δ*icsA Shigella*
Shigella flexneri M90T Δ*icsA* AfaI-dsRED	Harbours pBR322-AfaI-dsRED plasmid	This study	dsRED-Δ*icsA Shigella*
Escherichia coli DH5α	F^-, *Δ(argF-lac)169*, φ80d*lacZ58*(M15), *ΔphoA8*, *glnX44*(AS), λ^-, *deoR481*, *rfbC1*, *gyrA96*(NalR), *recA1*, *endA1*, *thiE1*, *hsdR17*	Cheng *et. al.* [371]	DH5α
Escherichia coli Stbl3™	F- glnV44 recA13 mcrB mrr hsdS20[rB-, mB-] ara-14 galK2 lacY1 proA2 rpsL20 xyl-5-leu mtl-1	Thermo Fisher Scientific, Cat. No. C737303	Stbl3

Table 2.2. Plasmids used in this study

Plasmid name	Selection markers	Source
pLKO.1-Puro	Ampicillin and puromycin	Addgene, Cat. No. 10878
pLKO.1-Blast	Ampicillin and blasticidin	Addgene, Cat. No. 26655
pLKO.1-NS-Blast*	Ampicillin and blasticidin	Addgene, Cat. No. 26701
pLKO.1-NS-Puro*	Ampicillin and puromycin	Addgene, Cat. No. 162011
pLKO.1- shRNA-92-Puro	Ampicillin and puromycin	This study
pLKO.1- shRNA-93-Puro	Ampicillin and puromycin	This study
pLKO.1- shRNA-94-Puro	Ampicillin and puromycin	This study
pLKO.1- shRNA-95-Puro	Ampicillin and puromycin	This study
pLKO.1- shRNA-71-Puro	Ampicillin and puromycin	This study
pLKO.1- shRNA-74-Puro	Ampicillin and puromycin	This study
pLKO.1- shRNA-80-Puro	Ampicillin and puromycin	This study
pLKO.1- shRNA-92-Blast	Ampicillin and blasticidin	This study
pLKO.1- shRNA-93-Blast	Ampicillin and blasticidin	This study
pLKO.1- shRNA-94-Blast	Ampicillin and blasticidin	This study

Plasmid name	Selection markers	Source
pLKO.1- shRNA-95-Blast	Ampicillin and blasticidin	This study
pLKO.1- shRNA-71-Blast	Ampicillin and blasticidin	This study
pLKO.1- shRNA-74-Blast	Ampicillin and blasticidin	This study
pLKO.1- shRNA-80-Blast	Ampicillin and blasticidin	This study
pEGFP-N1	Kanamycin	Clontech, Cat. No. 6085-1
pEGFP-C1	Kanamycin	Clontech, Cat. No. 6084-1
pEGFP-N1-RACK1	Kanamycin	This study (Constructed by Yunnuo Shi)
pEGFP-C1-RACK1	Kanamycin	This study (Constructed by Yunnuo Shi)
pLJM1-empty-puro	Ampicillin and puromycin	Addgene, Cat. No. 91980
pLJM1-GFP-RACK1	Ampicillin and puromycin	This study (Constructed by Yunnuo Shi)
pLJM1-RACK1-GFP	Ampicillin and puromycin	This study (Constructed by Yunnuo Shi)
pLJM1-RACK1	Ampicillin and puromycin	This study
pLJM1-EGFP	Ampicillin and puromycin	Addgene, Cat. No. 19319
pLV-F-tractin-GFP	Ampicillin and puromycin	Dr. Roy Duncan, Dalhousie University
pLJM1-EGFP-LC3	Ampicillin and blasticidin	Dr. Craig McCormick, Dalhousie University
pLV-F-tractin-mCherry	Ampicillin	Addgene, Cat. No. 85131

Plasmid name	Selection markers	Source
pBR322-AfaI	Ampicillin	Dr. Jost Enninga, Pasteur Institute, France
pBR322-AfaI-dsRED	Ampicillin	Rey *et. al.* [44]
pOrange-Galectin3	Kanamycin	Ray *et. al.* [147]
pEGFP-Actin	Kanamycin	Ray *et. al.* [147]
pOrange-Actin	Kanamycin	Ehsani *et.al.* [158]
psPAX2	Ampicillin	Addgene, Cat. No. 12260
pMD2.G	Ampicillin	Addgene, Cat. No. 12259

* Negative control (shRNA with a nonsense / scrambled sequence)

2.2 Mammalian cell lines and growth conditions

Cell lines used in this study were the human cervical epithelial carcinoma-derived cell lines HeLa Tet-Off (Takara Cat. No. 631156) and HeLa WT (ATCC Cat. No. CCL-2). Also, the human colon epithelial carcinoma cell lines CaCo-2 (ATCC Cat. No. HTB-37) and HT-29 (ATCC Cat. No. HTB-38) were used, along with the human embryonic kidney HEK-293 cell line (ATCC Cat. No. CRL-3216). HeLa Tet-Off cells harbour a tetracycline (Tet)-regulated transactivator that allows inducible tetracycline expression. However, HeLa Tet-Off cells were not used for inducible protein expression; they were used for shRNA-mediated RACK1 silencing. HeLa Tet-Off, HeLa WT, CaCo-2 and HT-29 cells were used for *Shigella* infections, and HEK-293 cells were used to produce lentiviral particles. All cell lines were cultured in DMEM supplemented with 10% heat-inactivated fetal bovine serum (FBS, Wisent, Cat. No. 080450) at 37 °C with 5% CO_2. Cells were passaged before reaching 100% confluency by adding 0.5 mL of 0.05% trypsin-EDTA (Wisent, Cat. No.325-042-CL) to T-25 flasks incubating at 37 °C until cells were dislodged from the flask. Cell suspensions were subsequently diluted to the desired cell density. Cells were not passaged more than 12 to 15 times to maintain experimental consistency and avoid cell line aberrations. A master stock set of 15 cryotubes of each cell line was prepared in DMEM supplemented with 10% DMSO (BioShop, Cat. No. DMS666.100) and stored in a liquid nitrogen container. Also, detection of *Mycoplasma* was performed every time a new cryotube was thawed from the liquid nitrogen storage as follows. Cells were fixed for 15 min with 4% paraformaldehyde (PFA, EM Sciences, Cat. No. 157-8-100) diluted in PBS. Next, the cells were stained with 100 ng/mL 4′,6-diamidino-2-phenylindole (DAPI, Invitrogen, Cat. No. D3571) for 10 min followed by microscopic observation (EVOS FL Auto 2). If cells presented DAPI+ (DNA) staining in the cytoplasm, they were considered contaminated and immediately discarded.

2.3 Molecular biology techniques

2.3.1 Polymerase chain reaction (PCR)

PCR amplifications were routinely carried out using 2X GoTaq®Green Master Mix (Promega, Cat. No. M7122) or Platinum Pfx DNA Polymerase (Invitrogen, Cat. No. 11708) following manufacturer's instructions. All oligonucleotides used as PCR primers and for lentivirus construction were synthesized by Integrated DNA Technologies, Inc. (IDT); their sequences are specified in Table 2.3. PCR primers were re-suspended in nuclease-free water (Invitrogen, Cat. No. 10977) to a concentration of 100 µM (frozen stock) and then diluted to a working solution concentration of 10 µM. A typical 25 µL PCR reaction consisted of 12.5 µL of 2X GoTaq®Green Master Mix (Promega, Cat. No. M7122), one µL of each primer working solution, 1 to 2 µL of template DNA, and nuclease-free water up to 25 µL. For colony PCR, single colonies of *E. coli* transformants were suspended in 50 µL of sterile ddH_2O and heated at 95 °C for 5 min in the thermocycler (Biometra T1) and centrifuged at 16000 x g (MIKRO 20, Hettich) for 1 min. Later, one µL of supernatant was used as a DNA template in PCR reactions.

2.3.2 Agarose gel electrophoresis

Electrophoresis of DNA was performed as follows: 1% agarose gels were made by dissolving 0.5 g of agarose (Thermo Fisher Scientific, Cat. No. BP160) in 50 mL of 1X TAE buffer (appendix A). Three µL of RedSafe (FroggaBio, Cat. No. 21141) were added to the melted agarose before pouring into a gel trail with a comb in place. PCR samples were directly loaded, whereas restriction digestion samples were mixed with 6X loading buffer (NEB, Cat. No. B7024S) before loading. The samples were subjected to electrophoresis at 100 Volts for 20 to 30 min. The ChemiDoc™ Imaging System (Bio Rad Laboratories Inc.) was used for DNA visualization and imaging.

2.3.3 Nucleic acid purification

Plasmid DNA purification (Wizard®PlusSV Miniprep DNA kit, Cat. No. A1465), DNA purification from agarose gels and PCR amplicon cleaning (Wizard® SV Gel and PCR Clean-Up System, Cat. No. A9282) were carried out using commercial kits from Promega as described by the manufacturer. According to the manufacturer's instructions, total RNA was isolated from HeLa Tet-Off cells using an RNeasy Mini Kit (Qiagen, Cat. No. 74104). Removal of contaminating DNA from RNA samples was performed using the DNA-free kit from Invitrogen™ (Cat. No. AM1906). An iScript cDNA synthesis kit (Bio-Rad, Cat. No. 1708891) was used to obtain the complementary DNA (cDNA) that was then used to amplify RACK1 using the primer pairs RACK1_F-SalI/RACK1_R- XbaI or RACK1_F- NheI/RACK1_R- PstI (Table 2.3). Plasmid DNA and cDNA concentrations were measured using a Nano-drop instrument (Thermo Fisher Scientific, Cat. No. ND-ONEC-W).

2.3.4 Competent *E. coli* and heat shock transformation

A single colony of the desired *E. coli* strain from a fresh LB agar plate culture was inoculated into 5 mL of LB and grown overnight at 37 °C with shaking (200 rpm). From the overnight culture, 500 µL were used to inoculate 50 mL of sterile pre-warmed LB. The culture was incubated at 37 °C with shaking until OD_{600} reached ~0.4. Then, the culture was transferred to a pre-chilled 50 mL tube and incubated on ice for 10 min, followed by centrifugation at 4000 x g (Hettich UNIVERSAL 32R) for 10 min at four °C. The supernatant was discarded, and bacterial cells were resuspended with 30 mL of a pre-chilled solution containing 80 mM $MgCl_2$ and 20 mM $CaCl_2$. The cell suspension was spun down by centrifugation at 4000 x g for 10 min at four °C, and the supernatant was discarded. The pellet was resuspended with 2 mL of pre-chilled $CaCl_2$ (0.1 M). Then, 0.5 mL of 80% sterile glycerol was carefully mixed in. The competent cells were stored at -80 °C as 100 µL aliquots. For heat shock transformation, one to three µL of plasmid DNA (~ 400 ng) were added to each tube of competent *E. coli* and incubated on ice for 20 min. Each transformation tube was heated at 42 °C on a dry bath (Mandel) for 90 sec and immediately placed on ice for 2 min. Next, 0.5 mL of warm LB was added to each tube and incubated

at 37 °C in a shaker incubator for 45 min. After this time, 100 µL of transformed cells were spread over an LB agar plate containing the appropriate antibiotic selection. Also, five µL of transformed bacteria were inoculated on a plain LB plate as the control for growth and the rest of the cells were inoculated on a second selection plate. All dishes were incubated overnight at 37 °C. The next day, single colonies were streaked on fresh selection plates or inoculated into 5 mL of LB supplemented with the corresponding antibiotic to make frozen glycerol stocks. Transformants were confirmed by colony PCR (section 2.3.1) and sequencing was done at GENEWIZ.

2.3.5 Competent *Shigella* and transformation by electroporation

A congo-red positive colony of the desired *Shigella* strain was inoculated into five mL TSB and incubated at 37 °C overnight with shaking (200 rpm). Then, the overnight culture was diluted 1 in 50 with TSB and incubated at 30 °C until OD_{600} reached 0.5 (~ 4 h). The culture was placed on ice for 10 min, and then the bacteria were harvested by centrifugation at 3000 x g for 10 min at four °C. The pellet was washed three times with ice-cold ddH_2O. After the final centrifugation, the bacteria were resuspended in 200 µL of ice-cold ddH_2O. Two µL of pBR322-AfaI-dsRED or pBR322-AfaI plasmids (Table 2.2) were added to 50 µL of bacteria suspension and transferred to a chilled 0.1 cm gap electroporation cuvette (Thermo Fisher Scientific, Cat. No. FB101). The cells were electroporated using program Ec1 (1.8 kV for 2.5 msec) of the Power-Pac 200 (Bio-Rad). Immediately after, 500 µL of warm TSB were added to the cuvette, the content was carefully mixed and transferred to a two mL centrifuge tube. The transformed bacteria were incubated at 37 °C with gentle shaking (100 rpm) for one h; then, 100 µL were plated on congo red TSA plates with ampicillin (100 µg/mL) selection. The next day, congo-red positive colonies were selected, resuspended in fresh TSB supplemented with 25% glycerol, and stored at -80 °C.

2.3.6 Plasmid construction

A lentiviral system delivered short hairpin (sh) RNAs into cells to decrease RACK1 expression. Sequences of seven non-overlapping shRNAs (Table 2.3) targeting different

regions of RACK1 mRNA (NM_006098.4) were obtained from The RNAi Consortium (TRC) portal (http://www.broadinstitute.org/rnai/public/gene/search). These shRNA sequences were designed to have the following configuration. Forward and reverse oligos pair with each other and result in two overhangs containing restriction sites for AgeI (forward) and EcoRI (reverse) that can be ligated to a pLKO vector (Table 2.2). Oligos were ordered from IDT (minimum synthesis, standard desalting) and re-suspended in nuclease-free water to obtain a 100 µM stock. Annealing of oligos was performed by mixing 1.5 µL of forward oligo (100 µM), 1.5 µL of reverse oligo (100 µM), five µL of 10X, NEB buffer 2 (Cat. No. B7002S), and 42 µL of nuclease-free water. This mixture was incubated for four min at 95 °C, 10 min at 70 °C, and then left to cool down in the thermocycler overnight. Next, the annealed oligos were ligated into lentiviral pLKO vectors containing either puromycin (pLKO.1-Puro, Table 2.2) or blasticidin (pLKO.1-Blast, Table 2.2) selection markers and transformed into *E. coli* as follows.

First, the plasmids were digested with AgeI (NEB, Cat. No. R3552S) and EcoRI (NEB, Cat. No. R3101S). The digestion mix was made by adding 10 µg of plasmid DNA, 20 µL of 10X Cutsmart buffer (NEB, Cat. No. B7204S), four µL of each digestion enzyme (10 units/µL), and nuclease-free water up to 200 µL. This mixture was incubated at 37 °C for three h and afterward separated on a 1% agarose gel to purify the digested plasmid. Second, a ligation reaction was set by mixing one µL of annealed oligos, 20 ng of digested plasmid, two µL of 10X ligase buffer (NEB, Cat. No. B0202S), one µL of T4 DNA ligase (NEB, Cat. No. M0202S) and nuclease-free water up to 20 µL. The ligation mixture was incubated overnight at 16 °C followed by enzyme inactivation by heating the mixture at 65°C for 10 minutes. Finally, three µL of ligation reaction were transformed into competent Stbl3 cells by heat shock (section 2.3.4). Transformants were inoculated in two mL of LB broth supplemented with carbenicillin (100 µg/mL) and incubated overnight. The next day the plasmids were purified with a miniprep kit (section 2.3.3). In total 14 constructs, containing shRNAs were generated to silence RACK1. Seven carried a puromycin cassette, and the other seven had the blasticidin cassette for antibiotic selection (Table 2.2). All plasmids generated were confirmed by Sanger sequencing (GENEWIZ) using the Human U6_F primer (Table 2.3).

GFP tagged versions of RACK1 were constructed to evaluate the subcellular localization of RACK1 in fixed and live cells. RACK1 was PCR amplified from HeLa cDNA using primer pair RACK1_F-SalI/RACK1_R- XbaI (Table 2.3) and high-fidelity Platinum Pfx DNA polymerase following the manufacturer's instructions. RACK1 was cloned into pEGFP-C1 and pEGFP-N1 (Table 2.2) to obtain N-terminus and C-terminus GFP-tagged versions of RACK1 (pEGFP-N1-RACK1 and pEGFP-C1-RACK1, Table 2.2). For this, pEGFP-C1, pEGFP-N1 and RACK1 amplicon were digested with SalI (NEB, Cat. No. R3138S) and XbaI (NEB, Cat. No. R0145S), and then ligated with T4 DNA ligase overnight at 16 °C. After heat inactivation at 65°C for 10 minutes, three μL of the ligase mixture were transformed into competent DH5α. Transformants were confirmed by colony PCR (section 2.3.1).

The GFP-tagged versions of RACK1 were subcloned into the mammalian expression plasmid pLJM1 (Table 2.2). For this, the plasmids pEGFP-N1-RACK1 and pEGFP-C1-RACK1, and pLJM1 were digested with NheI and XbaI and separated in a 1% agarose gel. The digested pLJM1 plasmid, EGFP-RACK1, and RACK1-EGFP fragments were gel purified and ligated overnight to generate the plasmids pLJM1-GFP-RACK1 and pLJM1-RACK1-GFP (Table 2.2). The ligation mixtures were transformed into Stbl3, and positive transformants were screened by colony PCR. Additionally, an untagged version of RACK1 was constructed as follows. RACK1 gene was PCR amplified from pEGFP-RACK1 plasmid using primers RACK1_F_NheI and RACK1_R_PstI (Table 2.3). The PCR product was digested with NheI and PstI (NEB, Cat. No.: R3131S and R0140S, respectively) and cloned into pLJM1 to generate pLJM1-RACK1 (Table 2.2). All plasmids were verified by sequencing (GENEWIZ).

Table 2.3. Oligonucleotides used in this study

Name	Sequence 5' to 3'	Restriction site
shRNA-92_F	CCGGTACCCTGGGTGTGTGCAAATACTCGAG TATTTGCACACACCCAGGGTATTTTTG	AgeI
shRNA-92_R	AATTCAAAAATACCCTGGGTGTGTGCAAAT ACTCGAGTATTTGCACACACCCAGGGTA	EcoRI
shRNA-93_F	CCGGGATGTGGTTATCTCCTCAGATCTCGAG ATCTGAGGAGATAACCACATCTTTTTG	AgeI
shRNA-93_R	AATTCAAAAAGATGTGGTTATCTCCTCAGAT CTCGAGATCTGAGGAGATAACCACATC	EcoRI
shRNA-94_F	CCGGAGGATGGCCAGGCCATGTTATCTCGA GATAACATGGCCTGGCCATCCTTTTTTG	AgeI
shRNA-94_R	AATTCAAAAAAGGATGGCCAGGCCATGTTA TCTCGAGATAACATGGCCTGGCCATCCT	EcoRI
shRNA-95_F	CCGGCAAGCTGAAGACCAACCACATCTCGA GATGTGGTTGGTCTTCAGCTTGTTTTTG	AgeI
shRNA-95_R	AATTCAAAAACAAGCTGAAGACCAACCACA TCTCGAGATGTGGTTGGTCTTCAGCTTG	EcoRI
shRNA-80_F	CCGGCAGACTCTGTTTGCTGGCTATCTCGAG ATAGCCAGCAAACAGAGTCTGTTTTTG	AgeI
shRNA-80_R	AATTCAAAAACAGACTCTGTTTGCTGGCTAT CTCGAGATAGCCAGCAAACAGAGTCTG	EcoRI
shRNA-71_F	CCGGGATCTGGGATTTAGAGGGAAACTCGA GTTTCCCTCTAAATCCCAGATCTTTTTG	AgeI
shRNA-71_R	AATTCAAAAAGATCTGGGATTTAGAGGGAA ACTCGAGTTTCCCTCTAAATCCCAGATC	EcoRI
shRNA-74_F	CCGGTCGAGATAAGACCATCATCATCTCGA GATGATGATGGTCTTATCTCGATTTTTG	AgeI
shRNA-74_R	AATTCAAAAATCGAGATAAGACCATCATCA TCTCGAGATGATGATGGTCTTATCTCGA	EcoRI

Name	Sequence 5' to 3'	Restriction site
Human U6_F	GACTATCATATGCTTACCGT	none
RACK1_F-SalI	ATTAGTCGACATGACTGAGCAGATGACCC	SalI
RACK1_R-XbaI	TAATTCTAGACTAGCGTGTGCCAATGGTCA	XbaI
RACK1_F-NheI	ATTAGCTAGCATGACTGAGCAGATGACCC	NheI
RACK1_R- PstI	ATTACTGCAGTTAGCGTGTGCCAATG	PstI
Fly RACK1 F	TTCGAGCGACACACTAAGGA	none
Fly RACK1 R	GACACGATCTGACGGTTATCG	none
Fly_Rpl23 F	GACAACACCGGAGCCAAGAACC	none
Fly Rpl23 l R	GTTTGCGCTGCCGAATAACCAC	none

2.4 Protein techniques

2.4.1 Preparation of whole-cell lysates

Cells were harvested by trypsinization and washed two times with PBS. Then, 200 µL of lysis buffer (2% SDS w/v, 50mM Tris/HCl pH 7.4) were added per million cells. Cell lysates were heated for five min at 95 °C (Standard Heatblock, VWR) and placed on ice before sonication for 30 sec at 25 watts, amplitude 40 (Sonics & Materials, Ultrasonic Processor VC50-1). Finally, the lysates were cleared by spinning down the debris at 15,000 x g for 10 minutes at four °C (Eppendorf, 5424R). Supernatants were transferred to new tubes and stored at -20 °C.

2.4.2 Protein quantification and sample preparation

Protein concentration was quantified using the BCA Protein Assay Kit (Thermo Fisher Scientific, Cat. No. 23225) following the manufacturer's instructions. Briefly, samples were diluted 1 in 2 ($<1x10^5$ cells) or 1 in 10 ($>1x10^6$ cells) with PBS. Then, 25 µL of each sample and each bovine serum albumin (BSA) standard, with concentrations ranging from 25 to 2000 µg/mL, were pipetted into a 96-well microplate. Then, 200 µL of working reagent were added to each well, and the microplate was incubated at 37 °C for 30 min. Absorbance at 562 nm was measured on a microplate reader (MBI, Asys UVM 340). The protein concentration of each sample was calculated using the BSA standard curve. Samples for electrophoresis were prepared by mixing 4:1 with 5X-SDS-PAGE loading buffer (320mM Tris-HCl pH 6.8, 40% glycerol, 8% SDS, bromophenol blue 0.02% w/v) and heated at 95 °C for 5 min in a thermoblock (Standard Heatblock, VWR).

2.4.3 SDS-polyacrylamide gel electrophoresis (SDS-PAGE)

Polyacrylamide gels (5% stacking gel and a 12% resolving gel, appendix A) were placed into an electrophoretic chamber (Mini-PROTEAN Tetra Cell from Bio-Rad) filled with 1X running buffer (25mM Tris, 250mM glycine, 0.1% SDS). Between 2.5 µg to 15

µg of protein (depending on protein expression levels) were loaded into separate wells along with three µL of protein ladder (Bio-Rad, Cat. No. 1610393). Proteins were separated first at 60 V (Bio-Rad PowerPac Basic Power Supply) for 15 min to facilitate protein migration into the stacking gel, and then at 150 V for one h (until the bromophenol blue dye front reaches the gel's bottom). After electrophoresis, the gel was stained with Coomassie blue stain or prepared for western blotting analysis.

2.4.4 Western blotting and relative protein expression quantification

Proteins were transferred from polyacrylamide gels to PVDF membranes (Bio-Rad, Cat. No. 1620177) using the Trans-Blot Turbo Transfer System from Bio-Rad (Cat. No.1704150). First, PVDF membranes were immersed in 95% ethanol until the membranes became translucent, and then, equilibrated for 5 min with 1X Trans-Blot® Turbo™ Transfer Buffer (Bio-Rad, Cat. No. 10026938). The transfer was performed using the Turbo Protocol (25 V, 1.3 A, 7 min run for RACK1, tubulin, and actin detection) or the 1.5 mm GEL protocol (2.5 A, up to 25 V, 10 min run for all other proteins detected in this study). After protein transfer, the PVDF membranes were removed from the cassette and rinsed briefly in Tris Buffered Saline with Tween 20 (TBST, 50 mM Tris-HCl pH 7.4, 150mM NaCl, 0.1% v/v Tween 20). In some instances, the membranes were stained for 10 min with Ponceau S (Allied Chemical, Cat. No.628, appendix A) to visualize protein bands. Then, the Ponceau S staining was removed by washing the membranes with PBS. Next, the membranes were incubated with blocking solution (5% skim milk dissolved in TBST) for one h, followed by overnight incubation at four °C with primary antibody (diluted in 5% BSA [BioShop, Cat. No. ALB003] in TBST). The next day, and after three washes with TBST, the membranes were incubated with the corresponding secondary HRP-bound antibodies (diluted in 5% BSA in TBST) for one h. Table 2.4 shows a list of antibodies used in this project. Proteins were detected using 1 mL of luminol-based Clarity Western ECL Substrate (Bio-Rad, Cat. No. 1705061), following manufacturer instructions. Chemiluminescence detection was performed using a ChemiDoc Imaging System.

Fiji software (version 2.3.0)[372] was used to quantify relative protein expression from western blots. For this, an equal size region of interest (ROI) was outlined around each

protein band (samples and loading controls) and background. Next, the mean intensity was measured using the ROI manager. An inverted intensity number was calculated by taking 255 (the maximum brightness value) and subtracting the measured mean intensity value (i.e., 255-value). Then, the background was subtracted from all values to obtain net intensities. The final relative quantification values were calculated by dividing the net intensity of the target band by the net intensity of the loading control. Of note, various loading controls were used for different western blots. This is because at the beginning of the project we did not have antibodies to detect tubulin or actin. Therefore, PonceauS dye or Coomassie-stained gel were used as loading controls to do the quantification. When these dyes where used, a prominent section of the blot or gel was selected to calculate relative expression.

2.4.5 Co-immunoprecipitation for mass spectrometry

Co-immunoprecipitation (Co-IP) using an anti-RACK1 antibody was performed to capture interacting proteins from HeLa cells infected with *Shigella*. WT HeLa cells were seeded on 15 cm culture plates and grown until ~80% confluence was reached. The monolayers were infected with WT *Shigella* (MOI 10) for 1.5 h. A set of cells was left uninfected as a control. After the infection, the cells were washed once with PBS and treated with 2 mL of trypsin for five min. The cells were then transferred to centrifuge tubes and washed two times by centrifugation at 1000 x g for five min. The supernatant was discarded, and the cells were resuspended in 2 mL of RIPA buffer (Santa Cruz, Cat. No. sc-24948) and passed 20 times through a needle (21 gauge). The lysates were homogenized by rotation for 15 min at four °C; then, cell debris was removed by centrifugation at 15,000 x g for 10 min at four °C. The protein concentration of the samples was determined using a BCA kit (section 2.4.2). Before the Co-IP, a pre-clearing step was performed by incubating 1.5 mg of protein of each sample (infected and uninfected cells) with four µg (10 µL) of IgG (Santa Cruz, Cat. No. sc-2025) and 40 µL of A/G PLUS-Agarose (Santa Cruz, Cat. No. sc-2003) for 30 min at four °C with rotation. The agarose beads were spun down at 1000 x g for 5 min at four °C. The supernatants of each sample were then separated into two tubes and incubated overnight at four °C with either 10 µL of anti-RACK1

antibody or 5 µL of IgG (control) antibody. The next day, 20 µL of A/G PLUS-Agarose beads were added to the samples and incubated for two h, at four °C with rotation. The beads were captured by centrifugation (1000 x g for 5 min at four °C) and washed four times with RIPA buffer. Finally, the beads were resuspended in 40 µL 2X SDS-PAGE loading buffer, and 10 µL were separated on two 12% polyacrylamide gels (section 2.4.3). One gel was stained with Coomassie dye to identify areas of the gel that were then excised and sent to the Taplin Biological Mass Spectrometry Facility for protein identification. The second gel was stained with silver stain for more sensitive detection of the proteins pulled down in the Co-IP.

Additionally, RACK1 interaction with Arp2, identified by mass spectrometry, was confirmed by targeted Co-IP. Briefly, 1 mg of protein (unused protein from the infections) was subjected to Co-IP using anti-RACK1 as bait. Then, the A/G PLUS-Agarose beads were washed by centrifugation and mixed with SDS-PAGE loading buffer. After polyacrylamide gel separation, the proteins were transferred to PVDF membranes and probed with anti-Arp2 (Table 2.4)

2.4.6 Coomassie and silver stain

Imperial™ Protein Stain, a Coomassie R-250 dye-based reagent, was used for protein visualization in polyacrylamide gels. After electrophoresis, the gels were washed three times for 5 minutes with distilled water and incubated for one h with Imperial™ Protein Stain (Thermo Fisher Scientific, Cat. No. 24615). The gels were incubated with water overnight to reduce the background. Gel images were captured using a ChemiDoc Imaging System. For silver stain, the polyacrylamide gels were fixed (50% methanol, 10% acetic acid in water) for 30 min and then incubated with 50% methanol for 15 min. After five washes with water, the gels were incubated with a 0.2 g/L sodium thiosulfate (Sigma, Cat. No. 217247) solution for one minute, then washed three times with water. The gels were afterward equilibrated with 0.2% silver nitrate (Sigma, Cat. No. 209139) for 30 minutes and briefly washed three times before developing with a 0.02% formaldehyde (Thermo Fisher Scientific, Cat. No. F79-1), 3% sodium carbonate (Sigma, Cat. No. 230952) solution

for 10 min. The reaction was stopped by transferring the gel to a 40 mM EDTA (Sigma, Cat. No. E9884) solution.

Table 2.4. Antibodies and fluorescent dyes used in this study

Name	Dilution and application	Source and Cat. No.
Anti-Actin-HRP	WB: 1/2000	Santa Cruz, sc-47778
Anti-Arp2	IF: 1/100, WB: 1/1000	Santa Cruz, sc-166103
Anti-Armadillo	IF: 1/100	DSHB, N27A1
Anti-EEA1	WB: 1/1000, IF: 1/100	Santa Cruz, sc-137130
Anti-LAMP1	WB: 1/1000, IF: 1/100	Santa Cruz, sc-20011
Anti-LC3	IF: 1/100	Novus Biotech, NB100-2220
Anti-GBP 1	IF: 1/100	Santa Cruz, sc-53857
Anti-GBP 4	WB: 1/1000, IF: 1/100	Novus Biotech, H00115361-B01P
Anti-mouse-Alexa-488	IF: 1/1000	Molecular Probes, R37120
Anti-mouse-Alexa-555	IF: 1/1000	Invitrogen, A32727
Anti-mouse-HRP	WB: 1/10000	Bio-Rad, 170-5047
Anti-rabbit-Alexa-488	IF: 1/1000	Invitrogen, A11008
Anti-rabbit-HRP	WB: 1/3000	Bio-Rad, 170-6515
Anti-RACK1	WB: 1/2000, IF: 1/100	Santa Cruz, sc-17754
Anti-RACK1-Alexa-647	IF: 1/100	Santa Cruz, sc-17754 AF647
Anti-rat-Alexa-555	IF: 1/1000	Invitrogen, A-21434
Anti-Tubulin-HRP	WB: 1/5000	Santa Cruz, sc-8035
DAPI (5 μg/μL)	Live-cell imaging: 1/2000, IF:1/50000	Invitrogen, D3571
Phalloidin-Alexa-555	IF: 1/100	Invitrogen, A34055
Phalloidin-Alexa-647	IF: 1/100	Invitrogen, A22287

HRP: horseradish peroxidase, WB: western blot. IF: immunofluorescence

2.5 RACK1 knockdown and stable/transient reporter cell lines

2.5.1 Lentiviral production

Stable RACK1 knockdown (RACK1-KD) cells and stable reporter cell lines were generated using lentiviral particles. The second-generation lentivirus system used was composed of the following plasmids: pMD2.G for expression of the cell attachment and fusion protein derived from Vesicular stomatitis virus (VSV-G), psPAX2 for expression of the HIV genes (Gag, Pol, Rev, and Tat) required for successful packaging, and a transfer plasmid (pLJM1 or pLKO.1) containing the construct of interest, the resistance cassette for selection and a packaging signal (Table 2.2). HEK-293T cells (1 x 10^6) were plated on 10 cm tissue culture dishes and grown until they reached 70-80% confluency. Transfection reactions were prepared by adding three µg of RACK1 knockdown plasmid (e.g., pLKO.1-shRNA-92-Puro) or pLJM1-GFP (transfection efficiency control), two µg of psPAX2, and one µg of pMD.2G to 500 µL of OptiMEM (Gibco, Cat. No. 31985-062). In a second tube, 18 µL of polyethyleneimine (PEI 1 mg/mL pH 7.0, Sigma, Cat. No. 765090) was added to 500 µL of OptiMEM. Both mixtures were gently mixed before slowly adding the plasmid mixture to the tube with PEI. The transfection mixture was incubated at room temperature for 20 min. After this time, HEK-293T cells were washed once (very gently) with 10 mL of PBS, and then 8 mL of serum-free, antibiotic-free DMEM was added. In a dropwise manner, 1mL of transfection mixture was added to each plate and gently mixed with swirling motion. The cells were incubated at 37 °C with 5% CO_2 for four to six hours before adding 1 mL of FBS. After 48h of transfection, the lentiviral particles were harvested by aspirating the media with a syringe. Cell debris was eliminated by filtering the media through a 0.45 µM syringe filter (Polyethersulfone). Lentiviruses carrying the plasmids pLJM1-GFP-RACK1, pLJM1-RACK1-GFP, pLJM1-RACK1, pLJM1-EGFP, pLV-F-tractin-GFP, and pLV-F-tractin-mCherry were generated using this protocol. Lentiviruses were stored as single-use aliquots (1 mL) at -80 °C.

2.5.2 Lentiviral transduction of target cells

Between 2.5 to 5.0 x 10^4 target cells were seeded on each well of a 12-well plate. The next day, the cells media was replaced with 1 mL/well of DMEM containing eight µg/mL

polybrene (Hexadimethrine bromide, Sigma, Cat. No. 107689) and 10% FBS. The lentiviruses were placed on a 37 °C dry bath until thawed. Then, 1 mL of lentivirus was added to the first well and gently mixed three times before transferring 1 mL to the next well, generating 1 in 2 serial dilutions (from 1/2 to 1/32). One well was left un-transduced to test antibiotic selection efficacy. After 24 (HeLa) or 48 h (Caco-2 and HT-29) of transduction, the cells media was replaced by DMEM with 10% FBS and puromycin (Gibco, Cat. No. A11138-03) or blasticidin (Gibco, Cat. No. A11139-03).

The optimal antibiotic concentration was determined beforehand by exposing the target cells to various concentrations of selection antibiotic. The minimum concentration of puromycin that resulted in the complete death of HeLa cells after 24 h was 1 μg/mL; for Caco-2 and HT-29 cells, 2 μg/mL resulted in total death after 48 h. Blasticidin selective concentration was 4 μg/mL for all cell lines but took 4 to 5 days to induce complete death. Lentiviral insertion in the cell's genome confers resistance to antibiotic selection. Thus, when cell death was observed in the un-transduced control well, the lentiviral dilution that caused approximately one-third of the cells to survive (still attached to the well) was identified. These cells were harvested by trypsinization and transferred to a six-well plate to generate a stable cell line. In this manner, most cells will only have one integration event. Two sets of putative RACK1 knockdown cells (with puromycin or with blasticidin resistance) were generated using this protocol. RACK1 silencing was confirmed by western blotting in only three out of the seven cell lines generated. Thus, the stable RACK1-KD cell lines named KD-92, KD-94 and KD-95 were selected for further analysis.

Additionally, cell lines carrying non-sense shRNAs (pLKO.1-NS-Blast or pLKO.1-NS-Puro) and cells stably expressing fluorescent proteins were generated using this protocol. The reporter proteins used for stable expression were RACK1-GFP, GFP-RACK1, GFP and GFP-LC3. Also, the F-tractin probe fused to GFP or mCherry was utilized to detect filamentous actin.

2.5.3 Transient expression of fluorescently tagged proteins

Three transfection reagents were used following manufacturer's instructions. FuGENE (Promega, Cat. No. E2311) transfection reagent was used when two plasmids were transfected (e.g., pOrange-Galectin3 and pEGFP-Actin) and X-tremeGENE (Sigma, Cat. No. 6365779001) was used for single plasmid transfections. Lipofectamine 2000 (Thermo Fisher Scientific, Cat. No. 11668019) was used to transfect pLJM1-GFP-RACK1 and pLJM1-RACK1-GFP into HeLa cells. Twenty-four hours before transfection, cells were seeded to obtain ~50-60% confluency. The transfection mixture contained 3.6 µL of transfection reagent and 0.8 µg of plasmid DNA added to 120 µL of OptiMEM. After incubation for 20 min at room temperature, five µL of the transfection mixture were added to 96-well plates, 15 µL to 4-well dishes or 100 µL to 12-well plates. Transfected cells were incubated 48 h before use to allow optimal transgene expression.

2.6 Proliferation assay (MTT)

The MTT (3-[4,5-dimethylthiazol-2-yl]-2,5-diphenyltetrazolium bromide, Sigma, Cat. No. 475989) assay was utilized to measure cellular proliferation of RACK1-KD cells. The principle of this assay is that viable cells reduce MTT to formazan crystals that can be dissolved using DMSO generating a coloured solution. The darker the solution, the higher the number of metabolically active cells. The assay was performed as follows. NS (non-sense shRNA), KD-92, KD-94, and KD-95 cell lines were seeded in a 96-well plate (2000 cells/well). After 24, 48, 72, 96, 120, and 144 hours of incubation, the medium was removed and replaced with 100 µL of fresh DMEM. Wells containing media only were included to measure background. Ten µL of 12 mM MTT solution were added to test wells, and the plate was incubated at 37 °C for 4 hours. Subsequently, 75 µL of medium were removed from the wells and discarded. Then, 50 µL of DMSO were added to each well to dissolve the formazan crystals formed. After incubation for 10 min at 37 °C, absorbance was read at 540 nm on a microplate reader (MBI, Asys UVM 340).

2.7 Gentamycin protection assay

This assay was used to evaluate *Shigella* growth in epithelial cells. Target cells (2.5 x10^5 cells/well) were seeded in 12-well plates. The following day, the cells were infected with 1 mL/well of bacterial inoculum at the desired MOI. The plate was left at room temperature (*Shigella* does not invade cells at this temperature) for 10 min to synchronize the infection. Then, the plate was incubated at 37 °C for 30 min. Afterward, the monolayers were washed once with PBS and treated for 15 min with DMEM supplemented with gentamycin (100 µg/mL) to eliminate extracellular bacteria. After 3 washes with PBS, the cells were lysed with 200 µL of NP-40 buffer (0.1% NP40, 50 mM Tris-HCl pH 7.5, 5 mM EDTA, 10% glycerol, 100 mM NaCl) for 5 min with slow shaking. The lysates were then transferred to a 96-well plate and serially diluted (1/10, 1/100, and 1/1000) using TSB. Ten µL of each dilution were plated on rectangular LB plates and incubated overnight at 37 °C. When several time points of infection were evaluated, the cells were incubated with DMEM after gentamycin treatment for the duration of the infection time (e.g., three h) and lysed as described. Pictures of the LB plates were taken after 24 h, which were used to count colony-forming units (CFU) using the cell counter tool from Fiji software. The CFU counting was normalized by the total protein concentration on each well. For this, the infected cells lysates were diluted 1 in 2 with PBS and assayed using the BCA kit (section 2.4.2).

2.8 *Shigella* infection of *Drosophila melanogaster*

Fly experiments were performed by Dania Shikara and Dr. Francesca Di Cara. Wild type flies W1118 Mex-Gal4 (a kind gift from Prof. Carl Thummel, University of Utah) and W1118 Mex-Gal4 RACK1-RNAi were used as control and experimental strains, respectively. RACK1 was depleted only in enterocytes using the RNAi stock 38198 from Bloomington Drosophila Stock Center. RACK1 silencing was confirmed using qPCR. Briefly, fly guts were embedded with TRIzol reagent (Thermo Fisher) and snap-frozen in liquid nitrogen. Total RNA was extracted using the RNeasy-Micro Kit (Qiagen) following the supplied protocol. RNA was reverse transcribed using the iScript cDNA Synthesis kit (Bio-Rad), and the synthesized cDNA was used for qPCR using the SYBR-Green PCR master mix (Kapa Biosystems) using a Realplex qPCR machine (Eppendorf). Samples were

normalized to Rpl23 gene expression using the 2-ΔΔCT method [373]. Forward and reverse primer sequences used in qRT-PCR are shown in Table 2.3. Age-matched female and male flies (20 per group) were used to measure fly survival. Crosses were kept at 25° C and then moved to 29° C for the oral infections. The bacterial inoculum used to infect the flies was prepared by spinning down a same day 500 mL culture of dsRED-WT *Shigella* with OD_{600}=0.5. The bacterial cells were then washed once with PBS and resuspended in 10 mL of 5% sucrose to obtain a concentrated inoculum with an approximate OD_{600} = 25. Twenty flies were fed on filter paper soaked in 5% sucrose (control) or 5% sucrose containing dsRED-WT *Shigella.* Flies were transferred to fresh vials every two days, and the number of dead flies was determined daily.

Additionally, immunofluorescence of fly guts was performed as follows. The guts were fixed in 4% paraformaldehyde diluted in PBS for 30 min, washed three times in PBST (PBS containing 0.3% Triton X-100), followed by blocking at room temperature in 5% goat serum diluted in PBST for one h. An anti-armadillo antibody was used for immunolabeling fly enterocytes. This antibody was incubated for 16 h at four °C diluted 1:10 in 5% normal goat serum. Then, the guts were incubated with anti-mouse bound to Alexa-488 (Table 2.4) for two hours at room temperature. Finally, guts were mounted in Prolong Gold Antifade. After 24 h curation, the samples were imaged using a confocal microscope (Zeiss LSM 880, Table 2.5). Z-stacks composed of 15 slices, separated by 1 µm, were captured with 20X magnification. Survival analysis was performed using R packages "`survival`" and "`survminer`". Statistical differences were calculated using a log-rank test (`survdiff` function).

2.9 Cell death evaluation

2.9.1 Annexin V apoptosis assay using flow cytometry

HeLa cells with or without RACK1-KD were seeded at 80-90% confluency (~$5x10^5$ cells/well) in 12-well plates. After 24 h, the cells were left uninfected or infected for 30 min with dsRED-WT *Shigella* (MOI 10) and then treated with gentamycin (100 µg/mL) for 15 min. Afterwards, the cells were carefully washed three times with pre-warmed (37

°C) PBS and incubated with fresh DMEM for 12 h at 37 °C and 5% CO_2. HeLa cells treated for 30 min with 0.88 mM hydrogen peroxide (H_2O_2, Thermo Fisher Scientific, Cat. No. H325500) were the positive control for apoptosis. After infection or H_2O_2 treatment, the cells were collected by trypsinization and washed three times with ice-cold PBS. Cells were then resuspended in 1X Annexin binding buffer (BD Bioscience, Cat. No. 556547) to obtain ~$1x10^5$ cells in 100 µL. Subsequently, the cells were stained for 15 min (at room temperature and protected from light) with 3 µL of Annexin V conjugated to FITC (BD Bioscience, Cat. No. 556547) to detect apoptotic cells, and 0.5 µL of 7-AAD (7-Aminoactinomycin D, Cayman Chemical, Cat. No. 11397) dye to identify membrane-permeable cells. After staining, the cells were diluted by adding 400 µL of 1X binding buffer. Apoptotic cells were immediately detected using a CytoFlex flow cytometer (Beckman Coulter, USA), equipped with a 50 mW 488 nm blue laser. The three fluorescent markers used were all excited with the 488 nm laser. The Annexin V-FITC signal was detected using a 525/40 emission bandpass filter, dsRED was detected using a 585/42 bandpass filter, and 7-AAD was detected using a 690/50 bandpass filter. Compensation of the fluorescent signals was performed using CytoFlex's operating software, CytExpert, using single stained controls for Annexin-FITC and 7-AAD, where cell death and apoptosis were induced by treating the cells with H_2O_2. The compensation control for dsRED was a sample of dsRED-WT *Shigella* diluted in PBS. Data were analyzed with FCS Express (De Novo Software, USA). Cells were identified using an initial side scatter plot (SSC) versus forward scatter (FSC). After which, potential double-cell events were removed from the analysis using a pulse-geometry gate (FSC height versus FSC area). Uninfected fully stained (Annexin V and 7-AAD) cells were utilized as gating and biological controls to identify *Shigella* infected cells, thus containing the dsRED signal. Apoptotic and necrotic cells were identified by plotting 7-AAD versus Annexin V-FITC.

2.9.2 Cytotoxicity detection assay

The Cytotoxicity Detection Kit (Sigma, Cat. No: 04744926001 - Roche) was used to evaluate cytotoxicity and cell lysis caused by *Shigella.* This assay measures lactate dehydrogenase (LDH) activity released from the cytosol of damaged cells into the

supernatant. The supernatants from infected and uninfected cells used in the Annexin V-7AAD assay (section 2.9.1) were collected. Any cell or cell debris was removed from the culture medium by centrifugation at 1000 x g for 5 min. Uninfected cells from each condition (control and RACK1-KD) were collected to determine the maximum LDH produced. Following the manufacturer's instructions, 100 µL of infected (sample) and uninfected (low LDH control) supernatants were plated in triplicate on a 96-well plate. Also, 100 µL of cells (high LDH control) and 100 µL of DMEM (background control) were plated. Five µL of lysis solution were added to the high LDH control wells and incubated at room temperature for 15 min with gently shaking. To determine LDH activity, 100 µL of the reaction mixture (for one reaction: 2.2 µL of catalyst mixed with 97.8 µL of dye solution) was added to each well. The plate was incubated for 10 min at room temperature, protected from light, and then the reaction was stopped by adding 50 µL of stop solution. The plate was shaken for 10 seconds before reading the absorbance at 492 nm. To determine the percentage of cytotoxicity caused by *Shigella*, the average absorbance value of the background control was subtracted from the average absorbance values of the samples, high and low controls. Then, the values were entered in the following equation:

$$Cytotoxicity\ (\%) = \frac{sample - \ low\ control}{high\ control\ - \ low\ control} \times 100$$

2.10 Immunofluorescence of fixed samples and data analysis

2.10.1 Immunofluorescence

Immunofluorescence staining was used in this study to evaluate the role of RACK1 at various steps during the infection process. With this purpose, infections were designed to capture *Shigella*'s early (entry to the host cell and vacuolar escape) and late infection events (actin tail polymerization and protrusion formation). Twelve mm round glass coverslips (VWR, Cat. No. 89015-725) were sterilized by autoclaving and placed on 4-well plates (Thermo Fisher Scientific, Nunc™, Cat. No. 144444). To improve cell attachment to the coverslip, they were coated with 20 µg/mL fibronectin (100 µL/coverslip. Sigma,

Cat. No. F1141) for one h, at room temperature. Fibronectin was then removed, and 2.5 x 10^5 cells were added to each well. Target cells were incubated for 24 h before infection. For early event evaluation, cells were infected with the desired *Shigella* strain (e.g., dsRED-WT) using an MOI of 50 for 30 min at 37 °C with 5% CO_2. After this time, the cells were carefully washed three times with PBS and fixed for 20 min with freshly diluted 4% PFA (in PBS). For late event evaluation, infections were carried out by adding an MOI of 10 to the cells and incubating for 30 min at 37 °C, followed by gentamycin (100 µg/mL) treatment for 15 min. The cells were carefully washed three times with PBS, fresh media was added before continuing the infection for 2 hours at 37 °C with 5% CO_2. Next, the cells were washed once with PBS and fixed with 4% PFA for 20 min. After fixation, the coverslips were washed three times with PBS and incubated with 250 µL of permeabilization solution (0.25% v/v Triton X-100 in PBS) for 10 min at room temperature. After three washes with PBS, the coverslips were incubated with 250 µL of blocking solution (1% BSA w/v and 0.3 M glycine in PBST [0.1% v/v Tween 20 in PBS]) for 30 min at room temperature. Primary antibodies were diluted in 1% BSA in PBST (as indicated in Table 2.4), and 100 µL drops were placed on a parafilm-covered dish. Each coverslip was carefully placed (cells facing down) on the antibody drop and incubated overnight in a humid chamber at four °C. The following day, the coverslips were put back on the 4-well plate and washed three times with PBST. As before, the coverslips were placed on drops containing the corresponding secondary antibodies bound to Alexa-488 or Alexa-555 (see Table 2.4 for dilutions) and incubated at room temperature for two h. Detection of RACK1 using anti-RACK1-Alexa-647 did not require a secondary antibody as it is already bound to a fluorophore. In some instances, phalloidin bound to Alexa-555 or Alexa-647 was added to the secondary antibody mixture to stain filamentous actin (F-actin). Subsequently, the coverslips were washed three times with PBST and incubated with 250 µL of DAPI (Table 2.4) for 20 min at room temperature. After three washes with PBST, the coverslips were mounted on glass slides using 3 µL of ProLong Diamond Antifade Mountant (Molecular Probes, Cat. No. P36965) and left overnight at room temperature for curation. The samples were stored at -20 °C until visualization was performed using various fluorescent microscopes (see Table 2.5).

2.10.2 Analysis of intracellular replication in fixed samples

Δ*icsA Shigella* was used to evaluate intracellular replication in control and RACK1-KD cells because this strain cannot form actin tails [185]. Therefore, the number of bacteria found inside cells reflects intracellular replication only, not secondary infections. For this experiment, cells expressing F-tractin-GFP (binds to actin) were infected with dsRED-Δ*icsA Shigella* (MOI 10) for 30 min and then treated with gentamycin (100 µg/mL) for 15 min. The cells were incubated at 37 °C with 5% CO_2 for three h before fixing as described in 2.10.1. Z-stacks composed of 6 slices 0.8 µm apart were captured at 63X magnification with a confocal microscope (Zeiss LSM 880 AxioObserver, Table 2.5).

Given that Δ*icsA Shigella* replicates to high numbers in the cytoplasm of infected cells, enumeration of individual bacteria was not possible. Instead, the area inside the cell occupied by bacteria and their fluorescence intensity (FI) was measured. For this, an automatic segmentation method was used (an example of the script can be found in Appendix B.1). First, the images were separated into two channels, one corresponding to cells (F-tractin-GFP) and one to bacteria (dsRED-Δ*icsA Shigella*). Independent average intensity z-projections were generated with the bacteria and cells z-stacks. To identify bacteria, `background` (rolling = 50) was subtracted, then a `Gaussian blur` (sigma = 2) filter was applied to the dsRED image projection. Next, this image was converted to a binary mask using `Huang's` threshold method with default values. The cells outlines were manually drawn using the polygon selection tool. A mask was created using the outlines of the cells. Then the bacteria and cells masks were used to identify particles (bacterial clusters) on each cell using Fiji's `Speckle inspector` plug-in (Fiji's BioVoxxel Toolbox). The ROI manager measured the area occupied by bacterial clusters and the area of the cells. The `speckle inspector` also assigned a cell ID number to each bacterial cluster. The FI of the clusters was also measured from the original average projection image of bacteria. These data were analyzed in R. The sum of the area occupied by bacterial clusters identified on each cell was normalized by the cell's area to account for cell size variability. The FI of bacteria was not normalized as the images were taken using the same microscope settings. Statistical differences between RACK1-KD and NS cells were evaluated using a Wilcoxon test.

2.10.3 Targeting of *Shigella* by guanylate-binding proteins (GBPs)

GBP1 and GBP4 are interferon-gamma (IFN-γ) induced proteins that bind to cytosolic *Shigella*, blocking actin-based motility [205]. GBPs association with *Shigella* in control and RACK1-KD cells was evaluated. HeLa cells expressing F-tractin-GFP were seeded in 12 mm rounded glass coverslips (1.5 x 10^5 cells/coverslip). After 24 h, the cells were treated with one ng/mL of IFN-γ (Abcam, Cat. No. ab259377) or with one μM of Ruxolitinib (RUX, Selleckchem, Cat. No. S1378), which is an IFN-γ signalling inhibitor. Untreated cells were incubated with DMEM only. After 16 h of treatment, cells were infected with WT *Shigella* (MOI 50) for 30 min followed by gentamycin (100 μg/mL) treatment for 15 min. Subsequently, the cells were carefully washed three times with warm PBS and incubated at 37 °C and 5% CO2 for 3 h. After this time, the cells were fixed and immunolabeled as described in 2.10.1 using DAPI (for DNA), anti-GBP1 or anti-GBP4 antibodies and their corresponding secondary antibodies (Table 2.4). Nine tiles composed of z-stacks (5 slices, 0.5 μm apart) with 10% overlap were captured per condition (untreated, IFN-γ and RUX) at 63X magnification using a confocal microscope (Zeiss LSM 880, Table 2.5).

To identify GBP1 positive (GBP1+) *Shigella* (GBP4 targeting was not quantified), the images were analyzed in Fiji as follows. All bacteria were identified from the average projections of the DAPI channel. Before bacterial segmentation, the `background` was subtracted (rolling = 50), and the `Mean` filter (radius = 2) was applied. The images were then converted into binary masks using `Huang's` thresholding with default settings. The masks were next used to count all bacteria using Fiji's `Analyze particles` tool. The particle size was set to 20 to 500 pixels to exclude nuclei (DAPI stains bacteria and cell nuclei), keeping only bacteria. Similarly, GBP1+ *Shigella* were identified from the average projection of the GBP1 channel (Alexa-555). `Background` subtraction (rolling = 50), `Mean` (radius = 2) and `Gaussian blur` (sigma = 2) filters, and `RenyiEntropy` threshold were applied to the images. More details on the Fiji macro can be found in Appendix B.2. The number of GBP1+ bacteria was obtained by running the `Analyze`

`particles tool` with default settings. Statistical significance was tested in R using a two-way analysis of variance (ANOVA).

2.10.4 Analysis of actin tails in fixed samples

Shigella modulates the host actin cytoskeleton machinery to induce actin tail polymerization [234]. Actin tail number and morphology were evaluated to assess if RACK1 plays a role in actin tail polymerization. RACK1-KD and control HeLa cells expressing F-tractin-GFP (binds actin) were infected with dsRED-WT *Shigella* and fixed as described in 2.10.1 (late infection steps). Z-stacks were acquired at 63X magnification containing six slices, 1.2 µm apart, using a confocal microscope (Zeiss LSM 880 AxioObserver, Table 2.5). Average projections of the top 4 slices were generated in Fiji. The bottom (closer to glass) slices were not included in the projection to avoid stress fibre interference in the analysis. The number of bacteria with and without actin tail was manually noted. Also, Fiji's polygon selection tool was used to manually define regions of interest (ROIs) around tails that were then added to the ROI manager. The following measurements were chosen from Fiji's analysis tab: `area, mean FI, circularity` (4pi[area/perimeter^2]), and `Feret's diameter`. Then, these parameters were measured using the ROI manager. The data generated was entered in R for further analysis and plotting. Statistical differences between control and RACK1-KD were analyzed using the Wilcoxon rank-sum test (Wilcoxon test) for tail's area, mean FI, and Feret's. Unpaired two-tail student's t-test (t-test) was used to evaluate the number of tailed bacteria. The statistical test was chosen based on the data distribution.

2.10.5 Quantification of Arp2 recruitment to *Shigella*

Shigella exploits the function of the Arp2/3 complex to trigger actin tail polymerization [234]. Given that RACK1 was found to interact with Arp2, the role of RACK1 on Arp2 recruitment to *Shigella*'s actin tail was assessed. For this, control (NS) and RACK1-KD (KD-92) HeLa cells infected with dsRED-WT *Shigella* (MOI 10) for two h were fixed and immunolabeled with DAPI and anti-Arp2. Images were taken on a Zeiss

710 confocal with 63X magnification. The number of Arp2 positive (Arp2+) *Shigella* were manually quantified.

2.11 Live-cell imaging and data analysis

Live-cell fluorescent microscopy was used extensively in this study. Live observation of *Shigella* infection provided spatial and dynamic information that could not be captured by solely evaluating fixed samples. This included entry foci formation dynamics, vacuolar escape, and intracellular motility assessed in the context of RACK1 silencing. Also, RACK1 subcellular localization during *Shigella* infection and LC3 (Microtubule-associated protein 1A/1B-light chain 3) targeting of bacteria were evaluated by live-cell imaging. Similarly, live microscopy was used to study *Shigella* growth and cell-to-cell spreading in cell monolayers using an aqueous two-phase (ATP) infection system and a modified plaque assay, respectively. To follow target proteins in real time, host cells were either transiently transfected with plasmids expressing a fluorescent fusion of the protein of interest (e.g., pEGFP-Actin), or the cells were stably transfected by lentiviruses (e.g., F-tractin-GFP).

For all live-cell imaging experiments, dishes and plates were coated with 20 µg/mL of fibronectin for one h. Infections were performed using WT, dsRED-WT, or dsRED-Δ*icsA Shigella*. During imaging, the cells were maintained in FluoroBrite DMEM (Gibco, Cat. No. A1896701) since this medium confers very low background fluorescence enhancing the signal-to-noise ratio of fluorophores. To preserve cell viability in long-term imaging experiments (>10h), FluoroBrite was supplemented with four mM L-glutamine (Wisent, Cat. No. 609-065-EL), ten µM HEPES (Gibco, Cat. No. 15630080) and 10% FBS (FluoroBrite complete). Live-cell imaging was performed using various microscopy configurations detailed in Table 2.5. Before analysis, all images were converted to 8-bit Tagged Image File Format (TIFF). Images and statistics were analyzed using Fiji (version 2.3.0) and R (version 4.1.1). The following sections describe the experimental approaches and the data analysis performed. Script examples can be found in appendix B.

2.11.1 Live-cell imaging of *Shigella* entry and vacuolar escape in HeLa cells

To study the role of RACK1 in entry and vacuolar escape, 6 x 10^3 cells/well of RACK1-KD or control HeLa were seeded on black 96-well plates (Thermo Fisher Scientific, Cat. No. 165305) and transfected with pOrange-Galectin3 (Gal-3, vacuolar rupture reporter) and pEGFP-Actin. After 48 h, the cells media was replaced by 50 µL of FluoroBrite. Infection was carried out by adding 50 µL of WT *Shigella* inoculum (MOI 10) right before image capture. Cells were imaged every 1 minute for 1.5 h at 37 °C and 5% CO_2 using a widefield microscope (Nikon Eclipse Ti, Table 2.5) with 40X magnification.

Because non-fluorescent bacteria were used in these experiments, the study of the early steps in *Shigella*'s infection cycle was through visualization of *Shigella*'s effects on the cell. These effects were evidenced by actin polymerization induction (detected with F-tractin-GFP) and damage of the vacuole (detected by Gal-3 recruitment). Gal-3 was used to confirming invasion as it only binds to the vacuole once it is damaged by *Shigella*. The number of infected cells was calculated by identifying HeLa cells with at least one Gal-3 positive (Gal-3+) signal by the end of imaging time. Similarly, the number of Gal-3 positive bacteria per cell was manually enumerated.

To analyze the early steps of infection, *Shigella* entry, vacuolar escape and actin tail polymerization where manually noted as follows. The time of *Shigella* entry was defined as the time (in the video) where the first signs of actin cytoskeleton reorganization induced by *Shigella* could be recognized (F-actin-GFP enrichment). After bacterial invasion, the recruitment of Gal-3 to the damaged *Shigella*-containing vacuole marked the time of vacuolar escape. Then, the first signs of actin polymerization in one pole of the bacterium (actin node time) and the time when actin tail elongation was first observed were also recorded (actin tail time). These time points were used to compare the early steps of bacterial infection in control and RACK1-KD cells as follows: escape time equalled to Gal-3+ time minus entry time; actin node time equalled to actin node time minus Gal-3+ time; and actin tail time was calculated by subtracting the Gal-3+ time from the actin tail time.

2.11.2 Evaluation of Δ*icsA Shigella* entry to HeLa cells

The Δ*icsA Shigella* strain was used to evaluate bacterial entry. This strain cannot spread from cell to cell due to a lack of actin tail polymerization reflecting the number of primary infected cells [185]. For this experiment, 2.5 x 10^4 RACK1-KD or control HeLa cells stably expressing F-tractin-GFP were seeded on black 96-well plate wells. After 24 h, the cells were infected with 100 µL of dsRED-Δ*icsA Shigella*. The inoculum was prepared by diluting an OD_{600} = 0.5 subculture 100 times in DMEM. The infection was carried out for 30 min at 37 °C with 5% CO_2, followed by 15 min of gentamycin (100 µg/mL) treatment. After this time, the cells were carefully washed three times with warm PBS, and 100 µL of fresh FluoroBrite was added to each well. The infected cells were incubated for 4 hours at 37 °C with 5% CO_2 before imaging using a widefield microscope (AxioObserver, see Table 2.5) at 10X magnification. To image a large field of view (>50% of the well's area), 16 smaller images referred to as tiles were captured. These tiles were imaged individually and later combined via stitching to a larger image using Zeiss Zen Black software.

Since the Δ*icsA* strain does not spread to other cells, the bacteria replicate to high numbers inside infected cells. As the cells become full of fluorescent bacteria, they are easily recognizable and counted by automatic segmentation. The area of 10 randomly chosen HeLa cells was measured using the F-tractin-GFP signal to identify the cell's body. The average area of these cells (400 pixels) was used as the threshold to select infected cells from the image channel corresponding to bacteria (dsRED). Any dsRED structure smaller than 400 pixels was not counted as an infected cell. The images were processed as follows. `Background` (rolling = 50) was subtracted from the dsRED images, and then a `Gaussian Blur` filter was applied (sigma = 5). This image was then transformed into a binary mask (`default` threshold) and used to calculate the number of infected cells by running the `Analyze particles` tool (size threshold = 400 to infinity, circularity = 1.2-1, exclude on edge). The output containing the number of infected cells per image was then transferred to R, where statistics were calculated using a t-test.

2.11.3 Evaluation of entry foci dynamics

Shigella induces host actin polymerization at the entry site, forming an F-actin-rich entry focus leading to bacterial uptake [158]. RACK1's role in actin focus formation and actin polymerization dynamics at the entry site was assessed as follows. RACK1-KD and control cells (1x105 cell/well) expressing F-tractin-GFP were seeded on 4-well 35 mm glass-bottom dishes (Greiner BioOne, Cat. No. 627870). The next day, the cell's media was replaced by 400 µL of FluoroBrite. A dsRED-WT *Shigella* inoculum was prepared by diluting a fresh culture (OD_{600} = 0.5) 10 times with prewarmed (37 °C) PBS. Image acquisition started immediately after infecting the cells with 100 µL of inoculum per well. Z-stacks (4 slices, 1.2 µm) were captured at 63X magnification every 2 minutes for two h at 37 °C with 5% CO2 using a confocal spinning disk (Zeiss Axio Observer Z.1 with Axiocam camera, Table 2.5).

Since F-actin was labelled with F-tractin-GFP, and *Shigella* expressed the dsRED marker, entry foci dynamics were easily tracked in the time-lapses captured. Entry foci were identified by increased F-actin enrichment around dsRED-WT *Shigella* over time. For this, average intensity z-projections of all z-stack image sequences were generated in Fiji. The background value, calculated by measuring FI in a cell-free area, was subtracted from the images. Then, the most extensive area reached by the entry focus was encircled using the oval selection tool and added to the ROI manager. Then, the area and FI (mean grey value) of the ROI (entry focus) was measured (`Multi Measure`) starting from the first signs of actin enrichment around *Shigella* until the FI returned to the basal level. The output of this analysis contained a series of area, mean FI and time values for each entry foci. These data were transferred to R to do statistical analyses. Of note, the area of the ROI was the same at all time points measured on a specific focus.

The mean FI of each focus at the time points measured was averaged and normalized by subtracting the lowest FI encountered in each data set (control and RACK1-KD). The area of each focus was calculated from the original ROI size as it reflects the most extensive area reached by the entry focus. The duration of each focus was calculated by multiplying the number of time points by 2 min (frame acquisition time). Then, statistical differences

in these parameters (mean FI, area, and duration of foci) between RACK-KD and control cells were analyzed using Wilcoxon test as the data was not normally distributed. Finally, the rate of actin polymerization at the entry foci was calculated using the R package "`growthrates`" (version 8.2). This package was initially designed to determine bacterial growth rates. The functions were adapted to use the increment in FI observed on each infection focus to estimate actin polymerization's mumax (maximum polymerization rate) using a logistic model (`grow_logistic` function). The equation used was

$$y = (K * y0)/(y0 + (K - y0) * exp(-mumax * time))$$

With K being the maximum FI, y0 was the lowest FI, and mumax was the maximum actin polymerization rate. The fitting of the FI curves by the model was visually verified, and curves not well described by the model were eliminated from the final data set. Differences in actin polymerization rates observed in control versus RACK1-KD cells were analyzed using Wilcoxon test. More details can be found in Appendix B.5.

2.11.4 Evaluation of *Shigella*'s intracellular motility

Shigella induces actin-tail polymerization at one pole of the bacterium, which confers intracellular motility [223]. For these experiments, $1x10^5$ F-tractin-GFP HeLa cells (control and RACK1-KD) were seeded in 4-well 35 mm glass-bottom dishes. A day after, the medium was replaced with 450 µL of FluoroBrite, and the infection was carried out by adding 50 µL of dsRED-WT *Shigella* (OD_{600} = 0.5 culture diluted 1 in 10 with PBS). Z-stacks (5 slices, 1 µm) of the cells were captured at 63X magnification every 30 sec to 1 min (indicated on figure legends) for two h at 37 °C and 5% CO_2 using a spinning disk microscope (Zeiss Axio Observer Z.1, with Evolve camera, Table 2.5).

The intracellular movements of dsRED *Shigella* propelled by fluorescently labelled actin tails (F-tractin-GFP) were recorded from the time-lapse images captured using Fiji software tools. For this, the z-stacks time-lapse images were transformed into average intensity projections. The first 2 (bottom) slices of the z-stack were not included in the projection to avoid stress fibre interference. Then, bacterial movements were manually recorded using Fiji's `Manual Tracking` tool. Trajectories were recorded for as long as

the bacterium was still visible but stopped when the bacterium was out of view or divided. The data generated by the tracking tool consisted of a series of x/y coordinates. The distance between x/y coordinates at two given time points was measured by the formula: $d = \sqrt{(x2 - x1)^2 + (y2 - y1)^2}$.

In R, the trajectories were analyzed with the "`trajr`" package (version 1.4.0) [374]. This package was not developed to characterize bacterial motility but to describe animal behaviour. However, some of the functions provided in the `trajr` package were useful to characterize *Shigella*'s trajectories. The `TrajBuild` function was used to import trajectories from multiple files and create a data frame containing a list of bacterial trajectories. Then, the function `TrajDerivatives` was used to calculate speed. The sinuosity index of the trajectories was calculated using `TrajSinuosity2`.This index describes how tortuous a trajectory is; thus, a low index indicates a more direct trajectory. Only trajectories with lengths ranging between 30 to 80 µm, which represented trajectories in the interquartile range of the data, were included in the sinuosity calculation. `TrajDirectionalChange` was used to measure the directional change (DC) of each pair of consecutive points in a trajectory from which the mean DC was calculated. A final index denominated tumbling time was generated using the function `TrajSpeedIntervals`. This function determines the time intervals within a trajectory where the trajectory speed is lower than a defined threshold. The minimum speed threshold (0.02 µm/sec) was defined as the mean of the values from the first quartile speed value in each data set (experiments 1 to 3). Then, the mean tumbling time was calculated from the output generated by the `TrajSpeedIntervals` function. Statistical differences between control and RACK1-KD were tested by Wilcoxon test for mean speed and mean tumbling time and t-test for DC and sinuosity. More details can be found in Appendix B.6.

2.11.5 RACK1 localization during *Shigella* infection

GFP-tagged versions of RACK1 were used to assess RACK1 subcellular localization during *Shigella* infection. Detection of actin was also desirable to study RACK1's interplay with the actin cytoskeleton. Therefore, HeLa cells stably expressing GFP-RACK1/F-

tractin-mCherry or RACK1-GFP/F-tractin-mCherry were seeded on 4-well bottom glass dishes ($1x10^5$ cells/well). One day later, the medium was replaced with 400 µL of FluoroBrite. Infection was carried out by inoculating 100 µL (for early events) or 50 µL (for late events) of a WT *Shigella* culture diluted ten times in DMEM. Cells were imaged every 1 (tail localization) or 2 (entry foci localization) minutes for two h at 37 °C with 5% CO_2 using a spinning disk confocal microscope (Zeiss AxioObserver Z.1 with Evolve camera, Table 2.5). The time-lapse images were taken as z-stacks (6 slices, 0.9 µm apart) with 63X magnification.

To evaluate if RACK1 co-localizes to *Shigella* at any point during infection, RACK1 recruitment to entry foci and actin tails were measured using Fiji. First, the z-stack time-lapses were transformed to average projections. To assess RACK1 recruitment to entry foci, an elliptical ROI was drawn around *Shigella*'s entry point and the changes in fluorescence intensity over time were measured. FI corresponding to GFP-tagged RACK1 and F-tractin-mCherry that labels F-actin was measured. RACK1 localization to actin tails at any point during actin mediated motility was assessed by measuring RACK1 FI in the area occupied by actin tails.

2.11.6 LC3 targeting of *Shigella*

The autophagy marker, microtubule-associated protein 1A/1B-light chain 3 (LC3), has been reported to target the *Shigella*-containing vacuole [172]. The vacuolar escape reporter Gal-3 was used to visualize LC3 co-localization with damaged *Shigella*-containing vacuoles. To test if RACK1 mediates binding of LC3 to the vacuole, RACK1-KD or control HeLa cells stably expressing GFP-LC3 were seeded on 4-well bottom glass dishes ($5x10^4$ cells/well) and transfected with pOrange-Galectin3 (Gal-3). After 48 h, the medium was replaced with 400 µL of FluoroBrite, and the cells were infected with 100 µL of WT *Shigella* diluted ten times in PBS. Z-stacks (17 slices, 0.2 µm) were captured every 1 min for 1.5 h using 60X magnification with a spinning disk microscope (Delta vision, Table 2.5) equipped with temperature (37 °C) and atmosphere control (5% CO_2). For data analysis, the z-stack time-lapse images were transformed into z-projections. Then, LC3 and

Gal-3 positive bacteria were manually enumerated using Fiji's `cell counter` tool. Statistical analyses were performed in R using a t-test.

2.11.7 Aqueous two-phase (ATP) infection system

Bacterial growth kinetics in HeLa cells was evaluated by live microscopy using an aqueous two-phase (ATP) infection system. Contrary to the gentamycin assay, the ATP method provides higher throughput, and bacterial growth can be recorded more often and for longer incubation times. Also, in this method, both the cells and bacteria were fluorescently labelled, thereby facilitating live observation of bacterial growth. HeLa cells stably expressing F-tractin-GFP were seeded on 96-well plates (Falcon, Cat. No. 353072) and grown to 100% confluency. On the day of infection, the cells were overlaid with 10% polyethylene glycol (PEG, Sigma, Cat. No. 94646). Then, a culture of dsRED-WT *Shigella* (OD_{600} = 0.5) was resuspended in 10% Dextran T500 (DEX, Pharmacosmos, Cat. No. 551005009007). The cells were infected with 0.5 µL of the DEX-bacteria mixture spotted in the center of each well by a robot (Biomek 4000). DEX and PEG do not mix, generating a physical barrier that maintains the bacterial inoculum on a discrete area of the cell monolayer and slows down the infection. The was incubated for one h at 37 °C. Then, the monolayers were washed carefully with pre-warmed (37 °C) PBS and incubated with DMEM containing gentamycin (100 µg/mL) for 15 min. The medium was then replaced with FluoroBrite complete supplemented ampicillin (100 µg/mL) to maintain bacterial fluorescence. Tiled images covering 50% of the well's area were taken every 15 min for 12 hours with 10X magnification at 37 °C and 5% CO_2 using an automated imager (EVOS FL Auto 2, Table 2.5).

FI increment was used to evaluate *Shigella* growth in the cell monolayer. For this, the time-lapse images corresponding to the dsRED channel (bacteria) were separated from the cells' channel (F-tractin-GFP). The DEX-PEG interphase restricted *Shigella* infection to a discrete area of the monolayer and its size was proportional to inoculum drop (0.5 µL). Thus, a circular region of interest (ROI 1) was manually assigned to the infected area, which contained the most bacteria in the last image of the video. Similarly, three smaller areas

corresponding to the background (no bacteria) were selected (ROIs 2-4). FI was measured over time in the ROIs 1 to 4 using the ROI's manager `Multi measure` tool.

Additionally, the area covered by cells (available for infection) inside ROI 1 at time point 0 (first image) was measured as follows. First, brighter spots (identify cell's center) were found using the `find maxima` tool (prominence = 15). Then, the original image was smoothed, and a `default` threshold was applied to obtain a binary mask. Next, the mask and find maxima's output were merged using the `image calculator` tool. The final image created was the input for the `Analyze particles` tool to obtain the area and number of cells. Cell number and background (ROIs 2-4) read-outs were used to normalize the FI quantified in ROI 1 and obtain the net bacterial growth. Statistical differences between control (NS) and RACK1-KD cell lines were analyzed by pairwise comparations at every time point using a t-test.

2.11.8 Modified plaque assay

Plaque assays are commonly used to test viral titers. As the pathogen spreads in the monolayer, it generates areas of infection called plaques that can be measured. The gold standard plaque assay method to evaluate *Shigella* spreading is performed using a dense agarose overlay that restricts extracellular diffusion. Then the cell monolayers are fixed and stained to visualize the plaques [375,376]. In these conditions, bacterial spreading cannot be observed in real-time. Thus, modifications were made to allow live observation of *Shigella*-induced plaques and cell death without disturbing the cell monolayers. For the modified plaque assay, cells expressing F-tractin-GFP (HeLa and HT-29) or GFP alone (CaCo-2) were seeded in black 96-well plates and grown to confluency. The monolayers were subsequently infected with a low MOI (OD_{600} 0.5 diluted 1000 times) inoculum of dsRED-WT *Shigella* for 30 min (HeLa and CaCo-2) or one h (HT-29). The cells were then treated with gentamycin (100 ug/mL) diluted in DMEM for 15 min to eliminate extracellular bacteria. After three washes with pre-warmed (37 °C) PBS, the monolayers were overlaid with 0.4% Methocel A4M (Sigma, Cat. No. 94378) diluted in FluoroBrite complete supplemented with 100 µg/mL ampicillin (to maintain *Shigella* fluorescence), and 2.5

ng/µL DAPI (to detect cell death). Infections were carried out at 37 °C with 5% CO_2 for 10 (HeLa), 15 (CaCo-2) or 72 (HT-29) h before imaging. To image around 50% of the well's area, 16 tiles were captured at 10X magnification using a widefield microscope (Zeiss Axio Observer Z.1, Table 2.5). Tiles were then stitched using Zeiss Zen Black software.

Shigella's cell-to-cell spreading was determined by analyzing the formation of plaques in the cell monolayer. Since *Shigella* was fluorescently labelled, plaque detection was performed by automatic segmentation. The images were separated into two channels (GFP = cells, dsRED = bacteria), and the `background` was subtracted from the dsRED channel images (rolling = 90). Then, the filters `Median` (radius = 10) and `Gaussian blur` (sigma = 10) were applied before transforming the images into masks using the `Mean` thresholding method with default settings. The commands `Dilate mask` and `Fill Holes` further defined the plaques contour. The final mask images were input to the `Analyze particles` (size = 0.1 to infinity) tool to identify plaques outlines. The area and number of plaques per image were calculated using the ROI manager tool. More details can be found in Appendix B.3. Quantification of secondary plaques (area < 4 μm^2) and statistical analysis (Wilcoxon test) were performed in R.

2.11.9 Real-time monitoring of *Shigella* cell-to-cell spreading

A similar setup to the one described in 2.11.8 was used in these experiments to assess *Shigella* cell-to-cell spreading in real-time. F-tractin-GFP HeLa cells (1 x 10^5) were seeded in 4-well glass-bottom dishes. The next day, cells were overlaid with 0.4% Methocel diluted in FluoroBrite complete supplemented with ampicillin (100 µg/mL). One hour before imaging, the cells were infected by adding 8 µl of dsRED *Shigella* (OD_{600} = 0.5) diluted 1000 times in PBS. The inoculum was placed in one corner of the well to allow slow diffusion of *Shigella*, reducing the number of infected cells. Infection foci, comprised of 1 infected cell, were located using the eyepiece of the microscope. Then, images were captured (9 tiles) at 40X magnification every 15 min for 15 h at 37 °C with 5% CO_2 using a spinning disk (Zeiss Axio Observer Z.1 with Evolve camera, Table 2.5).

Infection progression was followed over time from one initially infected cell. Since the time-lapse images were taken at high magnification, newly infected cells were quickly identified. The number of infected cells was manually noted in every time frame using Fiji's `Point` tool and added to the ROI manager to be counted. The output of this analysis had the number of infected cells found at every time frame. In R, the raw number of infected cells was used to calculate the cumulative sum of infected cells. This better represented infection progression because some cells detached during infection and were no longer visible. Statistical difference between control and RACK1-KD cells was evaluated using a t-test.

2.12 Characterizations of the role of RACK1 in actin cytoskeleton dynamics

2.12.1 Analysis of actin polymerization and depolymerization using actin-binding drugs.

The actin-binding drugs Jasplakinolide (Jasp, Thermo Fisher Scientific, Cat. No. J7473) and Cytochalasin D (CytoD, Thermo Fisher Scientific, Cat. No. PHZ1063) were utilized to assess the role of RACK1 in actin dynamics. For these experiments, control and RACK1-KD HeLa cells expressing F-tractin-GFP were seeded in 4-well glass-bottom dishes ($1x10^5$ cells/well). After 24 h, the medium was substituted with 300 µl of FluoroBrite and incubated for 15 min in the microscope's atmosphere-regulated chamber (37 °C, 5% CO_2) to stabilize the cells. Then, 200 µl of 0.5 µM Jasp or 200 µl of 100 µg/mL CytoD diluted in FluoroBrite were added to each well. Z- stack images (8 slices, 1µm apart) were captured at 40X magnification every 2 minutes for two h using a spinning disk microscope (Zeiss Axio Observer Z.1 with Evolve camera, Table 2.5).

Jasp and CytoD have opposite effects. Jasp is a potent inducer of actin polymerization leading to the formation of F-actin aggregates, whereas CytoD inhibits actin polymerization thereby inducing depolymerization of F-actin [377,378]. Automatic segmentation was used to analyze the effects of these drugs in RACK1-KD cells (see Appendix B.4 for details). First,

F-actin aggregate polymerization was assessed in the cells treated with Jasp. Maximum projection images were generated from the z-stacks corresponding to 0 and 2 h after Jasp treatment. The background (i.e., measuring FI in a cell-free area) was subtracted from each image. `Unsharp mask` (radius = 1, mask = 0.6) and `Median` (radius = 1) filters were applied to the images before transforming them to binary using a `Default` threshold. Cell's outlines were manually outlined from the original (not binary) image to create a mask. Then, both masks (cells and F-actin aggregates) were used as input for the `Speckle inspector` plugin. The output generated contained a set of ROIs (F-actin aggregates), indicating cell number, the number of aggregates per cell and the aggregates FI.

CytoD induces depolymerization of F-actin-rich structures such as stress fibres and cell adhesions. Thus, the slice from the z-stack that contained most stress fibres and adhesions at 0 min was selected to analyze CytoD effects on these structures after 1.5 h of treatment. Mask images were generated using the same segmentation settings for the Jasp analysis. But the detection of F-actin-rich structures was performed with the `Analyze particles` tool. The output generated was a list of actin-rich structures outlines used to measure the area and FI of the structures in the original image. Finally, statistical differences in the effects of the actin-binding drugs in RACK1-KD and control cells were assessed with Wilcoxon test.

2.12.2 Fluorescence Recovery After Photobleaching (FRAP)

FRAP was carried out following a protocol described by Carisey *et al* [379]. Briefly, $5x10^4$ control and RACK1-KD HeLa cells were seeded in 4-well glass-bottom dishes. Transfection was carried out as described in section 2.5.3 using plasmid pEGFP-Actin (15 ng/well). After 48 h, the medium was replaced with FluoroBrite supplemented with ten µM HEPES and 10% FBS. One hour before imaging, dishes were placed in the microscope's atmosphere-regulated chamber (37 °C with 5% CO2) to allow the medium to equilibrate. Cells expressing low, medium, and high levels of GFP-actin expression were selected using the microscope's eyepiece. Zeiss LSM 880 confocal microscope (Table 2.5) was used here with the following settings: time series, bleaching, and regions were selected in the

software's main menu. Images (16-bit, 512 x 512 pixels) were captured at 63X magnification using bi-directional scanning at speed 7. Pinhole size was set to 1 Airy Unit, and zoom factor was 2. The power of the 488 nm argon laser was set to 22% (gain: 652, offset: 62) during imaging and increased to 100% for the bleaching pulses. A bleaching area or ROI was defined using the regions menu. Then, three images were captured every 2 seconds, followed by bleaching the ROI for two iterations. Images continued to be captured every 2 sec for 172 sec after bleach (90 frames in total, including pre-bleach frames). Two distinct cell structures, stress fibres, and ruffles were analyzed in 25 control and 22 RACK1-KD cells.

The time-lapse images generated were analyzed in Fiji. The bleached area (ROI 1) was extracted from the image's metadata. Then, a cell-free area was selected to calculate background (ROI 2) FI, and the whole cell's area (ROI 3) was outlined using the polygon selection tool and added to the ROI manager. The ROI manager calculated FI of ROIs 1, 2, and 3 overtime. In R, the values in the first three rows (pre-bleach frames) were averaged. FRAP curves were normalized to obtain experimental recovery (Rnorm) values using the following formula:

$$Rnorm = \frac{(ROI\ 1\ - ROI\ 2\ )}{(ROI\ 3 - ROI\ 2)}$$

Rnorm curves were analyzed using the R package "`Frapplot`" (version 0.1.3). All FRAP curves acquired per condition (control or RACK1-KD) and cell structure (stress fibres, and ruffles) were averaged and plotted. The best-fitted curve for each data set was calculated using a non-linear least squares regression model.

$$y = ymax - (ymax\ - ymin) \times e^{-k*t}$$

Where ymax is maximum FI, ymin is minimum FI, k is the slope, and t is time. FI half recovery time ($t_{1/2}$) was calculated using the function `frapprocess.` Statistical differences were calculated using a t-test. More details of the analysis can be found in Appendix B.7.

Table 2.5. Microscopes used in this study and its specifications

Microscope brand and model	Microscope specifications	Camera/ detectors specifications and software	Experiments used for
Zeiss LSM 710 laser scanning confocal (upright)	LASERS: Argon 458/488 nm, HeNe 548-633 nm, Diode 405nm. LENSES: Plan Apochromat (APO) 63X Oil NA1.4. FILTERS: Zeiss 38, 43, 49.	DETECTORS: 6 channel confocal and transmitted light. SOFTWARE: Zen 2011	- Localization of EEA1, LAMP1 and LC3. - Area of control versus RACK1-KD cells (fixed samples) - Arp2 localization
Zeiss LSM 880 laser scanning confocal (inverted)	LASERS: Argon 458/488 nm, HeNe 548-633 nm, Diode 405-30. LENSES: Plan APO 20X air NA0.8, Plan APO 40X oil NA1.4, Plan APO 63X oil NA1.4. FILTERS: Zeiss 38, 46, 47, 49, 43.	DETECTORS: GaAsP, photomultiplier tube (PMT), AiryScan, and Transmitted light (T-PMT). SOFTWARE: Zen Black/ Zen Blue	- Analysis of actin tails (fixed samples) - Analysis of intracellular replication (fixed samples) - Targeting of *Shigella* by GBP1 - FRAP - Fly gut images
Leica TCS SP8 near super-resolution laser scanning confocal (inverted)	LASERS: Solid State 405, 488, 552 and 638 nm Spectral Viewing System. LENSES: HC Plan APO CS2 63X oil NA1.4. FILTERS: DAPI/FitC/TXRED, GFP, Rhod_LP.	DETECTORS: PMT and Hybrid Detectors (HyD). SOFTWARE: LASX	- RACK1 localization to entry and tail (fixed samples) - RACK1 and Gal-3 colocalization - RACK1 and GBP4 colocalization

Microscope brand and model	Microscope specifications	Camera/ detectors specifications and software	Experiments used for
Zeiss Axio Observer Z.1 spinning disk confocal (inverted)	LASERS: 405, 488, 561 and 639 nm. LENSES: Plan APO 40X oil NA1.4, Plan APO 63X oil 1.4. FILTERS: Zeiss 49, 38 and 77	CAMERAS: Axiocam MRm (1388 x 1040 pixels), Evolve 512 Delta EMCCD Camera (16um x 16 um pixel area) with high-speed imaging (67 fps). SOFTWARE: Zen Black	- Evaluation of entry foci dynamics (Axiocam) - Evaluation of *Shigella*'s intracellular motility (Evolve) - RACK1 localization to entry and tail (Evolve) - *Shigella*'s cell-to-cell spreading - Jasp and CytoD analysis (Evolve)
Zeiss Axio Observer Z.1 widefield (inverted)	LIGHT SOURCE: Zeiss Colibri 5. LENSES: Plan NEOFLUAR 10X NA0.3, EC Plan NEOFLUAR 20X NA 0.5. FILTERS: DAPI/GFP/CY3/CY5	CAMERA: Zeiss Axiocam 506 monochrome (2752 x 2208 pixels). SOFTWARE: Zen Blue 3.0	- *ΔicsA* entry - Modified plaque assay
Nikon Eclipse Ti widefield (inverted)	LIGHT SOURCE: Ti-illuminator EPI. LENSES: Pan Fluor DIC 40X NA 0.75.	CAMERA: CoolSNAP HQ2 monochrome. SOFTWARE: NIS-Elements AR	- Live-cell imaging of *Shigella* entry and vacuolar escape in HeLa cells

Microscope brand and model	Microscope specifications	Camera/ detectors specifications and software	Experiments used for
Delta vision spinning disk (inverted)	LIGHT SOURCE: InsightSSI. LENSES: Olympus Plan ApoN 60X NA 1.42. FILTERS: FITC, TRITC	CAMERA: PCO Edge CMO. SOFTWARE: DeltaVision experiment designer 6.5.2	- LC3 targeting of *Shigella*
EVOS FL Auto 2	LIGHT SOURCE: LED LENSES: 10X FILTERS: DAPI, GFP, YFP	High-sensitivity 1.3 MP CMOS monochrome	- Mycoplasma tests - ATP infection system

CHAPTER 3 RESULTS

Chapter three summarizes the main findings of this project divided into eight sections that align with the project's objectives. The first section established a cell line infection model to evaluate RACK1's roles in *Shigella* infection. In section two, I used the stablished cell line model and the model organism *Drosophila melanogaster* to study the effects of RACK1 silencing on *Shigella* infection (Objective 1). *Shigella* must invade epithelial cells to access their cytoplasm, where it replicates and induces actin-based motility. Therefore, I systematically evaluated how RACK1 influences the main steps of *Shigella*'s intracellular life cycle. Sections three and four describe the study of RACK1 function in *Shigella* entry into HeLa cells and vacuolar escape (Objective 2). Then, in section five, I assessed the involvement of RACK1 in intracellular replication of *Shigella* and cell death induction. In sections six and seven I studied the role of RACK1 in actin tail polymerization and cell-to-cell spreading (Objective 2). Finally, I attempted to decipher the mechanisms by which RACK1 manipulates actin cytoskeleton dynamics in section eight (Objective 3).

3.1 RACK1 silencing and characterization

The main objective of this project was to characterize how RACK1 controls the establishment of *Shigella* infection. Since *Shigella* is a strict human pathogen, finding a suitable model to study *Shigella* pathogenesis is challenging. The available animal models to study *Shigellosis* do not fully recapitulate many pathogenicity aspects such as characteristic diarrhea. Mouse, rat, and rabbit models are naturally resistant to oral *Shigella* infection and require extensive pre-treatment to allow colonization [380]. Therefore, I started my project by implementing a suitable human cell line model to study RACK1 functions during *Shigella* infection. Epithelial cell lines, such as HeLa, are among the most used models in the study of *Shigella* pathogenesis [381]. *Shigella* efficiently invades and replicates inside HeLa cells [382]. Conveniently, HeLa cells present a relatively large cytoplasmic space and are very flat, facilitating microscopic observation of structures in a single focal plane. Also, these cells are fast-growing (doubling time ~ 24 hours) and can be efficiently

transfected to enable genetic studies. Hence, HeLa cells were the primary model used in my project to study RACK1-*Shigella* interplay.

RACK1 expression was silenced using short-hairpin (sh) RNAs delivered by lentiviruses. Seven shRNAs were designed to target non-overlapping regions of the RACK1 mRNA. Three of the shRNAs successfully inhibited RACK1 expression in HeLa Tet-off cells (Figure 3.1.1). These shRNAs targeted the center of the mRNA sequence from nucleotide positions 504 to 761 and were used to generate the stable RACK1-knockdown (KD) cell lines KD-92, KD-94, and KD-95 (Figure 3.1.1). The stability of RACK1 silencing in HeLa Tet-off and HeLa WT was evaluated after 2, 3, and 4 cell passages. RACK1 expression levels remained significantly lower than the control shRNA (NS) in HeLa Tet-off cells in all cell passages tested (Figure 3.1.2 A-B). Unexpectedly, RACK1 expression in WT HeLa cells returned to normal levels in the fourth passage even under antibiotic selection (Figure 3.1.2 A and C). The Tet-Off strain is a HeLa HtTA-1 derivate that expresses a tetracycline (Tet)-regulated transactivator for inducible protein expression [383]. This cell line was not transfected with a vector containing a tetracycline-responsive promoter. Therefore, the Tet-Off system should not be active and should not affect the silencing. However, heterogeneity between HeLa cell line variants is well documented [384], perhaps explaining the varying capacity to maintain RACK1 knockdown observed in WT and Tet-off HeLa strains. Given that HeLa Tet-off (HeLa hereafter) maintained RACK1 silencing for longer, it was the cell line of choice for most experiments in this project. Also, HeLa Tet-off RACK1-KD-92 was selected for further experiments because this cell line consistently showed lower RACK1 expression levels than KD-94 and KD-95 (Figures 3.1.1 C, 3.1.2 B). A HeLa Tet-off cell line transduced with a nontargeting shRNA (NS) was used as a control for RACK1 expression.

Considering that RACK1 is involved in cell growth [5], the effect of RACK1 silencing in cell proliferation was evaluated. The proliferation rates of KD-92, KD-94 and KD-95 HeLa cell lines were significantly lower than the nontargeting control (NS) cells, as shown by the MTT assay (Figure 3.1.3 C). Moreover, RACK1-silenced cells exhibited cell adhesion impairment. Although not quantified, RACK1-KD cells were consistently loosely

attached to cell culture dishes and easily detached during washes. This phenotype is not surprising since RACK1 regulates focal adhesion assembly [328]. Cell adhesion was improved when treating dishes with fibronectin before experiments. The adhesion impairment might result in cell rounding. Therefore, the effect of RACK1 silencing in cell size was evaluated. Area measurements of cells grown in glass coverslips treated with fibronectin showed that RACK1 depletion in KD-92 did not impact cell size compared to the NS control (Figure 3.1.3 D).

Shigella targets the human colonic epithelium [385]. Therefore, RACK1 expression silencing was attempted in the biologically relevant cell lines CaCo-2 and HT-29. The same lentiviruses used to silence RACK1 in HeLa were utilized to transduce CaCo-2 and HT-29 cells. While KD-92 and KD-95 shRNAs significantly reduced RACK1 expression in CaCo-2 cells (Figure 3.1.4 A-B), RACK1 silencing was unsuccessful in HT-29 cells despite several attempts (Figure 3.1.4 C-D). In general, both cell lines were more resistant to transduction than HeLa cells. For example, CaCo-2 cells transduced with F-tractin-GFP (binds to F-actin) were no longer susceptible to transduction to knock down RACK1 (data not shown). Also, RACK1 silencing substantially impaired CaCo-2 cells' growth rate. For example, reaching 100% cell confluency took double the time compared to control (NS) CaCo-2 cells (data not quantified). Because of these limitations, CaCo-2 cells were unsuitable for evaluating actin dynamics during *Shigella* infection in RACK1-KD cells. However, the ability of CaCo-2 cells to spontaneously form an enterocyte-like confluent monolayer was desirable to assess *Shigella* cell-to-cell spreading [381]. The cells must be fluorescent for the spreading experiments to allow focal plane calibration during automatic image acquisition. To solve the problem of CaCo-2 double transduction impairment, I silenced RACK1 first. Then 48 h before infection, the cells were transduced with lentiviruses carrying GFP alone (pLJM1-EGFP). Although the transduction efficiency was low, it was enough to visualize the cells.

Figure 3.1.1. RACK1 expression silencing using shRNAs delivered by lentiviruses. **A.** Diagram showing the seven regions in the RACK1 mRNA targeted by shRNAs. Numbers above grey boxes indicate shRNA identifier number. **B.** Western blot analysis of RACK1 expression. HeLa cells transduced with lentiviruses harbouring seven shRNAs (shown in A) were harvested, lysed, and analyzed by western blotting using an anti-RACK1 antibody. Cells transduced with a non-targeting shRNA (NS) were used as the control. Ponceau S staining was the loading control. **C.** Relative expression of RACK1. Protein expression was quantified (see methods section 2.4.4) from the western blot shown in B and normalized to the loading control.

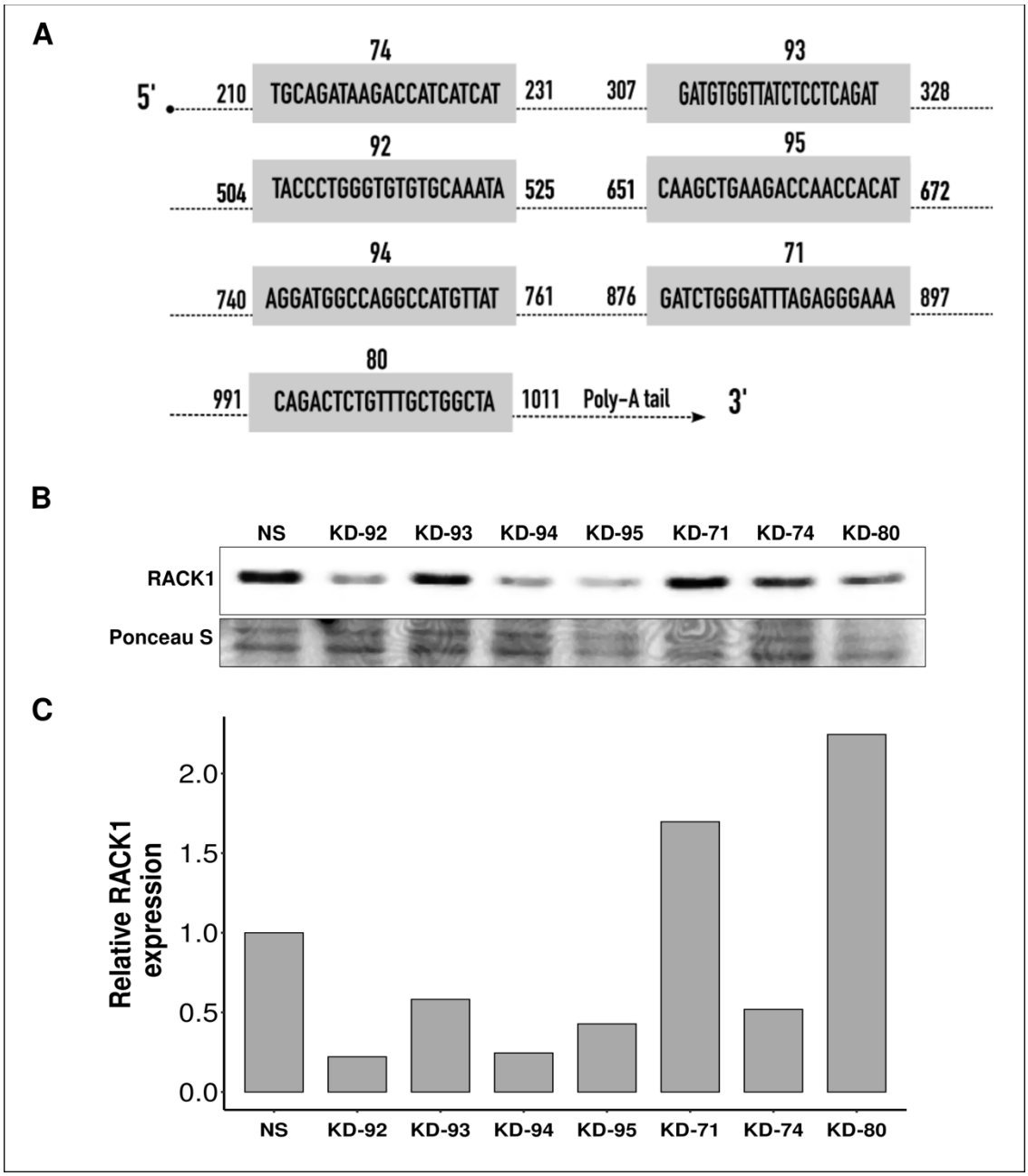

Figure 3.1.2. HeLa cells differentially maintain RACK1 silencing efficiency.
A. Western blot analysis of RACK1 expression in HeLa cells after various passages. HeLa Tet-off and wild-type (WT) cells were transduced with lentiviruses to silence RACK1 expression (KD-92, KD-94, and KD-95). NS cells were transduced with a non-targeting shRNA. After passages 2, 3, and 4, cells were collected, lysed and assayed by western blot. Ponceau S or tubulin was used as the loading control. RACK1 silencing is more stable in HeLa Tet-off than wild-type (WT) cells. RACK1 relative expression analyses in HeLa Tet-off (**B**) and WT HeLa (**C**). The bar plots show protein expression levels quantified from the western blots in A, RACK1 expression was normalized to loading control expression. Bars are means calculated from the three passages above and error bars denote standard deviation (SD), unpaired t-test. ns = not significant $p>0.05$, $^{**}p < 0.01$.

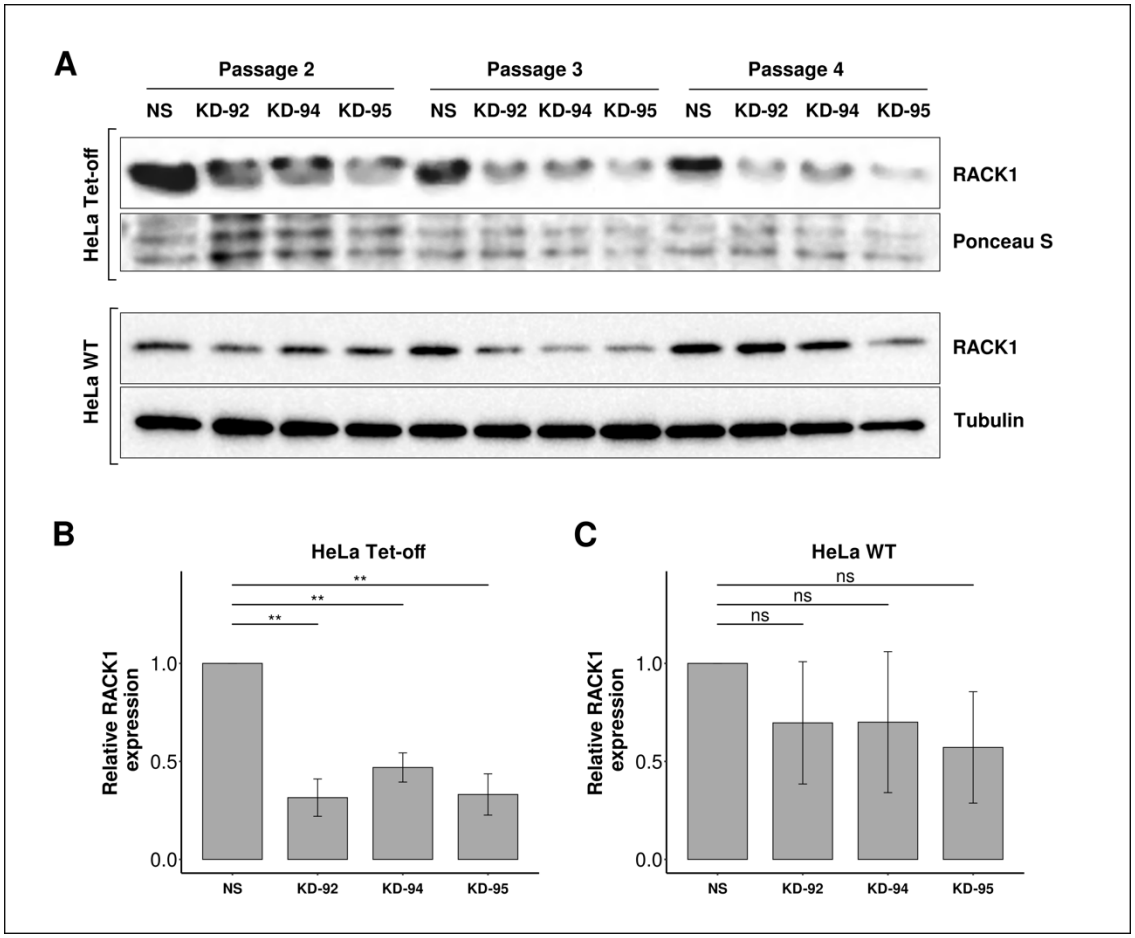

Figure 3.1.3. RACK1 silencing affects cell proliferation but not cell size.
A. Confirmation of RACK1 silencing by western blotting. Protein extracts from RACK1-knockdown (KD) HeLa Tet-off cells were immunolabeled using an anti-RACK1 antibody. Coomassie staining was the loading control. **B.** RACK1 relative expression analysis from the western blot shown in A. **C.** Cell proliferation curve. MTT, a colorimetric assay, was used to evaluate cell proliferation of RACK1-KD (KD-92, KD-94, and KD-95) and control (NS) cells at various time points. The line graph depicts absorbance at 540 nm (Abs_{540}) normalized to Abs_{540} at day 1. Error bars are SD from 4 replicates. Statistical differences were evaluated at every time point comparing NS to each RACK1-KD using unpaired t-test; only significant differences are marked, *** $p < 0.001$, ****$p < 0.0001$. **D.** Cell area quantification. Control (NS) and RACK1-KD (KD-92) cells were fixed and stained with phalloidin-Alexa-555. The size of cells was measured using Fiji software. Dots inside the boxplot represent the area of cells from 3 independent experiments. Numbers under the boxplots correspond to the number of cells analyzed. Unpaired t-test. ns = not significant $p>0.05$.

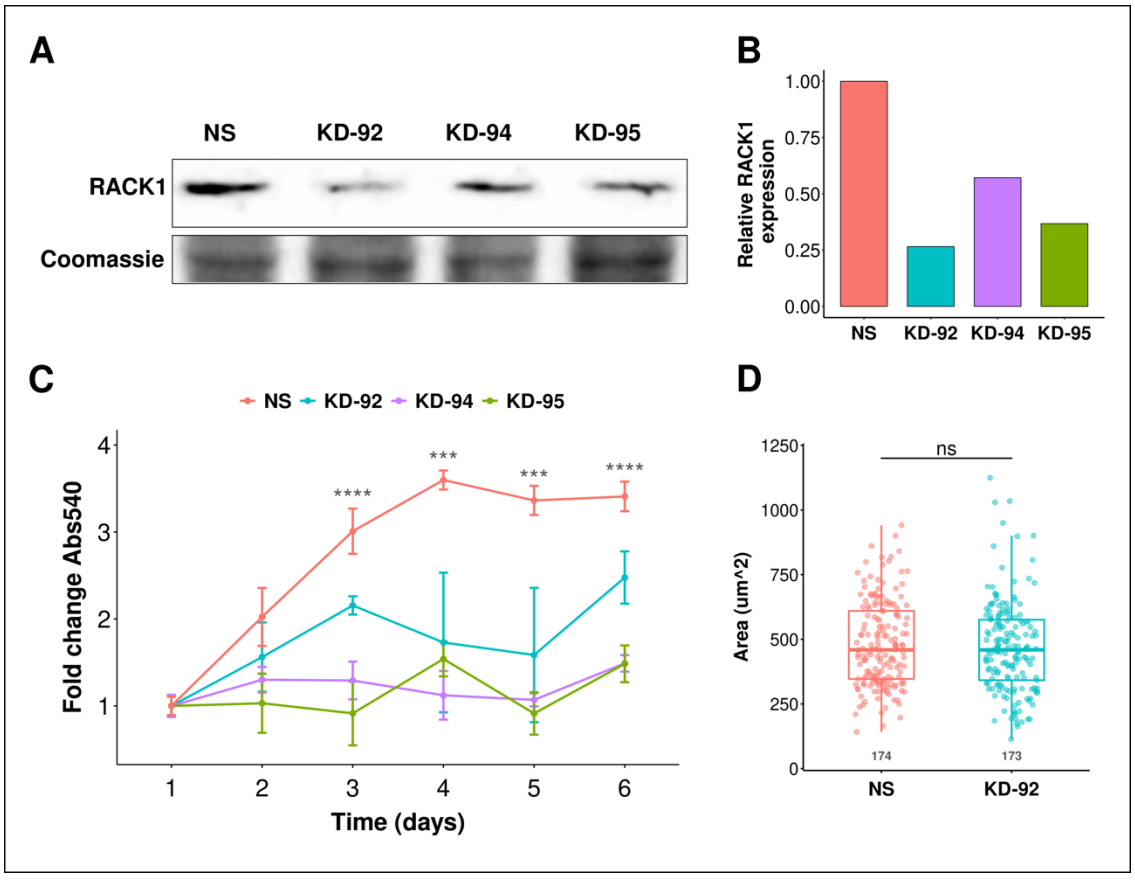

Figure 3.1.4. RACK1 expression was silenced in CaCo-2 but not in HT-29 cells.
Evaluation of RACK1 silencing by western blotting. CaCo-2 and HT-29 cells were transduced with lentiviruses to knock down RACK1 expression. Protein extracts from CaCo-2 (**A**) and HT-29 cells (**C**) were immunolabeled using an anti-RACK1 antibody. Tubulin was the loading control used. RACK1 relative expression analysis of CaCo-2 (**B**) and HT-29 (**D**) cells. Bar plots show fold change over NS protein expression levels (relative to tubulin). Bar height is the mean calculated from the western blots above and two other blots (not shown) from separate cell passages. Error bars are SD, unpaired t-test. ns = not significant $p>0.05$, *$p < 0.05$.

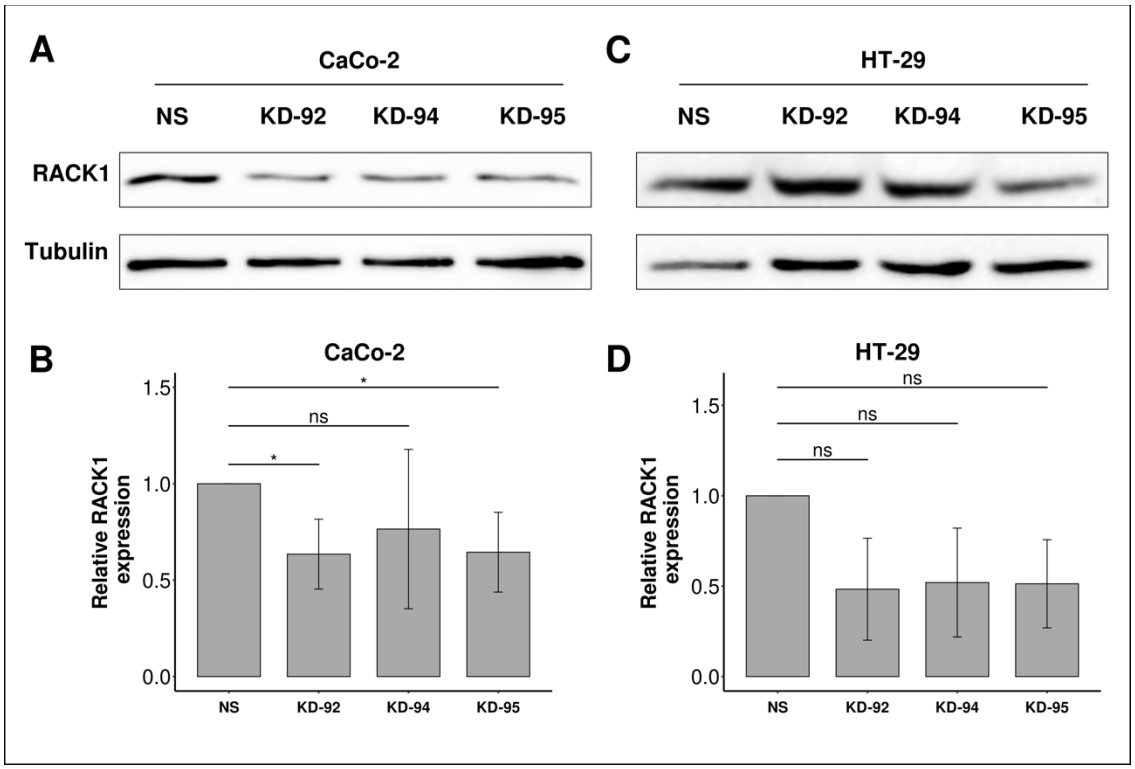

3.2 RACK1 modulates *Shigella* infection of HeLa cells and *Drosophila melanogaster*

3.2.1 Silencing RACK1 impairs *Shigella* growth in HeLa cells

We decided to use *Shigella flexneri* (*Shigella* hereafter) as the model strain in this project because most of the current knowledge on mechanisms underlying *Shigella* pathogenesis derives from studies of this species. First, it was crucial to evaluate the optimal conditions for *Shigella* infection in HeLa cells before the possible effects of RACK1 silencing could be studied. The gentamycin protection assay was employed to analyze *Shigella*'s capacity to invade, multiply intracellularly and spread in the HeLa cell monolayer. These three steps in the *Shigella* infection cycle result in bacterial growth, which can be evaluated by counting colony-forming units (CFU). In the gentamycin assay, infected cells are treated with gentamycin to eliminate extracellular *Shigella*. Then, the host cells are lysed, and the number of intracellular bacteria is quantified as CFUs (Figure 3.2.1 A-B).

Various infection times, dish sizes and multiplicity of infection (MOI) ratios were evaluated to identify the optimal conditions to analyze *Shigella* growth. The MOI ratio represents the number of bacteria per host cell in a given infection setup. An MOI of 1 implies one bacterium will infect one cell, but this depends on the time allowed for infection. As shown in Figure 3.2.1 C, the CFU/mL recovered from cells seeded in a 96-well plate and infected with MOI 50 and 100 were not different before four hours post-infection, indicating that the cells became saturated with higher MOIs, and bacterial internalization was similar. The sharp increase in CFU observed after five h of infection using MOI 100 reflects exponential intracellular replication and cell-to-cell spreading of *Shigella* (Figure 3.2.1 C). If incubated longer, a similar trend should be observed with MOI 10 and 50. As expected, higher CFU were recovered from cells grown in a bigger well-size plate (12-well, Figure 3.2.1 D). With this setting, similar CFUs were recovered after one h of infection from MOI 1 and 10, suggesting there is not much cell-to-cell spreading at this time.

Consistent with a higher MOI, more bacteria were recovered after 2 and 3 h of infection from cells infected with MOI 10 than from MOI 1 (Figure 3.2.1 D). The growth curve obtained from MOI 10 in a 12-well plate setting reflected exponential intracellular replication and gradual cell-to-cell spreading of *Shigella* in a convenient time frame (Figure 3.2.1 D). Hence, the standard condition used for most experiments was as follows: cells seeded in 12-well plates were infected with an MOI of 10 for 30 min, treated with gentamycin and lysed every hour up to 3 or 4 hours to recover intracellular bacteria. Notably, the WT *Shigella* strain (M90T) used in this study expresses the adhesive fimbrial AfaI protein from *Escherichia coli* carried in the pBR322-AfaI plasmid [368]. *Shigella* strains expressing AfaI bind to the host cell with high efficiency [103], explaining why a low bacterial MOI was enough to obtain prolific infection in only half an hour (Figure 3.2.1 D).

An Δ*icsA* mutant strain harbouring the pBR322-AfaI plasmid was utilized in this study. IcsA is an outer membrane protein that localizes to one pole of *Shigella,* where it induces actin tail polymerization [223]. The Δ*icsA* mutant can invade cells and replicate, but it cannot polymerize actin tails or spread to neighbouring cells [100]. Infection condition standardization for the Δ*icsA* mutant revealed rapid intracellular replication (Figure 3.2.1 E). Cells infected with MOI 50 or 10 yielded similar CFU after one h of infection, suggesting similar invasion rates. However, after two h, Δ*icsA Shigella* rapidly replicates intracellularly, reaching higher CFUs in the cells infected with MOI 50 than with MOI 10. The yield of bacteria recovered at 2 and 4 h post-infection with MOI 50 was similar, probably due to cell lysis induced by high numbers of Δ*icsA* in the cytoplasm. The content of lysed cells is lost in the gentamycin assay washes before adding NP40 buffer (see methods section 2.7) hence the apparent lack of growth after four h of infection (Figure 3.2.1 E). Since MOI 10 shows gradual growth of the Δ*icsA* strain, this condition was used for most experiments involving Δ*icsA Shigella*. Furthermore, actin-tail polymerization was confirmed by immunofluorescence of HeLa cells infected with an MOI 10 of WT or Δ*icsA Shigella*. As shown in Figure 3.2.1 F, WT *Shigella* induced polymerization of prominent actin tails at two hours post-infection. In contrast, the cell infected with Δ*icsA* appeared full of bacteria that are not associated with actin tails (Figure 3.2.1 F).

Next, the role of RACK1 in *Shigella* growth was evaluated. Western blot analysis demonstrated effective silencing of RACK1 expression in the RACK1-KD stable cell lines KD-92, KD-94 and KD-95 compared to control NS cells (Figure 3.2.2 A). Growth curves determined by gentamycin protection assay showed significantly less CFU of *Shigella* recovered per µg of protein from RACK1-KD than from NS cells 2 and 3 h post-infection (Figure 3.2.2 B). As mentioned in section 3.1, RACK1-KD cells exhibit impaired adhesion; thus, the CFU counting was normalized by total protein concentration per well to account for cell number fluctuations. The *Shigella* growth inhibition phenotype observed in RACK1-KD cells was reproduced in four separate experiments (Supplementary Figure 2, Appendix C). The complementation of this phenotype was assessed by introducing an extra copy of *RACK1* into the genome of the KD-92 cells using lentiviruses. RACK1 gene expression, driven by the cytomegalovirus (CMV) promoter, was sufficient to re-establish RACK1 expression to NS levels in the KD-92 cell line (Figure 3.2.2 C-D). Rescuing RACK1 expression led to the recovery of the *Shigella* growth defect observed in RACK1-KD cells (Figure 3.2.2 E).

To further confirm the phenotype of defective *Shigella* growth observed in the RACK1-KD cells, fluorescent quantification of bacterial proliferation was evaluated using an aqueous two-phase (ATP) infection system followed by live-cell imaging. Briefly, a 0.5 µL droplet of dsRED-WT *Shigella* suspended in dextran (DEX) was inoculated into F-tractin-GFP (labels F-actin) HeLa cells covered with polyethylene glycol (PEG)-rich media (Figure 3.2.3 A). The DEX-PEG interface generated a physical barrier between the cells and the bacterial inoculum, slowing the infection rate. It also allowed spatially distinct localization of the infection area defined by the size of the droplet. After one hour of infection, the DEX-PEG mixture was removed, and the cells were treated with gentamycin to eliminate extracellular bacteria. Then, the defined infection area was imaged every 15 min for 12 h (Figure 3.2.3 A). The fluorescence intensity (FI) increment overtime was used to report the growth of *Shigella*. Figure 3.2.3 B shows example images of a typical ATP time-lapse experiment. A low fluorescent signal corresponding to *Shigella* was observed

after 240 min of infection. As *Shigella* multiplied and spread in the cell monolayer, the FI signal increased, showing prominent areas of infection after 585 min (Figure 3.2.3 B).

Shigella growth curves in RACK1-KD (KD-92, KD-94, KD-94) HeLa cells were determined using the ATP system. Consistent with the gentamycin assay results, less *Shigella* growth was observed in RACK1-KD cell lines than in control (NS) cells (Figure 3.2.3 C). The growth curves of *Shigella* in RACK1-KD cells appeared flat and slightly shifted to the right compared to NS, indicating a slower replication rate or a spreading impairment (Figure 3.2.3 C). Although the ATP methodology had limited sensitivity at low bacterial concentrations (all growth curves were flat the first 200 min), assessing *Shigella*'s growth through FI allowed better quantification of bacterial growth kinetics than with the gentamycin assay as more time points can be evaluated. In addition to the temporal resolution, the 96-well format of the ATP assay presented the advantage of high throughput and supported multi-channel measurements (e.g., F-tractin-GFP and dsRED).

Interestingly, although not statistically significant, an increase in *Shigella* growth was observed in control (NS) cells harbouring an extra copy of *RACK1* (Figure 3.2.2 E). This finding prompted the investigation of RACK1 overexpression effects on *Shigella* infection. Stable RACK1 expression of GFP-tagged and untagged versions of RACK1 was achieved by lentivirus transduction. Surprisingly, HeLa cells expressing GFP-tagged versions of RACK1 showed similar expression levels to cells transduced with the GFP control construct (Figure 3.2.4 A-B). HeLa cells carrying the untagged version of RACK1 showed marked overexpression suggesting the GFP tag interferes with RACK1 expression (Figure 3.2.4 A-B). Also, when monitoring GFP fluorescence in the cells transduced with GFP-tagged RACK1, rapid fluorescence loss after cell passages was observed (data not shown). Loss of fluorescence suggests that the population of cells that did not integrate the fluorescent copy of RACK1 or did not express the extra copy proliferated better, ultimately outgrowing the cells expressing GFP-tagged RACK1. Another explanation for the low level of total RACK1 expression obtained could be a miscalculation of the total levels of GFP-bound RACK1 due to overexposure of the band corresponding to endogenous RACK1.

HeLa cells stably expressing the GFP-bound and untagged RACK1 were infected with *Shigella,* and growth was determined by gentamycin protection assay. Significantly more *Shigella* was recovered from cells expressing untagged RACK1 compared to the GFP control after 3 h (Figure 3.2.4 C). Even though the cells transduced with GFP-RACK1 and RACK1-GFP showed close to basal levels of RACK1 in the western blot, significantly more *Shigella* was recovered from them than from the GFP-only control (Figure 3.2.4 B-C). These data suggest that increasing RACK1 expression levels is beneficial and promotes *Shigella* growth.

Still, overexpression of GFP-tagged RACK1 was desirable to monitor expression levels by fluorescent signal in living cells. Thus, HeLa cells were transfected with the high expression plasmid pEGFP harbouring N- and C- terminus tagged versions of RACK1. Forty-eight hours after transfection, these cells were infected with *Shigella,* and growth was evaluated by gentamycin assay. RACK1 protein expression was assessed by western blot. For this, the protein extracts from three separate experiments were pooled before RACK1 immunodetection. As shown in Figure 3.2.5 A and B, only cells transfected with RACK1-GFP showed higher expression levels than control cells treated with transfection reagent alone. Consistent with the results observed in cells stably expressing RACK1 (Figure 3.2.4), transient overexpression of GFP-tagged RACK1 promotes *Shigella* growth (Figure 3.2.5 C). Again, the expression of both GFP-tagged versions of RACK1 resulted in significantly higher *Shigella* yield, despite basal RACK1 levels found in cells transfected with GFP-RACK1 (Figure 3.2.5 C). Pooling the cell lysates from infections performed on separate days might not accurately represent the levels of RACK1 expression. Together, the RACK1 silencing, and overexpression experiments suggest that *Shigella* has evolved a mechanism to manipulate RACK1 function to establish a replicative niche within epithelial cells.

Figure 3.2.1. Standardization of HeLa cells infected by *Shigella flexneri*.
A. Experimental design of the gentamycin protection assay. HeLa cells (green) were incubated with bacteria (red) for 30 minutes to allow for infection, then were treated with gentamycin (100 µg/mL) to eliminate extracellular bacteria. After cell lysis, the samples were serially diluted and inoculated on LB agar plates. **B**. Example LB plate showing *Shigella* growth after 24 h. Colony-forming units (CFU) were enumerated in the last two rows (dilutions 1 in 100 and 1 in 1000) and averaged. **C** and **D**. Standardization of the gentamycin assay using different multiplicities of infection (MOIs) and plate formats. HeLa Tet-off cells seeded in a 96-well plate (**C**) or 12-well plate (**D**) were infected with WT *Shigella* as described in A. CFU per mL were calculated at various time points. Time in the x-axis is time post initial infection. Thus, time 0 represents the number of bacteria that invaded the cells after 30 min of infection. Error bars in **C** are standard deviation (SD) from three replicates. Error bars in **D** are SD from two replicates. **E**. Standardization of Δ*icsA* *Shigella* infection. The graph shows growth curves of Δ*icsA* in HeLa Tet-off cells seeded in a 12-well plate and infected with MOI 1 and 10 as described in A. Error bars are SD from three replicates. Time in the x-axis is time post initial infection. **F**. Confocal images of HeLa cells infected with WT (top) and Δ*icsA* *Shigella* (bottom). Cells infected with an MOI of 10 were fixed after two h post-infection and labelled with DAPI (cyan) and phalloidin-Alexa-555 (magenta). Actin tails (white arrowhead) are formed by WT *Shigella* but not by the Δ*icsA* strain. Scale = 10 µm.

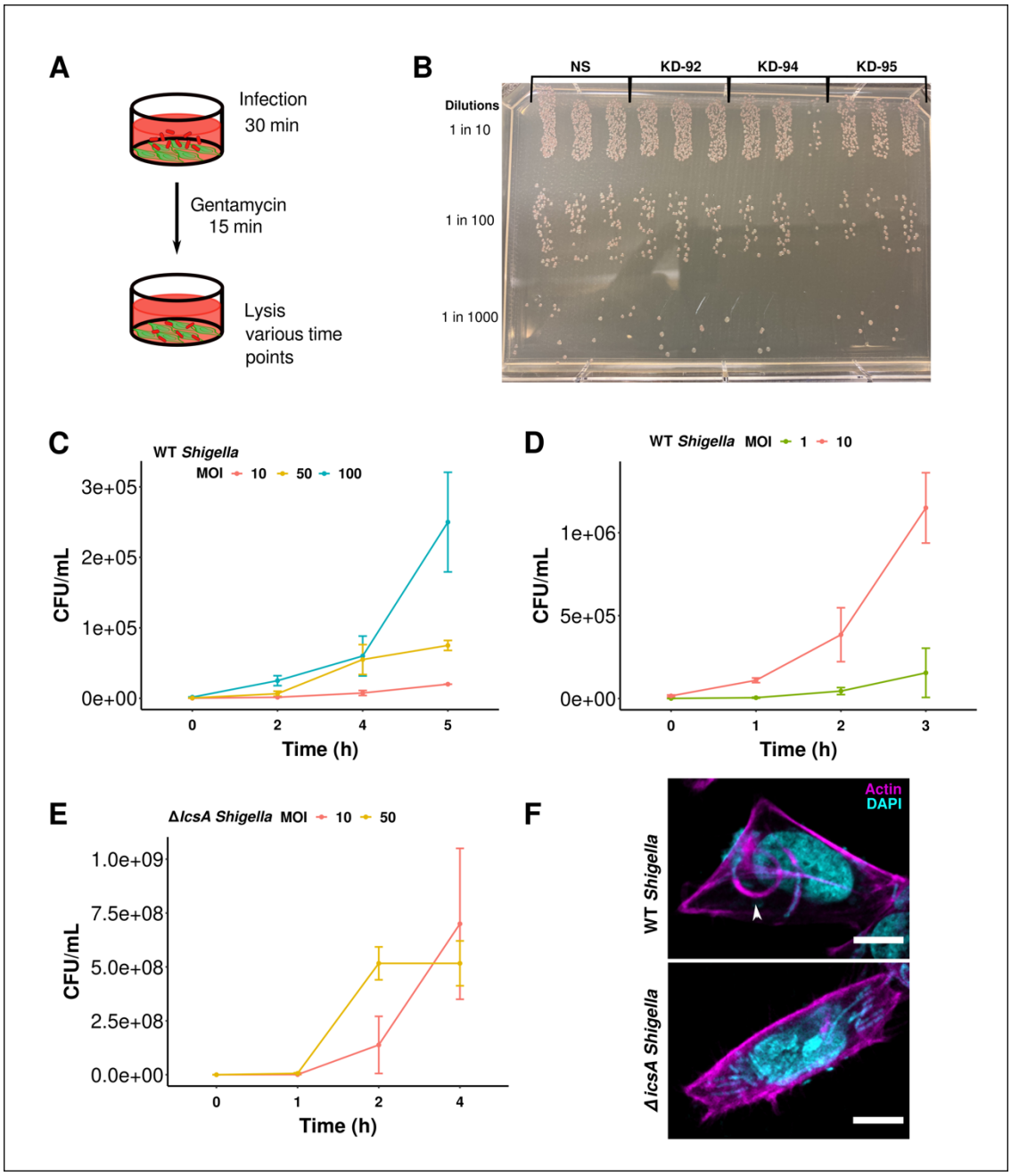
A
Infection
30 min
Gentamycin
15 min
Lysis
various time
points
B
NS
KD-92
KD-94
KD-95
Dilutions
1 in 10
1 in 100
1 in 1000
C
WT Shigella
MOI 10 50 100
CFU/mL
3e+05
2e+05
1e+05
0e+00
0
2
4
5
Time (h)
D
WT Shigella MOI 1 10
CFU/mL
1e+06
5e+05
0e+00
0
1
2
3
Time (h)
E
ΔIcsA Shigella MOI 10 50
CFU/mL
1.0e+09
7.5e+08
5.0e+08
2.5e+08
0.0e+00
0
1
2
4
Time (h)
F
Actin
DAPI
WT Shigella
ΔIcsA Shigella

Figure 3.2.2. RACK1 silencing inhibits *Shigella* growth in HeLa cells.
A. Confirmation of RACK1 silencing by western blotting. Protein extracts from RACK1-KD (KD-92, KD-94 and KD-95) and control (NS) HeLa cells were immunolabeled using anti-RACK1. Anti-Tubulin and anti-Actin antibodies were used as loading controls. **B**. Growth curves determined by gentamycin protection assay. RACK1-KD and control (NS) cells were infected with WT *Shigella* (MOI 10), treated with gentamycin (100 µg/mL) and lysed at various time points to quantify intracellular bacteria. Colony-forming units (CFU) were divided by total protein concentration to normalize differences in cell number. Significantly less *Shigella* was recovered from RACK1-KD than NS cells after 2 and 3 h. The growth curves shown are from one representative experiment out of 4 (Supplementary Figure 1, Appendix C). Error bars represent SD from one experiment in triplicate. Unpaired t-test *$p < 0.05$, ***$p < 0.001$. **C**. RACK1 expression restoration by introducing an extra copy of the *RACK1* gene. Protein extracts from NS and KD-92 cells transduced with lentiviruses carrying the RACK1 gene (pLJM1-RACK1) were immunoblotted with anti-RACK1 and anti-Tubulin (loading control). **D**. Relative expression quantification. The bar graph shows RACK1 relative expression quantified from the western blot in C, and two other experiments (not shown). Error bars are SD. Unpaired t-test *$p < 0.05$. **E**. Restoration of *Shigella* growth in RACK1-KD cells by introducing an extra copy of *RACK1*. *Shigella* growth was evaluated by gentamycin protection assay after two h of infection. The bar graph shows the fold change in CFU per µg of protein (CFU/µg). Results represented as mean ± SD from 3 independent experiments. Unpaired t-test *$p < 0.05$.

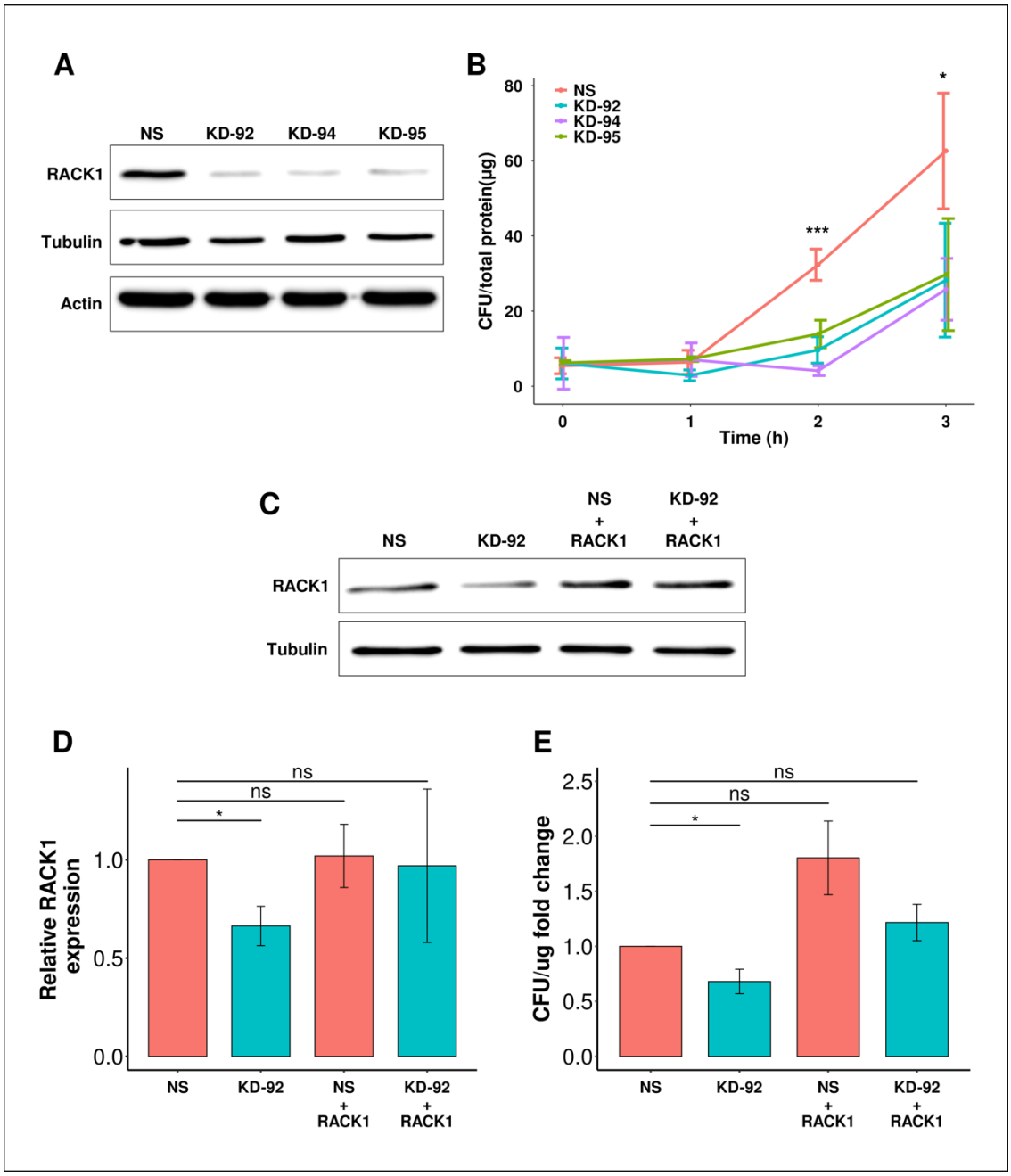
A
NS
KD-92
KD-94
KD-95
RACK1
Tubulin
Actin
B
NS
KD-92
KD-94
KD-95
CFU/total protein(μg)
Time (h)
*
***
C
NS
KD-92
NS + RACK1
KD-92 + RACK1
RACK1
Tubulin
D
Relative RACK1 expression
ns
ns
*
E
CFU/ug fold change
ns
ns
*

Figure 3.2.3. *Shigella* growth impairment was confirmed in RACK1-KD cells using an aqueous two-phase (ATP) infection system.

A. Diagram of the ATP infection method. Target cells (expressing F-tractin-GFP) seeded in black 96-well plates and overlaid with polyethylene glycol (PEG) were infected with dsRED-WT *Shigella* resuspended in dextran (DEX). DEX and PEG generate a physical barrier restricting the infection to a discrete area. After one h of infection, the cells were treated with gentamycin (100 µg/mL) for 15 min and then overlaid with the low background media FluoroBrite. Infection progression was recorded by time-lapse microscopy using an EVOS imager. Images were taken every 15 min for 12 h, at 10X magnification. **B**. Photomicrographs of NS cells stably expressing F-tractin-GFP (binds to actin) infected with dsRED-WT *Shigella* at 240 min (left) and 585 min (right) after infection. The top row shows images of bacteria coloured in cyan, and the bottom row shows merged images of cells (actin in magenta) and bacteria. Scale bar = 1 mm. **C**. *Shigella* growth curves in HeLa cells determined by ATP infection system coupled to time-lapse microscopy. RACK1-KD (KD-92, KD-94, KD-94) and control (NS) cells stably expressing F-tractin-GFP were infected with dsRED-WT *Shigella* as described in A. Bacterial fluorescence intensity (FI) fold change was quantified as a proxy to evaluate bacterial growth and normalized to the number of HeLa cells available for infection at time 0. Results represented as mean ± SD from three separate experiments. * Indicate time points where growth difference was statistically significant. Unpaired t-test **p < 0.01.

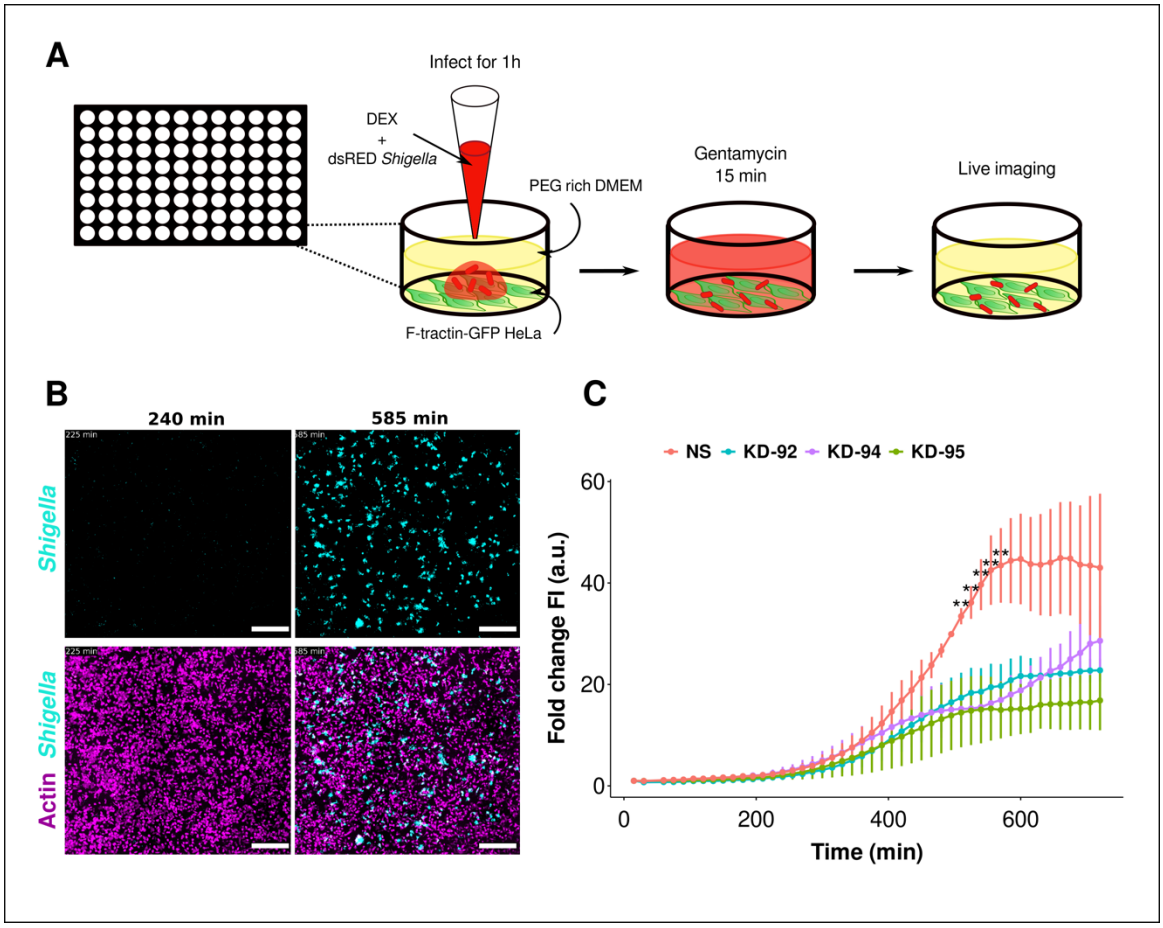

Figure 3.2.4. Stable RACK1 overexpression promotes *Shigella* growth in HeLa cells. RACK1 overexpression was obtained in HeLa cells by transducing with lentiviruses harbouring GFP-tagged versions of RACK1 (pLJM1-GFP-RACK1, pLJM1-RACK1-GFP) or untagged RACK1 (pLJM1-RACK1). Cells transfected with GFP alone (pLJM1-EGFP) were used as basal expression control. *Shigella* growth in these cells was assessed by gentamycin assay after three h of infection. **A.** Western blot analysis of infected cell lysates showing RACK1 detection using anti-RACK1. The loading control was Coomassie staining of the SDS-PAGE gel used for protein transference. **B**. Relative expression quantification from western blot in A. The bar plot shows RACK1 protein levels relative to loading control. Protein quantification corresponding to GFP-tagged RACK1 (top band in lanes 1 and 2 shown in A) was added to wild-type RACK1 (bottom band in lanes 1 and 2 shown in A) to obtain total expression levels. **C**. *Shigella* growth in cells stably overexpressing RACK1. Bars show CFU/mg represented as mean ± SD from three replicates of one experiment. Unpaired t-test *p < 0.05, ** p < 0.01.

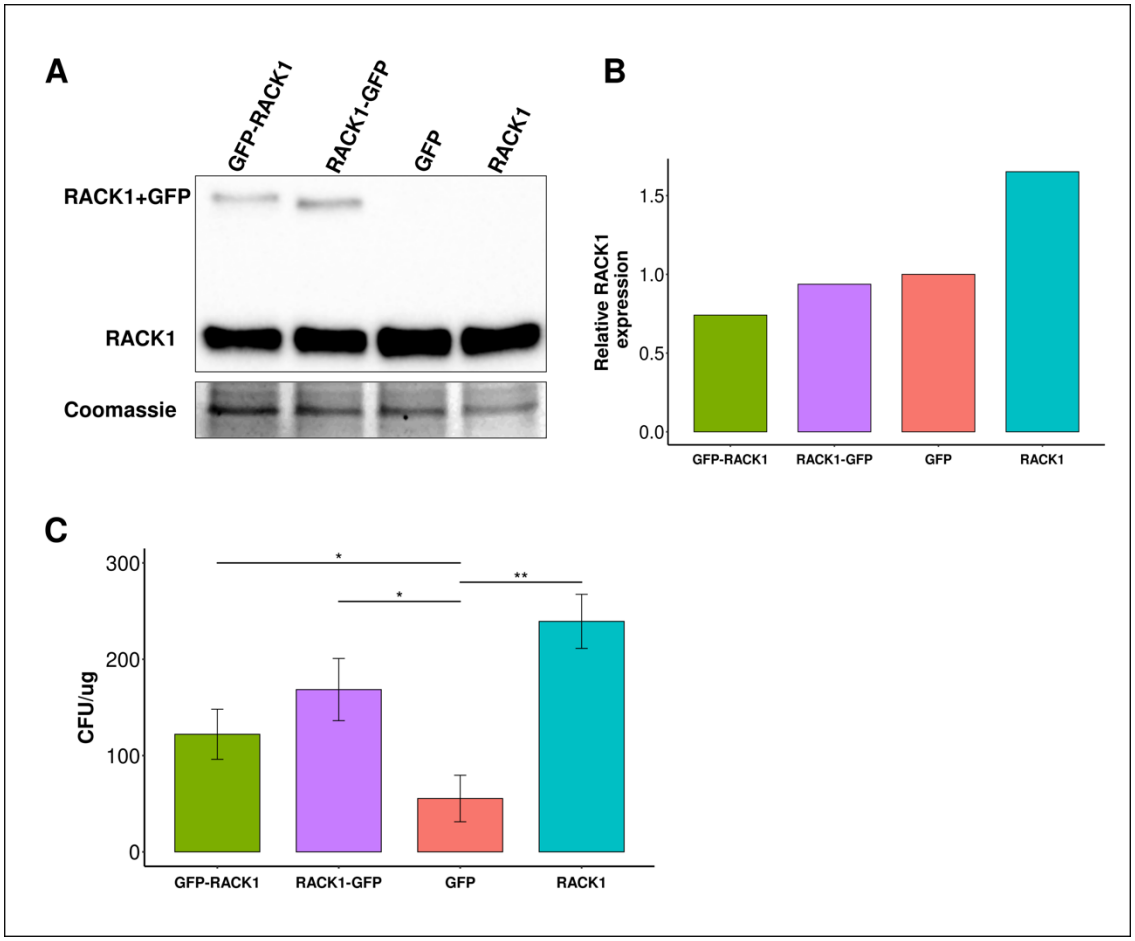

Figure 3.2.5. Transient RACK1 overexpression promotes *Shigella* growth in HeLa cells.

Transient overexpression of RACK1 was achieved by transduction of HeLa cells with pEGFP-C1-RACK1 (GFP-RACK1) or pEGFP-N1-RACK1 (RACK1-GFP). Cells treated only with lipofectamine (transduction reagent) were the negative control. After 48 h, these cells were infected with WT *Shigella* and growth was assessed using the gentamycin assay. **A.** Western blot analysis of RACK1 overexpression in infected cell lysates. Tubulin was the loading control. **B.** Bar plot of RACK1 relative expression quantification from western blots in A. Protein quantification corresponding to GFP-tagged RACK1 (top band in lanes 1 and 2 shown in A) was added to wild-type RACK1 (bottom band in lanes 1 and 2 shown in A) to obtain total expression levels. These values were normalized to the loading control. **C.** *Shigella* growth in cells transiently overexpressing RACK1. Growth is shown as CFU/mg fold change. Error bars are SD from three separate experiments. Unpaired t-test *p < 0.05.

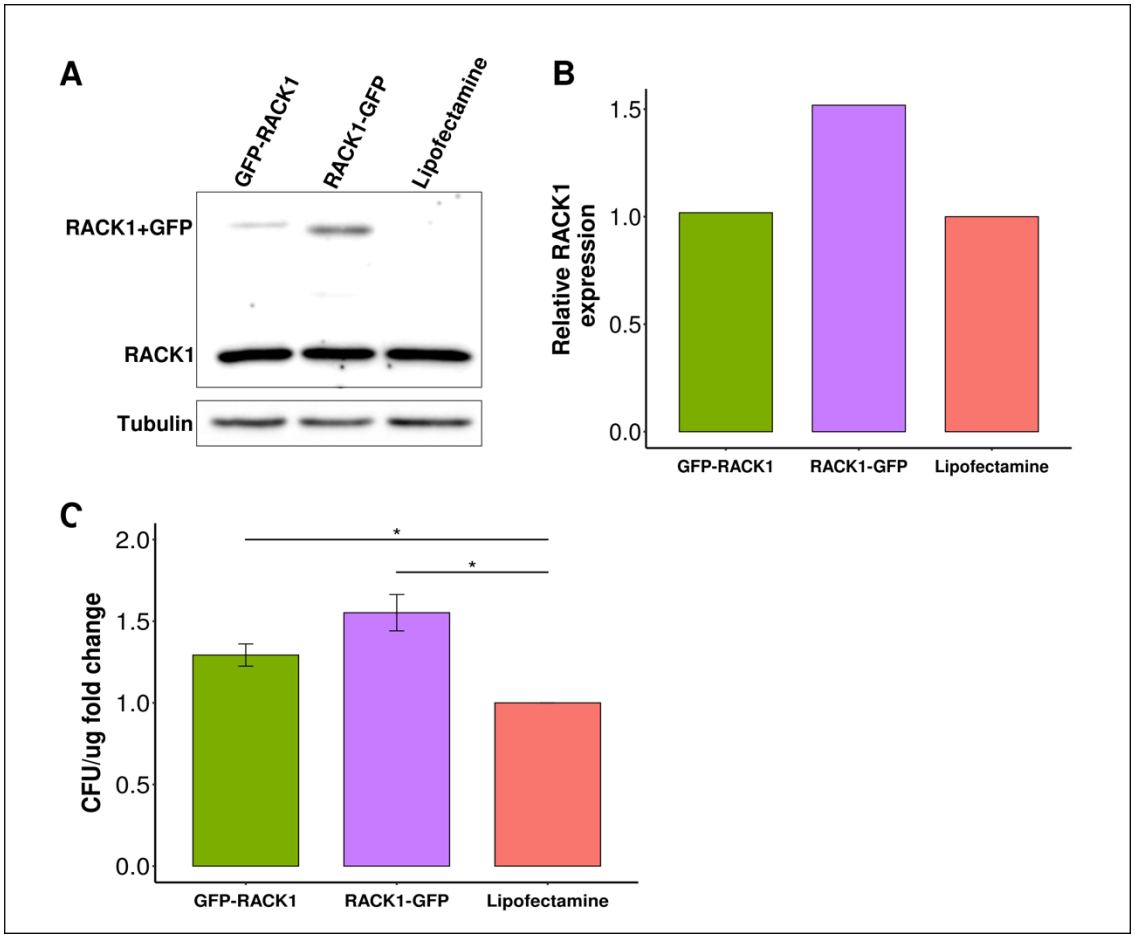

3.2.2 RACK1 silencing protects *Drosophila melanogaster* from *Shigella* infection

Shigella and other human enteropathogens can cause intestinal pathology in flies [386,387]. There is considerable conservation between mammalian and *Drosophila* intestinal physiology [388]. Thus, flies have become a useful model to study intestinal infections [389]. I used the fly gut model to study the role of RACK1 during *Shigella* infection *in vivo*. Because RACK1 is essential at multiple steps of *Drosophila* development [390], RACK1 expression was knocked down only in enterocytes. Real-time PCR confirmed RACK1 silencing (Figure 3.2.6 A). Flies were fed with dsRED-WT *Shigella* mixed in sucrose or sucrose alone for 19 days. RACK1-KD and control flies started to succumb to the infection after ten days (Figure 3.2.6 B). The mortalities observed in the RACK1-KD flies were similar to those fed with sucrose only. Survival probability analysis revealed that control flies had a lower survival probability than RACK1-KD flies (Figure 3.2.6 B).

Microscopic analysis of the midguts of infected control flies revealed distortion of the digestive tract with lumen dilation and bacterial accumulation. Also, the epithelial lining appeared thinner in some areas (Figure. 3.2.6 C). The guts from infected RACK1-KD flies appeared less colonized by *Shigella* with a smaller lumen space and tissue dysplasia (Figure. 3.2.6 C). I also evaluated if *Shigella* invaded the enterocytes of flies. Optical sections of 2.5 μm (z-stack slice = 0.25 μm) were examined to determine the spatial localization of bacteria. *Shigella* was found attached to the luminal border of the enterocytes in control (Figure 3.2.6 D, black arrowhead) and RACK1-KD flies but not within the cells. Given this result, the mechanism behind the resistance of RACK1-KD flies to *Shigella* infection must not involve cell invasion. The proliferation of enteric epithelial cells in flies is characteristic of cell differentiation in response to infection [391]. Perhaps, the tissue dysplasia observed in RACK1-KD indicates a more efficient innate immune response is established in RACK1-KD guts. Nevertheless, the reduced mortality and less bacterial colonization observed in RACK1-KD flies indicate a pivotal role of RACK1 during *Shigella* colonization of the fly intestine.

Figure 3.2.6 RACK1 silencing protects *Drosophila melanogaster* from *Shigella* infection.

RACK1 was depleted in *D. melanogaster* enterocytes using RNAi. Control and RACK1-KD age-matched female and male flies were fed on filter paper soaked in 5% sucrose (sugar) or 5% sucrose containing dsRED-WT *Shigella* (OD_{600} = 25). The number of dead flies was determined daily. **A**. Quantification of *RACK1* mRNA transcript levels in control and RACK1-KD fly guts. Results are shown as fold change relative to control. Bars are mean ± SD from one experiment in triplicate. **B**. Kaplan-Meier survival curve of *D. melanogaster* following infection with *Shigella*. Survival probability was analyzed using the log-rank test. n = starting number of flies. **C-D**. Representative confocal micrographs of *D. melanogaster* guts. Fly guts were fixed and immunolabeled with anti-armadillo to label enterocytes (magenta). Z-stacks were captured on a confocal Zeiss 880. **C**. Maximum projection images of guts from control (top row) and RACK1-KD (bottom row) flies fed with *Shigella* (cyan, left column) and fed with sugar only (right column). The images are maximum projections from z-stacks (18 to 20 slices, 1 µm apart) captured with 20X magnification. The white arrowhead indicates an area with thinner epithelial lining accompanied by bacterial accumulation. Scale bar = 100 µm. **D**. Orthogonal view of an infected gut from a control fly. The image shows XZ and YZ planes (depth 2.5 µm) of the point indicated in the 2D image (yellow lines intersection). This image was captured with 63X magnification. *Shigella* (cyan) appears confined to the gut lumen (black arrowhead). Scale bar = 10 µm.

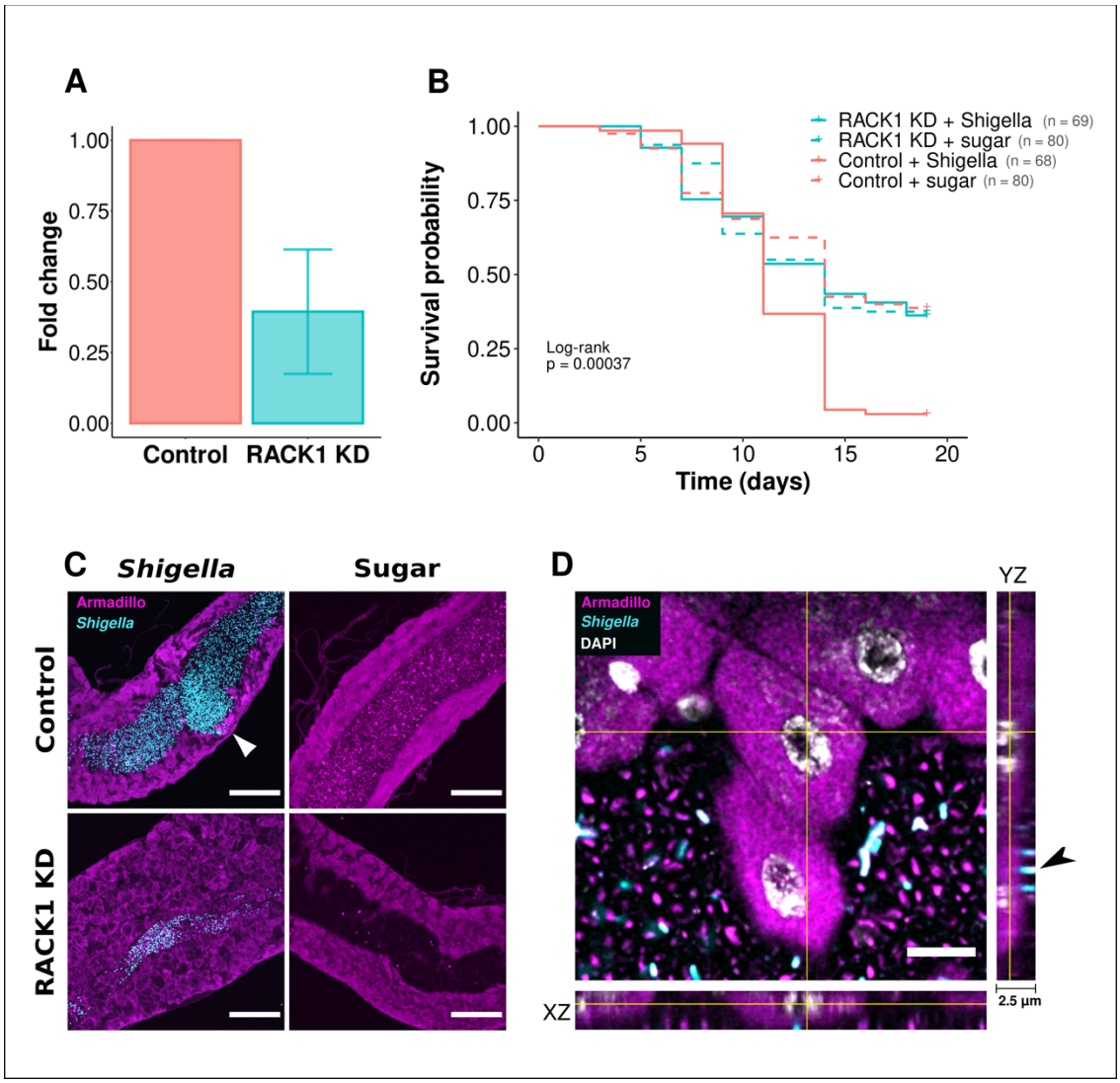
A
Fold change
1.00
0.75
0.50
0.25
0.00
Control
RACK1 KD
B
Survival probability
1.00
0.75
0.50
0.25
0.00
0
5
10
15
20
Time (days)
RACK1 KD + Shigella (n = 69)
RACK1 KD + sugar (n = 80)
Control + Shigella (n = 68)
Control + sugar (n = 80)
Log-rank
p = 0.00037
C
Shigella
Sugar
Control
RACK1 KD
Armadillo
Shigella
D
Armadillo
Shigella
DAPI
YZ
XZ
2.5 µm

3.2.3 Steps of *Shigella* intracellular life cycle studied in this project.

Shigella's ability to establish an intracellular life cycle depends on several bacterial and host cell functions [95]. First, internalization by epithelial cells (ECs) requires the action of T3SS effectors that trigger profuse actin polymerization and membrane ruffling forming an entry focus that leads to bacterial uptake (Figure 3.2.7 a). Then, *Shigella* rapidly damages the bacterium-containing vacuole and escapes into the cytoplasm, where it replicates (Figure 3.2.7 b and c). Avoidance of EC defense mechanisms, such as apoptosis or autophagy, is crucial to allow intracellular replication (Figure 3.2.7 c). Subsequently, *Shigella* hijacks the host's actin cytoskeleton machinery to acquire intracellular motility. Through the action of its adhesin IcsA, *Shigella* induces actin polymerization at one pole of the bacterium, forming an actin-tail that propels *Shigella* through the cytoplasm (Figure 3.2.7 d). Motile *Shigella* eventually encounters the EC plasma membrane inducing the formation of a membrane-bound cell extension called protrusion. Finally, neighbouring cells endocytose bacteria-containing protrusions, from which *Shigella* escapes and continues its replicative cycle (Figure 3.2.7 e). The following sections (3.3 to 3.7) focus on understanding how RACK1 facilitates the establishment of *Shigella*'s intracellular life cycle. RACK1's role in each step described in Figure 3.2.7 (a-e) was systematically assessed mainly by fluorescence microscopy techniques including immunofluorescence and live-cell imaging.

Figure 3.2.7. Critical steps of *Shigella* intracellular life cycle studied in this project. (**a**) *Shigella* (cyan) invades epithelial cells by injecting T3SS effectors into the host cell cytosol, inducing profuse actin polymerization and plasma membrane remodelling. Localized actin polymerization sites, called filamentous-actin (F-actin, magenta) foci, lead to membrane ruffling around *Shigella* internalizing the bacterium. (**b**) Shortly after entry into the primarily infected cell (left), *Shigella* damages the membrane of the phagocytic vacuole escaping to the cytoplasm where it proliferates (**c**). *Shigella* is a non-motile bacterium but can acquire actin-based motility. (**d**) Shigella induces actin polymerization in one pole of the bacterium, forming an actin node that elongates to form a prominent actin-tail. When motile *Shigella* reaches the cell periphery, it deforms the plasma membrane forming a membrane protrusion that projects into an adjacent cell (right). (**e**) The membrane protrusion is endocytosed by the neighbouring cell, which becomes secondarily infected as *Shigella* escapes the vacuole and continues its replicative cycle. The role of RACK1 (green) in *Shigella's* life cycle was assessed, evaluating each critical step (a-e) shown in this diagram.

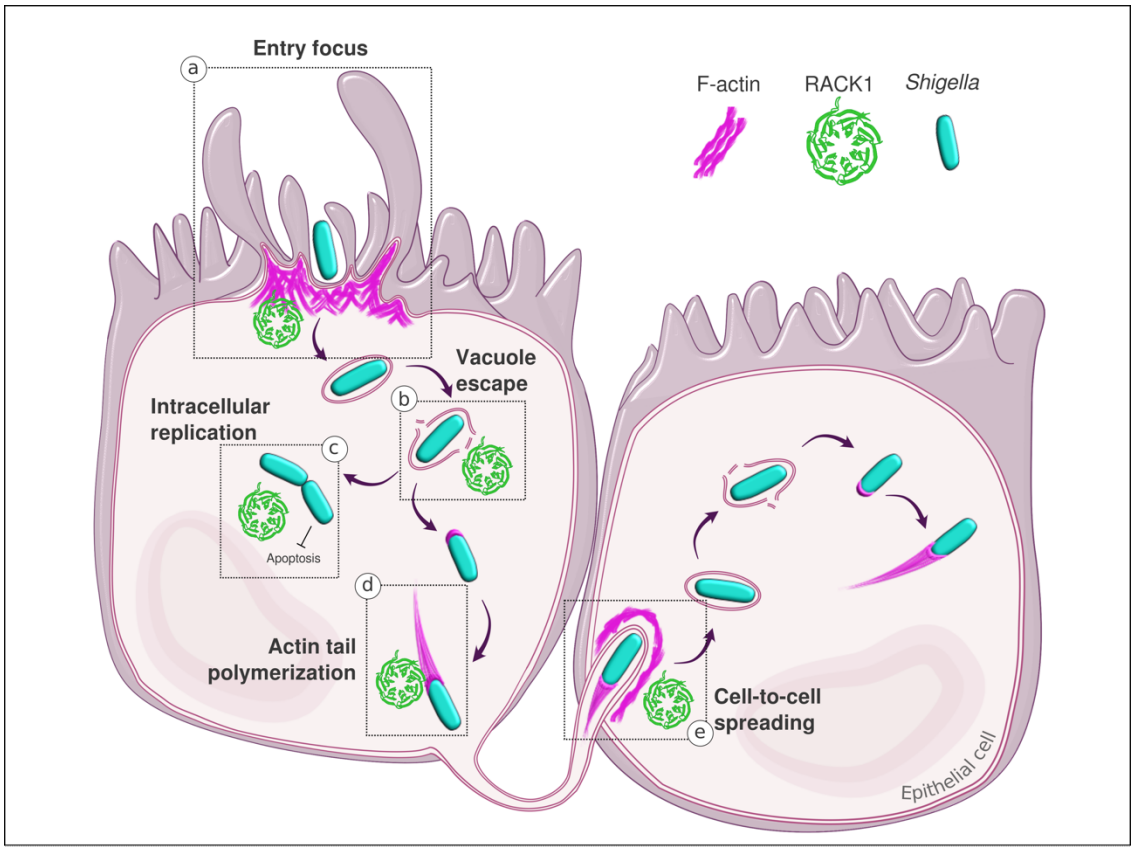

3.3 RACK1 silencing reduces *Shigella* invasion of HeLa cells

Shigella triggers membrane ruffling and profuse actin polymerization, forming an entry focus to invade epithelial cells. This process is mediated by multiple bacterial and host cell factors [392]. Hence, the entry focus is the first critical step where *Shigella* could encounter RACK1. Confocal images of HeLa cells infected with *Shigella* and immunolabeled with anti-RACK1-Alexa-647 were captured to evaluate RACK1 localization to entry foci. The images revealed that RACK1 was enriched around *Shigella* in the entry focus and that RACK1 and actin seem to partially co-localize (Figure 3.3.1 A, inset). Similar results were observed when analyzing time-lapse infections of HeLa cells stably expressing GFP-tagged RACK1 and F-tractin-mCherry (binds to F-actin). HeLa cells expressing high and low levels of the fluorescently tagged proteins were imaged to avoid the chance of misinterpreting channel crosstalk (bleed-through) as RACK1 localization. Figure 3.3.1 B shows selected images from a time-lapse of a HeLa cell expressing low levels of F-tractin-mCherry and high levels of RACK1-GFP being infected with *Shigella*. Although the bacterium was not fluorescently labelled and could not be seen, enrichment of actin and RACK1 around *Shigella* was evident (Figure 3.3.1 B, yellow arrows). In this set of images, F-actin assembled around *Shigella,* forming a tight actin envelope previously described as an actin cocoon [164]. This structure was observed in a low percentage (~25%, data not shown) of invading *Shigella*; thus, the nature and dynamics of actin cocoon formation were not evaluated in this project.

Quantification of FI increment over time in a region of interest (ROI, green and red ovals in Figure 3.3.1 B) around *Shigella* showed that RACK1 is recruited early to the entry focus and remains there even after the actin signal starts declining (Figure 3.3.1 C, 720 sec). To further confirm that RACK1 localizes around *Shigella* during entry, HeLa cells expressing RACK1-GFP were infected with dsRED fluorescent bacteria. Z-stacks were used to generate a Simulated Fluorescence Process (SFP) volume image. For this analysis, an algorithm transforms the fluorescent signal into a distribution of fluorescent dye, computing a 2D image that shows the data as it would have appeared in reality (with

shadows and lights). Figure 3.3.1 D shows an SFP volume image where RACK1 accumulates (appears brighter) around *Shigella*.

Since RACK1 is recruited to the entry focus, I next evaluated the effect of RACK1 silencing on *Shigella* invasion of HeLa cells. *Shigella* induces actin polymerization at the entry site, resulting in filamentous (F)-actin accumulation in F-actin foci structures. The F-actin focus increase in size over time until *Shigella* is internalized, followed by F-actin focus depolymerization, and recovering of plasma membrane basal state (Figure 3.3.2 A). The dynamics of *Shigella*-induced entry foci were studied by time-lapse imaging using F-tractin as a live-cell actin reporter. F-tractin is a peptide derived from the rat neuronal inositol 1,4,5-triphosphate 3-kinase A (ITPKA) that binds actin filaments [393]. HeLa cells expressing F-tractin bound to GFP were infected with fluorescent *Shigella* (dsRED-WT *Shigella*). The most extensive area reached by the entry focus was encircled to create an ROI (Figure 3.3.2 A). The area and average FI inside that fixed-size ROI (e.g., white circle in Figure 3.3.2 A) were measured from the first signs of actin polymerization around *Shigella* until the FI returned to basal level (more details in methods section 2.11.3).

Measurements of foci area showed no significant differences between RACK1-KD (154±113 μm^2) and control cells (137±133 μm^2, Figure 3.3.2 B). The FI of the focus represents the amount of F-actin polymerized around *Shigella* during entry. I calculated the average FI from the FI measured at each time point (more details in methods section 2.11.3). There was no significant difference between the foci FI in control (17.2±10.6 a.u.) and KD-92 cells (15.4±10.7 a.u., Figure 3.3.2 C). However, when analyzing the actin foci FI increment over time, it was evident that the foci formed in RACK1-KD cells reached maximum fluorescence later than NS cells (Figure 3.3.2 D). Also, the FI curves appeared shorter in the control cells (Figure 3.3.2 D). Thus, I quantified the duration of actin foci. As suspected, the foci lasted significantly longer in RACK1-KD cells (11.1±7.02 min) than in control cells (6.29±4.19 min, Figure 3.3.2 E). Similar FI and area of the foci in KD-92 and NS cells but longer foci duration in KD-92 cells indicates there might be a size or actin accumulation threshold necessary for bacterial internalization. In RACK1-KD cells, this threshold takes longer to be achieved, suggesting RACK1 regulates actin foci dynamics.

To further understand how RACK1 modulates foci formation, I quantified the rate of F-actin polymerization at the entry site. The increment in actin FI over time observed on each infection focus was utilized to estimate the actin polymerization maximum rate using a logistic model (more details in methods section 2.11.3). Figure 3.3.3 A shows an example of an entry focus FI curve (dots) and its best-fitted curve (blue line), from which the maximum rate of actin polymerization was calculated. The logistic regression analysis revealed a modest but significant reduction in the rate of actin polymerization in KD-92 cells ($0.0085\pm0.007\ sec^{-1}$) compared to NS ($0.0121\pm0.008\ sec^{-1}$, Figure 3.3.3 B), suggesting that RACK1 enhances actin polymerization around bacteria during entry. The slower rate of F-actin polymerization could also be interpreted as a reduced F-actin polymerization rate. This finding is consistent with the extended focus duration observed in RACK1-KD cells (Figure 3.3.2 E). A slow rate of F-actin polymerization could extend entry foci duration until enough actin polymerization has occurred before *Shigella* is internalized, also explaining the similar average FI of foci observed in Figure 3.3.2 C.

RACK1 silencing negatively impacted actin foci formation dynamics, which could reduce bacterial internalization. To determine if RACK1 silencing impairs invasion, I evaluated the number of infected cells in RACK1-KD and control (NS) HeLa cells. Given that the *Shigella* strains used in this project expressed the *E. coli* adhesin AfaI, binding to a cell or even actin foci formation might not necessarily reflect internalization. To distinguish bacteria adhered to the cell surface from bacteria truly internalized, I used galectin-3 (Gal-3) as a marker of invasion. Gal-3 is recruited around the *Shigella*-containing vacuole (SCV) when the bacterium damages the vacuolar membrane to access the cytoplasm. HeLa NS and KD-92 expressing F-tractin-GFP, and fluorescent Gal-3 were infected with WT *Shigella,* and time-lapse videos were recorded for 1.5 h. Microscopy images confirmed that fluorescently tagged Gal-3 accumulates around damaged SCVs, revealing how the vacuolar membrane attaches tightly around the bacterium (Figure 3.3.4 A, arrowhead). A cell was classified as infected if it had at least one Gal-3+ bacterium over the course of the time-lapse captured. KD-92 cells (62.1±16.4%) showed ~17% fewer infected cells than control cells (78.6±12.5%, Figure 3.3.4 B). Quantification of the number

of Gal-3+ bacteria per cell confirmed the reduction of *Shigella* invasiveness observed in RACK1-KD cells. NS cells had, on average, 3±2 Gal+ *Shigella* per cell, whereas KD-92 had 2±1 Gal+ bacteria per cell (Figure 3.3.4 C).

Quantifying Gal-3+ *Shigella* does not distinguish between primary and secondary infections. Secondary infections happen when *Shigella* invades a neighbouring cell through actin tail mediated membrane protrusion formation. I utilized the Δ*icsA Shigella* strain, which is deficient in cell-to-cell spread, to evaluate if RACK1 silencing affected primary bacterial invasion. RACK1-KD and control HeLa cells stably expressing F-tractin-GFP were infected with dsRED-Δ*icsA Shigella* for 30 min before eliminating extracellular bacteria with gentamycin. The infected cells were incubated for four h to allow enough time for *Shigella* to replicate intracellularly before imaging. Given that Δ*icsA* cannot spread to neighbouring cells, this strain replicates to high numbers in the cytoplasm making infected cells easily identifiable by automatic segmentation (see methods 2.10.2). The number of infected cells was significantly reduced in the KD-92 cell line (~12% fewer infected cells) compared to the NS control (Figure 3.3.4 D), indicating that RACK1 enhances primary infection of HeLa cells. The study of secondary infections resulting in cell-to-cell spreading will be presented in section 3.7.

In summary, RACK1 localization to *Shigella*'s entry site promoted efficient actin polymerization and invasion. When RACK1 expression was silenced, fewer infected cells and fewer *Shigella* per cell were found. Moreover, RACK1 mediated the primary invasion of HeLa cells. These findings suggest that the impairment of *Shigella* invasion observed here contributes to lower CFU recovered from HeLa cells as described in section 3.2.

Figure 3.3.1. RACK1 is recruited to *Shigella*'s entry focus in HeLa cells.
A. Confocal images showing RACK1 localization around bacteria during entry. HeLa cells expressing F-tractin-GFP (actin) infected with WT *Shigella* (MOI 50) were fixed and stained with DAPI to mark DNA and anti-RACK1-Alexa-647. Cells were imaged at 63X magnification with a Leica TCS SP8 microscope. The top row presents individual channels, which are merged in the images in the second row. White arrowheads highlight two entry foci. The white box marks an inset region of interest (ROI) with an entry focus; scale bar = 10 μm. **B**. Selected confocal images from a time-lapse showing RACK1 and actin recruitment to *Shigella*'s entry site (yellow arrowhead). HeLa cells expressing RACK1-GFP and F-tractin-mCherry were infected with WT *Shigella* (MOI 50). Images were captured every 1 min with a 63X objective on a Zeiss spinning disk microscope. Yellow arrowheads highlight the initiation of an entry site. Green and red ovals highlight an ROI around the entry focus. Scale bar = 10 μm. **C**. Quantification of fluorescence intensity (FI) fold change over time in the ROI (*Shigella's* entry site) shown in B. Simultaneous recruitment of RACK1 (green) and actin (red) to the entry site was observed. **D**. Simulated Fluorescence Process (SFP) volume view of a confocal image generated with Huygens Software. The image, captured on a Zeiss spinning disk with a 63X objective, shows a HeLa cell expressing RACK1-GFP (green) invaded by dsRED-WT *Shigella* (red). Scale bar = 10 μm.

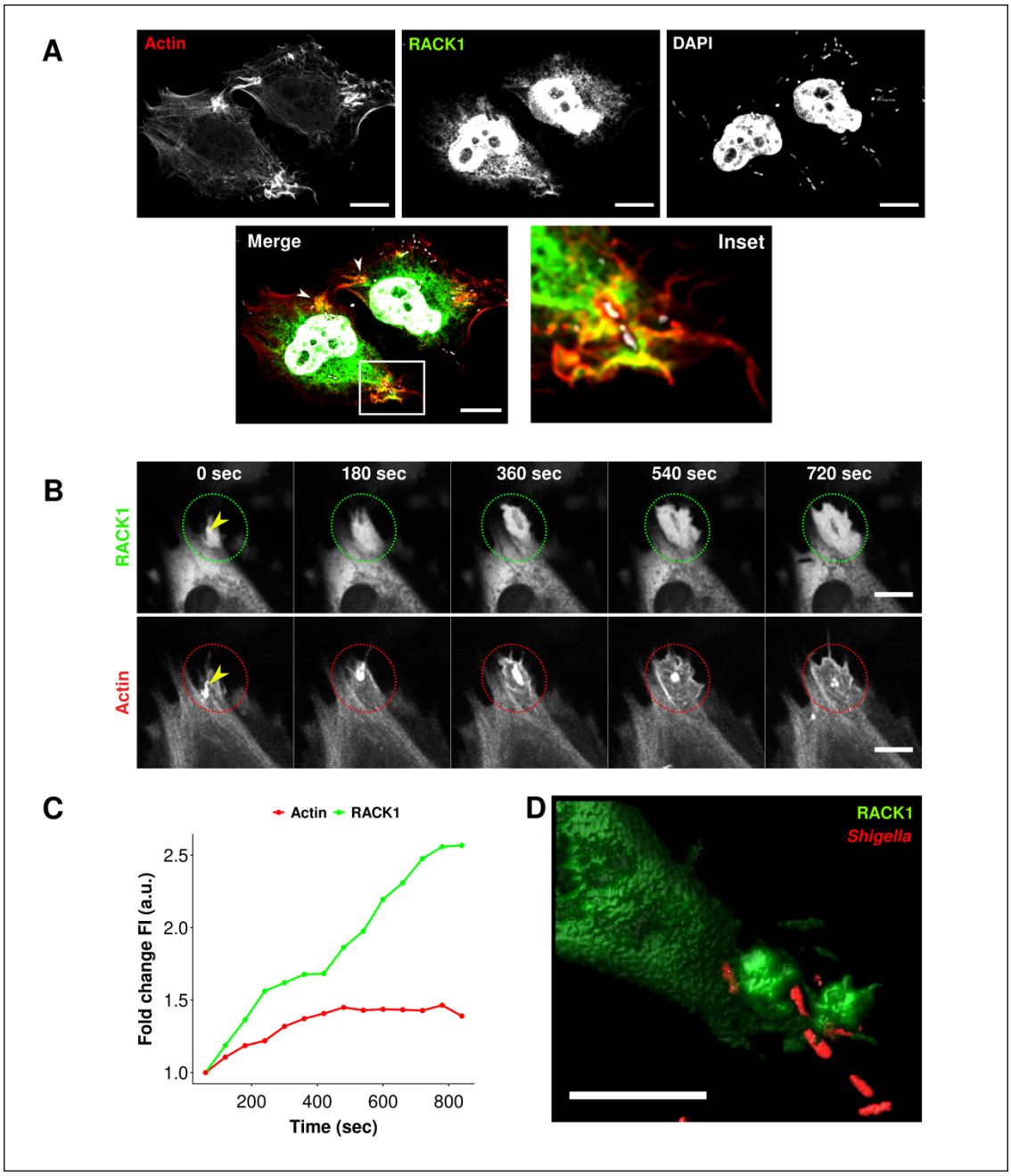
A
Actin
RACK1
DAPI
Merge
Inset
B
0 sec
180 sec
360 sec
540 sec
720 sec
RACK1
Actin
C
Actin
RACK1
Fold change FI (a.u.)
2.5
2.0
1.5
1.0
200
400
600
800
Time (sec)
D
RACK1
Shigella

Figure 3.3.2. RACK1 silencing increases entry foci duration but does not affect foci area or fluorescence intensity.

A. Confocal images from a time-lapse showing actin polymerization to *Shigella*'s entry site. HeLa cells stably expressing F-tractin-GFP (binds to actin, shown in magenta) were infected with dsRED-WT *Shigella* (MOI 10, shown in cyan). Z-stack images (4 slices, 1.2 μm apart) were captured every 2 min with a 63X objective on a Zeiss spinning disk microscope. The figure shows a maximum projection of the original Z-stack. The white dotted-line ovals mark a region of interest (ROI) enclosing the boundaries of the entry focus at its maximum size. Scale bar = 10 μm. **B**-**E**. Analysis of entry foci dynamics. NS and KD-92 cells expressing F-tractin-GFP and infected with dsRED-WT *Shigella* (MOI 10) were imaged as described in A. Entry foci were identified by the profuse recruitment of actin to the site of bacterial entry. **B**. Maximum area of entry foci. As shown in A, the foci area was determined by arbitrarily fitting an oval (ROI) around the foci when it reached its maximum area. Dots inside the boxplot represent individual foci. **C**. Average fluorescence intensity (FI) of entry foci. Actin FI of foci was measured over time within the assigned ROI's area (as shown in A). The FI from each time frame was averaged and normalized by subtracting the lowest FI encountered in each data set (NS and KD-92). Each dot in the boxplot represents the FI of one entry focus. a.u. = arbitrary units. **D**. Graph shows actin FI change over time of the entry foci analyzed in B and C. **E**. Foci duration calculated from the curves shown in D. Numbers under the box plots in B, C and E are the foci analyzed and correspond to one experiment out of three (Supplementary Figure 2, Appendix C). Statistical differences in B, C and E, were calculated by Wilcoxon-test; ns = not significant $p>0.05$, ****$p < 0.0001$.

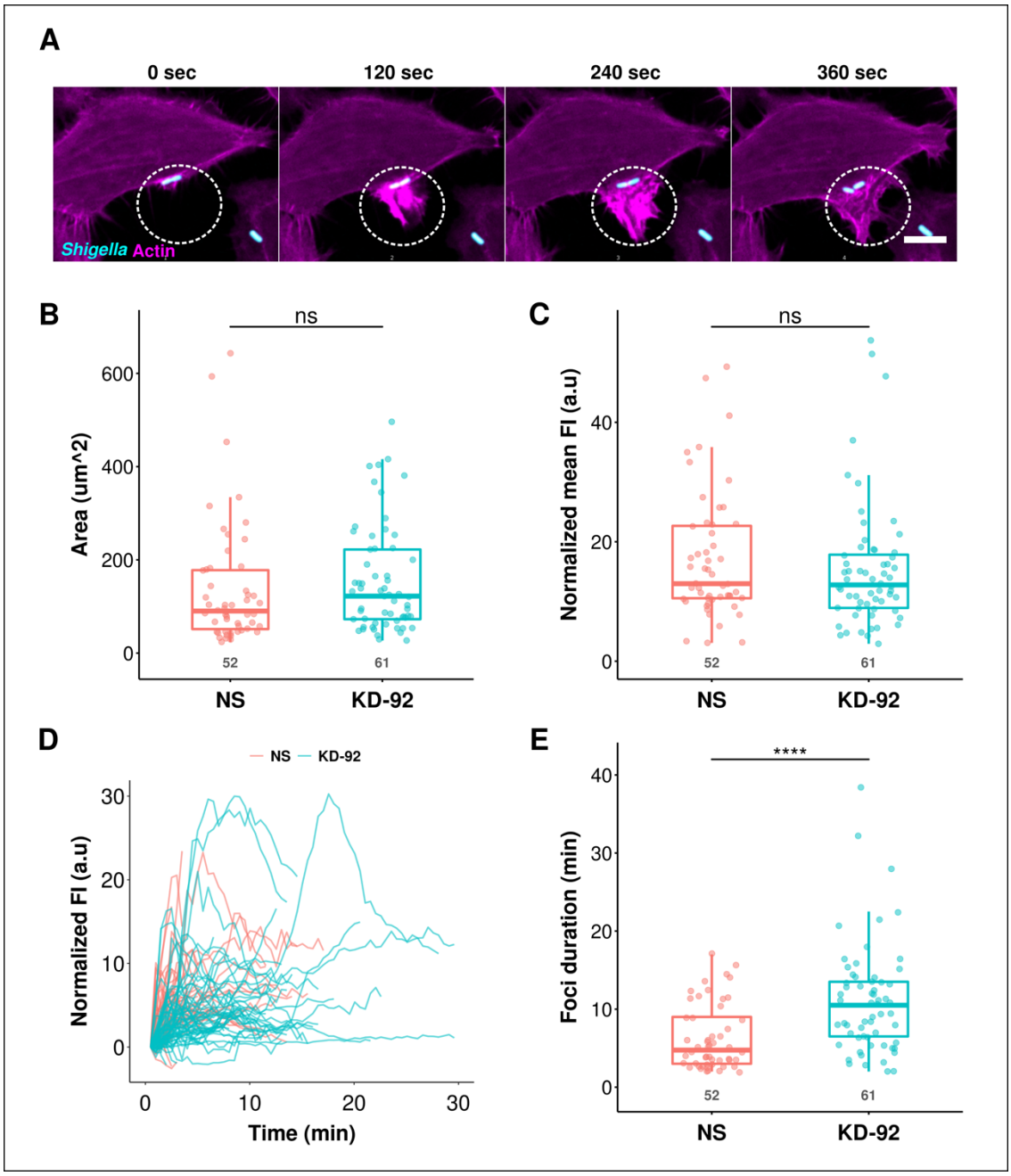
A
0 sec
120 sec
240 sec
360 sec
Shigella Actin
B
ns
Area (um^2)
600
400
200
0
52
61
NS
KD-92
C
ns
Normalized mean FI (a.u)
40
20
0
52
61
NS
KD-92
D
NS
KD-92
Normalized FI (a.u)
30
20
10
0
0
10
20
30
Time (min)
E
****
Foci duration (min)
40
30
20
10
0
52
61
NS
KD-92

Figure 3.3.3. Silencing RACK1 reduces the actin polymerization rate to *Shigella*'s entry focus.

A. Example of the analysis of one entry focus using a logistic model to describe the rate of actin polymerization. Pink dots denote the actual fluorescence intensity (FI) value at each time point. The maximum rate (max. rate) of actin polymerization was calculated as the slope of the fitted curve (blue line). a.u.=arbitrary units **B**. Boxplots showing the maximum rate of actin polymerization to entry foci calculated as described in A. Each dot represents the actin polymerization rate of one entry focus. Numbers under the box plots are the foci analyzed and correspond to one experiment out of three (Supplementary Figure 2, Appendix C). Wilcoxon-test *p < 0.05.

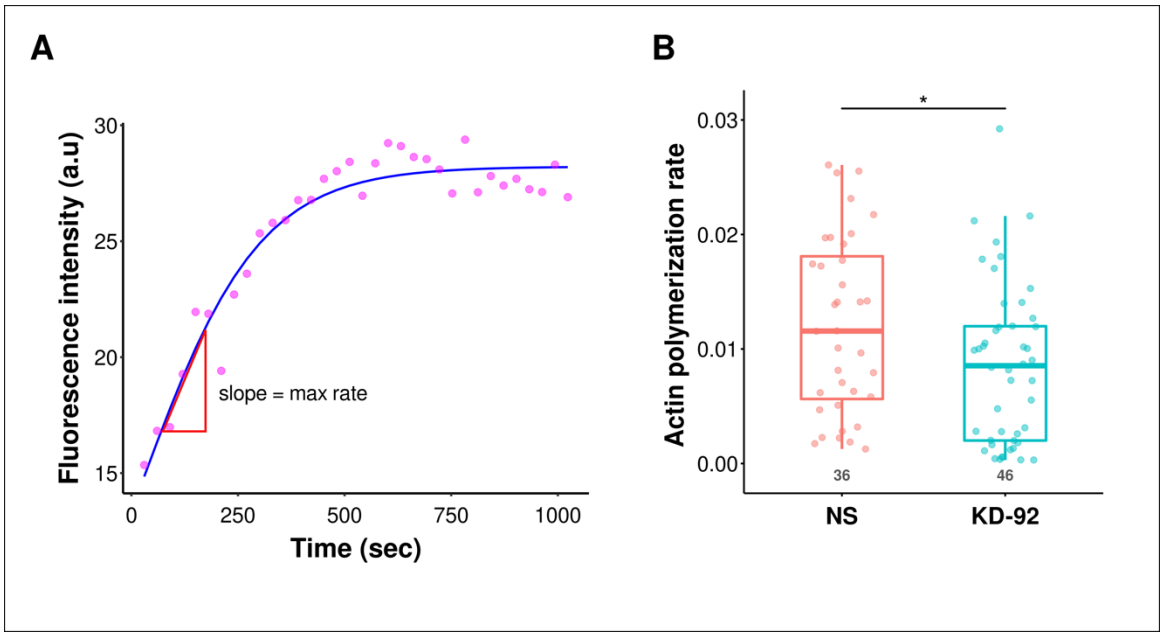

Figure 3.3.4. Knocking down RACK1 expression reduces *Shigella* entry into HeLa cells.

A. Image of a HeLa cell stably expressing F-tractin-GFP (green) and transfected with pOrange-Galectin3 (Gal-3, red). Gal-3 is a marker for vacuole lysis. Damage to the vacuole membrane by *Shigella* triggers the recruitment of Gal-3 around the bacterium (arrowhead). **B** and **C**. Evaluation of *Shigella* entry in Hela cells. RACK1-KD (KD-92) and control (NS) cells transiently co-expressing galectin3-orange and pEGFP-Actin were infected with WT *Shigella* (MOI 50). Images were taken every 1 min for 1.5 h on a Nikon widefield microscope with a 40X objective. **B**. Boxplots depicting percentage (%) of infected cells per field of view. Cells with at least one Gal-3 positive bacterium observed over the course of the video (1.5 h) were considered infected. Each dot represents the % of infected cells found in one field of view (a total of 12 videos for each condition). The total number of cells analyzed from 3 separate experiments is indicated under the plots. Unpaired t-test *$p < 0.05$. **C**. Boxplots show the number of Gal-3 positive bacteria found per cell. Numbers under the boxplots indicate the number of infected cells analyzed and pooled from 3 separate experiments. Statistical differences were calculated with Wilcoxon-test; ****$p < 0.0001$. **D**. Quantification of the number of cells infected with Δ*icsA Shigella*. The Δ*icsA* strain cannot spread from cell to cell, better reflecting the number of infected cells. NS and KD-92 cells expressing F-tractin-GFP were infected with dsRED-Δ*icsA Shigella* for four h and then imaged on a Zeiss widefield AxioObserver with 10X magnification. Error bars are SD from one experiment performed in triplicate. Unpaired t-test ***$p < 0.001$.

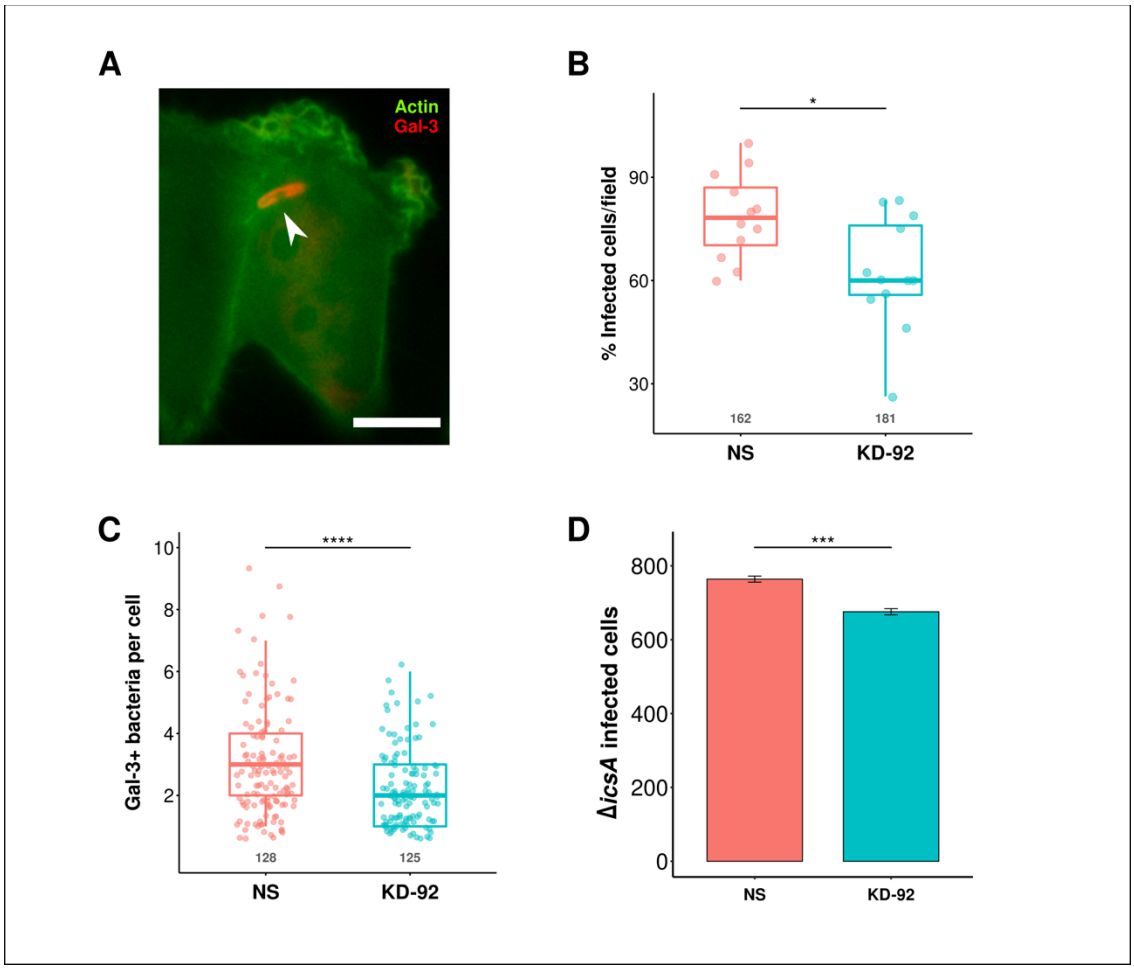
A
Actin
Gal-3
B
*
% Infected cells/field
90
60
30
162
181
NS
KD-92
C
****
Gal-3+ bacteria per cell
10
8
6
4
2
128
125
NS
KD-92
D
***
ΔicsA infected cells
800
600
400
200
0
NS
KD-92

3.4 Study of the role of RACK1 in vacuolar escape

I started by assessing if RACK1 is recruited to *Shigella*-containing vacuole (SCV). Shortly after host cell invasion, *Shigella* damages the endocytic vacuole, triggering the recruitment of Gal-3, after which the bacterium accesses the cytoplasm [157]. Hence, Gal-3 accumulation was used as a vacuolar damage reporter and to visualize the vacuole. RACK1 was immunodetected using anti-RACK1-Alexa-647. Confocal images of *Shigella* infected cells showed that RACK1 did not co-localize with Gal-3+ SCV (Figure 3.4.1 A).

To determine if RACK1 participates in vacuolar escape, RACK1-KD and control (NS) HeLa cells transfected with pOrange-galectin-3 were infected with *Shigella* and analyzed by time-lapse microscopy. The images in Figure 3.4.1 B show a typical sequence of events observed at early infection stages. First, *Shigella* induces actin polymerization at the entry site (marked as entry time, 0 min). Then Gal-3 is recruited to the damaged *Shigella*-containing vacuole (5 min). *Shigella* induces actin polymerization at one pole of the bacterium forming an actin "node" that elongates into an actin tail (10-19 min). As the bacterium becomes motile, it peels off and moves away from the vacuolar membrane remnants (19.5-20.5 min). These events mark significant milestones for *Shigella*'s intracellular life cycle. Thus, they were used to compare infection dynamics in RACK1-KD and NS cells. The vacuolar escape time (Gal-3+ time minus entry time), actin node (node time minus Gal-3+ time), and actin-tail time (actin tail elongation minus Gal-3+ time) were calculated. As shown in Figure 3.4.1 C, there was no significant difference in vacuolar escape time observed in control cells (8.42±5.2 min) and RACK1-KD cells (8.4±5.6 min). Similarly, there was no difference in node time (NS=10.9±7.7 min, KD-92=11.7±7.6 min) and actin tail time (NS=16.6±10.4 min, KD-92=17.7±10.6 min), suggesting that RACK1 is not involved in the early stages of infection that occur after *Shigella* entry foci mediated internalization (Figure 3.4.1 C).

Markers of endocytic trafficking play a vital role in the early step of *Shigella* invasion into epithelial cells leading to vacuolar rupture [154]. Thus, I evaluated if the tethering protein Early Endosomal Antigen 1 (EEA-1) and the Lysosomal-Associated Membrane Protein 1

(LAMP-1) were recruited to the SCV. Consistent with early vacuolar escape, EEA1 association with *Shigella* was rarely found (Figure 3.4.2 A, top row) and LAMP1 was not associated at all with the SCV (Figure 3.4.2 A, middle row). Therefore, these markers were not used for further experiments.

The microtubule-associated protein light-chain 3 (LC3) is an autophagy marker recruited to *Shigella* vacuolar membrane remnants. LC3 targeting leads to autophagosome formation, which captures and degrades the membrane remnants [168]. Confocal images of HeLa cells infected with *Shigella* confirmed LC3 recruitment to *Shigella* (Figure 3.4.2 A, lower row). Given that RACK1 participates in autophagosome biogenesis [285], I thought RACK1 could play a role in recruiting LC3 to the SCV. Therefore, I evaluated LC3 targeting to Gal-3+ SCV and membrane remnants in RACK1-silenced and control HeLa cells. These cells expressed GFP-LC3 and Gal-3-Orange and were infected with WT *Shigella*. Live-cell confocal microscopy confirmed LC3 recruitment to Gal-3+ SCVs. In this experiment, *Shigella* was not fluorescently labeled, but if there was LC3 binding to cytosolic *Shigella* or to the SCV before Gal-3 targeting, an LC3+ bacterial shape should appear. No such structures were observed in any of the videos captured. Only Gal-3+/LC3+ SCVs and membrane remnants were found (Figure 3.4.2 B), suggesting cytoplasmic *Shigella* is not targeted by LC3. The time-lapses also showed that LC3+ structures resembling vesicles were recruited to the LC3+/Gal3+ SCV. These vesicles remained close to the LC3+/Gal3+ membrane remnants after the bacterium exited the vacuole and until the Gal-3 signal disappeared (Figure 3.4.2 B, yellow arrowheads). This approach also demonstrated that LC3 targeted less than 27% of all Gal-3+ SCVs (Figure 3.4.2 C). Furthermore, high variability was observed in the frequency of LC3+/Gal3+ SCVs found in control (NS) cells. Half of the cell population analyzed (2 fields of view) showed around 25% of LC3+/Gal3+ SCV, and the other half showed as low as 10% LC3+/Gal3+ SCVs (Figure 3.4.2 C). Although the differences were not statistically significant, there was a reduction in LC3 recruitment to Gal-3+ *Shigella* in RACK1-KD cells (11.7±3.4%) compared to control (18±9.2%, Figure 3.4.2 C). Although 80 and 57 Gal3+ bacteria were analyzed in the NS and KD-92 cells respectively, it is important to note that these values are the results of only one experiment comprising four fields of view per condition (Figure

3.4.2 C). Thus, more experiments need to be performed to elucidate the role of RACK1 in LC3 targeting and possibly autophagy during *Shigella* infection.

To summarize, the time for *Shigella* to escape the SCV, to form an actin node and the time to start actin tail elongation was not altered in RACK1-silenced cells. Furthermore, RACK1, EEA1 and LAMP1 did not colocalize with the SCV. RACK1 seems to play a role in LC3-tagging of *Shigella*'s vacuole membrane remnants, but the results were not definitive. Thus, I can conclude that RACK1 does not modulate the escape of Shigella from the endocytic vacuole.

Figure 3.4.1. RACK1 does not localize to the *Shigella* containing vacuole and does not affect vacuolar escape.

A. Confocal image of a HeLa cell transfected with pOrange-Galectin3 (Gal-3, red) and infected with WT *Shigella*. The cells were fixed after infection and stained with DAPI (blue) and anti-RACK1-Alexa-647 (green). Scale bar = 10 μm. **B**. Selected widefield images from a time-lapse showing entry, vacuolar escape, and actin tail formation. RACK1-KD (KD-92) and control (NS) HeLa cells transfected with pEGFP-Actin (green) and Gal-3 (red) were infected with WT *Shigella* (MOI 50). Images were taken every 30 sec for 1.5 h on a Nikon Eclipse widefield with a 40X objective. The arrowhead indicates an entry focus at time 0 where profuse actin polymerization can be observed. Gal-3 recruitment to the damaged *Shigella*-containing vacuole (SCV) marks vacuolar escape time (5 min). Actin accumulation in a pole of the bacterium indicates actin node formation (10 min), which gradually elongates, forming an actin tail (13 to 20.5 min). As *Shigella* becomes motile, it peels off Gal-3+ SCV membrane remnants (19.5 min). Scale bar = 5 μm. **C**. Schematization of the successive steps shown in B (top row) and quantification of early infection events (bottom row). Escape time was calculated by subtracting the entry time from the vacuole escape time (left boxplot). The center plot shows the actin node formation time minus vacuole escape time. The right plot shows actin tail elongation minus vacuole escape. Numbers under boxplots represent the number of events evaluated. Statistical significance was determined from three independent experiments combined. Wilcoxon-test; ns = not significant $p>0.05$.

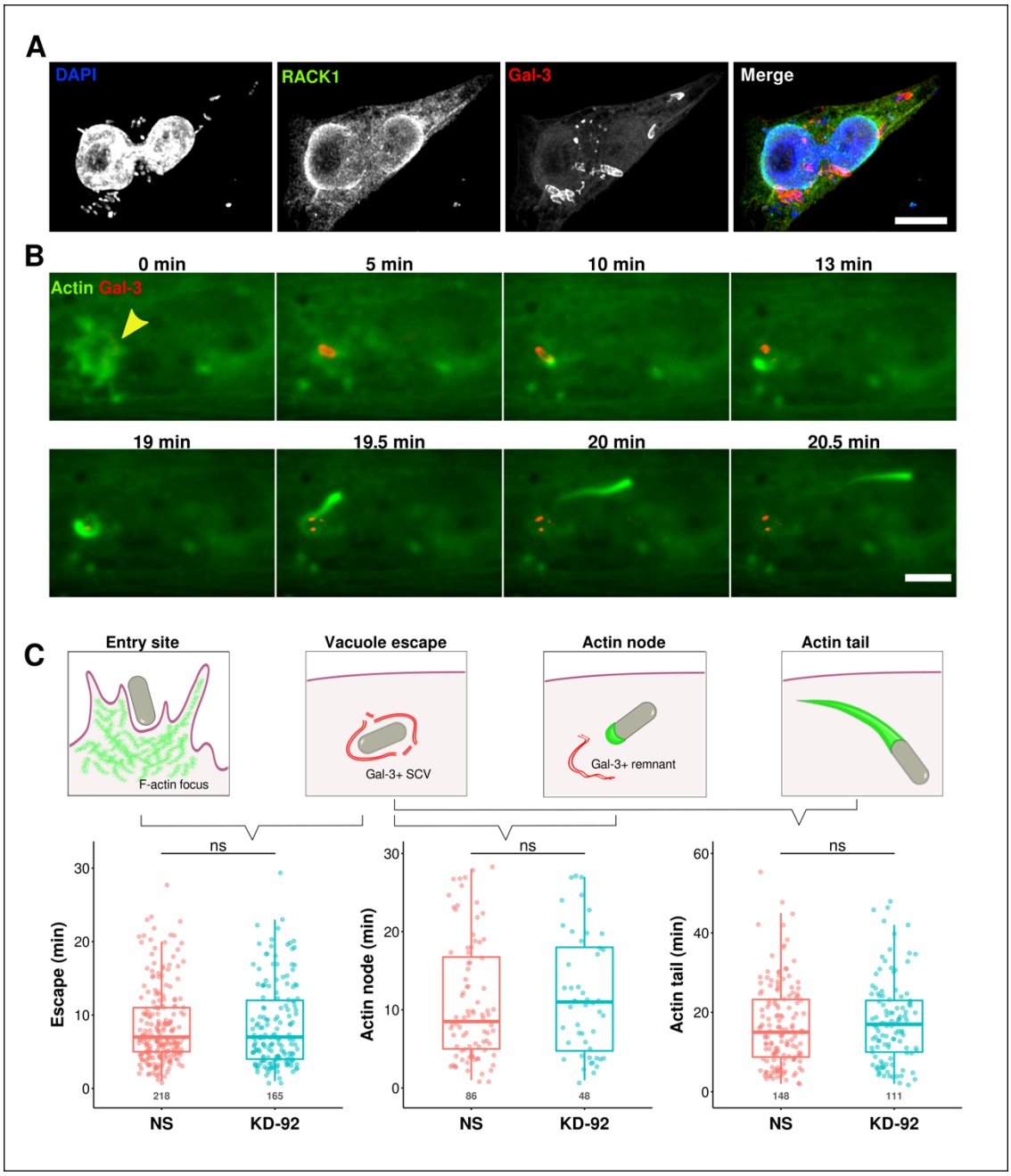
A
DAPI
RACK1
Gal-3
Merge
B
0 min
5 min
10 min
13 min
Actin Gal-3
19 min
19.5 min
20 min
20.5 min
C
Entry site
Vacuole escape
Actin node
Actin tail
F-actin focus
Gal-3+ SCV
Gal-3+ remnant
ns
Escape (min)
Actin node (min)
Actin tail (min)
218
165
86
48
148
111
NS
KD-92

Figure 3.4.2. Evaluation of endocytic markers and LC3 recruitment to *Shigella*.
A. Confocal images of HeLa cells infected with WT *Shigella* (MOI 50) for one h. After fixation, the cells were stained with DAPI (cyan), phalloidin-Alexa-555 (grey) and anti-EEA1, anti-LAMP1 or anti-LC3 (red). Images were captured on the Zeiss 710 confocal. The yellow arrowheads show EEA-1 targeting (top row) and LC3 targeting (bottom row) to one bacterium. Scale bar = 10 μm. **B**. LC3 colocalizes to Gal-3 positive *Shigella*. HeLa cells stably expressing GFP-LC3 and transfected with pOrange-Galectin3 (Gal-3, red) were infected with WT *Shigella*. Z-stacks (17 slices, 0.2 μm) were captured every 1 min for 1.5 h on the Delta vision spinning disk with 60X magnification. The panel shows a maximum projection of time-lapse images where LC3 (green) colocalizes with Gal-3 positive membrane remnants (red) generated when *Shigella* escapes the vacuole. The arrowheads mark LC3+ vesicle-like structures. Scale bar = 5 μm. **C**. RACK1 silencing does not impact LC3 localization to *Shigella*. RACK1-KD (KD-92) and control (NS) HeLa cells co-expressing GFP-LC3 and pOrange-Gal-3 were infected and imaged as described in B. Each dot in the boxplot represents the percentage of double-positive (LC3+ and Gal-3+) *Shigella* found in one field of view from one experiment. Numbers under the plots show the quantity of Gal-3+ bacteria evaluated. Unpaired t-test; ns = not significant $p>0.05$.

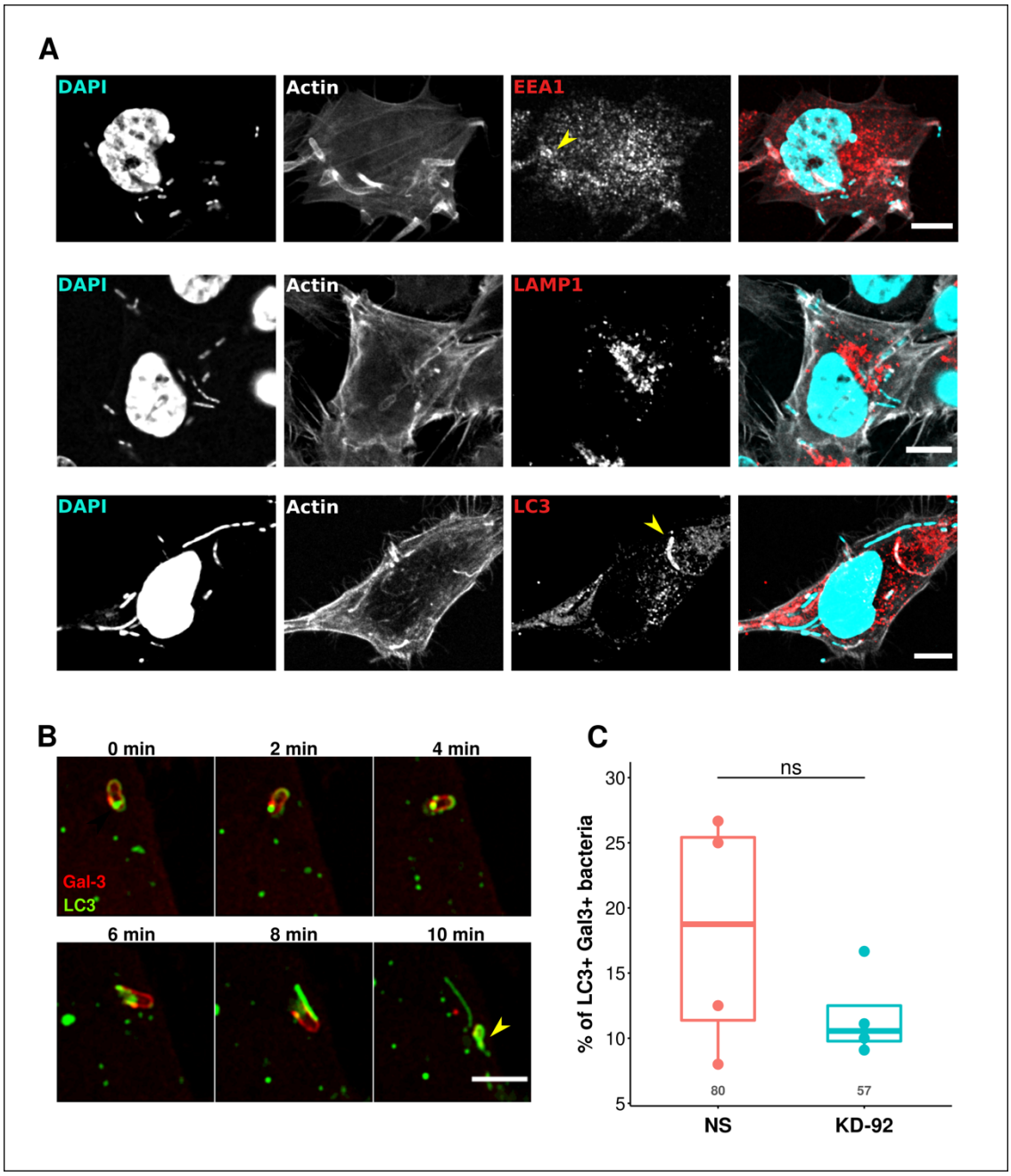
A
DAPI
Actin
EEA1
DAPI
Actin
LAMP1
DAPI
Actin
LC3
B
0 min
2 min
4 min
Gal-3
LC3
6 min
8 min
10 min
C
ns
% of LC3+ Gal3+ bacteria
30
25
20
15
10
5
80
57
NS
KD-92

3.5 Study of RACK1 functions during *Shigella* intracellular replication and cell death induction

The establishment of an intracellular replicative niche requires extensive modulation of host cell functions. After escape into the cytosol, *Shigella* is protected from phagocytic degradation and gains access to many nutrients promoting bacterial replication [394]. However, cytoplasmic *Shigella* faces specific host defence mechanisms. Cell death by apoptosis is a well-established host defence mechanism that eliminates infected cells resulting in pathogen elimination [395]. In this section, I studied the role of RACK1 during *Shigella*'s intracellular replication and cell death inhibition. First, RACK1 recruitment to cytoplasmic *Shigella* was assessed. HeLa cells were infected with fluorescent *Shigella* for 2 h before confocal imaging to ensure enough bacteria had reached the cytoplasm and started replication. The images showed no co-localization between RACK1 and the bacterium (Figure 3.5.1 A). A fluorescence intensity profile, along a line drawn across a bacterium, showed no RACK1 enrichment in the proximity of *Shigella* (Figure 3.5.1 B).

Then, to study the role of RACK1 in intracellular bacterial replication, HeLa cells were infected with the Δ*icsA* mutant. As explained before, *icsA* deletion prevents cell-to-cell spread, thereby simplifying the analysis of intracellular replication. The number of bacteria found inside cells reflects intracellular replication only, not secondary infections. After three hours of infection, HeLa cells appeared full of dsRED-Δ*icsA Shigella* (Figure 3.5.1 C). In most cells, it was difficult to distinguish individual bacterial cells to enumerate them. I addressed this issue by measuring the area occupied by bacterial clusters inside each cell and used this measurement as a proxy for bacterial replication. When comparing RACK1-KD with control cells, no significant differences were found in the area covered by Δ*icsA Shigella* (NS=0.09±0.07 μm^2, KD-92=0.111±0.07 μm^2, Figure 3.5.1 D). I also measured the FI of the bacterial clusters as a complementary measurement to estimate intracellular growth. Similar to the bacterial clusters' area analysis, the FI of bacterial cells showed no significant differences between RACK1-KD and NS cells (NS=171±194 a.u., KD-92=124±115 a.u., Figure 3.5.1 E). These findings indicate that RACK1 silencing does not affect *Shigella* intracellular replication.

Host cell death is an essential immune mechanism against intracellular pathogens. Pathogen-induced cell death may occur by apoptosis (programmed, non-lytic) or necrosis (inflammatory, lytic) [189]. *Shigella* actively controls the timing of epithelial cell death, delaying apoptosis and necrosis to allow enough time for intracellular replication [396]. Given that RACK1 has pro-apoptotic functions [292,397], I evaluated if RACK1 protects HeLa cells from *Shigella*-mediated cell death inhibition. If that is the case, then control cells should have more apoptotic cells upon *Shigella* infection than RACK1-KD cells. Apoptosis and necrosis were measured by flow cytometry using annexin V-FITC and 7AAD double staining. Cells undergoing early and late stages of apoptosis are detected by Annexin V, whereas 7AAD stains necrotic and late apoptotic cells. I evaluated these parameters at various time points (data not shown) and found 12 h post-infection with MOI 10 showed enough apoptotic cells to allow detection of any differences between RACK1-KD and control cells. Most cells in the uninfected NS control sample were alive (>95%, Figure 3.5.2 A, left). Whereas in the infected sample 44.57% of cells were alive, 36.66% were early apoptotic, 10.89% were late apoptotic, and only a small fraction was necrotic (7.89%, Figure 3.5.2 A, right). When analyzing these parameters in RACK1-silenced cells, only KD-95 cells showed a significant reduction in the percentage of late apoptotic cells (Figure 3.5.2 C). No significant differences were observed in necrotic and early apoptotic cells (Figure 3.5.2 B and D). Lastly, *Shigella*-induced cell cytotoxicity was assessed by detecting the release of lactate dehydrogenase (LDH) into the media. Again, no significant differences were found between RACK1-KD and control cells (Figure 3.5.2 E).

Pyroptosis, a different form of pro-inflammatory cell death induced by *Shigella,* facilitates bacterial egress from macrophages and subsequent invasion of enterocytes [50,52]. Once *Shigella* reaches the cytoplasm of epithelial cells, the bacterium is targeted by IFN-γ–induced guanylate-binding proteins (GBPs), which bind the bacterial surface [205]. GBPs promote caspase-4 activation inducing pyroptosis. However, *Shigella* uses the T3SS effector OspC3 to dampen caspase-4 activation, thereby inhibiting pyroptosis [201]. I first evaluated whether RACK1 colocalizes with GBPs and *Shigella* by immunofluorescence. Confocal images showed no co-localization between RACK1 and GBP4 but confirmed

GBP4 targeting of *Shigella* even without IFN-γ induction (Figure 3.5.3 A). Since GBP1 binds directly to LPS, initiating the hierarchical recruitment of GBP4 and other GBPs [205]. I evaluated GBP1 recruitment to *Shigella* in RACK1-KD and control cells treated with IFN-γ after 3 h of infection. Figure 3.5.3 B confirms previously reported GBP1 binding to *Shigella* in IFN-γ induced HeLa cells [205]. Quantification of GBP1+ bacteria showed an expected increment of ~ 7% more GBP1 targeting in NS cells treated with IFN-γ compared to untreated (Table 3.1, Figure 3.5.3 C). In KD-92 cells GBP1 targeting increased from 2.2% in untreated cells to 15.6% in IFN-γ treated cells (~13% more, Table 3.1). However, there were no significant differences in GBP1 targeting between RACK1-KD cells and control (NS) cells even after IFN-γ induction (Figure 3.5.4 C). Treatment with Ruxolitinib, an IFN-γ signalling inhibitor, did not alter GBP1 recruitment to *Shigella* in either cell line (Figure 3.5.3 C).

The results presented in this section showed that RACK1 silencing did not affect *Shigella*'s intracellular replication. RACK1 was not enriched around cytoplasmic *Shigella* and when evaluating Δ*icsA* replication within HeLa cells, no difference was found in the area occupied by Δ*icsA Shigella* in RACK1-KD and control cells. WT *Shigella* induced apoptosis in HeLa cells after 12 h of infection. However, RACK1 silencing did not affect apoptosis induction except for the KD-95 cell line that showed fewer apoptotic cells. Likewise, no differences were found in *Shigella*-induced LDH release. Furthermore, GBP1 and GBP4 recruitment to cytoplasmic *Shigella* was not affected by RACK1 silencing. Therefore, I conclude that *Shigella's* intracellular replication and modulation of host cell death is not mediated by RACK1.

Table 3.1. Percentage of *Shigella* targeted by GBP1 in control (NS) and RACK1-KD (KD-92) HeLa cells treated with IFN-γ or Ruxolitinib (RUX).

Condition	%GBP1+ *Shigella**	Standard deviation	Total bacteria analyzed
NS/untreated	3.9	1.6	1523
NS/IFN-γ	11	2.6	1192
NS/RUX	3.7	2.2	1522
KD-92/untreated	2.2	1.6	1368
KD-92/IFN-γ	15.6	4.8	849
KD-92/RUX	4.2	2.3	906

*Percentages are from three replicates of one experiment.

Figure 3.5.1. RACK1 does not play a role in *Shigella*'s intracellular replication.
A. Average projection micrograph showing a HeLa cell infected with *Shigella*. Two h post-infection with dsRED-WT *Shigella* (MOI 10, red), the cells were fixed and immunolabeled with anti-RACK1-Alexa-647 (grey). Z-stacks images (15 slices, 0.25 µm apart) were captured on a Leica SP8 confocal with a 63X objective. A yellow segment marks the area measured in the intensity profile shown in B. The dotted blue line highlights the cell's area. Scale bar = 10 µm. **B**. Line intensity profile to analyze RACK1 localization around *Shigella*. The graph shows fluorescence intensity (FI) values in the line segment drawn across a bacterium (yellow line in A) for dsRED and RACK1 channels. The dotted blue line marks the average FI of RACK1 in the whole cell area (shown in A). **C**-**E**. Control (NS) and RACK1-KD (KD-92) HeLa cells stably expressing F-tractin-GFP were infected with dsRED-Δ*icsA Shigella* (MOI 10) for three h before fixing. Z-stacks (6 slices 0.8 µm) were captured at 63X magnification with a Zeiss LSM 880 confocal. **C**. Maximum projection micrograph showing an NS HeLa cell infected with Δ*icsA Shigella*. Scale bar = 15 µm. **D**. Quantification of Δ*icsA Shigella* intracellular growth. Δ*icsA* replicated rapidly to high numbers making individual bacteria enumeration impractical. Thus, the area covered by bacteria on each cell was quantified instead. Each dot represents the area of bacteria quantified in one cell. **E**. Quantification of the total bacterial fluorescence intensity (FI) per cell. FI was used as a proxy to evaluate Δ*icsA Shigella* growth. Dots represent the sum of bacterial FI found on each cell. Numbers under the boxplots in D and E are the number of cells analyzed from two separate experiments. Wilcoxon test; ns = not significant $p>0.05$.

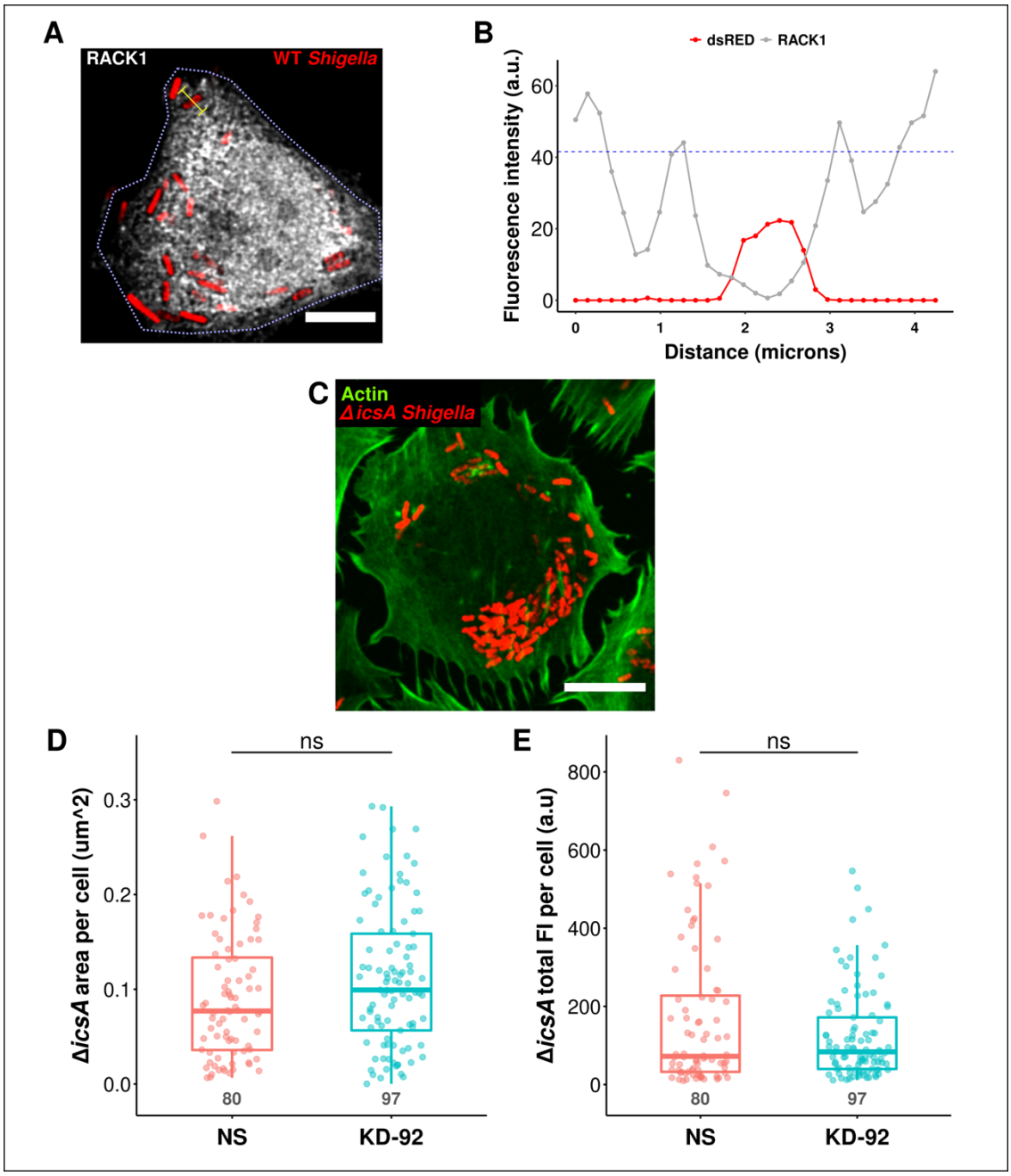
A
RACK1
WT Shigella
B
dsRED
RACK1
Fluorescence intensity (a.u.)
60
40
20
0
0
1
2
3
4
Distance (microns)
C
Actin
ΔicsA Shigella
D
ns
ΔicsA area per cell (um^2)
0.3
0.2
0.1
0.0
80
97
NS
KD-92
E
ns
ΔicsA total FI per cell (a.u)
800
600
400
200
0
80
97
NS
KD-92

Figure 3.5.2. Silencing of RACK1 expression does not affect Shigella-induced cell death.

A-D. RACK1-KD (KD-92, KD-94, KD-95) and control (NS) HeLa cells were infected with dsRED-WT *Shigella* (MOI 10) for 12 h. Uninfected cells were used to measure basal levels of apoptosis. Apoptosis was measured by flow cytometry using annexin V-FITC and 7AAD double staining. **A.** Pseudocoloured density plots showing uninfected (right) and infected (left) single-cell events found in NS cells. In each plot quadrant, top-left shows necrotic cells (annexin−, 7AAD+); top-right shows late apoptotic cells (annexin+, 7AAD+); bottom-left shows viable cells (annexin−, 7AAD−), and bottom-right shows early apoptotic cells (annexin+, 7AAD−). Bar graphs show fold change of early apoptotic (**B**), late apoptotic (**C**) and necrotic (**D**) cells found in infected RACK1-KD cells over uninfected control. Results represented as mean ± SD of four independent experiments. More than 10,000 events per cell line were analyzed in each experiment. Unpaired t-test; ns = not significant $p>0.05$, *$p<0.05$. **E**. Evaluation of cytotoxicity induced by *Shigella*. LDH release was analyzed in supernatants collected from the cells infected as described in A-D. The bar plot shows the mean ± SD of three independent experiments. Unpaired t-test; ns = not significant.

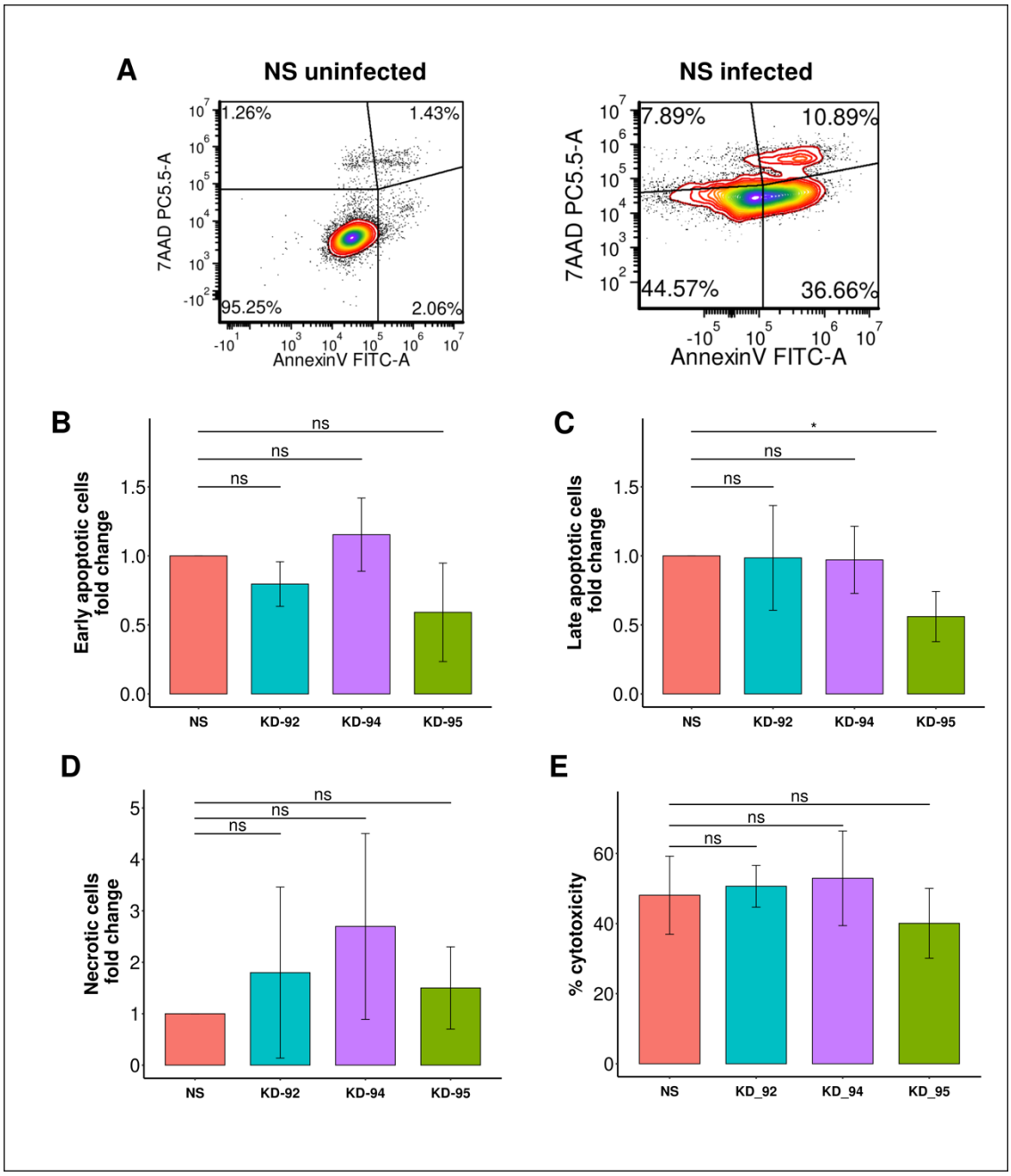
A
NS uninfected
NS infected
7AAD PC5.5-A
AnnexinV FITC-A
1.26%
1.43%
95.25%
2.06%
7.89%
10.89%
44.57%
36.66%
B
Early apoptotic cells fold change
C
Late apoptotic cells fold change
D
Necrotic cells fold change
E
% cytotoxicity
ns
*
NS
KD-92
KD-94
KD-95
KD_92
KD_94
KD_95

Figure 3.5.3. Targeting of *Shigella* by guanylate-binding protein (GBP) 1 and 4 is not affected by RACK1 silencing.

A. Confocal micrographs of a HeLa cell infected with WT *Shigella* (MOI 10). Cells infected for three h were fixed and stained with DAPI (blue), anti-RACK1-Alexa-647 and anti-GBP4. The image was captured on a Leica SP8 confocal with 63X magnification. Scale bar = 10 µm. **B**. Confocal micrograph of a HeLa cell infected with WT *Shigella*. The cells were treated with Interferon-gamma (IFN-γ, 1 ng/mL) for 16 h before *Shigella* infection. After three h of infection, the cells were fixed and stained with DAPI, anti-GBP1 and phalloidin-Alexa-555. The micrograph was captured on the Zeiss 880 confocal with 63X magnification. Scale bar = 10 µm. **C**. Quantification of GBP1 positive *Shigella*. Control and RACK1-KD HeLa cells stably expressing F-tractin-GFP were treated with IFN-γ (1 ng/mL), Ruxolitinib (RUX, 1 µM) for 16 h or left untreated. The cells were subsequently infected with WT *Shigella* (MOI 50) for three h, fixed, and stained with DAPI and anti-GBP1. Z-stacks (5 slices, 0.5 µm apart) were captured at 63X magnification on a Zeiss 880 confocal. The bar plot shows the mean ± SD of one experiment in triplicate, where more than 900 bacteria were counted per group. Statistical significance was tested using a two-way analysis of variance (ANOVA) followed by Tukey HSD (Honest Significant Differences) for multiple pairwise-comparison between group means. Only significant differences are shown; **p<0.01, ****p<0.0001.

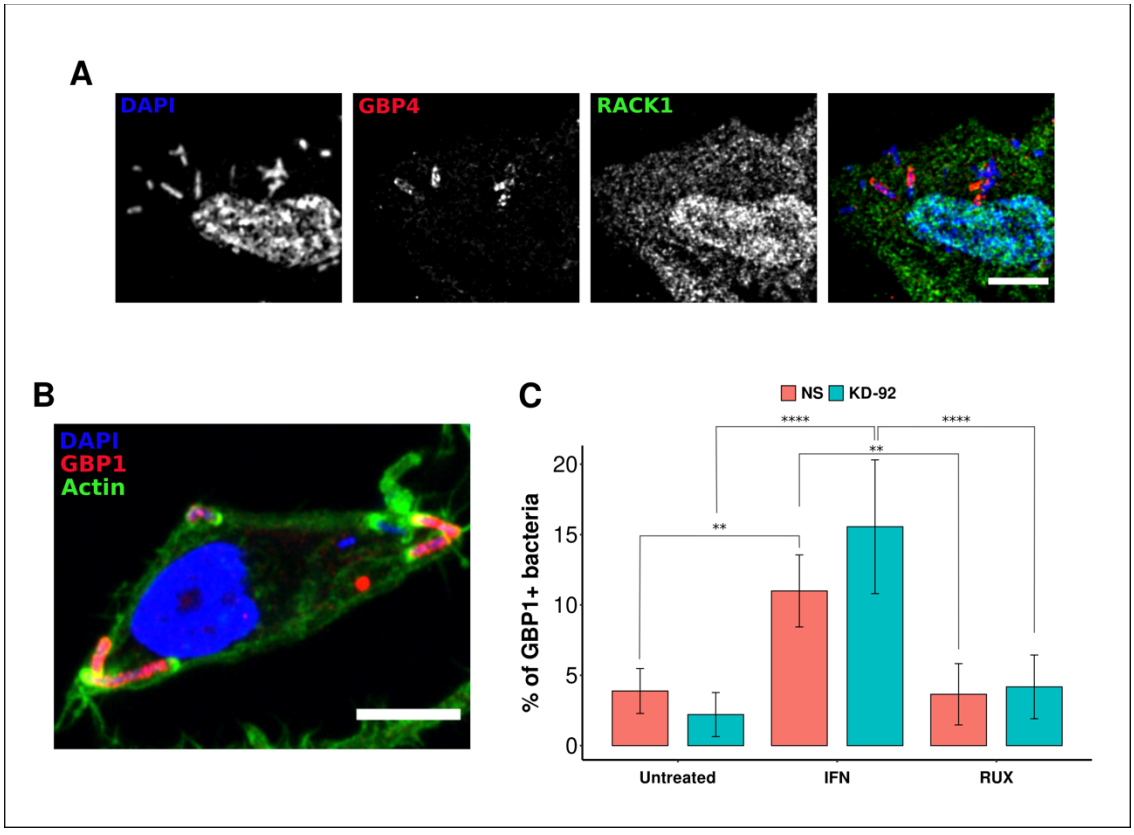

3.6 RACK1 silencing affects actin tail polymerization

Given that RACK1 was involved in actin polymerization during *Shigella* invasion of HeLa cells, I sought to investigate the role of RACK1 in actin tail formation. First, I evaluated whether RACK1 is recruited to *Shigella*'s actin tail. After careful analysis of various experiments, including live microscopy of cells expressing RACK1-GFP (data not shown) and confocal imaging of fixed samples, no co-localization between the actin tail and RACK1 was found (Figure 3.6.1 A). Since RACK1 and actin are recruited to the entry focus without clear colocalization, I thought RACK1 could promote actin tail polymerization even though it does not colocalize with the tail. The effect of RACK1 silencing on actin tail polymerization was evaluated by infecting control and RACK1-KD HeLa cells expressing F-tractin-GFP (binds F-actin) with dsRED-WT *Shigella* for three h to allow actin tail formation. As suspected, many *Shigella* inside control cells had polymerized an actin tail, while in KD-92 cells, most *Shigella* appeared untailed (Figure 3.6.1 B). Quantification of tailed and untailed bacteria confirmed this observation. A bacterium was counted as tailed when the actin tail was elongated; bacteria with actin nodes were not considered tailed (see figure 3.4.1 B-C for reference on the actin node). On average, 42.4% (±15.1%) of bacteria were associated with an actin tail in control cells, the percentage of tailed bacteria was 41.5% less in KD-92 cells (24.8±12.5%, Figure 3.6.1 C). These findings indicate that RACK1 promotes for actin tail polymerization.

Furthermore, I quantified the area and FI of the actin tails. For this analysis, all actin structures associated with *Shigella* were manually outlined, including actin nodes, and short and long actin tails. The tails' area among *Shigella* infecting RACK1-KD cells was significantly reduced compared with tails formed in control cells. On average, actin tails in control cells were 3.89±3.21 μm^2 while in KD-92, they were 1.97±1.7 μm^2 (Figure 3.6.1 D). Nevertheless, the average fluorescence intensity of the tails was similar in both conditions (NS=3.28±2.1 a.u., KD-92=3.2±1.8 a.u., Figure 3.6.1 E). I analyzed if there was any correlation between the area and the average FI of the tails. Interestingly, in KD-92 cells the area of the tails showed a weak negative correlation to the FI ($r= -0.22$, $p=0.0003$),

thus smaller tails showed a slight tendency to be brighter (Figure 3.6.1 F). The correlation was not significant in NS cells ($r = -0.11$, $p = 0.08$, Figure 3.6.1 F).

Analysis of the tail's area does not provide information about the tail's shape. For example, a long and thin tail could have the same area as a short and thick tail. I wanted to know if RACK1 silencing, apart from inducing a reduction of tailed bacteria, also affected the shape of the tails. Therefore, I used the shape descriptors circularity and Feret's diameter to evaluate *Shigella*'s tail shapes. The Feret's diameter was defined as the longest distance between two points along the tail's boundary (Figure 3.6.2 A). Actin tails formed in NS cells (4.91±3.2 μm) had a significantly higher Feret's diameter than tails in KD-92 cells (3±1.9 μm), indicating that actin tails are longer in control cells (Figure 3.6.2 A). Similar results were obtained when testing tail circularity. This shape parameter measures the level of roundness. A circularity value of 1.0 describes a perfect circle, whereas values closer to 0.0 indicate an elongated shape. Most of the actin tails polymerized in NS cells had a circularity value lower than 0.25, which indicates an elongated shape (Figure 3.6.2 C). Whereas in RACK1-KD cells, two populations of tails were found. A small population of elongated tails (circularity ~0.3) and a second larger population with a more rounded shape (circularity ~0.6, Figure 3.6.2 C). In sum, these analyses showed fewer bacteria associated with actin tails in RACK1-KD cells, and these tails were smaller and less elongated than the tails formed in control cells.

To explore the actin tail defect observed in RACK1-KD cells, I evaluated bacterial motility by live-cell imaging. I reasoned that a reduction in the number of tails and polymerization of shorter tails should directly impact intracellular motility. To assess this, F-tractin-GFP-HeLa cells (NS and KD-92) infected with *Shigella* were imaged every 60 sec for two h. Bacteria movements were manually tracked (trajectories), as explained in Figure 3.6.3 A. Briefly, a series of x,y coordinates were manually recorded at every time frame in the time-lapse movie. Using these data points, distance and speed were calculated for every segment on each trajectory (Figure 3.6.3 A). Visual inspection of the tracks displayed in an x,y coordinate plot (starting point 0,0) readily showed distinct patterns in the bacterial trajectories recorded in NS and KD-92 cells (Figure 3.6.3 B). *Shigella*

trajectories in control cells were more linear and appeared more dispersed from the center of the plot than trajectories in RACK1-KD cells (Figure 3.6.3 B). The trajectories' colours in Figure 3.6.3 B reflect the mean speed of the trajectories ranging from dark blue (slow) to red (fast). Most trajectories in the control cells were light blue to yellow, indicating more rapid movements than the trajectories found in KD-92 cells, which were mostly dark blue. On average, the speed of *Shigella* in NS cells was 0.045±0.021 μm/sec, whereas the speed in RACK1-KD cells was 0.03±0.021 μm/sec (Figure 3.6.3 B-C).

Parameters such as sinuosity index and directional change have been applied to characterize movement paths of animals and bacteria [398,399] The sinuosity index describes a trajectory's tortuosity, integrating changes of direction and step lengths (distance) between them. A trajectory with a low sinuosity index indicates a more direct trajectory than one with a high index. Longer trajectories are inevitably more tortuous than very short trajectories. Therefore, sinuosity was calculated only for trajectories with lengths between 30 to 80 μm. Surprisingly, *Shigella* trajectories were significantly more tortuous in RACK1-KD cells (0.81±0.26) than in control cells (0.71±0.23, Figure 3.6.3 D). Directional change (DC) indicates how much (in degrees) the bacterium changes its direction of movement. DC differs from sinuosity as it is based solely on direction changes and does not take step length into account. Although no significant differences were found in the DC of trajectories in control and RACK1-KD cells, the data showed high variability in *Shigella*'s trajectories ranging from straight (mostly linear, DC= 5.8°/min) to convoluted (non-linear, 37.2°/min), with an average DC of 21.6±6.1°/min in control cells (Figure 3.6.3 E).

The large variability in DC values observed in *Shigella* trajectories prompted the analysis of tumble events. Tumbles are stop events characteristic of bacterial motility that result in an erratic change of the trajectory's direction [400]. Tumbling events in *Shigella*'s trajectories were identified by setting a minimum speed threshold (0.02 μm/sec). Figure 3.6.3 F shows two representative *Shigella* trajectories of similar length from NS and KD-92 cells, highlighting tumbling events (black outlined dots). The NS trajectory has fewer stop events (6 stops out of 14 steps) than the KD-92 (10 stops out of 17 steps) trajectory

(Figure 3.6.3 F). Interestingly, tumbling events were followed by a decrease in speed (more than one tumble) without abrupt changes in the direction of movement in both trajectories (Figure 3.6.3 F). Analysis of run events (speed > 0.02 μm/sec) followed by one or more tumbles showed that *Shigella* trajectories in RACK1-KD cells are interrupted by significantly longer pauses (more than one tumble) compared with control cells (Figure 3.6.3 G). On average, *Shigella* expends 3.6±3 min tumbling in control cells; this time doubled in KD-92 cells (6.6±5 min, Figure 3.6.3 G). During trajectory recording, I observed that bacterial motility stops when *Shigella* loses or reduces the length of its tail (data not shown). To resume movement, *Shigella* must induce actin tail polymerization again. Thus, longer tumbling events are consistent with the actin-tail polymerization defect found in RACK1-KD cells (Figures 3.6.1 C and 3.6.3 G).

In summary, *Shigella* polymerized fewer actin tails in RACK1-KD cells, which were smaller and less elongated than in control cells. Thereby, *Shigella* moved at a slower speed. RACK1 silencing also increased the time *Shigella* expended tumbling due to actin-tail shortening or actin-tail loss. Prolonged tumbling made the trajectories more convoluted (higher sinuosity). These experiments showed that RACK1 promotes *Shigella* actin-tail polymerization and perhaps also to re-polymerize (or maintain) the tail to resume movement after tumbling events.

Figure 3.6.1. RACK1 does not localize to *Shigella*'s actin tail, but it promotes actin tail polymerization.

A. Photomicrograph of a HeLa cell stably expressing F-tractin-GFP infected with dsRED-WT *Shigella* (cyan). After fixation, the cells were immunolabeled with anti-RACK1-Alexa-647 (green) and imaged with a Leica SP8 confocal. A bacterium associated with a long actin tail (magenta) is visible at the center of the cell. **B-F**. RACK1-KD (KD-92) and control (NS) HeLa cells expressing F-tractin-GFP were infected with dsRED-WT *Shigella* (MOI 10) for three h and then fixed. Z-stacks (6 slices, 1.2 µm) were acquired at 63X magnification on a confocal Zeiss 880. **B.** Representative confocal images of control (NS) and RACK1-KD (KD-92) cells infected with dsRED-WT *Shigella*. Green arrowheads indicate bacteria (cyan) associated with actin tails (magenta). **C.** Percentage of tailed *Shigella* per field. Each dots represent the percentage of tailed bacteria found per field of view (image). Numbers under the boxplots are total bacteria counted, pooled from four separate experiments. Unpaired t-test **$p < 0.01$. The tails' area (**D**) and mean fluorescence intensity (FI; **E**) were determined by manually outlying actin tails. Dots inside the box plots un number underneath represent individual tails pooled from three separate experiments. Wilcoxon-test; ns = not significant $p>0.05$, **** $p < 0.0001$. **F**. Linear correlation analysis between area and FI of the tails shown in D and E. Regression lines are shown for each group. r = Pearson's correlation coefficient.

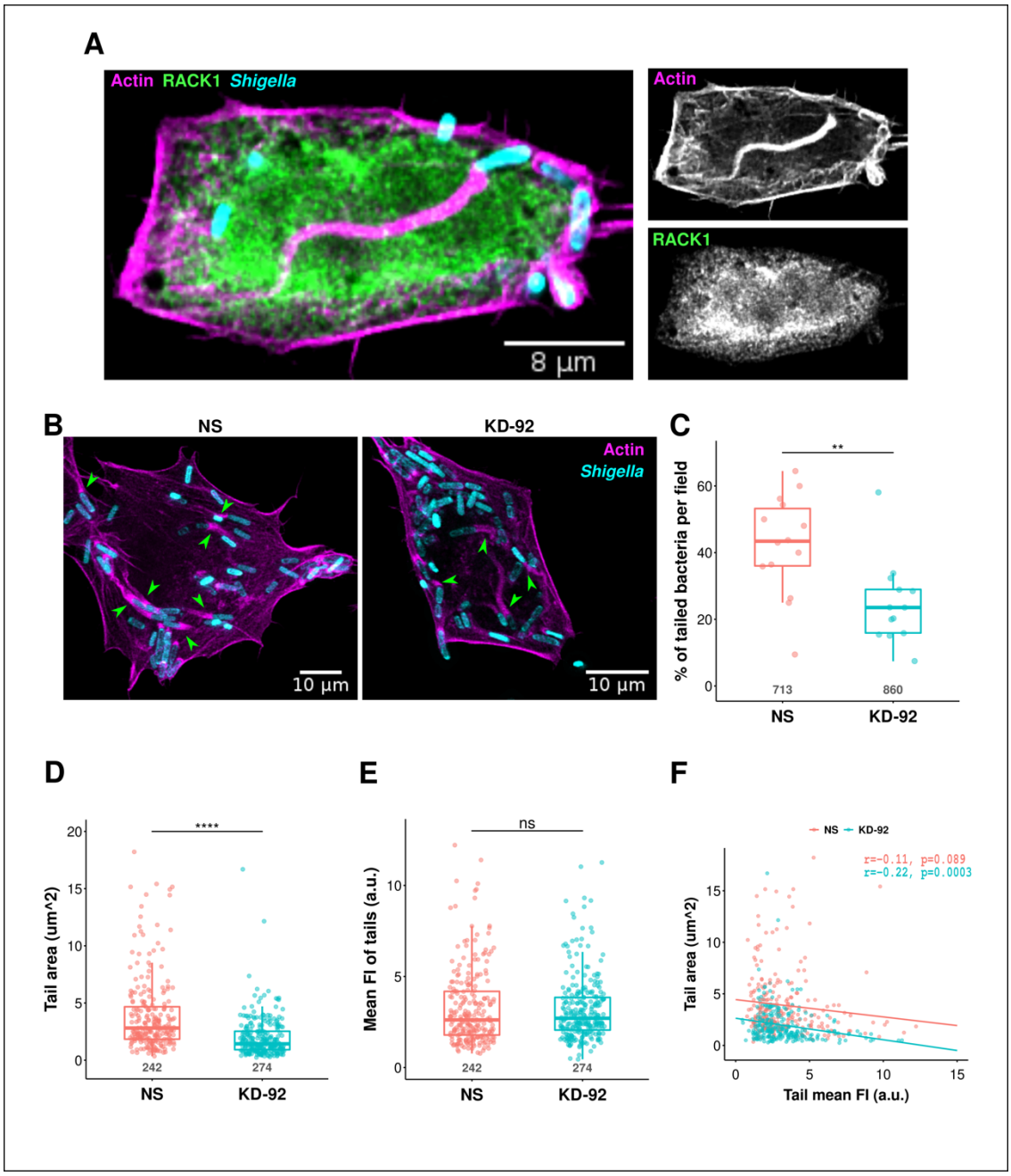
A
Actin RACK1 Shigella
8 µm
Actin
RACK1
B
NS
KD-92
Actin
Shigella
10 µm
10 µm
C
**
% of tailed bacteria per field
713
860
NS
KD-92
D
****
Tail area (um^2)
242
274
NS
KD-92
E
ns
Mean FI of tails (a.u.)
242
274
NS
KD-92
F
NS KD-92
r=-0.11, p=0.089
r=-0.22, p=0.0003
Tail area (um^2)
Tail mean FI (a.u.)

Figure 3.6.2. RACK1 silencing impairs actin tail elongation.
A-C. RACK1-KD (KD-92) and control (NS) HeLa cells expressing F-tractin-GFP were infected with dsRED-WT *Shigella* (MOI 10) for three h and then fixed. Z-stacks (6 slices, 1.2 µm) were acquired at 63X magnification on a confocal Zeiss 880. Actin tails were manually outlined using Fiji software. **A**. Schematic of Feret's diameter calculation. Feret's diameter is the longest distance between two points along a region of interest boundary. Diagrams of bacteria with short (top) and long (bottom) actin tails are shown. Outlines of the actin tails are presented on the right. The red segments represent Feret's diameter. **B**. Boxplots showing the Feret's diameter of actin tails calculated as shown in A. Dots inside the boxplot and number underneath represent actin tails analyzed from three separate experiments. **C**. Density plot of actin tails circularity. Circularity was calculated with *circularity = 4pi(area/perimeter^2)*. A circularity value of 1.0 indicates a perfect circle. As circularity approaches 0.0, it indicates an increasingly elongated shape. Diagrams of bacteria exemplify tail shapes with high (right) and low (left) circularity. n = number of tails analyzed. Dashed lines indicate means. Statistical differences in B and C were calculated with Wilcoxon-test; **** $p < 0.0001$.

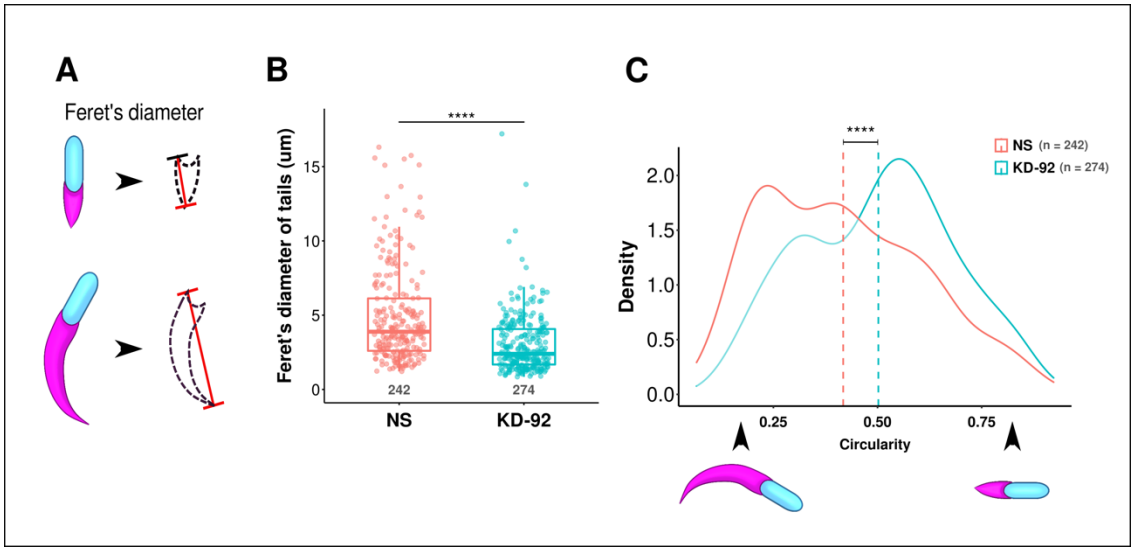

Figure 3.6.3. Knocking down RACK1 expression reduces *Shigella*'s actin-mediated motility.

A. Schematics illustrating trajectory tracking. A typical *Shigella* (cyan) trajectory displays multiple direction changes and actin-tail (magenta) lengths. Bacterial positions were recorded as x,y coordinates (black dots inside bacteria) in every time frame (equal time intervals). The distance between two points was calculated as $d = \sqrt{(x2 - x1)^2 + (y2 - y1)^2}$. The black arrow indicates movement direction, and the red arrow indicates time progression. Distance and time were used to calculate segment speed. **B-G**. F-tractin-GFP control (NS) and RACK1-KD (KD-92) HeLa cells were infected with dsRED-WT *Shigella*. Z-stack images (5 slices, 1 µm) were captured every 60 sec for two h on a Zeiss spinning disk with 63X magnification. Bacterial trajectories were manually tracked, as explained in A, using Fiji and characterized using the "trajr" package in R (see methods section 2.11.4 for details). **B**. *Shigella* trajectories in NS (left) and KD-92 (right) cells. Trajectories were shifted to originate from point (0,0) in the coordinate plot. Colours represent trajectories' mean speed (µm/sec). **C**. Trajectories' mean speed. Dots inside the boxplots and numbers underneath represent trajectories analyzed from three experiments. Wilcoxon-test; **** $p < 0.0001$. **D**. Sinuosity index of *Shigella* trajectories. The sinuosity index describes how tortuous a trajectory is. A low index indicates a more direct trajectory. Trajectories with lengths between 30 to 80 µm were analyzed (n below boxplots). The dots show trajectories' indexes from three independent experiments. Unpaired t-test; ** $p < 0.01$. **E**. Trajectories' mean directional change (DC). The DC of each pair of consecutive points in a trajectory was measured to calculate the mean DC. The trajectories analyzed were the same as shown in D (n below boxplots). **F**. Example of two bacterial trajectories from NS and KD-92 cells. Dots are x,y positions with equal time frame intervals. Segments represent the distance between two points. Black outlined dots indicate positions where the speed was lower than 0.02 µm/sec (tumbling). **G**. Trajectories tumble time. The tumble analysis identified transitions between high-speed movements to slow movements. A minimum speed threshold of 0.02 µm/sec was defined to identify trajectory segments where bacterial motility was slow (tumbling). Trajectories with one or more tumbling events were selected, and the mean time bacteria remained in this stationary state was quantified. Dots are trajectories from three experiments. Numbers under boxplots represent trajectories with one or more tumble events. Wilcoxon-test; **** $p < 0.0001$.

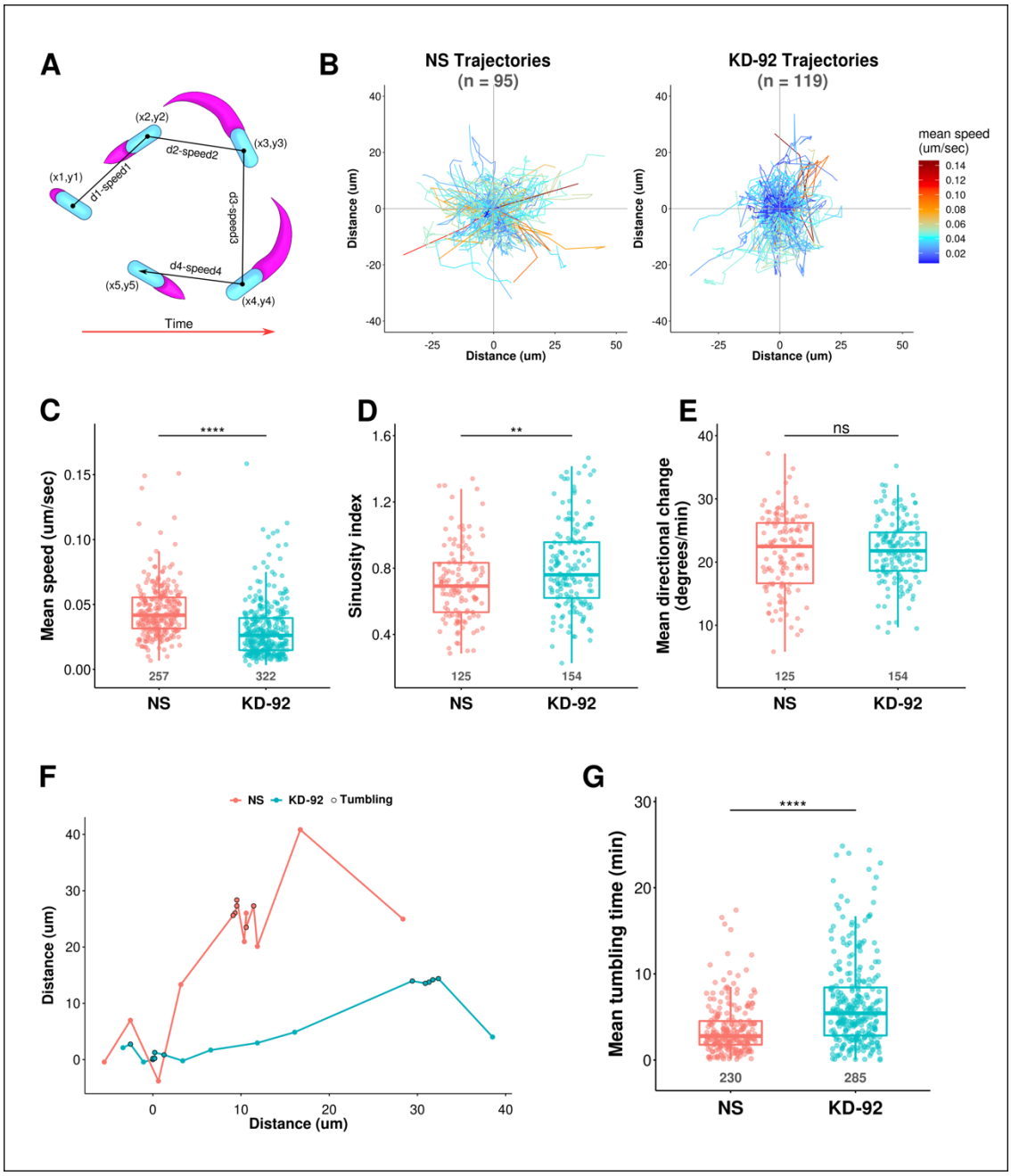
A
(x1,y1)
(x2,y2)
(x3,y3)
(x4,y4)
(x5,y5)
d1-speed1
d2-speed2
d3-speed3
d4-speed4
Time
B
NS Trajectories
(n = 95)
KD-92 Trajectories
(n = 119)
Distance (um)
mean speed
(um/sec)
0.14
0.12
0.10
0.08
0.06
0.04
0.02
C
Mean speed (um/sec)
****
257
322
NS
KD-92
D
Sinuosity index
**
125
154
NS
KD-92
E
Mean directional change
(degrees/min)
ns
125
154
NS
KD-92
F
NS
KD-92
Tumbling
Distance (um)
G
Mean tumbling time (min)
****
230
285
NS
KD-92

3.7 RACK1 silencing inhibits *Shigella* cell-to-cell spreading

Shigella relies on actin-tail polymerization for bacterial motility within infected cells and cell-to-cell spreading. When tailed bacteria reach the cell's periphery, they push the membrane out, forming *Shigella*-containing membrane protrusions that extend into adjacent cells. These protrusions are subsequently endocytosed by neighbouring cells resolving into double-membrane vacuoles, from which *Shigella* escapes [215]. Therefore, I assessed whether the intracellular motility impairment observed in RACK1-KD cells affects *Shigella* cell-to-cell spreading.

Plaque-based assays are commonly used to determine the titer of lytic viruses. This methodology has been previously adapted to study *Shigella* cell-to-cell spreading [375,376]. As *Shigella* spreads in the cell monolayer, it forms areas of infection called plaques. The size of the plaques reflects the efficiency of bacterial spreading. In the standard plaque assay, the cells are covered with a dense agarose overlay after infection to restrict diffusion in the media of free *Shigella* thereby promoting direct cell-to-cell spreading. After incubation for 72 h, the cells are fixed and stained with Giemsa to visualize the plaques [376]. The agarose overlay prevents time-lapse analysis of bacterial spreading, and excessive manipulation (fixing/staining) disturbs the plaques. I developed a modified plaque assay to solve these impediments and allow live observation of *Shigella* cell-to-cell spreading. Briefly, cell monolayers stably expressing F-tractin-GFP were infected with a low MOI of dsRED-WT *Shigella* for 30 min (Figure 3.7.1 A). Methocel, a non-toxic, transparent polymer that becomes increasingly viscous at temperatures higher than 29 °C [401], was used as the overlay to restrict *Shigella*'s extracellular diffusion. The modified assay did not require fixation or staining steps for plaque visualization since both the cells and bacteria were fluorescent (Figure 3.7.1 A-B). Thus, imaging of the plaques could be performed at various time points. Plaque boundaries were identified using automatic segmentation, as shown in Figure 3.7.1 B (see section 2.11.8 for detailed methodology). Areas of infection less than four μm^2 (average area of one HeLa cell) away from primary plaques (area > $4\mu m^2$) were classified as secondary plaques, resulting from *Shigella*'s diffusion in the media rather than cell-to-cell spreading (Figure 3.7.1 B).

Shigella formed plaques in HeLa cell monolayers regardless of the presence of Methocel after ten h and 20 h of infection (Figure 3.7.2 A). However, the monolayers that were not overlaid with Methocel showed more secondary plaques (area < 4μm^2) compared to Methocel treated cells after 20 h (Figure 3.7.2 A-B). The number of secondary plaques in the cells treated with Methocel at ten h was reduced by 50% after 20h due to small plaque "fusion" into one bigger plaque. This effect was not observed in no-Methocel conditions (Figure 3.7.2 B). The area of primary plaques formed in cells overlaid with Methocel (176±15.5 um^2) at ten h post-infection was smaller than in no-Methocel conditions (213±9.1 um^2), indicating some degree of cell-to-cell spreading restriction caused by the overlay (Figure 3.7.2 C). However, after 20 h of infection, the plaques formed under Methocel (366±56.1 um^2) were significantly bigger than those in no-Methocel (134±60) monolayers which is consistent with a reduction in the number of secondary plaques (Figure 3.7.2 B-C). Bigger plaques resulted from fewer bacteria diffusing away into the media of Methocel overlaid cells, therefore limiting spread to a cell-to-cell modality only. These findings validated the use of Methocel to restrict convection flows in the culture medium, preventing secondary plaque formation while allowing *Shigella* cell-to-cell spreading.

The modified plaque assay method was used to assess plaque formation in the colonic epithelial cell lines CaCo-2 and HT-29. As *Shigella* spreads in the monolayer, the cell's membrane permeability is compromised, causing cell death. Thus, the otherwise cell-impermeant DNA dye DAPI was added to the overlay medium to detect dead cells. The plaques formed in HT-29 cells after 20 h of infection were similar in size to those generated in HeLa cells after ten h, showing that *Shigella* spreading in HT-29 cells is considerably slower (Figure 3.7.3 A). Moreover, after 72 h of infection, the size of the plaques in HT-29 increased considerably, and a prominent halo of DAPI+ nuclei surrounded the plaques indicating *Shigella* causes massive cell death in HT-29 cells (Figure 3.7.3 A). *Shigella* disseminated at a similar rate in HeLa and CaCo-2 cells. After 10 h of infection, the plaques generated in HeLa cells had an average size of 0.132±0.11 mm^2, while in CaCo-2 cells the plaques were 0.313±0.24 mm^2 after 15 h of infection (Figure 3.7.3 B). Although this was

not quantified, *Shigella* seems to induce a more extensive zone of cell death in CaCo-2 than in HeLa cells (Figure 3.7.3 A). Given that RACK1 silencing was successful only in HeLa and CaCo-2 cells (Figure 3.1.4), I evaluated the role of RACK1 in *Shigella* spreading using these cell lines. Conveniently, the 96-well format of the modified plaque assay allowed simultaneous analysis of control (NS), KD-92, KD-94, and KD-95 cell lines. Of note, secondary plaques were not included in this analysis. The plaques' areas were significantly reduced in all three HeLa and CaCo-2 RACK1-KD cell lines (Figure 3.7.3 B). These findings reveal an impairment of *Shigella* cell-to-cell spreading in RACK1-KD cells consistent with a defect in actin tail polymerization and reduced actin-mediated motility.

Taking advantage of the transparent nature of Methocel, I captured time-lapse images of infected cells overlaid with Methocel at high magnification (40X) to follow infection progression. *Shigella* spreading to neighbouring cells was assessed manually over time, starting from one infected cell (i.e., infection focus, Figure 3.7.4 A). *Shigella* infected a new HeLa cell every 15 to 30 min during the first 3 hours of infection. After this time, *Shigella's* spreading slowed down, infecting a new cell every 45 min to one h (Figure 3.7.4 A). Analysis of the cumulative number of infected cells recorded over ten h of infection showed a significant reduction of *Shigella's* cell-to-cell dissemination in RACK1-KD cells (Figure 3.7.4 B). Together, the plaque assay and time-lapse spreading results are consistent with RACK1 having a pivotal role in actin tail polymerization, leading to efficient *Shigella* spreading in epithelial cells.

Figure 3.7.1. Plaque assay procedure and data analysis.
A. Diagram of the plaque assay methodology. Cells expressing a fluorescent probe (e.g. F-tractin-GFP) seeded in black 96-well plates to 100% confluency were infected with dsRED-WT *Shigella* (OD_{600} = $5x10^{-4}$) for 30 min. The cells were treated with gentamycin (100 µg/mL) to eliminate extracellular bacteria for 15 min. The monolayers were overlaid with 0.4% Methocel diluted in FluoroBrite supplemented with DAPI to identify dead cells. After 10 to 20 h of infection, images were captured at 10X magnification using a Zeiss widefield microscope. Methocel addition to the monolayers restricts the diffusion of bacteria in the media, promoting cell-to-cell spreading. Areas of bacterial dissemination are called plaques. **B**. Plaque assay data analysis workflow. In this example, the top micrograph shows HeLa cells expressing F-tractin-GFP (binds to F-actin) infected with dsRED-WT *Shigella*. Preprocessing of the image involves splitting channels (middle row images) and modifying the image corresponding to bacteria (dsRED channel) to detect the plaques (bottom row) by automatic segmentation. Areas of infection smaller than the average area of one cell (4 μm^2) were considered secondary plaques and were not included in the plaque area quantification analysis. The inset image shows primary plaques (red arrowheads) and secondary plaques (green arrowheads). Yellow outlines show the plaques' perimeter. Scale bar of images = 1mm, inset = 100 µm)

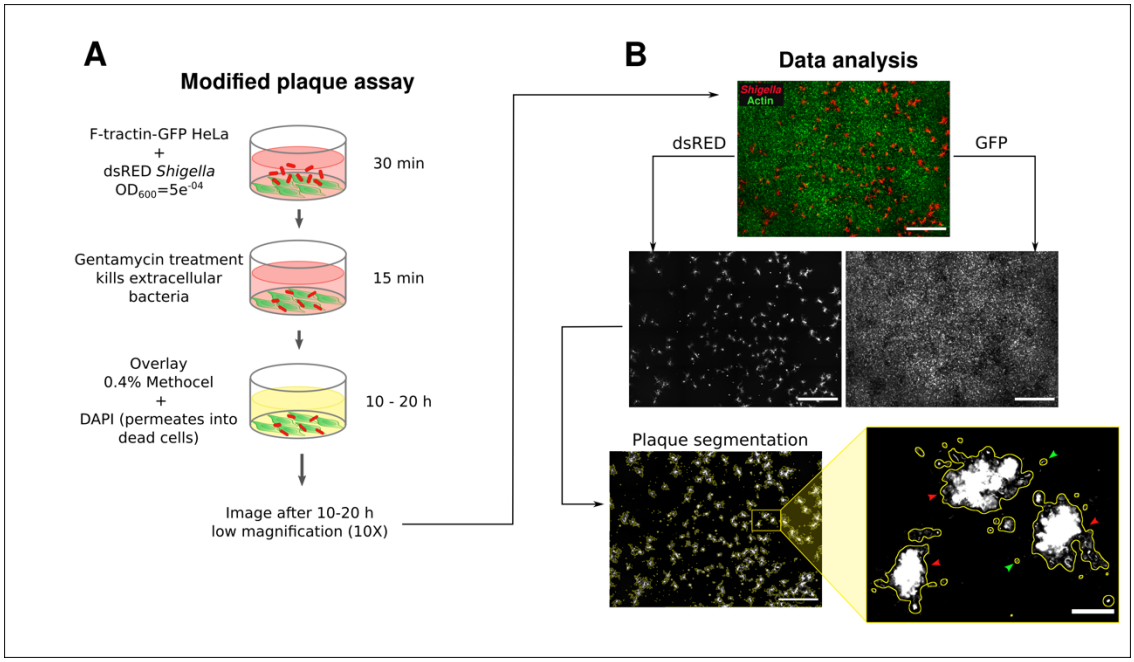

Figure 3.7.2. Methocel efficiently restricts *Shigella* diffusion through the media reducing secondary plaque formation.
F-tractin-GFP expressing HeLa cells were infected with dsRED-WT *Shigella* for 30 min. The cells were then treated with gentamycin (100 µg/ml) for 15 min before overlaying them with 0.4% Methocel diluted in FluoroBrite, supplemented with DAPI (0.1 ng/mL) or with FluoroBrite alone. The monolayers were imaged 10 and 20 h post-infection on a widefield Zeiss Z1 with 10X magnification. As *Shigella* infects the cell monolayer, it forms areas of infection called plaques. The area of the plaque is proportional to the spreading capacity of *Shigella*. **A**. Widefield micrographs of *Shigella* plaques formed on HeLa cells (cells are not shown), after 10 (top row) and 20 h (middle row) of infection in the presence of Methocel (left column) or without Methocel (right column). The last row contains inset images highlighting primary (red outlines) and secondary plaques (green outline). Scale bar = 1mm. Bar plots showing number of secondary plaques (**B**) and area of primary plaques (**C**) formed by *Shigella* in cells with or without Methocel after 10 and 20 h of infection. The bars show mean ± SD from one experiment in triplicate. Statistical significance was tested with two-way ANOVA followed by Tukey HSD; ns = not significant $p>0.05$, *$p < 0.05$, **$p < 0.01$.

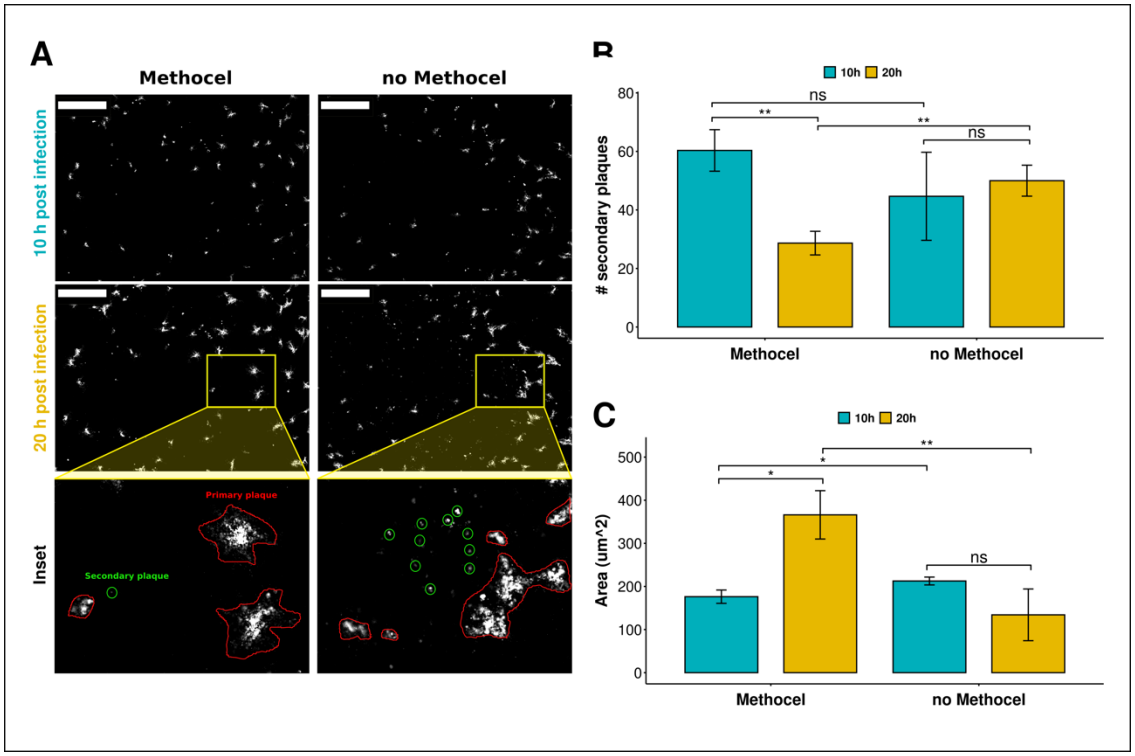

Figure 3.7.3. RACK1 silencing reduces the plaque area formed by *Shigella* in HeLa and CaCo-2 cells.

Bacterial spreading was analyzed using the modified plaque assay. Cells expressing F-tractin-GFP (HeLa, HT-29) or GFP (CaCo-2) were infected with dsRED-WT *Shigella* and overlaid with 0.4% Methocel supplemented with DAPI (0.1 ng/mL). The cells were imaged 10 (HeLa), 15 (CaCo-2), 20 and 72 (HT-29) h post-infection on a widefield Zeiss Z1 with 10X magnification. **A.** Representative images showing *Shigella* plaques formed on HT-29, HeLa, and CaCo-2 cells (green). *Shigella* plaques (red) appear surrounded by dead cells (blue). Infection length is indicated at the top of each image. Scale bar = 200 µm. **B.** Boxplots show the plaque areas formed in HeLa (left) and CaCo-2 cells (right). *Shigella*'s plaque boundaries were identified by automatic segmentation using Fiji. Numbers under the boxplots show plaque number. Dots are plaques from one out of three experiments (Supplementary Figure 3, Appendix C). Wilcoxon-test; **p < 0.01, ****p < 0.0001.

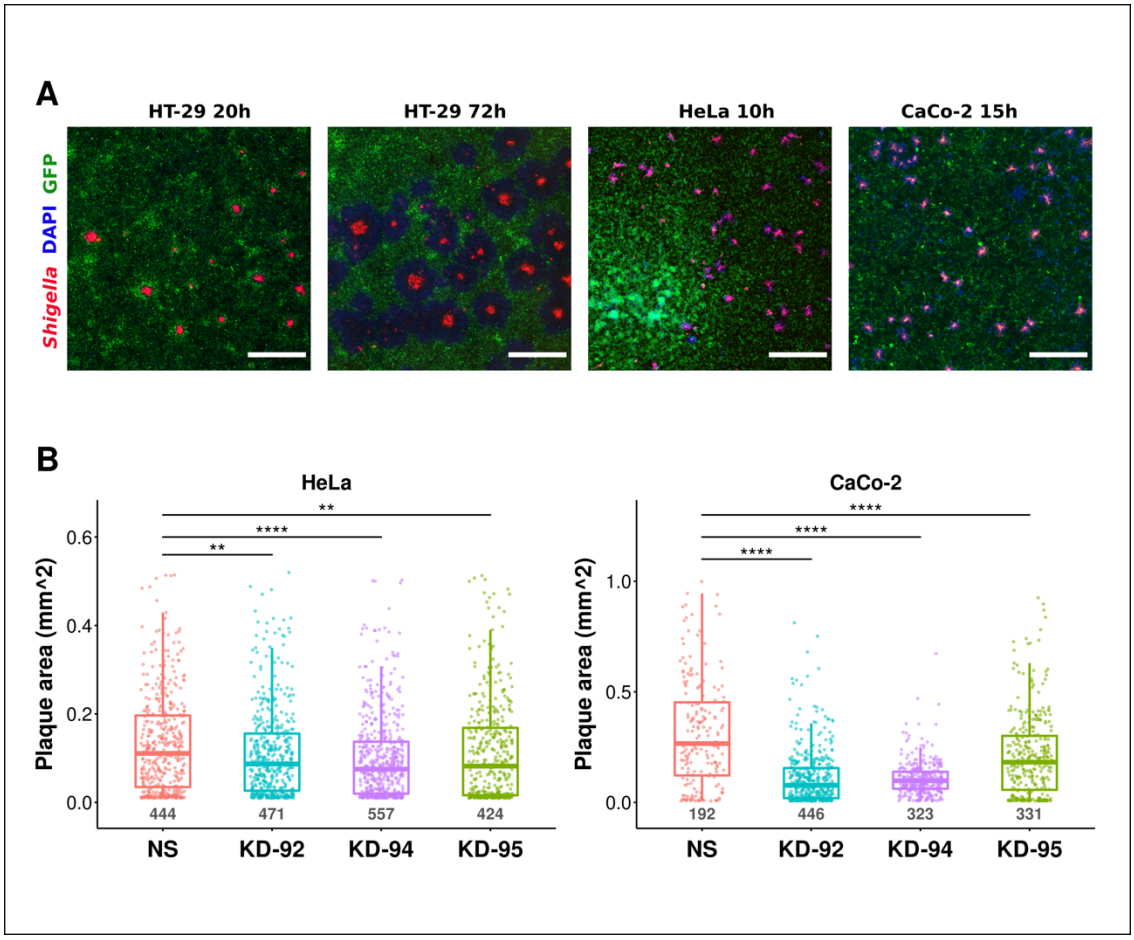

Figure 3.7.4. RACK1 enhances *Shigella* cell-to-cell spreading in HeLa cells.
A. Time-lapse confocal images of HeLa cells infected with dsRED-WT *Shigella*. Infected cells overlaid with 0.4% Methocel were imaged every 15 min for ten h on a Zeiss spinning disk with 40X magnification. Infection spreading was quantified by noting the number of infected cells at each time point, starting from one single infected cell (0 min). Bacteria are shown in red and cells in grey (cells expressing F-tractin-GFP that binds to actin). Yellow outlines highlight infected cells. The line plot shows the progression of *Shigella* spreading in three infection foci, including the one shown in the images. **B**. Line plot showing the cumulative number of infected cells over time. Control and RACK1-KD HeLa cells were infected as in A. The number of infected cells found at each time point was used to calculate the cumulative sum of infected cells. The spreading curves are shown as mean ± SD from three experiments, where 19 (NS = 10, KD-92 = 9) infection foci were analyzed. Unpaired t-test; *$p < 0.05$, **$p < 0.01$, ***$p < 0.001$, ****$p < 0.0001$, only significant points shown.

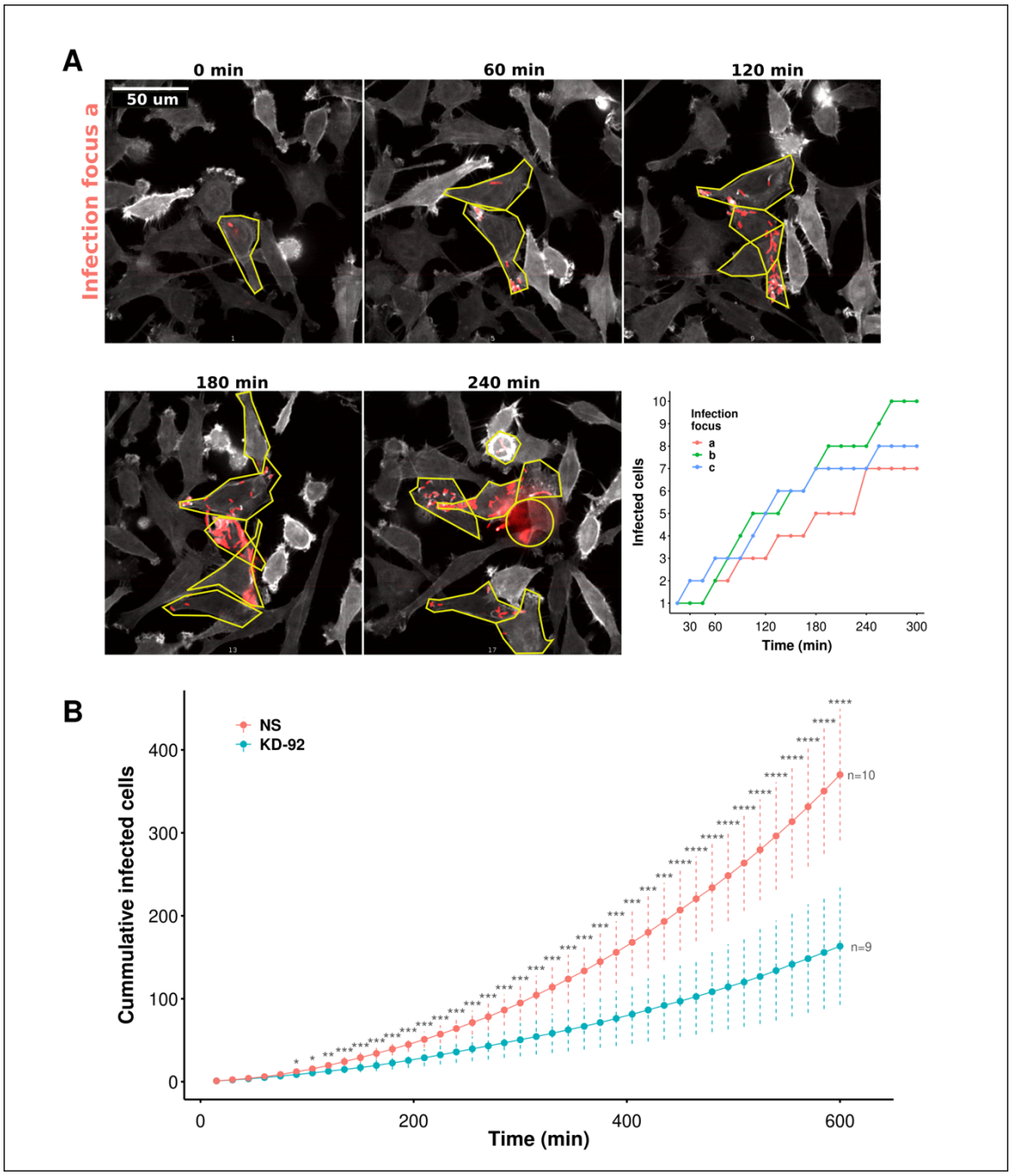
A
0 min
60 min
120 min
50 um
Infection focus a
180 min
240 min
Infection focus
a
b
c
Infected cells
Time (min)
B
NS
KD-92
Cummulative infected cells
Time (min)
n=10
n=9

3.8 RACK1's role in actin cytoskeleton dynamics

Type 3 secreted effectors promote *Shigella* infection through direct interaction with an extensive array of host proteins [95]. I used co-immunoprecipitation (Co-IP) coupled to mass spectroscopy (MS) to test if RACK1 interacts with *Shigella* secreted proteins. I pulled down RACK1 interacting proteins from *Shigella*-infected and uninfected HeLa cells using an anti-RACK1 antibody. Silver staining of the Co-IP product showed no apparent differences between infected and uninfected cells (Figure 3.8.1 A). Before sending the samples for MS analysis, RACK1 interacting proteins were excised from a Coomassie-stained gel discarding the antibody's heavy and light chains (Figure 3.8.1 B). Although no interactions were found between RACK1 and any *Shigella* protein in the conditions tested, the MS analysis identified 19 cytoskeleton-related proteins as RACK1 interacting partners (Table 3.2), several of which have been implicated in *Shigella* infection. For example, binding of the secreted effector IpaC to the intermediate filament protein vimentin allows a conformational change on IpaC required for efficient T3SS activation [402]. Silencing of non-muscle myosin heavy chain IIA in HeLa cells reduces *Shigella* cell-to-cell spreading [403]. Moreover, actin and actin-binding proteins (ABPs) are critical for *Shigella* invasion and actin-mediated motility [404]. In particular, Arp2, part of the actin nucleator Arp2/3 complex, is essential for bacterial entry and for actin tail assembly. *Shigella* invasion depends on membrane ruffling mediated by Arp2/3 dependent actin polymerization. Activation of the Arp2/3 complex during entry is facilitated by cortactin Cdc42 and Rac proteins [115,234]. Once in the cytoplasm, *Shigella*'s surface protein IcsA recruits N-WASP, subsequently activating the Arp2/3 complex stimulating actin tail polymerization [213,234].

RACK1 interaction with the Arp2/3 complex could therefore promote actin-tail polymerization. Co-IP followed by immunoblot showed that RACK1 weakly interacts with Arp2 (Figure 3.8.2 A). To facilitate data analysis, I evaluated if RACK1 silencing impairs Arp2 localization to *Shigella*'s surface but not to the entry focus. Confocal imaging of HeLa cells infected with dsRED-WT *Shigella* and immunolabeled with anti-Arp2 confirmed Arp2/3 complex recruitment to *Shigella'*s tail (Figure 3.8.2 B). Of note, the samples analyzed here were counter stained with DAPI only, actin was not labeled. Given that actin

tails were not visible, I enumerated Shigella that were associated to any Arp2+ structure. However, no significant differences were found in the percentage of Arp2+ bacteria in RACK1-KD cells compared to control. From the bacteria analyzed, 47.1±18.8% and 48.5±15.7% were associated with Arp2 in NS and KD-92 cells, respectively (Figure 3.8.2 C). This result indicates that RACK1 is not involved in Arp2/3 recruitment to the actin-tail.

Considering the findings shown in the previous sections, RACK1 is likely a regulator of actin cytoskeleton dynamics. Thus, I evaluated if RACK1 plays a role in actin polymerization independent of *Shigella*. Drugs that manipulate actin polymerization are routinely used to study cytoskeleton dynamics [405,406]. Thus, the actin-binding compounds jasplakinolide (Jasp) and cytochalasin D (CytoD) were utilized to gain more insight into the role of RACK1 in actin polymerization. These drugs modulate actin filament polymerization. The synthesis of actin filaments involves simultaneous actin polymerization and depolymerization. For this, ATP-bound G-actin monomers are added to the filament's fast-growing barbed end while ADP-bound G-actin is dissociated from the slow-growing pointed end [226,227]. Thus, actin filaments are maintained in a dynamic equilibrium of polymerization and depolymerization, also known as actin filament turnover.

Jasp inhibits filament depolymerization and induces actin polymerization into F-actin amorphous aggregates [407]. Treatment with 0.2 μM Jasp for two h caused the formation of multiple actin aggregates throughout the cytoplasm in control and RACK1-KD HeLa cells (Figure 3.8.3 A). If RACK1 facilitates actin polymerization, RACK1 silenced cells should be less susceptible to the effect of Jasp. Indeed, the aggregates formed in RACK1-KD seemed less abundant than those formed in NS cells (Figure 3.8.3 A). Automatic segmentation was used to detect the F-actin aggregates. Although this approach failed to identify very dim aggregates, most actin puncta were detected and analyzed (Figure 3.8.3 B). The segmentation analysis showed that the total area of F-actin aggregates per cell was significantly reduced in RACK-KD conditions. On average, the total aggregate area found in an NS cell was 41±31 μm^2, whereas in a KD-92 cell the F-actin aggregate area was reduced to 29.7±26 μm^2 (Figure 3.8.3 C). Similarly, the aggregates' FI was decreased

significantly in KD-92 (44±30.3 a.u.) compared to NS cells (56.5±35.6 a.u., Figure 3.8.3 D). Again, the number of aggregates per cell was reduced in KD-92 cells, consistent with an impairment in actin polymerization. An average of 14±9 actin aggregates were found per NS cell, and 10±7 aggregates were found per KD-92 cell (Figure 3.8.3 E). These data show that RACK1 promotes Jasp-induced actin polymerization.

CytoD, a fungal toxin, stimulates actin depolymerization and blocks polymerization by binding to the actin filament barbed end [406]. Like Jasp, CytoD treatment (40 μg/mL) disrupted the cytoskeleton, forming small actin aggregates, but stress fibre disassembly was the most dramatic effect (Figure 3.8.4 A). I reasoned if RACK1 promotes actin depolymerization, actin filaments should be preserved in RACK1-KD cells treated with CytoD. No readily apparent differences were observed in CytoD treated control and RACK1-D cells (Figure 3.8.4 A). Nevertheless, segmentation was performed to identify F-actin-rich structures such as stress fibres and cell adhesions (Figure 3.8.4 B). Quantification showed no significant difference in the area (NS = 6.8±7.5 μm^2, KD-92 = 6.7±6.9 μm^2) and FI (NS = 2.8±0.23 a.u., KD-92 = 2.8±0.22 a.u.) of F-actin-rich structures found in control and RACK1-KD cells (Figure 3.8.4 C-D), suggesting that RACK1 is not involved in CytoD mediated actin depolymerization.

Fluorescence recovery after photobleaching (FRAP) has been widely used to analyze the dynamics of actin polymerization [408]. FRAP measures the diffusion kinetics of a fluorescently-tagged protein of interest after photobleaching with a high-power laser. HeLa cells transfected with GFP-actin were bleached in a rectangular region of interest (ROI), and the fluorescence recovery was followed by time-lapse imaging (Figure 3.8.5 A). FRAP was assessed in two characteristic actin-rich cellular structures, stress fibres and membrane ruffles (Figure 3.8.5 A). GFP-actin fluorescence was fast to recover in membrane ruffles; actin filaments were visible six seconds after bleaching indicating fast actin turnover. In contrast, stress fibre fluorescence took longer to be recovered (180 sec), indicating these structured have a slower actin turnover rate (Figure 3.8.5 A).

Next, I evaluated the turnover of actin filament assembly in RACK1 silenced cells. Analysis of the fitted recovery curves obtained from membrane ruffles revealed faster actin turnover in control than in RACK1-KD cells (Figure 3.8.5 B). A significant difference was confirmed by calculating the halftime of recovery ($t_{1/2}$), which was 11.3±4.6 sec for NS cells and 30.2±8.2 sec for KD-92 cells (Figure 3.8.5 C). On the other hand, no significant difference was found in stress fibre actin turnover in NS ($t_{1/2}$ = 16.1±9.3) and KD-92 ($t_{1/2}$ = 20±11.3) cells (Figure 3.8.5 D-E). Furthermore, the recovery curves confirmed a slower actin turnover in stress fibres than in membrane ruffles (Figure 3.8.5 B-D).

To recapitulate the data presented in this section, RACK1 binds to actin cytoskeleton-related proteins involved in *Shigella* infection, from which the RACK1-Arp2 interaction was confirmed. However, localization of the actin nucleator Arp2/3 complex to *Shigella*'s actin tail was not regulated by RACK1. Thus, the actin tail defect observed in RACK1-silenced cells might not be dependent on Arp2/3 binding to the tail. Actin binding drugs revealed that RACK1 promotes actin polymerization but not depolymerization. FRAP experiments supported these findings showing significant actin-turnover inhibition in RACK1-KD cells.

Figure 3.8.1. Study of RACK1 interactome in *Shigella*-infected HeLa cells.
WT HeLa cells uninfected or infected with WT *Shigella* (MOI 10) for 1.5 h were lysed. The protein extracts were subjected to co-immunoprecipitation (Co-IP) using 10 µL of anti-RACK1 antibody or 5 µL of IgG (control) antibody. After Co-IP, equal amounts of protein were separated by SDS-PAGE. **A**. Silver-stained gel showing detection of the proteins pulled down in the Co-IP. **B**. Coomassie-stained gel showing the excised gel sections (red rectangles) analyzed by mass spectrometry. The light and heavy chains of anti-RACK1 antibody were discarded.

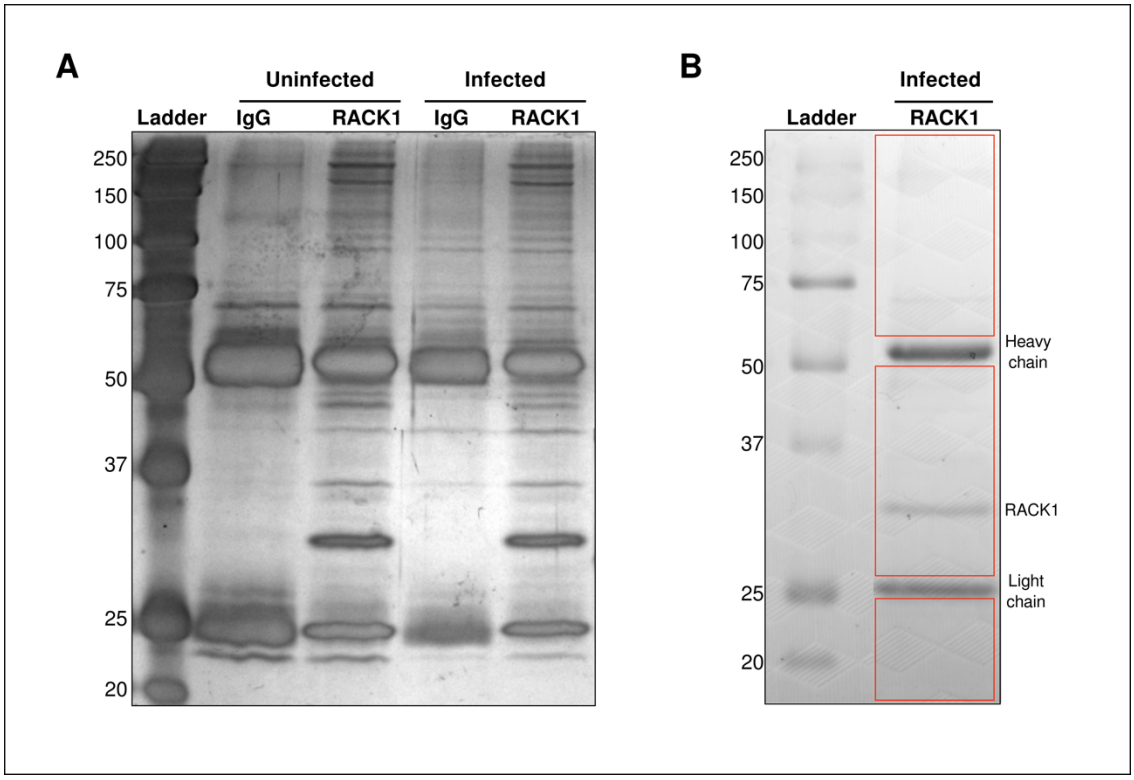

Table 3.2. Cytoskeleton related proteins identified as RACK1 binding partners by Co-IP-MS

Actin and ABPs	Microtubules and intermediate filaments	Motors
Filamin-A (6)	Tubulin alpha-1A (3)	Myosin heavy chain 9 (1)
Alpha-actin-2 (5)	Tubulin beta-2A (1)	Myosin heavy chain 7 (1)
Cofilin 1 (2)	Tubulin beta-3 (1)	Unconventional myosin-IXa (1)
F-actin-capping protein subunit beta (2)	Tubulin beta-1 (1)	
F-actin-capping protein subunit alpha-1 (1)	Tubulin beta-4A (1)	
Alpha-actinin-4 (1)	Vimentin (1)	
Beta-actin (1)		
Arp2 (1)		
Profilin-1 (1)		
Vinculin (1)		

Number of unique peptides are shown in parenthesis.
ABPs: actin binding proteins

Figure 3.8.2. RACK1 is not required for Arp-2 recruitment to *Shigella*.
A. Confirmation of RACK1-Arp2 interaction. HeLa cell lysate was subjected to co-immunoprecipitation (Co-IP) using anti-RACK1. The immunoprecipitated proteins were analyzed by western blotting using anti-Arp2. **B-C**. Control (NS) and RACK1-KD (KD-92) HeLa cells infected with dsRED-WT *Shigella* (MOI 10) for two h were fixed and immunolabeled with DAPI and anti-Arp2. Images were taken on a Zeiss 710 confocal with 63X magnification. **B**. Confocal micrograph showing an infected HeLa cell. The two yellow arrowheads indicate *Shigella* (red) associated with Arp2 (green) at one pole. Scale bar = 10 µm. **C**. Quantification of the percentage of Arp2 positive (%Arp2+) *Shigella*. Dots represent %Arp2+ bacteria found per image from three experiments (55 images per condition). The total number of bacteria analyzed is shown at the base of the boxplots. Unpaired t-test; ns = not significant p>0.05.

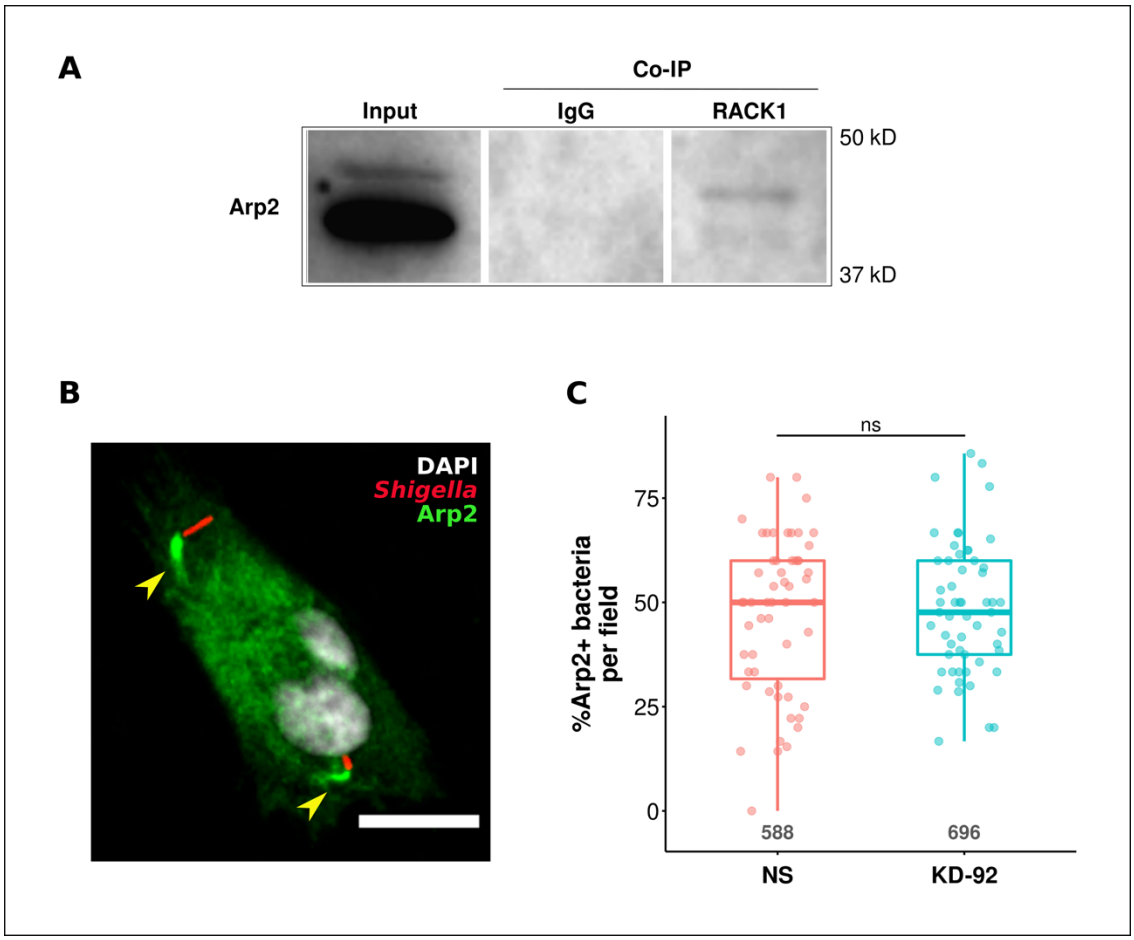

Figure 3.8.3. Filamentous-actin (F-actin) aggregate formation is reduced in RACK1-KD cells treated with jasplakinolide.
Control (NS) and RACK1-KD (KD-92) HeLa cells expressing F-tractin-GFP were treated with 0.2 µM of the actin-stabilizing toxin jasplakinolide (Jasp). Z-stack images (8 slices, 1µm apart) were captured before and after two h of treatment on a Zeiss Z.1 spinning disk with 40X magnification. **A**. Representative maximum projection images of cells treated with Jasp at 0 and 2 h. F-actin is shown in grey. Scale bar = 50 µm. **B**. Example of F-actin aggregate segmentation. F-actin (grey) aggregates (red outlines) were detected using Fiji's automatic segmentation. Cell outlines (green) were manually drawn. Scale bar = 30 µm. **C**. Total F-actin aggregates area per cell. Each dot represents the sum of the actin aggregate areas on each cell. **D**. Total fluorescence intensity (FI) per cell. The aggregate FI was normalized to the average FI of cells before the addition of Jasp. Dots represent the sum of the aggregate FI found per cell. **E**. Number (#) of F-actin aggregates per cell. Numbers under the boxplots in C, D and E indicate the number of cells analyzed from 2 independent experiments. Wilcoxon-test; ***p<0.001, ****p<0.0001.

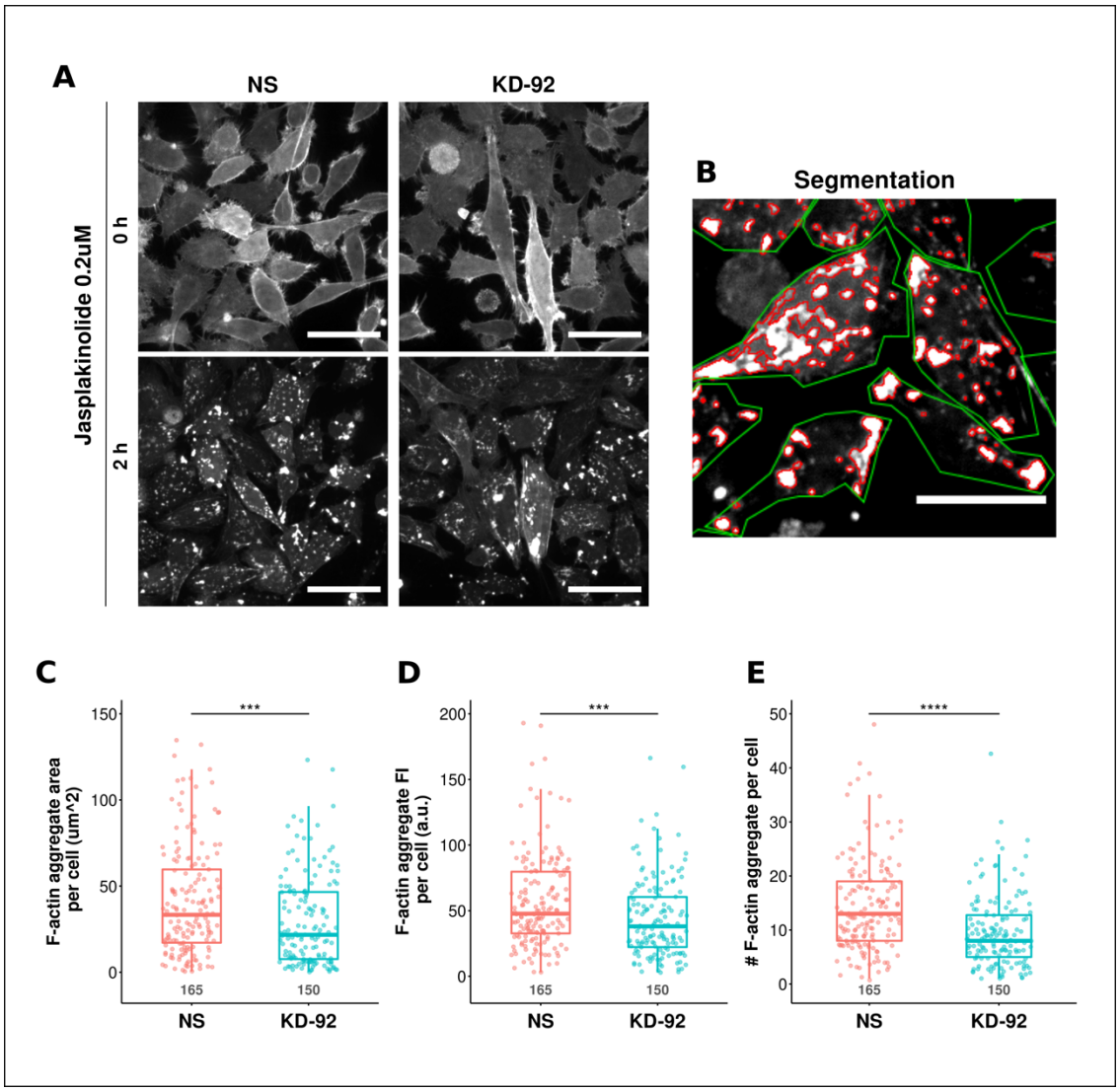

Figure 3.8.4. Cytochalasin D (CytoD) mediated disruption of filamentous actin (F-actin) is not affected by RACK1 silencing.
Control (NS) and RACK1-KD (KD-92) HeLa cells expressing F-tractin-GFP were treated with 40 µg/mL of CytoD. Z-stack images (10 slices 0.54 µm apart) were captured before and after 1.5 h of treatment on a Zeiss Z.1 spinning disk with 40X magnification. **A**. Representative images of cells treated with CytoD at 0 and 1.5 h. The images show F-actin-rich structures such as stress fibres and cell adhesions. Scale bar = 50 µm. **B**. Example image of the automatic segmentation performed to identify F-actin-rich structures (red outlines). The focal plane containing more stress fibres and adhesions was analyzed from each image. Scale bar = 20 µm. Area (**C**) and fluorescence intensity (FI, **D**) quantification of F-actin-rich structures. FI was normalized to the average FI of cells before the addition of CytoD. Numbers under the boxplots indicate the number of F-actin-rich structures detected by segmentation on four fields of view. Data shown in C and D are from 1 experiment. Wilcoxon-test; ns = not significant p>0.05.

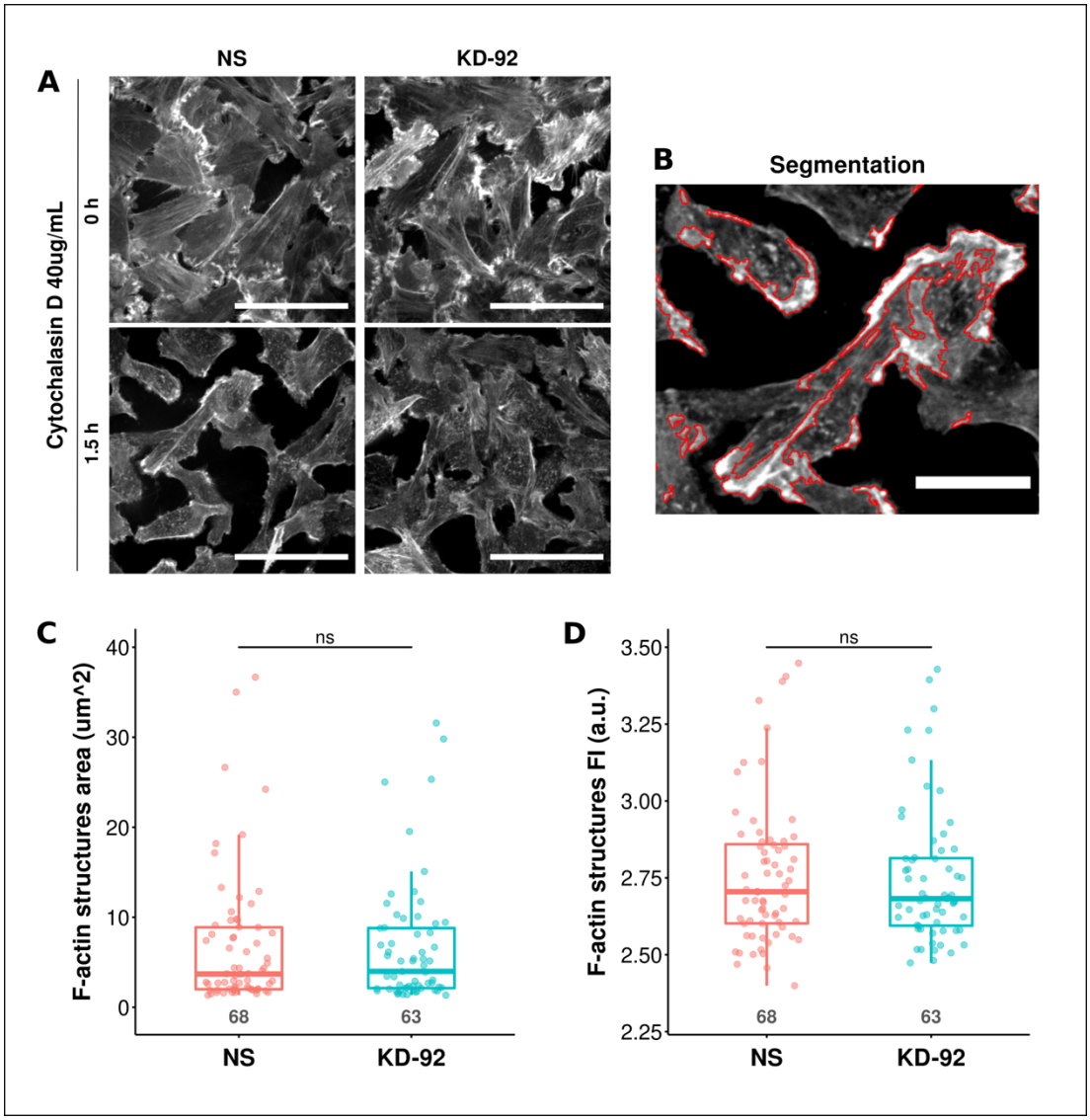

Figure 3.8.5. RACK1 silencing affects actin turnover in membrane ruffles but not in stress fibres.

Fluorescence Recovery After Photobleaching (FRAP) was performed in control (NS) and RACK1-KD (KD-92) HeLa cells transfected with pEGFP-Actin. A Zeiss LSM 880 confocal was used to capture three images before bleaching a region of interest (ROI), then images were captured every 2 sec for 180 sec. Stress fibres and ruffles were imaged in 25 NS and 22 RACK1-KD cells. **A**. Selected confocal images from a time-lapse showing FRAP of EGFP-Actin. Red ROIs show the bleached area in a membrane ruffle (top row) and a stress fibre region (bottom row). A whole-cell area ROI (yellow) was defined to measure fluorescence loss due to imaging. A cell-free area was selected to calculate the background (green ROI). Scale bar = 10 μm. EGFP-Actin fluorescence recovery over time in membrane ruffles (**B**) and stress fibres (**D**) from NS and KD-92 cells. Solid lines represent best-fit curves for the data calculated using a non-linear least squares regression model. Ribbons show the ±SD of the samples analyzed. **C** and **E**. Box plots show the bleached region's time to recover half of its final fluorescence intensity. The half time was calculated from the data shown in B (ruffles) and D (stress fibres). Numbers under the boxplots represent the number of cells analyzed per condition. Unpaired t-test; ns = not significant $p>0.05$, ****$p<0.0001$.

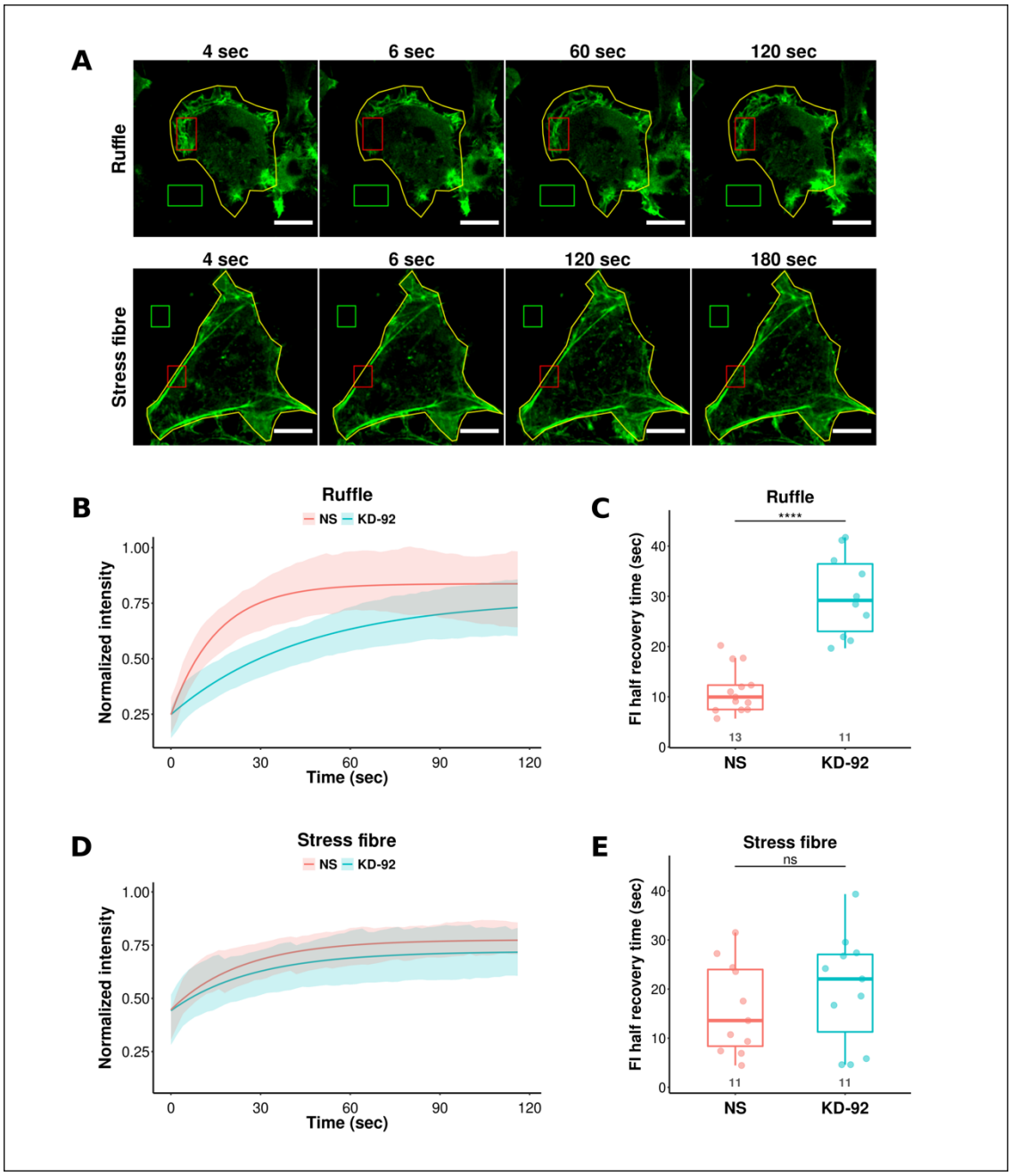
A
4 sec
6 sec
60 sec
120 sec
Ruffle
4 sec
6 sec
120 sec
180 sec
Stress fibre
B
Ruffle
NS
KD-92
Normalized intensity
1.00
0.75
0.50
0.25
0
30
60
90
120
Time (sec)
C
Ruffle
****
FI half recovery time (sec)
40
30
20
10
0
13
11
NS
KD-92
D
Stress fibre
NS
KD-92
Normalized intensity
1.00
0.75
0.50
0.25
0
30
60
90
120
Time (sec)
E
Stress fibre
ns
FI half recovery time (sec)
40
30
20
10
0
11
11
NS
KD-92

CHAPTER 4 DISCUSSION

Shigella is a strictly human pathogen that subverts the host's cell machinery to support its intracellular lifestyle. Through its T3SS, *Shigella* secretes bacterial effectors that manipulate the host cytoskeleton, forming an F-actin-rich entry focus, which facilitates bacterial internalization. After escape from the *Shigella*-containing vacuole (SCV), this pathogen replicates in the cytoplasm and induces IcsA-mediated actin tail polymerization. Polymerization of an actin tail is pivotal for bacterial intracellular motility and cell-to-cell spread. RACK1, a host scaffold protein, participates in numerous aspects of cellular function in eukaryotic organisms, including cell signalling, proliferation, and migration. RACK1's role in cytoskeleton dynamics is not well understood. Nevertheless, the current literature shows that RACK1 is a crucial player in focal adhesion assembly, interacting with various actin-binding proteins. Therefore, it is possible RACK1 participates during *Shigella* infection. I hypothesized that *Shigella flexneri* requires RACK1 to manipulate actin cytoskeleton dynamics, leading to efficient invasion and cell-to-cell spreading. To test this hypothesis, I aimed to characterize the effect of RACK1 silencing on the intracellular growth of *Shigella* in HeLa cells and colonization of the *Drosophila melanogaster* intestine. I systematically evaluated the role of RACK1 in the main steps of *Shigella*'s life cycle within HeLa cells, including cell invasion, vacuolar escape, intracellular replication, actin tail polymerization and cell-to-cell spreading. Lastly, I focused on understanding the general impact of RACK1 silencing on cellular actin polymerization dynamics without *Shigella* infection.

Herein, I found that silencing RACK1 inhibited *Shigella* growth in HeLa cells due to impaired bacterial invasion and cell-to-cell spreading. Accordingly, RACK1 overexpression in HeLa cells resulted in higher *Shigella* yield. Surprisingly, RACK1 silencing protected flies from *Shigella* infection by an unidentified mechanism. Live-cell microscopy analysis of epithelial cells infected with *Shigella* showed that RACK1 localization to the entry focus is crucial for efficient actin polymerization around *Shigella* to facilitate efficient invasion. However, bacterial escape from the SCV, intracellular replication and modulation of host cell death were not affected by RACK1. Although

RACK1 did not colocalize with *Shigella*'s actin tail, RACK1 promoted actin tail polymerization and elongation, which mediated swift intracellular motility and allowed efficient cell-to-cell spreading. Furthermore, co-IP coupled to mass spectrometry analysis revealed the interaction of RACK1 with many cytoskeleton-related proteins, prompting the study of actin dynamics. Treating cells with actin-binding drugs revealed that RACK1 promotes actin polymerization but not depolymerization. FRAP experiments supported these findings showing that RACK1 enables normal actin-turnover. Together these results are consistent with RACK1 having a pivotal role in actin cytoskeleton modulation, leading to efficient *Shigella* invasion, and spreading in epithelial cells.

4.1 RACK1 promotes *Shigella* infection *in vitro* and *in vivo*

My thesis work focused on characterizing the role of RACK1 in the interactions between *Shigella* and epithelial cells. Given that RACK1 is an essential protein, highly expressed in most tissues [409], knockout of the RACK1 gene cannot be achieved in most eukaryotic organisms [284,390,410]. Instead, I silenced the expression of RACK1 in various epithelial cell lines using shRNAs. However, HeLa cells quickly regained basal expression levels and silencing RACK1 in HT-29 cells was unsuccessful (Figures 3.1.2 and 3.1.4). Moreover, cells transfected with a high expression plasmid carrying RACK1 under the control of the CMV promoter, only showed modestly increased RACK1 expression (Figure 3.2.5), suggesting the cellular level of RACK1 is tightly regulated. Indeed, an aberrant expression of RACK1 has been linked to many cancers [289]. RACK1 promotes cell proliferation and metastasis in multiple myeloma and breast, liver and prostate cancers [306,411,304,412]. Consistent with these findings, RACK1 silencing in HeLa cells reduced cell proliferation (Figure 3.1.3 C).

A growing body of evidence shows that RACK1 plays an essential role in viral pathogenesis. RACK1 is required for viral translation, replication, and release of many RNA viruses [348,353,354]. However, only a few reports have linked RACK1 to bacterial infections in mammals. Protein-protein interaction screenings have shown bacterial secreted effectors bind to RACK1. For example, the vacuolating toxin VacA of *H. pylori* binds to RACK1, but the outcome of this interaction was not well-characterized [9].

Moreover, RACK1 binds to the *Mycobacterium tuberculosis* secreted effector EST12, activating the NLRP3 inflammasome and pyroptosis. Significantly, RACK1-mediated recognition of EST12 reduces mycobacterial loads within macrophages and mice lungs [8]. These findings are supported by Duan *et al.,* showing that RACK1 knockdown (KD) impairs NLRP3 assembly, attenuating caspase-1 activation and IL-1β secretion induced by ATP in LPS-primed macrophages [361]. In contrast to *Mycobacterium*, *Shigella* promotes macrophages cell death by pyroptosis. *Shigella* activates NLRP3 or NLRC4 inflammasomes via the T3SS effectors IpaH4.5 and IpaH7.8, and the T3SS components MxiH and MxiI [50,198,199,413,414]. Inflammasome activation leads to caspase-1-mediated pyroptosis releasing intracellular bacteria and promoting massive tissue inflammation, which benefits *Shigella*'s invasion of the epithelium [54].

In this work, I found RACK1 promotes the growth of *Shigella* in HeLa cells. RACK1 silencing reduced the number of colony-forming units (CFU) recovered from cell lysates, whereas RACK1 overexpression increased bacterial burden in HeLa cells (Figures 3.2.2 to 3.2.5). This was an interesting phenotype, given that the evidence mentioned above points towards RACK1 functioning as a defence molecule. I did not assess the role of RACK1 in macrophages infected with *Shigella*, but it is possible that *Shigella* exploits RACK1-mediated activation of NLRP3 to promote pyroptosis in these cells.

Furthermore, RACK1 silencing in *Drosophila* enterocytes reduced fly mortality caused by *Shigella* infection (Figure 3.2.6), suggesting RACK1 plays a pro-virulence role. This finding contrasts with the protective function RACK1 exerts in *Caenorhabditis elegans* infected with *Shigella* [10]. In this model, worms showed total mortality after six days of feeding with live *Shigella*. Infection of flies with *Shigella* was not as lethal, only inducing mortality after ten days of feeding with *Shigella* (OD_{600} = 25). A significant reduction of survival probability compared to sugar-fed flies was found after 15 days of *Shigella* feeding. In our model, RACK1 silencing increased the survival probability of flies fed with *Shigella* to control levels (Figure 3.2.6 B). In contrast, partial deletion of RACK1 in *C. elegans* reduces survival probability and increases *Shigella* CFU recovered from infected worms [10]. Also, RACK1 deletion reduces P38 and JNK MAPKs activation resulting in

NLP-*29* antimicrobial peptide downregulation [10]. These results suggest *R*ACK1-mediated regulation of NLP-*29* expression is responsible for the innate immune response against *Shigella* infection in *C. elegans* [10]. In *Drosophila*, the immune deficiency (Imd) pathway controls the production of antimicrobial peptides (AMPs) [415]. Interestingly, the Ras/MAPK pathway inhibits Imd, subsequently limiting AMPs production [416]. Thus, the RACK1-MAPKs interaction might have differential functions depending on the organism, promoting AMP production in worms while inhibiting AMPs in flies. In that scenario, silencing RACK1 in flies could reduce Ras/MAPK-mediated Imd inhibition resulting in increased AMPs production and resistance to infection.

Microscopic analysis of infected control fly guts showed *Shigella* accumulation in the lumen of the intestines without invasion of enterocytes (Figure 3.2.6 C-D). Similar findings were reported in *C. elegans* [417], suggesting that worm and fly death is not mediated by *Shigella* invasion of epithelial cells and is most likely caused by bacterial accumulation and possible blockage of the intestine. The lack of invasion observed was expected due to the experimental conditions used. Infections were carried out at 29 °C; at this temperature, *Shigella*'s T3SS is not active due to the H-NS repressor inhibiting activation of the transcriptional cascade that culminates with T3SS assembly and activation.

Although *Shigella* did not invade the epithelium, guts from RACK1-KD flies infected with *Shigella* showed signs of tissue hyperplasia and intestinal lumen reduction, which was occupied by fewer bacteria than in control guts (Figure 3.2.6 C). Intestinal hyperplasia is characteristic of tissue regeneration induced by injury or infection in *Drosophila* guts [418]. Feeding flies with *Pseudomonas aeruginosa* causes intestinal stem cell (ISC) expansion to rebuild the damaged epithelium [391]. *Drosophila* wingless (Wg) and Janus kinase (JAK)/Signal Transducer and Activator of Transcription (STAT) pathways control ISC proliferation [389]. It has been reported that RACK1 sequesters inactive STAT in a complex with viral proteins, blocking downstream signalling in human cell lines infected with the measles virus [419]. Thus, RACK1 silencing in *Drosophila* could make STAT available for activation, resulting in JAK/STAT-mediated ISC proliferation.

Notably, dysfunction in the Wnt pathway, Wg's human counterpart, is related to colorectal cancer development [420]. Moreover, RACK1 degradation has been shown to induce hyperactivation of the Wnt/β-catenin signalling pathway in gastric cells, promoting cancer progression [421,422]. Therefore, RACK1 is a negative regulator of this pathway. Silencing RACK1 expression in flies could promote ISC proliferation via overstimulation of the Wg pathway protecting the flies from *Shigella*-induced damage of the gut epithelium. RACK1 is also a negative regulator of Wnt/β-catenin signalling in zebrafish [421]. The zebrafish model has emerged as an attractive alternative to study shigellosis since the major pathogenic events observed in humans are recapitulated, including epithelial cell invasion, macrophage cell death and inflammatory destruction of the host epithelium [423]. Also, RACK1 silencing can be easily achieved using morpholino oligonucleotides, and the optical clarity of embryos allows non-invasive real-time imaging [421,424]. Again, the temperature of infection most likely inhibits T3SS activity in the zebrafish model. Thus, the validity of any non-mammalian model used to study *Shigella* pathogenesis is questionable.

In summary, Although *Shigella* did not invade *Drosophila* enterocytes, RACK1-KD in the fly gut resulted in reduced mortality. Moreover, less *Shigella* was recovered from RACK1-KD HeLa cells due to invasion and cell-to-cell spreading impairment. These results support the hypothesis that *Shigella* benefits from RACK1's function to promote infection in epithelial cells and flies. However, the fly results must be interpreted with caution as the T3SS, pivotal for mammalian infection is not active at temperatures lower than 32 °C. Nevertheless, these findings raise questions about which of the many known functions of RACK1 and which of its interacting partners are involved in the pro-bacterial activity of RACK1 in mammalian epithelial cells. To answer these questions, I systematically evaluated the role of RACK1 on the critical steps of *Shigella's* intracellular life cycle.

4.2 *Shigella* requires RACK1 to manipulate the host actin cytoskeleton

4.2.1 RACK1 promotes *Shigella* invasion of HeLa cells

Induction of entry focus formation in epithelial cells (ECs) is the first step where *Shigella* come into close contact with the host cell. *Shigella* injects type 3 secretion system (T3SS) effectors that stimulate profuse actin polymerization and membrane ruffling culminating with bacterial internalization [108]. IpaB and IpaC constitute the primary *Shigella* effectors that trigger the concerted steps, leading to bacterial entry [92]. These proteins are situated at the tip of the T3SS and assemble into the translocon, a multimeric structure within the host plasma membrane [94]. Following membrane insertion of the translocon, IpaC interacts with the intermediate filament protein vimentin, stabilizing the translocon and triggering effector secretion through the translocon pore [402]. Vimentin has been shown to interact with RACK1, an interaction also found in this work (Table 3.1), to form a complex with the focal adhesion kinase (FAK) promoting focal adhesion (FA) assembly and cell adhesion [318]. Vimentin is also required to recruit and activate Rac1 for actin polymerization in the FA [320]. The early recruitment of RACK1 to the *Shigella* entry site reported here (Figure 3.3.1 B) could therefore facilitate IpaC and vimentin interaction, promoting bacterial secretion and subsequent entry foci formation.

IpaC also recruits the Src kinase to the entry site, and its activation allows phosphorylation of cortactin [425,116]. Active cortactin forms a complex with Crk, an adapter protein activated by Abl, another host tyrosine kinase required for *Shigella* invasion [115,118]. The cortactin-Crk complex triggers Arp2/3 activation and subsequent polymerization of branched actin filaments [115]. IpaC further promotes actin polymerization and membrane ruffling by indirectly activating the small GTPases Cdc42 and Rac1 [112]. Additionally, *Shigella* secrets IpgB1 and IpgB2, effectors that mimic guanine nucleotide exchange factors (GEFs), to maintain Cdc42 and Rac1 in an active state [119,120]. The recruitment and activation of these host factors by *Shigella* effectors generate profuse local actin polymerization required for invasion.

Since RACK1 was recruited around *Shigella* during cell invasion (Figure 3.3.1 B), it is possible RACK1 is involved in actin foci formation. Indeed, when analyzing entry foci dynamics, I found that the actin foci lasted on average 6.29±4.19 min. This result is consistent with a previous study that reported the foci reached maximum actin fluorescence intensity (FI) in ~ 7 min [158]. Silencing RACK1 increased entry foci duration to an average of 11.1±7.02 min. However, the area and FI of the foci were not affected by RACK1-KD. It is possible that the area and FI were similar to control cells because *Shigella* may require a minimum size or amount of actin accumulation in the entry site to promote invasion. Thus, in RACK1-KD cells, the foci duration was extended until the minimum size or FI level was reached. A limitation of the analysis used here is that only the maximum area and average FI of the foci were calculated (see methods section 2.11.3 for details). Instead, a segmentation algorithm that detected the area occupied by the foci at all time points rather than measuring only the maximum area could have given more accurate information about foci size progression. Also, measurements of the cumulative FI of the foci over time could show the total amount of actin recruited. On the other hand, the lack of similar analysis in the literature to compare these findings highlights the poor understanding of the modifications of actin cytoskeleton dynamics induced by *Shigella* during cell invasion.

RACK1 is a known regulator of Src and other members of the Src kinase family, such as Fyn and Lck [266,321–323,330]. RACK1 binding stabilizes these kinases in their inactive form while shuttling them to their site of action. For example, the release of Src from RACK1 sequestration enables kinase activation and phosphorylation of FAK, leading to FA assembly [266,270]. Furthermore, the FAK-Src complex promotes the activation of Rac1 and Cdc42, inducing actin polymerization [426]. RACK1 interaction with Src also mediates the formation of an actin ring required for osteoclasts adhesion to bone [329]. Overexpression of RACK1 missing the Src-binding domain causes a loss of central FAs and actin stress fibres in CHO cells, suggesting RACK1-Src interaction is critical for actin cytoskeleton homeostasis [328]. Perhaps it is through its interaction with Src that RACK1 promotes actin polymerization during *Shigella* invasion, probably enabling the phosphorylation of Src substrates at the entry focus. In support of this hypothesis, measurements of F-tractin-GFP FI changes around *Shigella* during entry revealed a significant reduction in the rate of actin

polymerization in RACK1-silenced cells compared to control (Figure 3.3.3). In this analysis, I measured the increment of FI arbitrary units per time frame on each focus and determined the maximum actin polymerization rate using a logistic regression model. Although this methodology is not the most appropriate to measure actin polymerization, the reduction in actin polymerization rate found in RACK1-KD cells (Figure 3.3.3 B) suggests RACK1 promotes actin polymerization. The link between RACK1, Src and actin polymerization during *Shigella* invasion remains to be confirmed by further studies.

Analyses of actin polymerization rate are usually performed *in vitro* using purified components (e.g. actin, actin nucleator, ATP, etc.) or cell extracts [427,428]. Although the methodology used here is not the most appropriate to measure actin polymerization I could speculate *in vitro* measurements of actin polymerization rates in the presence of RACK1 should increase the rate of filament elongation. Although in the co-IP experiment, actin was found as an interacting partner of RACK1, only partial colocalization between RACK1 and actin was observed in the entry focus (Table 3.1 and Figure 3.3.1 A). Previous studies support the lack of RACK1 and actin colocalization [324–326]. Interestingly, RACK1 is a substrate of Abl kinase [271]. RACK1 phosphorylation by Abl promotes FAK activation, indicating that RACK1 activity is tightly regulated during FA assembly and possibly during *Shigella*-induced actin polymerization [271]. Therefore, a whole lysate extract should be used instead of purified components to study the actin polymerization rate *in vitro* since the action of RACK1 seems to be mediated by secondary players rather than by direct binding to actin.

Another critical *Shigella* effector required for invasion is IpaA, which binds to the FA components vinculin and talin [138,145]. The IpaA-vinculin interaction promotes actin depolymerization at *Shigella*'s entry site, enhancing actin turnover [140,142]. Deleting *IpaA* reduces bacterial internalization by 20% after 30 min of infection, while vinculin overexpression increases bacterial internalization up to 10 times in HeLa cells [137]. Although deficient in internalization, the Δ*ipaA* mutant induces actin foci at a frequency similar to WT *Shigella*. When Tran Van Nhieu *et al.* analyzed the percent of bacteria associated with actin foci, they found WT *Shigella* colocalized with actin foci during the first 15 minutes

of infection. No actin foci-associated bacteria were found after 30 min of infection. However, the Δ*ipaA* mutant remained associated with actin foci after 30 min of infection, suggesting an extension in foci duration [137]. These findings are consistent with my observations in RACK1-KD cells, where the entry foci lasted longer. I believe longer foci duration caused a reduction in the number of infected cells and the number of internalized bacteria (Gal3+ *Shigella*) per cell (Figure 3.3.4 B-C). Notably, I found that RACK1 interacts with vinculin (Table 3.1), an interaction validated by Filho *et al*. showing RACK1 binds to vinculin upon mast cell activation [326]. Filho *et al*. suggested the RACK1-vinculin interaction could mediate antigen-induced F-actin rearrangements [326]. Perhaps the interaction of RACK1 with vinculin mediates IpaA-induced actin rearrangements facilitating *Shigella* invasion.

Interestingly, the bacterial pathogen *Yersinia pseudotuberculosis* which also uses a T3SS to translocate effector proteins into host cells, secretes the effector YopK which interacts with RACK1. This interaction promotes the phagocytosis resistance of *Y. pseudotuberculosis* [7], a process called antiphagocytosis required to escape destructiopoln by macrophages. YopK regulates translocation of other bacterial effector that impair actin cytoskeleton rearrangements blocking phagocytosis [429]. In contrast, *Shigella* uses T3SS effectors to induce invasion of host cells, a process that involves profuse actin polymerization promoted by RACK1 (Figures 3.3.2-3). Perhaps the interaction between RACK1 and YopK inhibits phagocytosis by blocking RACK1-mediated actin polymerization. Although our Co-IP coupled to MS analysis did not yield any *Shigella* effectors as RACK1 interactor, *Yersinia* and *Shigella* directly or indirectly exploit RACK1 activity to promote pathogenesis.

Given that many host proteins targeted by *Shigella* are interacting partners of RACK1, it is not surprising RACK1 silencing results in actin polymerization defects and invasion impairment. *Shigella* hijacks the same pathways and protein components involved in FA assembly. Thus, evaluating Src, Cdc42, Rac1 and vinculin recruitment and activation in RACK1-silenced cells during *Shigella* infection would be of great interest to elucidate the mechanism underlying RACK1's control of *Shigella*'s entry foci. More importantly, the invasion defect observed in RACK-KD cells might contribute to the growth defect

found in the gentamycin assay (Figure 3.2.2 A), as a lower invasion rate could slow down primary and secondary infections. Additionally, I used a Δ*icsA* mutant of *Shigella* which cannot spread from cell to cell, thus facilitating evaluation of primary infected cells. Similar to WT *Shigella*, Δ*icsA* infected fewer RACK1-KD cells than control cells showing primary infection of HeLa cells relies on RACK1-dependant actin foci polymerization (Figure3.3.4 D).

4.2.2 RACK1 is not involved in *Shigella* vacuolar escape

The mechanisms used by *Shigella* to escape the containment of the endocytic vacuole are not well understood. Insertion of the IpaB-IpaC translocon into the vacuolar membrane has been suggested as the primary mechanism [151,92]. While IpaC has a predominant role since expression of IpaC by the normally membrane-bound intracellular bacterium *Salmonella* leads to vacuolar lysis [150]. However, no single *Shigella* effector deletion completely abolishes vacuolar escape, underlining the multifactorial nature of the process. On the other side, many host factors assist vacuolar rupture [154]. The most remarkable are the endocytic markers Rab5, Rab11 and EEA1, revealing a pivotal role of vesicle trafficking and the endocytic pathway in vacuolar escape [154]. However, *Shigella* actively blocks the endocytic maturation process by secreting the inositol 4-phosphatase IpgD, which induces PI5P accumulation in endosomal membranes, blocking the binding of the endosome markers EEA1 and LAMP-1/2 [154,166]. Consistent with these findings, *Shigella* was rarely found in association with EEA1 (Figure 3.4.2 A, top row), and no association of LAMP1 was observed here (Figure 3.4.2 A, middle row). However, one limitation of this experiment is that the cells were not pre-treated with chloroquine to inhibit endosome-lysosome fusion and subsequent loss of LAMP1 signalling. Other authors have reported around 20% of LAMP-1 colocalization with *Shigella* in chloroquine-treated macrophages [430,431]. Thus, I might have missed the LAMP1 targeting of SCVs in HeLa cells.

Massive accumulation of Rab11 positive macropinosomes follows *Shigella* entry into epithelial cells along with transient recruitment of Rab5 vesicles [154,162]. Recruitment of galectin-3 (Gal-3), a host protein that binds to exposed glycans, to the SCV marks initial

damage to the vacuolar membrane [157,159]. Just before Gal-3 recruitment, the Rab11 positive macropinosomes bind to the SCV, suggesting they trigger vacuolar damage [154,160]. *Shigella* uses IpgD to promote macropinosome formation and vacuolar escape, as demonstrated by a phosphatase inactive IpgD mutant that fails to recruit Rab11-macropinosomes and shows delayed escape time [154,162]. However, since the macropinosomes do not fuse with the SCV, it is unclear how they promote escape [162]. After vacuolar damage, *Shigella* exits from the SCV, followed by vacuole fragmentation into membrane remnants that quickly lose Gal-3 signal [158,160].

I investigated whether RACK1 was required for the early events of *Shigella*'s infection cycle following internalization. Although RACK1 did not colocalize with Gal-3+ SCVs (Figure 3.4.1 A), I sought to assess whether RACK1 silencing affects vacuolar escape. For this, I used live-cell microscopy to capture the dynamics of *Shigella* infection steps right after internalization. No significant difference was detected in the time needed for *Shigella* to escape the SCV between control and RACK1-KD cells (Figure 3.4.1 C). On average, the SCV turned positive for Gal-3 8.42±5.2 min after entry foci initiation in both control and RACK1-KD cells. This result aligns with several studies that report vacuolar escape occurs between 7 to 10 min after *Shigella* is internalized by HeLa cells [158,154,164,147]. I also measured the time between Gal-3 recruitment and the first signs of actin polymerization at one pole of the bacterium. *Shigella* induced the formation of an actin node after ~11 min in control cells and after ~12 min in RACK1-KD cells (Figure 3.4.1 B-C). The actin node then elongated to form an actin tail in ~ 17 min in control cells and ~18 min in RACK1-KD cells (Figure 3.4.1 B-C). Similarly, Ray et al. reported that *Shigella* triggers actin tail polymerization ~19 min after internalization [147]. While no significant differences were found between control and RACK1-silenced cells, it was interesting to see that the early events in the *Shigella* life cycle follow a reproducible timeline.

The membrane remnants generated after *Shigella* exits the SCV act as danger signals triggering autophagy [167,168]. Xenophagy, a selective form of autophagy, captures invading pathogens inside autophagosomes that fuse with lysosomes to degrade their content [169]. Ubiquitinated Gal-3+ SCVs and membrane remnants are recognized by the xenophagy

receptors p62 and NDP52, which subsequently recruit the canonical autophagy marker LC3 [168,171,172]. Given that RACK1 participates in autophagosome biogenesis [285], I sought to evaluate if RACK1 played a role in recruiting LC3 to the SCV. But first, I assessed if LC3 colocalized with *Shigella*. Confocal imaging of infected Hela cells confirmed LC3 colocalization with *Shigella* (Figure 3.4.2 A, lower panel). Then, I performed live imaging on *Shigella*-infected cells expressing GFP-LC3 and Gal-3-Orange. LC3 was associated with SCVs as soon as the vacuoles turned Gal-3 positive (Figure 3.4.2 B, 0 min), but LC3 was not recruited to cytosolic bacteria. A critical limitation of this experiment is that *Shigella* was not fluorescently labelled. Thus, the possibility of LC3 binding to cytosolic bacteria could not be discarded entirely. However, Campbell-Valois et al. supports my findings. Using a *Shigella* strain expressing a transcription-based secretion activity reporter (TSAR), the authors showed that LC3 is only recruited around secreting bacteria within vacuoles and not cytoplasmic *Shigella* [172].

The time-lapses also showed LC3+ vesicles were recruited to the LC3+/Gal3+ SCV and seemed to engulf Gal-3+ membrane remnants (Figure 3.4.2 B, 10 min). This observation suggests LC3+ membrane remnants are cleared by autophagy. However, only 18% of all Gal-3+ SCVs were targeted by LC3 (Figure 3.4.2 C). Thus, an alternative mechanism must remove the membrane remnants generated after *Shigella* exits the SCV. Another possibility is that *Shigella* inhibits LC3 binding to the SCV. Indeed, VirA and IcsB act synergistically to antagonize LC3 binding to the SCV, as demonstrated by the increased number of LC3-positive and LAMP-2-positive SCVs found in VirA and IcsB single and double mutants [167,172].

When analyzing the effect of RACK1-KD in LC3 targeting, I found a reduction in the percentage of LC3+/Gal3+ SCVs (~12%) compared to control (~18%, Figure 3.4.2 C). Although this difference was not statistically significant, RACK1 may promote LC3 localization to the SCV. Notably, high variability was observed in the frequency of LC3+/Gal3+ SCVs found in control cells. Since I only conducted this experiment once, due to time constraints, I cannot draw any conclusions about the role of RACK1 in LC3 targeting to SCVs.

4.2.3 RACK1 silencing does not impact *Shigella* intracellular replication or apoptosis inhibition

One of the hallmarks of *Shigella* infection is its ability to replicate to high numbers within epithelial cells without impacting the host cell's energy production, despite ongoing pyruvate and amino acid exploitation by *Shigella* [382,394]. RACK1 has been linked to amino acid metabolism in yeast [432]. Therefore, a reduction in nutrient availability might have caused the growth defect of *Shigella* observed in RACK1-KD cells. The Δ*icsA* mutant has been used before to test intracellular replication since this deletion prevents spread between host cells, simplifying the analysis of bacterial replication [394]. Δ*icsA Shigella* grew to high numbers in the cytoplasm of infected cells, rendering individual cell counting impractical (Figure 3.5.1 C). Thus, I evaluated intracellular bacteria total area and FI as a proxy of bacterial growth. No significant difference was found in these two parameters between RACK1-KD and control cells (Figure 3.5.1 D-E), indicating RACK1 does not affect intracellular replication. While similar image-based approaches have been used before to quantify intracellular bacteria replication [433,434], this could also be done by staining with bromodeoxyuridine (BrdU). This thymidine analogue is incorporated into replicating DNA and has been used to evaluate *Listeria monocytogenes* intracellular growth [435].

Active bacterial replication in the cytoplasm leads to the accumulation of PAMPs recognized by the inflammasome triggering cell death. Using a complex array of effectors, *Shigella* antagonizes apoptosis, necrosis-necroptosis, and pyroptosis of epithelial cells. IpgD, VirA, OspC1 and *Shigella*'s LPS block apoptosis by inhibiting caspase-8 and caspase-3 activation [135,191–193]. *Shigella* regulates cell death timing by secreting OspD2 and OspD3. OspD2 inhibits VirA-mediated necrosis and OspD3 antagonizes OspC1's indirect induction of necroptosis [192,436]. Furthermore, *Shigella* uses the effectors OspC3 and the ubiquitin ligases IpaH7.8 and IpaH9.8 to impair pyroptosis, maintaining epithelial cell integrity to safeguard its intracellular replication niche [200,201,203,204]. RACK1 has both pro- and anti-apoptosis functions, depending on cellular conditions or interacting partners [289]. Thus, I evaluated whether RACK1 had a role in *Shigella*-mediated inhibition of cell death pathways.

Flow cytometry analysis of apoptosis and necrosis was performed using annexin V-FITC-7AAD double staining. Except for KD-95, no significant differences were found in cell death levels induced by *Shigella* in RACK1-KD cells compared to control cells (Figure 3.5.2). KD-95 showed fewer late apoptotic cells than control cells, suggesting RACK1 may have a pro-apoptotic role during *Shigella* infection. However, it is difficult to draw any conclusions since none of the other parameters, including cell cytotoxicity, were altered (Figure 3.5.2). A limitation of these experiments was the length of infection. *Shigella* did not induce detectable apoptosis earlier than 12 h after infection. After such a long incubation time, intracellular bacterial numbers were probably very high, rendering the cells prone to lysis and agglomeration. Lysed cells were lost, and cell clusters were not included in the analysis, possibly underestimating the levels of apoptosis in KD-95 cells. A better approach would be to evaluate earlier events in cell death, such as caspase activation. The use of *Shigella* mutants defective in cell death inhibition could be helpful too. For example, OspC3 modifies caspase-4, blocking its activation and subsequent cleavage of the pore-forming protein GSDMD which triggers pyroptosis [202]. In contrast, a Δ*ospC3* mutant induces GSDMD cleavage detectable by western blotting [192,202]. Similarly, a Δ*ospC1* mutant has been used to evaluate apoptosis by detection of caspase-8 cleavage, which is usually absent in cells infected by the WT strain [192].

Cytosolic *Shigella* is also targeted by IFN-γ–induced GBPs, which promote caspase-4 activation, leading to pyroptosis [201,205]. I evaluated whether RACK1 was involved in GBP binding to *Shigella*. When treating cells with IFN-γ, a modest increment in GBP1 binding to *Shigella* was observed in RACK1-KD cells compared to control (Figure 3.5.3 C, Table 3.1). However, this was not statistically significant, confirming that RACK1 is not involved in *Shigella*-mediated inhibition of cell death pathways. Conversely, I found 3.9% of *Shigella* were GBP1+ in untreated control cells, which increased to 11% in IFN-γ treated cells (Table 3.1). Most studies report between 30 to 40% of GBP1 targeting after IFN-γ induction [205,437]. This discrepancy was probably due to the longer infection time used here; most studies measure GBP targeting one h after infection. Here I infected the cells for three h before GBP1 immunostaining. The low percentage of GBP1+ bacteria might indicate

Shigella manages to escape GBP recognition. Indeed, Wandel *et al.* showed that *Shigella* uses IpaH9.8, an E3 ubiquitin ligase, to target GBPs for degradation by the proteasome [205].

4.2.4 RACK1 promotes *Shigella* actin tail polymerization, actin-mediated motility and cell-to-cell spreading

After escape from the SCV, *Shigella* induces actin polymerization at one pole of the bacterium, forming an actin node that quickly elongates into an actin tail (Figure 3.4.1 B). The actin tail confers actin-mediated motility and allows bacteria to engage the host cell membrane, forming *Shigella*-containing protrusions that infect neighbouring cells [100,214,215]. The molecular mechanisms enabling actin tail polymerization have been extensively studied in *Shigella* and other cytoplasmic pathogens [4]. *Shigella*'s outer membrane protein IcsA is the central mediator of actin tail polymerization and bacterial intracellular motility [100,219]. IcsA preferentially localizes to the old pole of the bacterium, where it recruits the actin polymerization machinery [223].

The essential proteins required for *in vitro* IcsA-mediated actin polymerization are N-WASP, Arp2/3, cofilin and ADF/capping protein [232]. In the cell, the nucleation promoting factor N-WASP remains in an auto-inhibited stage established by intramolecular interactions between the verprolin homology-cofilin-acidic (VCA) domain and the GTPase binding domain (GBD) [438]. Activation is usually mediated by Cdc42, which binds to the GBD to release the VCA domain [231]. Likewise, IcsA binds to the GBD, displacing the VCA domain, which activates the actin polymerization complex Arp2/3 [233]. Then, the active Arp2/3 complex binds to the side of an actin filament, initiating actin polymerization, forming a branch [117,234]. Both Cdc42 and IcsA mediated actin polymerization require the binding of Toca-1 to N-WASP to increment actin polymerization efficiency [235,439]. The recruitment of Toca-1 to *Shigella*'s surface preceding actin tail polymerization seems to be mediated by IcsB [175]. Profilin, an actin monomer-binding protein, also binds to N-WASP, promoting actin tail polymerization [237]. Moreover, phosphorylation of N-WASP by Bkt and Abl kinases prompts N-WASP recruitment to *Shigella* and actin tail polymerization [118,236]. Therefore, aside from the minimum requirements for *in vitro* polymerization, many host

factors are required for *Shigella*-mediated actin tail polymerization *in vivo*, and most converge on N-WASP activity modulation.

Given that RACK1 promoted efficient actin focus formation during *Shigella* invasion, I hypothesized that RACK1 was also needed for actin tail polymerization. Indeed, when I evaluated the number of *Shigella* associated with actin tails, I found a significant reduction in the percentage of tailed bacteria in RACK1-KD cells compared to control. On average, 42.4% of *Shigella* were associated with actin tails in control cells, which was reduced to 24.8% when RACK1 expression was silenced (Figure 3.6.1 B-C). Other studies have reported between 30 to 41% of tailed *Shigella* in HeLa cells and up to 60% in mouse-embryo fibroblasts (MEFs) [175,205,440]. Reduction in the percentage of tailed bacteria has been related to various host factors. For example, Toca-1 silencing leads to 28% less tailed *Shigella* [235]. Transient expression of a truncated N-WASP without the profilin-binding site reduces actin tails to 12% [237].

Shigella infecting MEFs from mice lacking Abl kinase induce 55% fewer actin tails than Abl+ MEFs [440]. Burton *et al*. reported that Abl phosphorylates N-WASP, promoting actin tail polymerization. Interestingly, *Shigella* infecting cells expressing an N-WASP mutant lacking the Abl-phosphorylation site form abnormal actin tails ~3 μm shorter than tails formed in MEFs expressing WT N-WASP [440]. Although I used a different method to measure the length of the tails, a comparable reduction in tail length was observed here. In RACK1-KD cells, *Shigella* polymerized less elongated tails, ~2 μm shorter than those formed in control cells (Figure 3.6.2). RACK1 is phosphorylated by Abl, which promotes RACK1 association with FAK and subsequent focal adhesion assembly [271]. Therefore, it is plausible that Abl-mediated phosphorylation of RACK1 enhances RACK1 activity during actin tail polymerization.

Given that RACK1 is a known kinase scaffold [5], RACK1 could also stabilize active Abl and shuttle the kinase to its active site, facilitating N-WASP phosphorylation. In this scenario, RACK1-KD cells would behave like Abl null cells. Indeed, as in Abl null cells, fewer *Shigella* were associated with actin tails and the tails formed were shorter in RACK1-

KD cells (Figure 3.6.1-2). Furthermore, and in agreement with the invasion impairment observed in RACK1-KD cells (Figure 3.3.4 B-C) in this study, *Shigella* invasion is also reduced in Abl null MEFs, which was due to decreased Crk phosphorylation [118]. Active Crk binds to cortactin, triggering Arp2/3-mediated actin polymerization and subsequent *Shigella* internalization [115]. Thus, Abl controls *Shigella* entry and actin tail polymerization by phosphorylating Crk and N-WASP, respectively. Assessment of N-WASP and Crk phosphorylation in RACK1-KD cells could help decipher the role that RACK1 plays in modulating Abl function during *Shigella* infection.

Another intracellular pathogen that also induces actin tail polymerization is *Listeria. monocytogenes.* The intracellular life cycles of *Shigella* and *Listeria* are very similar. However, the mechanism used for actin tail polymerization is quite different. *Listeria* uses ActA, which mimics N-WASP, to directly activate the Arp2/3 complex initiating actin polymerization [232]. Given that RACK1 regulation of actin polymerization seems to be related to Abl-mediated phosphorylation of N-WASP, I suspect RACK1 might not promote polymerization of *Listeria*'s tails.

The Arp2/3 complex is essential for *Shigella* entry and actin tail assembly [115]. Depleting the Arp2/3 complex from platelet extracts completely abolishes actin tail formation by *E. coli* expressing IcsA, while tail polymerization and motility are rescued by adding purified Arp2/3 complex [234]. Here I found RACK1 interacts with Arp2, one of the seven subunits forming the Arp2/3 complex (Figure 3.8.2 A). Immunofluorescent detection of Arp2 (Figure 3.8.2 B) confirmed previous observations describing the Arp2/3 complex localizes throughout the length of *Shigella*'s actin tail [441,442]. Then, I evaluated whether RACK1 silencing impairs Arp2 localization to *Shigella* but found no significant difference in the percentage of Arp2+ bacteria in RACK1-silenced cells compared to control cells (Figure 3.8.2 C). Moreover, RACK1 did not colocalize with the actin tail (Figure 3.6.1 A), suggesting the role of RACK1 in actin tail polymerization is indirect and does not involve Arp2/3 recruitment to *Shigella.*

Having determined that actin tail polymerization is impaired in RACK1-KD cells, I investigated whether the observed reduction in tail length could affect *Shigella*'s

intracellular motility. Understanding the actin-mediated motility behaviour of *Shigella* could also provide information on how the tail determines the bacterial path and speed. Most descriptions of bacterial movement patterns use models that do not accurately describe intracellular motility, such as *E. coli* and other extracellular flagellated bacteria [443]. Among actin-propelled bacteria, *Listeria monocytogenes* has been widely used to describe actin tail polymerization dynamics and motility [444]. Unfortunately, the study of *Shigella*'s actin-mediated movements has been neglected, probably because *Shigella* is not motile in Xenopus egg extracts, which is a commonly used experimental system for actin-based motility [445].

Live-cell imaging was used here to characterize *Shigella*'s actin-mediated intracellular motility. I manually tracked bacterial trajectories by following *Shigella*'s movements along the focal plane. The recorded trajectories were then used to analyze various parameters, including speed, sinuosity, and directional change of *Shigella* trajectories. There is significant variability in the rate of *Shigella* movement reported in the literature, mainly depending on experimental settings and cell types. In infected cells, *Shigella* moves at a speed between 0.05 to 0.43 μm/sec, the lowest was in HT-29 cells, while the highest speed was found in Vero cells [225,236,237,440,441,446]. *E. coli* expressing IcsA moves at an average speed of 0.14 μm/sec in Xenopus egg extract, similar to the rates documented for *Listeria* (0.2 μm/sec) in the same experimental settings [113,441]. In this work, the speed of *Shigella* in control HeLa cells was 0.045±0.02 μm/sec (Figure 3.6.3 B-C). This is seven times slower than the speed reported in HeLa cells by Mostowy et al. (0.32 μm/sec) and comparable to the rates described in *Shigella* infecting HT-29 cells [181,236]. The discrepancy of my findings with those described in the literature could be due to the methodology used here. I measured the average speed of trajectories recorded from images taken every 1 min for two h. Consequently, the trajectories were recorded over many time frames, whereas Mostowy et al. measured *Shigella* speed from trajectories followed for 1 to 10 min (images were taken every 10 sec) [181]. In this manner, the authors probably missed low-speed intervals commonly observed in *Shigella* trajectories (Figure 3.6.3 F).

Although there was substantial variability in the speed of the trajectories analyzed, RACK1 silencing significantly reduced the speed of *Shigella*'s actin-mediated motility (Figure 3.6.3 B-C). This was not surprising since a reduction in tail length has been shown to minimize speed [440]. Moreover, the bacterial trajectories generated in RACK1-KD cells were less dispersed than in control cells (Figure 3.6.3 B), suggesting less continuous (intermittent) movements. Therefore, I evaluated if RACK1 silencing correlated with intermittent low-speed intervals. For this, I empirically determined a threshold speed (0.02 μm/sec) by analyzing time points where *Shigella* showed little to no displacement. These low-speed intervals were called tumble events, and faster speed intervals were called run events. Tumbling events are characteristic of flagellated bacteria motility, resulting in an erratic change in the trajectory's direction [400]. Conversely, in *Shigella* trajectories, tumbling events were followed by a decrease in speed (more than one tumble) without abrupt changes in the direction of movement (Figure 3.6.3 F). When comparing tumble times in control and RACK1-KD cells, *Shigella* trajectories from RACK1-KD cells were interrupted by significantly more tumbling events (Figure 3.6.3 G). These interruptions should directly impact speed, as demonstrated by analysis of *Listeria* trajectories in bovine brain extracts artificially thickened with methylcellulose to slow bacterial motility [447].

During trajectory recording, I observed that bacterial motility stopped when *Shigella* lost or reduced the length of its tail and resumed movement when the tail elongated again (data not shown). This observation, along with the increased tumble event frequency found in RACK1-silenced cells, suggests RACK1 mediates actin tail elongation, reducing the time *Shigella* expends tumbling. Less tumbling probably results in more linear trajectories. I tested this by determining trajectory sinuosity and average directional change (DC). As suspected, the sinuosity index was significantly lower in control cells than in RACK1-KD cells (Figure 3.6.3 D). This means the trajectories were less tortuous in control cells. I could have done a correlation analysis to confirm the link between less tumbling and low sinuosity index. In contrast to the sinuosity results, there were no significant differences in the average DC of trajectories recorded in control and RACK1-KD cells (Figure 3.6.3 E). Interestingly, high variability in the trajectories' DCs was found, suggesting *Shigella* trajectories experience random changes in direction probably determined by physical

obstacles and host cell boundaries. This has been demonstrated in *Listeria* trajectories. Motile *Listeria* colliding with mitochondria results in directional changes and more convoluted trajectories than bacteria moving in mitochondria-free domains [448]. Therefore, it is possible *Shigella* loses/shortens its tail upon mitochondria encounter, and RACK1 mediates actin tail re-polymerization/elongation helping *Shigella* resume motility.

Furthermore, it has been reported that the natural variation in *Listeria* trajectory speed arises from temporal fluctuations in actin tail density [449]. Quantification of actin tail FI could be used to determine the relative density of the tail and correlate it to speed changes during bacterial trajectories [449]. Although I did not measure actin tail fluorescence in the time-lapse experiments, I was able to quantify the average FI of actin tails in fixed samples. Surprisingly, no significant differences were found in the tail's FI measured in control and RACK1-KD cells (Figure 3.6.1 E). I also quantified the tail's area and found a significant reduction in the size of the tails formed in RACK1-KD cells compared to control cells (Figure 3.6.1 D). Moreover, a weak negative correlation between tail area and FI was found in RACK1-KD cells, suggesting smaller tails tend to be more fluorescent. However, this correlation was not significant in control cells (Figure 3.6.1 F). It is challenging to interpret these findings since I only calculated the average FI per tail and not the total FI per tail.

From the tail's area calculations and trajectory speed results, I could predict that smaller tails, although probably denser (higher FI), provide less propelling force than longer and dimmer tails. Studies of *Listeria*'s actin tails support this hypothesis. Soo and Theriot reported a negative correlation between speed and tail density [449]. The authors observed that as the *Listeria* trajectory speed increased, the density (FI) of the tail decreased, and the tail stretched further behind the bacterium (tail elongation) [449]. Thus, the length of the actin tail positively correlates to bacterial speed, while the tail's density negatively correlates to speed. These findings agree with the observations reported here. Longer tails and higher speed trajectories were found in control cells, whereas shorted tails and slower speed trajectories were observed in RACK1-KD cells (Figures 3.6.2 and 3.6.3 C). Measurement of the FI variations of the actin tail during *Shigella* trajectories will clarify the correlations between actin tail density and its propelling force.

Shigella can access the cytosol of adjacent cells without transiting through the extracellular milieu. Propelled by an actin tail, *Shigella* deforms the host cell's membrane forming a bacteria-containing protrusion that projects into neighbouring cells [238]. As the protrusion moves away from the primary infected cell, it collapses and resolves into a membrane-bound compartment endocytosed by the target cell [250]. To gain access to the cytoplasm of the secondary infected cell, *Shigella* escapes a double-membrane vacuole derived from the primary and secondary infected cells' membranes [450]. Given that cell-to-cell spreading relies on actin-based motility, I suspected RACK1-KD silencing would also impair spreading as *Shigella*'s motility was impaired in these cells. Therefore, I assessed *Shigella*'s cell-to-cell spread using a modified plaque assay.

Plaque-based assays are commonly used to determine the titer of lytic viruses and have been adapted to assess *Shigella* cell-to-cell dissemination [375,376]. As *Shigella* spreads in a confluent cell monolayer, it forms areas of infection called plaques. The size of the plaques correlates with the efficiency of bacterial spreading. I improved the classical plaque assay by using the nontoxic polymer Methocel instead of a dense agarose overlay to restrict bacterial extracellular dissemination. The translucent nature of Methocel allowed live-cell imaging of the infected monolayers without disturbing *Shigella*'s plaques with cumbersome fixing and staining procedures. In addition, the 96-well format of the modified assay provided high throughput screenings capabilities. Most analyses of *Shigella* cell-to-cell spreading found in the literature used the classical plaque assay that requires longer infection times (48-72 h) to visualize the plaques after Giemsa staining [243,451,452]. Since I imaged *Shigella* plaques using a microscope, less incubation time was required to obtain prominent plaques. Consequently, the plaque size reported by other authors is significantly bigger than what I report here. For example, Duncan-Lowey et al. reported an average plaque area of ~0.6 mm^2 for CaCo-2 cells and ~0.35 mm^2 for MEFs after 48 h of infection with *Shigella* [248]. With the methodology developed here, *Shigella* plaques formed in HeLa cells had an average area of 0.132±0.11 mm^2 after ten h of infection; and the plaques formed in CaCo-2 cells were 0.313±0.24 mm^2 after only 15 h of infection (Figure 3.7.3 B). Thus,

aside from the advantages of live-cell imaging and high throughput, the modified plaque assay conveniently reduced experiment time.

Having determined the best conditions for the modified plaque assay, I then assessed the impact of RACK1 silencing on the ability of *Shigella* to form plaques in HeLa and CaCo-2 cells. Consistent with a defect in intracellular motility, the plaque area was significantly reduced in all three HeLa and CaCo-2 RACK1-KD cell lines analyzed (Figure 3.7.3 B). To further confirm these findings, I captured high magnification time-lapse images of infected HeLa cells overlaid with Methocel and manually followed cell-to-cell spreading that originated from one infected cell. *Shigella* infected a new cell every 15 to 30 min during the first 3 hours of infection. After this time, *Shigella*'s spreading rate slowed down, infecting a new cell every 45 min to one h (Figure 3.7.4 A). To my knowledge, this is the first time the rate of *Shigella* spreading has been characterized in this manner. A study assessing *Listeria* spreading, with similar imaging resolution as used here, reported a small percentage of bacteria infecting far away cells [453]. These "pioneer" bacteria determined the size of the infection plaque. I did not observe such pioneer behaviour in *Shigella* infected monolayers. This might be due to the Methocel restricting the diffusion of extracellular bacteria in the media, which probably better represents the gradual spreading of *Shigella* in the colonic epithelium. Furthermore, consistent with the plaque assay results, the cumulative number of infected cells over ten h of infection was significantly reduced in RACK1-KD cells compared with control (Figure 3.7.4 B). Together, these results are consistent with a pivotal role of RACK1 in actin tail modulation, leading to efficient *Shigella* spreading in epithelial cells.

4.3 RACK1 plays a role in actin filament turnover

The actin cytoskeleton is a complex network in the cell's cytoplasm, exerting various functions, including cell motility, cell division, endocytosis, and vesicular trafficking. The building block of the actin cytoskeleton is globular (G) actin that assembles into polar double helix filaments (F-actin) [454]. The resulting filaments have a fast-growing barbed end where ATP-bound G-actin monomers are added and a slow-growing pointed end from

which ADP-bound G-actin is dissociated [226,227]. *De novo* F-actin polymerization starts with a nucleation phase where a G-actin trimer or nucleus is formed. Nuclei assembly triggers rapid filament elongation that stabilizes after reaching a steady-state equilibrium between polymerization and depolymerization [226]. *De novo* filament formation is kinetically unfavourable, yet actin filaments in live cells polymerize and depolymerize very rapidly. F-actin turnover is regulated by a large group of actin-binding proteins (ABPs) classified according to their functions. These include G-actin binding proteins, actin nucleators, and severing and capping proteins [455]. Monomer binding proteins such as profilin maintain a pool of unpolymerized actin and inhibit actin nucleation [456]. Profilin function is counteracted by actin nucleators, such as the Arp2/3 complex and formins, which initiate branched and unbranched filaments, respectively [117,240]. Capping proteins bind and stabilize filaments while severing proteins, such as ADF/cofilin, break filaments generating two uncapped ends available for rapid polymerization [457,458].

The results from *Shigella* invasion, actin tail polymerization, intracellular motility and cell-to-cell spreading analyses suggest that RACK1 is likely a regulator of actin cytoskeleton dynamics during *Shigella* infection. This raised the question of whether RACK1's function is specific to *Shigella*-mediated manipulation of the actin cytoskeleton or responds to other actin polymerization inducers. Actin turnover can be pharmacologically manipulated using actin binding drugs, such as jasplakinolide (Jasp) and cytochalasin D (CytoD) [406,377,459]. Conversely, Jasp induces actin filament stabilization *in vitro*, while *in vivo* it disrupts actin filaments, inducing polymerization of G-actin into amorphous aggregates [377,407]. As reported in the literature, treatment with 0.2 μM Jasp caused the formation of multiple actin aggregates throughout the cytoplasm of HeLa cells (Figure 3.8.3 B) [407,460]. I quantified the number of aggregates, total aggregate area, and their total FI per cell to assess the extent of actin polymerization induction. Upon Jasp treatment, RACK1-KD cells developed fewer actin aggregates than control cells, and the aggregates were smaller and dimmer, indicating they contained less F-actin (Figure 3.8.3 C-E). Therefore, RACK1 silencing rendered the cells less susceptible to the effects of Jasp, suggesting RACK1 promotes actin polymerization. This observation was consistent with the actin polymerization impairment observed in RACK1-KD cells infected with *Shigella*.

To assess if RACK1 also regulates actin depolymerization, I treated the cells with CytoD, a fungal toxin that binds to the filament's barbed end, preventing actin filament elongation [406]. Since depolymerization is not inhibited, the net effect of CytoD treatment is actin depolymerization. Small actin aggregates or puncta were formed after CytoD treatment, but disassembly of stress fibres and cell adhesions was the most prominent effect (Figure 3.8.4 A). Other studies have described similar results, reporting a significant cell size reduction after long-term treatment with CytoD [378,461,462]. Given that the cells were treated for only 1.5 h, I measured the area and FI of F-actin-rich structures but not the size of the cells. I reasoned that if RACK1 participates in actin depolymerization, RACK1-silenced cells should maintain more F-actin-rich structures than control cells. No significant differences were found in the area and FI of F-actin-rich structures left after CytoD treatment in control and RACK1-KD cells (Figure 3.8.4 C-D), suggesting that RACK1 is not involved in CytoD mediated actin depolymerization.

Furthermore, I used fluorescence recovery after photobleaching (FRAP) to evaluate actin polymerization dynamics in real-time. In FRAP, the protein of interest is tagged to a fluorophore, whose fluorescence is irreversibly photobleached within a discrete region using a high-power laser. The fluorescence is recovered over time as new fluorescent proteins replace the bleached ones. Here I used GFP-tagged actin to quantify the rate of fluorescence recovery in control and RACK1-KD cells. F-actin assembles into complex structures ranging from rapidly polymerizing branched networks found in membrane protrusions (membrane ruffles) to more stable thick actin bundles called stress fibres (SFs) [463]. Thus, I evaluated actin turnover in SFs and ruffles to capture slow and rapid actin polymerization processes. As expected, GFP-actin fluorescence was recovered faster in membrane ruffles than in SFs (Figure 3.8.5 A). The halftime of recovery ($t_{1/2}$) was 11.3±4.6 sec for membrane ruffles and 16.1±9.3 sec for SFs. Similar $t_{1/2}$ times have been reported by other authors validating my results [464,465].

Interestingly, when I assessed the turnover of actin filament assembly in RACK1-silenced cells, I found a significant increase in fluorescence recovery times in ruffles but

not in SFs compared to control cells (Figure 3.8.5 C and E). The ruffle results were consistent with a defect in actin polymerization in RACK1-KD cells. Another explanation of the slower actin turnover observed in RACK1-KD is that the lack of RACK1 promoted filament stabilization. A Jasp control could help elucidate the role of RACK1 in actin turnover.

The similar turnover rates observed in SFs from control and RACK1-KD cells were intriguing, especially because RACK1 overexpression has been reported to increase the number of SFs in CHO cells [327]. SF polymerization is controlled by the small GTPase RhoA and its effectors Rho-associated protein kinase (ROCK) and Dia1 [466,467]. ROCK inhibits ADF/cofilin-mediated disassembly of filaments, while the formin Dia1 facilitates the polymerization of long non branched actin filaments [467,468]. There are conflicting reports about the link between RACK1 and RhoA. In breast cancer cells, RACK1 was shown to promote migration through interaction with RhoA and activation of the RhoA/Rho kinase pathway [469], while RACK1 silencing in Jurkat cells does not affect RhoA activation. This indicates RACK1-mediated regulation of RhoA is cell type specific.

In contrast to SFs, rapid plasma membrane movements such as those found in ruffles are governed by Abl and Src kinases [470,471], and involve Cdc42/Rac1-mediated activation of N-WASP [472]. Active N-WASP subsequently activates the Arp2/3 complex promoting actin polymerization in membrane ruffles. Since RACK1 is a substrate and regulates Abl and Src activation [271,473,328,474], RACK1 activity likely promotes actin turnover in highly dynamic structures rather than stable ones. Additionally, Abl and Src are involved in *Shigella* entry to host cells, and Abl is required for actin tail polymerization [116,118,425,440]. Therefore, RACK1 likely promotes actin polymerization during *Shigella* infection through Cdc42/Rac1-N-WASP rather than RhoA GTPase. It is also possible Src and Abl promote N-WASP activation thereby increasing actin polymerization rate. Overall, the actin-binding drug experiments revealed that RACK1 promotes actin polymerization but not depolymerization. FRAP analysis supported these findings showing significant actin-turnover inhibition of membrane ruffles in RACK1-KD cells.

4.4 Model of RACK1 function in *Shigella* infection

In conjunction with previous reports of RACK1 functions and *Shigella* regulation of host factors, my thesis results led me to propose a model of RACK1's role during *Shigella* infection. As schematized in Figure 4.1, **(a)** *Shigella* induces profuse actin polymerization and membrane ruffling, forming an F-actin entry focus leading to bacterial uptake by epithelial cells (ECs). RACK1 activity promotes fast actin polymerization at the entry foci, probably through its interaction with Abl and Src kinases. Active Src contributes to *Shigella* entry by activating cortactin while Abl phosphorylates Crk. Active Crk binds active cortactin leading to Arp2/3-mediated actin polymerization of branched networks. These networks rapidly deform the membrane, forming membrane ruffles that engulf the bacterium. **(b)** After internalization, *Shigella* remains in the vacuole for ~8 min before damaging the vacuole's membrane and escaping to the cytoplasm peeling off the membrane remnants. **(c)** In the cytoplasm, *Shigella* induces actin polymerization at one pole of the bacterium forming an actin node that elongates into an actin tail conferring intracellular motility. RACK1 promotes actin tail polymerization and tail elongation. The mechanism here could also be mediated by RACK1-Abl interaction since Abl is required for actin tail polymerization. Abl phosphorylates N-WASP, enhancing its activation, leading to recruitment of the Arp2/3 complex inducing actin tail elongation. **(d)** Motile *Shigella* encounters obstacles in the cytoplasm such as mitochondria or the cell's membrane leading to actin tail loss and tumbling behaviour. A nonmotile bacterium can either replicate or re-polymerize and elongate a new actin tail to resume movement. Here, the activity of RACK1 is also needed, as demonstrated by the increased tumbling time found in RACK1-KD cells. **(e)** As *Shigella* elongates its tail, propulsion force accumulates in the bacterium's back pole, eventually deforming the EC's membrane to form a bacterium containing membrane protrusion. This protrusion is then endocytosed by a neighbouring cell. In RACK1-KD cells, *Shigella* cannot elongate its tail as efficiently as in control cells. Short-tailed bacteria are probably less likely to accumulate enough force to form protrusions, which in consequence impairs cell-to-cell spreading. **(f)** Notably, RACK1 regulation of actin polymerization is not restricted to *Shigella* infection. RACK1 mediates Jasplakinolide-induced polymerization of actin aggregates. Additionally, as demonstrated by FRAP

experiments, RACK1 regulates actin turnover in membrane ruffles, likely involving Src and Abl kinases signalling.

Figure 4.1. Model of RACK1 function in *Shigella* infection.
Diagram describing the various steps during *Shigella*'s intracellular replication cycle where RACK1 is involved. **a.** RACK1 (green) is recruited to the entry focus promoting actin polymerization, likely by interacting with Src and Abl. These kinases phosphorylate (P) cortactin and Crk, respectively. The cortactin-Crk complex activates Arp2/3-mediated actin polymerization of branched filaments. **b**. The bacterium rapidly escapes from the *Shigella*-containing vacuole (SCV), generating membrane remnants. **c.** RACK1 promotes actin tail polymerization and elongation, probably by facilitating Abl-mediated phosphorylation of N-WASP. Active N-WASP recruits the Arp2/3 complex to one pole of the bacterium inducing actin tail polymerization. **d.** As *Shigella* rapidly moves through the cell's cytoplasm, it encounters mitochondria which could slow down motility by inducing actin tail shortening or actin tail loss. **e.** Untailed *Shigella* replicates and induces actin tail polymerization, requiring RACK1 to regain motility. **f.** Aside from infection, RACK1 promotes actin turnover in membrane ruffles, which is likely mediated by Abl and Src kinases. Similarly, RACK1 facilitates jasplakinolide (Jasp)-induced polymerization of F-actin aggregates.

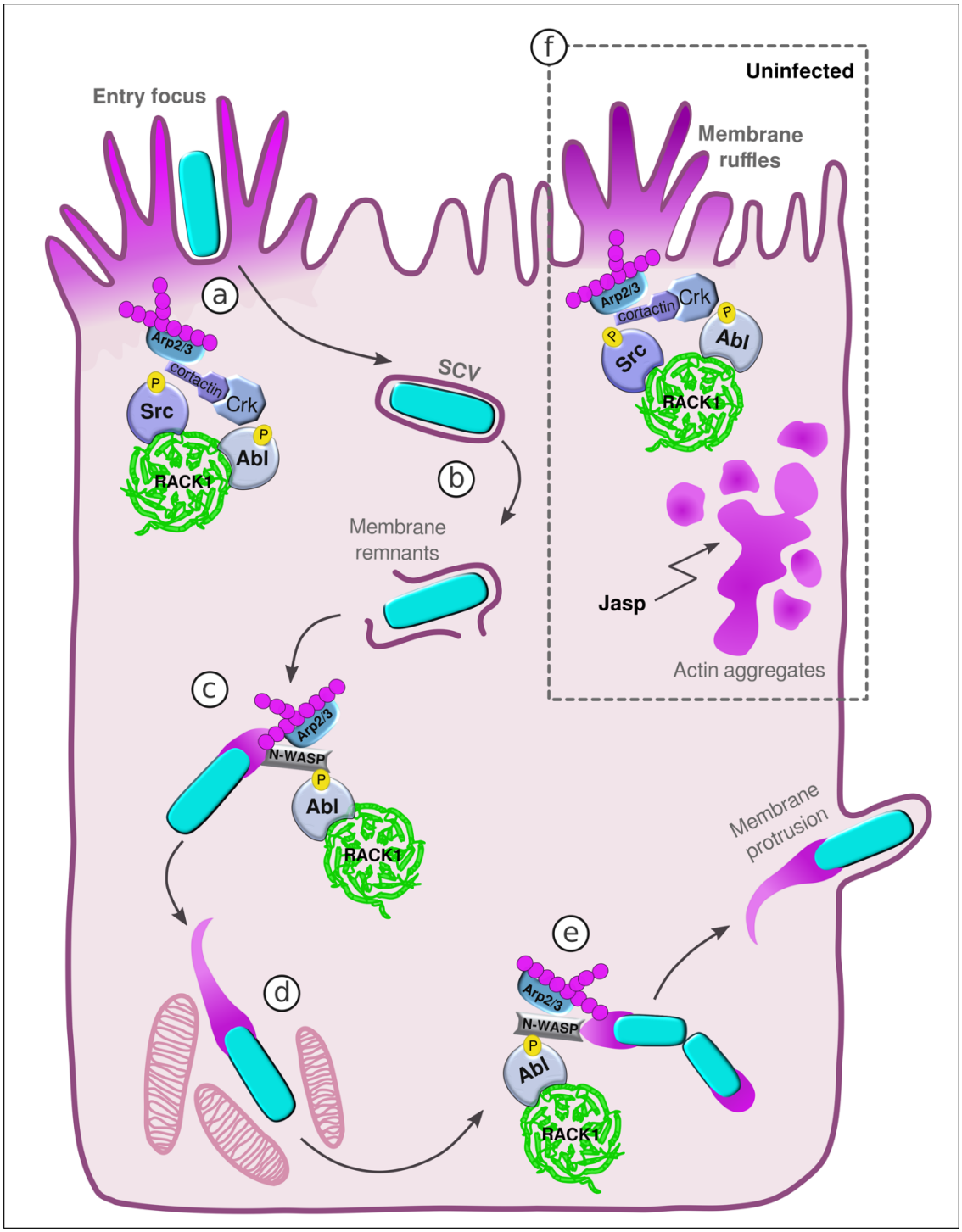
Entry focus
a
Arp2/3
cortactin
Crk
Src
P
Abl
RACK1
SCV
b
Membrane
remnants
c
Arp2/3
N-WASP
P
Abl
RACK1
d
e
Arp2/3
N-WASP
P
Abl
RACK1
Membrane
protrusion
f
Uninfected
Membrane
ruffles
Arp2/3
cortactin
Crk
P
Src
Abl
RACK1
Jasp
Actin aggregates

4.5 Concluding remarks and further work

Considering the burden of diarrhoeal diseases in low- to middle-income countries, understanding how one of the most prevalent causal agents, the strictly human pathogen bacterium *Shigella*, invades, replicates and spreads in the intestine is essential. Here I provide new insights into *Shigella*'s mechanisms to subvert the host actin cytoskeleton. I hypothesized that *Shigella flexneri* exploits the host scaffold protein RACK1 to manipulate actin cytoskeleton dynamics leading to efficient invasion and spreading. To test this hypothesis, I systematically investigated the role of RACK1 in all the critical steps of *Shigella*'s intracellular life cycle.

Using advanced microscopy techniques and automated image data analysis, I characterized yet another function of the already multifunctional RACK1. I discovered that RACK1 promotes *Shigella* growth in HeLa cells and mediates colonization of *Drosophila*'s intestine. An in-depth analysis of *Shigella* infection dynamics revealed that RACK1 is recruited to the entry site, and it is required for *Shigella*-mediated induction of actin polymerization at the entry focus promoting bacterial internalization. RACK1 also promoted actin tail polymerization and tail elongation enhancing *Shigella*'s intracellular motility. Efficient actin tail elongation ensures the bacterium engages the host cell membrane with enough force to form *Shigella*-containing protrusions allowing infection of neighbouring cells. Pharmacologically induced actin polymerization demonstrated that RACK1's role in actin polymerization is not specific to *Shigella* infection. FRAP experiments further confirmed that RACK1 promotes actin turnover in rapidly polymerizing membrane ruffles. In contrast, RACK1 was not required for *Shigella* escape from the vacuole, intracellular replication, LC3 targeting blockage and cell death inhibition.

Although the mechanism by which RACK1 stimulates actin polymerization was not identified, I propose RACK1 promotes actin polymerization through its interaction with the kinases Abl and Src. These two kinases are involved in *Shigella* internalization, and Abl is also required for actin tail polymerization. The use of RACK1 mutants lacking the Src and Abl binding domains could confirm the direct link between RACK1 interaction

with these kinases and actin dynamic modulation. Since RACK1 is a known kinase regulator, future experiments should also evaluate Abl and Src activation in RACK1 silenced cells. For this, phosphorylation of the Src substrate cortactin and Abl substrate Crk can be assessed using commercially available antibodies. Actin polymerization *in vitro* using whole cell lysates could be used to confirm RACK1's observed increases of actin polymerization rates. Given that *Shigella* hijacks the same pathways and protein components involved in focal adhesion assembly, evaluating FAK, Cdc42, Rac1 and vinculin activation in RACK1-silenced cells during *Shigella* infection would further elucidate the mechanism underlying RACK1 control of *Shigella*-induced actin polymerization.

Overall, this work shows how *Shigella* relies on the scaffold protein RACK1, a regulator of many key signalling pathways, to invade and spread in epithelial cells. Therefore, RACK1 could be a potential drug target to control *Shigella* colonization of the colonic epithelium. A possibility supported by the colonization impairment observed in *Drosophila* intestines depleted of RACK1 expression. Finally, this research also provides new assays and data analysis methodologies to study *Shigella* infection and actin cytoskeleton dynamics.

APPENDIX A MEDIA, BUFFERS, AND OTHER SOLUTIONS

Antibiotics:

Ampicillin: 100 µg/mL diluted in 70% ethanol (EtOH, Sigma, Cat. No. A9518-5G)

Kanamycin: 50 µg/mL diluted in ddH_2O

Carbenicillin: 100 µg/mL in ddH_2O

Gentamycin: 100 µg/mL diluted in ddH_2O

1X Phosphate-Buffered Saline (PBS)

140 mM NaCl (Bioshop, Cat. No. SOD004.205)

3 mM KCl (Sigma, Cat. No. 7447-40-7)

8 mM Na_2HPO_4 (BioShop, Cat. No. SPD579.500)

1 mM KH_2PO_4 (Sigma, Cat. No. P5655-500G)

Adjust pH to 7.4

50X TAE buffer

242 g Tris-base (Life technologies, Cat. No.15504-020)

57.1 mL glacial acetic acid (Fisher Scientific, Cat. No. A38-212)

100 mL 0.5M EDTA, pH 8 (Anachemie, Cat. No. 37560-300)

ddH2O to 1 litre

Dilute to 1X before use.

12% resolving gel for SDS-PAGE

For 1 mini gel of 1 mm (7.5 mL)

3.2 mL ddH20

1.8 mL of 1.5 M Tris-HCl pH 8.8 (Fisher Scientific, Cat. No. BP153-500)

2.25 mL of 40% w/v Acrylamide/Bis-acrylamide [37.5:1] (BioShop, Cat. No. ACR005.502)

75 mL of 10% SDS (Fisher Scientific, Cat. No. BP166100)

75 mL of 10% ammonium persulfate (APS, Fisher Scientific, Cat. No. BP179-100)

7.5 µL of N- Tetramethylethylenediamine (TEMED, Sigma, Cat. No. 110-18-9)

4% Stacking gel for SDS-PAGE

For 2 mini gels of 1 mm (3 mL)

1.9 mL ddH20

750 µL of 0.5 M Tris-HCl pH 6.8

300 µL of 40% w/v Acrylamide/Bis-acrylamide [37.5:1]

30 µL of 10% SDS

30 µL of 10% APS

3 µL of TEMED

10 X Ponceau S

For 100 mL:

2 g Ponceau S (Allied Chemical, Cat. No. 628)

30 g trichloroacetic acid (Sigma, Cat. No. T9159-100G)

30 g sulfosalicylic acid (Sigma, Cat. No. 304851-84-1)

Add ddH_20 up to 100 mL

APPENDIX B FIJI MACROS AND R SCRIPTS

B.1. Fiji Macro for section 2.10.2: Analysis of intracellular replication in fixed samples

The following macro was executed in Fiji to measure the area covered by Δ*icsA Shigella* and fluorescence intensity.

```
//First prep the images by converting to .tiff

//then run this to make average projections of the cells and bacteria channels
separately
//run as a chunck from line 9 to 21
//change line 19, see below
  imgArray = newArray(nImages);
  for (i=0; i<nImages; i++) {
    selectImage(i+1);
    imgArray[i] = getImageID();
  }

//now we have a list of all open images, we can work on it:
  for (i=0; i< imgArray.length; i++) {
    selectImage(imgArray[i]);
   // INSERT MACRO HERE
   run("8-bit");
   run("Duplicate...", "duplicate channels=1");  //change here for cells channel
=1 or     bacteria channel = 2
   run("Z Project...", "projection=[Average Intensity]");
  }

//close all images that won't be needed, keep the AVE proj

//Manually outline cells to create a mask:
//using the Polygon tool select the area of complete cells, do not include
incomplete cells.
//example
      makePolygon(444,13,412,5,219,0,209,12,217,45,205,80,225,104,260,127,301,137
,416,95,427,67);
      roiManager("Add");//add to ROI manager
// do the same with all the cells

//in the ROI manager, measure area and mean grey value of all cells, and save
results
      roiManager("Measure");
      saveAs("Results",
"/home/karla/Documents/880/IcsA_06.05.2021_3h/cells_area_FI/CellsAVE_NS_IcsA-
5.csv");

//transform the cell's ROIs into a mask to be used with the speckle inspector
tool
      selectWindow("AVG_NS_IcsA-3h_5-1"); //with the cell's mask selected
      run("Binary (0-255) mask(s) from Roi(s)", "show_mask(s) s
      save_in=/home/karla/Documents/SpinningDisk_Dal/20201215/Jasp_exp3_p2/Masks/
s     suffix=[] save_mask_as=tif rm=[RoiManager[size=8, visible=true]]");
      run("Invert"); //to select cells not background in next step
```

```
//For the bacteria segmentation:
//Select the AVERAGE image and run this to make a mask
//make sure to test the threshold that fits best
//from line 45-55
      run("Duplicate...", " ");
      run("Subtract Background...", "rolling=50");
     run("Gaussian Blur...", "sigma=2");
      //run("Threshold...");
      resetThreshold();
      //setAutoThreshold("Huang dark no-reset"); //For 06.05 expt
      setAutoThreshold("Li dark");  //For 09.05 expt
      setOption("BlackBackground", false);
      run("Convert to Mask");
      run("Set Measurements...", "area mean display redirect=None decimal=4");
      run("Analyze Particles...", "display summarize add");

//now input the cells and bacteria mask into the speckle inspector tool
//primary = cells mask
//secondary = bacteria mask
      run("Speckle Inspector", "primary=Masks secondary=AVG_NS_IcsA-3h_5-1
redirect=None show=secondary secondary_object");
      roiManager("Show All");

//manually eliminate any bacteria outside the cells if any
//example below
      roiManager("Select", 63);
      roiManager("Delete");

//select the original AVERAGE image of the bacteria and apply the ROIs
//at this point each ROI (bacteria clump) will have a cell number assigned
//ROI manager run measure area and mean grey value, then save the data
      roiManager("Show All");
      roiManager("Measure");
      saveAs("Results",
"/home/karla/Documents/880/IcsA_06.05.2021_3h/Speckles_area_FI/speckle_NS_IcsA_5.cs
v");
      run("Close All");

// do the same with all images
// End of script
```

B.2. Fiji Macro for section 2.10.3: Targeting of *Shigella* by guanylate-binding proteins (GBPs).

The following macro was executed in Fiji to measure the number of all bacteria and the number of GBP+ bacteria.

```
//first define the preprocessing steps
//For the GBP1 positive bacteria --> channel 2
run("Duplicate...", "duplicate channels=2");
run("Subtract Background...", "rolling=50");
run("Mean...", "radius=2");
run("Gaussian Blur...", "sigma=1");

//setThreshold(27, 255);
setOption("BlackBackground", false);
setAutoThreshold("RenyiEntropy dark no-reset");
run("Convert to Mask");
run("Analyze Particles...", "exclude clear summarize add"); //remove "clear" when
running in batch!!!

//Bacteria segmentation to do the counting
//For all the bacteria --> DAPI channel
//set up the code to get the best segmentation
      run("Duplicate...", "duplicate channels=1");
      run("Grays");
      run("Subtract Background...", "rolling=50");
      run("Mean...", "radius=2");
//setThreshold(19, 255);
      setAutoThreshold("Huang dark no-reset");
      setOption("BlackBackground", false);
      run("Convert to Mask");
//Adjust the size here to obtain only bacteria not nucleus
      run("Analyze Particles...", "size=20-500 pixel exclude clear summarize
add");
 //remove "clear" when running in batch!!!

//For the GBP+ bacteria --> GBP+ use red channel
//set up the code to get the best segmentation
      run("Duplicate...", "duplicate channels=1");
      run("Grays");
      run("Subtract Background...", "rolling=50");
      run("Mean...", "radius=2");
//setThreshold(19, 255);
      setAutoThreshold("Huang dark no-reset");
      setOption("BlackBackground", false);
      run("Convert to Mask");
      run("Analyze Particles...", "size=0-inf pixel exclude clear summarize add");
 //remove "clear" when running in batch!!!
```

```
//                            RUN MACRO BATCH
//Insert the above steps to obtain data for GBP+ bacteria first and then all
bacteria
// clear the results table of any previous measurements
      run("Clear Results");
// The next line prevents ImageJ from showing the processing steps during
// processing of a large number of images, speeding up the macro
      setBatchMode(true);
// Show the user a dialog to select a directory of images,make sure the directory
only has the required images. other files make macro fail
      inputDirectory = getDirectory("Choose a Directory of Images");
// Get the list of files from that directory
      fileList = getFileList(inputDirectory);
      for (i = 0; i < fileList.length; i++)
      {
      processImage(fileList[i]);
      }
      setBatchMode(false); // Now disable BatchMode since we are finished
      updateResults();  // Update the results table so it shows the filenames

// Show a dialog to allow user to save the results file
      outputFile = File.openDialog("Save results file");
// Save the results data
      saveAs("results",outputFile);
      function processImage(imageFile)
      {
// store the number of results before executing the commands
      prevNumResults = nResults;
      open(imageFile);

// Get the filename from the title of the image that's open
// We do this instead of using the imageFile parameter
      filename = getTitle();
//Copy here the parameters set to segment the bacteria e.g.
//For all bacteria --> DAPI channel
      run("Duplicate...", "duplicate channels=1");
      run("Grays");
      run("Subtract Background...", "rolling=50");
      run("Mean...", "radius=2");
//setThreshold(19, 255);
      setAutoThreshold("Huang dark no-reset");
      setOption("BlackBackground", false);
      run("Convert to Mask");
//Adjust the size here to obtain only bacteria not nucleus
// ONLY GET THE SUMMARY DATA
      run("Analyze Particles...", "size=20-500 pixel exclude summarize add");
      // Now loop through each of the new results
      for (row = prevNumResults; row < nResults; row++)
      {
            setResult("Filename", row, filename);
      }
      close("*");  // Closes all images
}// end of script
```

B.3. Fiji Macro for section 2.11.8: Modified plaque assay.

This macro was executed in Fiji to measure the area of the plaques formed by *Shigella* in HeLa and CaCo-2 cells.

```
// batch mode of a directory of images
run("Clear Results"); // clear the results table of any previous measurements
// The next line prevents ImageJ from showing the processing steps during
// processing of a large number of images, speeding up the macro
setBatchMode(true);
// Show the user a dialog to select a directory of images
//have only images on the directory, other files make macro fail
inputDirectory = getDirectory("Choose a Directory of Images");
//make sure the directory only has the required images
// Get the list of files from that directory
// NOTE: if there are non-image files in this directory, it may cause the macro to
crash
fileList = getFileList(inputDirectory);
for (i = 0; i < fileList.length; i++)
{
    processImage(fileList[i]);
}
setBatchMode(false); // Now disable BatchMode since we are finished
updateResults();  // Update the results table so it shows the filenames

// Show a dialog to allow user to save the results file
//outputFile = File.openDialog("Save results file");
// Save the results data
//saveAs("results",outputFile);
function processImage(imageFile)
{
      // store the number of results before executing the commands, so we can add
the filename just to the new results
      prevNumResults = nResults;
      open(imageFile);
      // Get the filename from the title of the image that's open for adding to
the results table
      // We do this instead of using the imageFile parameter so that the directory
path is not included on the table
      filename = getTitle();
//if using an image stack, add "stack" at the end where indicated
//substract background depending on images
run("Subtract Background...", "rolling=50 stack"); //stack
run("Maximum...", "radius=5 stack");//stack
      run("Median...", "radius=10 stack");//stack
      run("Gaussian Blur...", "sigma=15 stack");//stack
```

```
//change the threshold settings acording to data
//MinError --> HeLa plaques
//Huang --> CaCo plaques, depends on plaques
      setOption("BlackBackground", true);
      run("Convert to Mask", "method=MinError background=Dark calculate black");
//this one was too permisive
      run("Convert to Mask", "method=Huang background=Dark calculate
black");//this method worked well for caco expts 28.05 and 25.05
      run("Convert to Mask", "method=Default background=Dark calculate
black");//default worked better for 15.05
run("Dilate", "stack");//,"stack"
      run("Fill Holes", "stack");//,"stack"
      run("Duplicate...", "duplicate");
      run("Subtract Background...", "rolling=90 stack");
      run("Median...", "radius=10 stack");
      run("Gaussian Blur...", "sigma=10 stack");
      run("Convert to Mask", "method=Mean background=Dark calculate");
      run("Dilate","stack");
      run("Dilate", "stack");
      run("Fill Holes","stack");

// You should adjust the size input according to the sizes of nuclei in your
images
//run("Analyze Particles...", "size= 1-Infinity circularity=0-1.00 summarize add
stack");

      run("Analyze Particles...", "size= 0.1-Infinity circularity=0-1.00 exclude
summarize add stack");

      // Now loop through each of the new results, and add the filename to the
"Filename" column
      for (row = prevNumResults; row < nResults; row++)
      {
            setResult("Filename", row, filename);
      }

      close("*");  // Closes all images
} // end of script
```

B.4. Fiji Macro for section 2.12.1: Analysis of actin polymerization and depolymerization using actin-binding drugs.

This macro was used to segment F-actin aggregates and F-actin-rich structures in cells treated with Jasp and CytoD.

```
//open Max projection version of the video
//duplicate last time point of the video

//KD92 images show slower actin polymerization thus the Factin normal structures
(stress fibers)
//are picked up by the segmentation
//substract diferent values and use different threshold to efficiently pick up
real Factin speckles
run("Duplicate...", " ");
run("Subtract...", "value=25"); //12 for images 9-12
run("Unsharp Mask...", "radius=1 mask=0.60");
run("Median...", "radius=1");

setAutoThreshold("Li dark");
setAutoThreshold("Default dark");
setThreshold(30, 255);//25  for images 9-12
run("Convert to Mask");

//manually make mask of cells and tramsform to mask
run("Binary (0-255) mask(s) from Roi(s)", "show_mask(s)
run("Invert"); // to get the cells in black
//save mask of cells

//open all videos and run this
//make sure the videos are set in the last time point
imgArray = newArray(nImages);
  for (i=0; i<nImages; i++) {
    selectImage(i+1);
    imgArray[i] = getImageID();
  }
  //now we have a list of all open images, we can work on it:
  for (i=0; i< imgArray.length; i++) {
    selectImage(imgArray[i]);
    // INSERT MACRO HERE
       run("Duplicate...", " ");
       run("Subtract...", "value=25"); //12 for images 9-12 //25 for 13-16
       run("Unsharp Mask...", "radius=1 mask=0.60");
       run("Median...", "radius=1");

       setAutoThreshold("Li dark");
       setAutoThreshold("Default dark");
       setThreshold(30, 255);//25  for images 9-12  //30 for 13-16
       run("Convert to Mask");
  }
```

```
//use the "Speckle Inspector" to analyze the F-actin granules
run("Speckle Inspector", "primary=mask_14_cells.tif secondary=mask_14_granules.tif
redirect=None show=secondary speckle statistic secondary_object");

//open the AVErage projection version of the video and duplicate the last time
point
//use the ROIs from the inspector to measure area and mean FI of all the granules
inside the cells selected in the cells mask
//save the results
selectWindow("Jasp-0.2uM_exp3-p2_t2h.czi - Jasp-0.2uM_exp3-p2_t2h.czi #14_14-
1.tif"); //ave projection
roiManager("Show All");
roiManager("Measure");
saveAs("Results",
"/home/karla/Documents/SpinningDisk_Dal/20201215/Jasp_exp3_p2/Results_granules_NS-
14.csv");

//use the inspector again to measure the speckles and clasify them using a size
threshold
//first only select the granules bigger than 25 pixels
run("Speckle Inspector", "primary=mask_14_cells.tif secondary=mask_14_granules.tif
redirect=None min_secondary_size=25 show=secondary speckle statistic
secondary_object");
close();
//copy the data from the speckle list only and save

//repeat selecting the granules smaller than 25
run("Speckle Inspector", "primary=mask_14_cells.tif secondary=mask_14_granules.tif
redirect=None max_secondary_size=25 show=none speckle statistic
```

```
//for dtermining the FI at time point 0 of the treated cells
//open all the time 0 images
//run:
imgArray = newArray(nImages);
  for (i=0; i<nImages; i++) {
    selectImage(i+1);
    imgArray[i] = getImageID();
  }
  //now we have a list of all open images, we can work on it:
  for (i=0; i< imgArray.length; i++) {
    selectImage(imgArray[i]);
    // INSERT MACRO HERE
   //run("Duplicate...", " ");
   run("Images to Stack", "name=Stack_AVE_t0 title=[] use");
  }

//SAVE THE STACK
saveAs("Tiff",
"/home/karla/Documents/SpinningDisk_Dal/20201215/Jasp_exp3_p2/AVE_proj/Stack_AVE_t
0.tif");
run("Close All");

//Prepare the stack for segmentation
run("Duplicate...", "duplicate");
run("Subtract...", "value=2 stack");
run("Gaussian Blur...", "sigma=2 stack");
//use the weka segmentation tool to segment the cells and then transform it to a
mask
call("trainableSegmentation.Weka_Segmentation.trainClassifier");
call("trainableSegmentation.Weka_Segmentation.getResult");
selectWindow("Classified image");
run("Convert to Mask", "method=Huang background=Dark calculate");
run("Watershed", "stack");

//generate the ROIs and apply them to the AVE images of time point 0
run("Analyze Particles...", "clear add stack");
selectWindow("Stack_AVE_t0.tif");
roiManager("Show All");
roiManager("Measure");
saveAs("Results", "/home/karla/Documents/SpinningDisk_Dal/20201211/Jasp-
0.2_p3/Results_cells_t0.csv");
run("Close All");

//script ends here
```

B.5. R script for section 2.11.3: Evaluation of entry foci dynamics.
This script describes how to calculate actin polymerization to the entry foci using the package "`growthrates`".

```
#install.packages("growthrates")
library(growthrates) #To calculate actin recruitment
library(tidyverse) # data handling
library(ggthemes) #aesthetics
library(ggpubr) #plots
library(reshape2) #data handling
library(cowplot) #visualization of multiple plots in one page
#-------------------------------------------------------------------------------
#Determine maximum growth rates by nonlinear fits for a series of experiments
#NS Data
splitted.data <- multisplit(Mean1 ~ time | Label, data = FociNS)

## show which experiments are in splitted.data
names(splitted.data)

## get table from single experiment
dat <- splitted.data[["AVG_Entry_12-1-2.tif"]]
dat
fit0 <- fit_spline(dat$time, dat$Mean1)
fit1 <- all_splines(Mean1 ~ time | Label ,data = FociNS, spar = 0.1)
res_fit1 = results(fit1)
fit0

## initial parameters
p <- c(coef(fit0), K = max(dat$Mean1))

#use the lowest mean value of the group as y0
p2   <-c(y0 = 4, mumax = 0.003091225 , K = max(dat$Mean1))
## avoid negative parameters
lower = c(y0 = 1, mumax =       0.00001, K = 1)
upper = c(y0 = 1, mumax = 0.1, K = 64)
## fit all models
fit2 <- all_growthmodels(Mean1 ~ time | Label,
                         data = FociNS,
                         FUN=grow_logistic,
                         p = p,
                         lower = lower,
                         ncores = 2)

res_fit2 <- results(fit2)
plot(res_fit1$mumax, res_fit2$mumax, xlab="smooth splines", ylab="logistic")
```

```
## experimental: nonlinear model as part of the formula
fit3 <- all_growthmodels(Mean1 ~ grow_logistic(time, parms) | Label,
                         data = FociNS,
                         p = p,
                         lower = lower,
                         ncores = 2)
par(mfrow =c(6,5))
par(mar =c(2.5, 4, 2, 1))
plot(fit3)
dev.off()
res_fit3 = results(fit3)
plot(res_fit2$mumax, res_fit3$mumax, xlab="smooth splines", ylab="logistic")

#fix some strange fittings by changing the min y
p2   <-c(y0 = 2, mumax = 0.003091225, K = max(dat$Mean1))
fit4 <- all_growthmodels(Mean1 ~ grow_logistic(time, parms) | Label,
                         data = FociNS,
                         p = p2,
                         lower = lower,
                         ncores = 2)
par(mfrow =c(4,4))
par(mar =c(2.5, 4, 2, 1))
plot(fit4)
dev.off()
res_fit4 = results(fit4)


#-------------------------------------------------------------------------------
#Determine maximum growth rates by nonlinear fits for a series of experiments
#KD data
splitted.data_kd <- multisplit(Mean1 ~ time | Label, data = Foci92)

## show which experiments are in splitted.data
names(splitted.data_kd)

## get table from single experiment
dat_kd <- splitted.data_kd[["AVG_Entry_8-1-1.tif"]]
dat_kd
fit0_kd <- fit_spline(dat_kd$time, dat_kd$Mean1)
fit1_kd <- all_splines(Mean1 ~ time | Label ,data = Foci92, spar = 0.1)
res_fit1_kd = results(fit1_kd)
```

```
## initial parameters
p_kd <- c(coef(fit0_kd), K = max(dat_kd$Mean1))
p_kd
#use the mumax value from p_kd
p_kd2  <- c(y0 = 3, mumax = 6.148241e-04, K = max(dat_kd$Mean1))
p_kd2

#find the highest Mean value in the Foci92 data to determine upper K
## avoid negative parameters
lower_kd = c(y0 = 1, mumax =    0.00001, K = 1)
upper_kd = c(y0 = 1, mumax = 0.1, K = 67)

## fit all models
fit2_kd <- all_growthmodels(Mean1 ~ time | Label, data = Foci92,
FUN=grow_logistic,
                            p = p_kd, lower = lower_kd, ncores = 2)
par(mfrow =c(4, 4))
par(mar =c(2.5, 4, 2, 1))
plot(fit2_kd)
dev.off()
res_fit2_kd <- results(fit2_kd)
dev.off()
plot(res_fit1_kd$mumax, res_fit2_kd$mumax, xlab="smooth splines", ylab="logistic")

## experimental: nonlinear model as part of the formula
fit3_kd <- all_growthmodels(Mean1 ~ grow_logistic(time, parms) | Label, data =
Foci92,
                            p = p_kd, lower = lower_kd, ncores = 2)
par(mfrow =c(6, 4))
par(mar =c(2.5, 4, 2, 1))
plot(fit3_kd)
dev.off()
res_fit3_kd = results(fit3_kd)

fit4_kd <- all_growthmodels(Mean1 ~ grow_logistic(time, parms) | Label, data =
Foci92,
      p = p_kd2, lower = lower_kd, ncores = 2)

par(mfrow =c(4, 4))
par(mar =c(2.5, 4, 2, 1))
plot(fit4_kd)
dev.off()

res_fit4_kd = results(fit4_kd)
```

```
#Compare the results

#Fit 3 with grow_logistic
boxplot(res_fit3$mumax,res_fit4_kd$mumax)
ggdensity(res_fit3 ,
          x = "mumax",
          add = "mean", rug = TRUE
)
wilcox.test(res_fit3$mumax,res_fit4_kd$mumax)
t.test(res_fit3$mumax,res_fit4_kd$mumax)

wilcox.test(res_fit3$y0,res_fit3_kd$y0)
t.test(res_fit3$y0,res_fit3_kd$y0)



#fit4 for kd and fit 3 for NS work better, they have better fits
boxplot(res_fit3$mumax,res_fit4_kd$mumax)
wilcox.test(res_fit3$mumax,res_fit4_kd$mumax)
#p-value = 0.006447
t.test(res_fit3$mumax,res_fit4_kd$mumax)
#mean of x  mean of y
#0.023924372 0.008920061


#make the plot
res_fit3 = res_fit3 %>% mutate(ID = "NS")
res_fit4_kd = res_fit4_kd %>% mutate(ID = "KD-92")

#merge the data frames using the functions
ALL_gr = bind_rows(res_fit3, res_fit4_kd)

ggdensity(ALL_gr ,
          x = "mumax",
          add = "mean", rug = TRUE,
          color = "ID", palette = c("#00AFBB", "#E7B800")
)
wilcox.test(mumax ~ ID, ALL_gr) #p-value = 0.006447

#END OF SCRIPT
```

B.6. R script for section 2.11.4: Evaluation of *Shigella*'s intracellular motility.

The script below describes how the `trajr` package was used to analyze *Shigella* trajectories.

```
library(tidyverse) #for data handling
library(trajr) #to analyze trajectories
library(ggpubr) #for plotting
library(reshape2) #for data handling
library(ggthemes) #for aesthetics
library(dplyr) #for data handling

###Movement analysis of data from 10052021, dsRED Shigella

#import data
setwd("~/Documents/SpinningDisk_Dal/dsRED_tails/20210510/ManualTrack") #desktop
computer
NS_08 = read.csv("Results from WT_exp4_2h_10052021_08 in µm per sec.csv", header =
TRUE)
NS_07 = read.csv("Results from WT_exp4_2h_10052021_07 in µm per sec.csv", header =
TRUE)
NS_03 = read.csv("Results from WT_exp4_2h_10052021_03 in µm per sec.csv", header =
TRUE)
KD_01 = read.csv("Results from WT_exp4_2h_10052021_01 in µm per sec.csv", header =
TRUE)
KD_02 = read.csv("Results from WT_exp4_2h_10052021_02 in µm per sec.csv", header =
TRUE)

#Modify the track.n number so then files can be merged and have unique track IDs
NS_08$Track.n. = sub("^", "08_",  NS_08$Track.n.)
NS_07$Track.n. = sub("^", "07_",  NS_07$Track.n.)
NS_03$Track.n. = sub("^", "03_",  NS_03$Track.n.)

KD_01$Track.n. = sub("^", "01_",  KD_01$Track.n.)
KD_02$Track.n. = sub("^", "02_",  KD_02$Track.n.)

#MERGE THE FILES
#To join two data frames (datasets) vertically, use the rbind function. The two data
frames must have the same variables, but they do not have to be in the same order.

NS_ALL  = rbind(NS_08,NS_07,NS_03)
KD_ALL = rbind(KD_01,KD_02)

#Scale data frame to dimensions in um and time in sec
#remember to change this depending on video information
# time interval: 121.50 sec
# pixel size: 0.2116403 um
pixel <- function(x, na.rm=FALSE) (x*0.2116403)
Interval = 121.50 #sec

Scaled_NS = NS_ALL %>%
  mutate_at(c("X","Y"), pixel, na.rm = TRUE) %>%
  group_by(Track.n.) %>%
  dplyr::mutate(time = Interval*seq_len(n()))
```

```
Scaled_KD = KD_ALL %>%
  mutate_at(c("X","Y"), pixel, na.rm = TRUE) %>%
  group_by(Track.n.) %>%
  dplyr::mutate(time = Interval*seq_len(n()))

#CREATE THE FILES
# Split by track id
splited_NS <- split(Scaled_NS, Scaled_NS$Track.n.)
splited_NS[[1]]
splited_92 <- split(Scaled_KD, Scaled_KD$Track.n.)
splited_92[[2]]

#Prep the data for the Traj package
# Save the files -->set new directory as working directory if necessary
setwd("~/Documents/SpinningDisk_Dal/dsRED_tails/20210510/ManualTrack/Trajectories/"
)

lapply(names(splited_NS), function(x){
  write_csv(splited_NS[[x]], path = paste(x, ".csv", sep = ""))
})

lapply(names(splited_92), function(x){
  write_csv(splited_92[[x]], path = paste(x, ".csv", sep = ""))
})

#put the name of the files on a list
namesoffilesNS = names(splited_NS) %>% paste(".csv", sep = "")
namesoffiles92 = names(splited_92) %>% paste(".csv", sep = "")
namesoffilesNS
namesoffiles92

#make a function to read multiple files into Traj
readMultiple = function(namesoffiles){
  coords = read.csv(namesoffiles, stringsAsFactors = FALSE)
}

#import the data as one Traj object with multiple trajectories
csvStruct = list(x = 3, y = 4,time = "time") #x = "X", y = "Y" remember to change
time2 by time only
rootDir = '.' #means here, or change if necessary

1/Interval
# 0.008230453--> fps
Traj_NS = TrajsBuild(namesoffilesNS,
                     fps =  0.008230453,
                     spatialUnits = "um",
                     timeUnits = "s",
                     csvReadFn = readMultiple,
                     csvStruct = csvStruct,
                     rootDir = rootDir,
                     smoothP = NULL,
                     smoothN = NULL)

Traj_NS[[1]]
TrajLength(Traj_NS[[1]])
TrajStepLengths(Traj_NS[[1]])
```

```
Traj_92 = TrajsBuild(namesoffiles92,
                     fps =  0.01698081,
                     spatialUnits = "um",
                     timeUnits = "s",
                     csvReadFn = readMultiple,
                     csvStruct = csvStruct,
                     rootDir = rootDir,
                     smoothP = NULL,
                     smoothN = NULL)

Traj_92[[1]]


# ------------------------------------------------------------------------
#      Characterize the trajectories using several indexes
#-------------------------------------------------------------------------

quantile(ALL_Traj$Mean_speed)
0%         25%         50%         75%        100%
0.006762468 0.017164745 0.029539614 0.045563595 0.158410984
min(ALL_Traj$Mean_speed)
0.006762468

quantile(ALL_Traj_2$Mean_speed)
0%         25%         50%         75%        100%
0.003280733 0.021555177 0.034339456 0.044735459 0.149112101
min(ALL_Traj_2$Mean_speed)
0.003280733

quantile(ALL_Traj_3$Mean_speed)
0%         25%         50%         75%        100%
0.005703551 0.024409148 0.038360517 0.054051642 0.150957673
min(ALL_Traj_3$Mean_speed)
0.005703551

(0.017164745+0.021555177+0.024409148)/3
#0.02104302

Max_tumbling_speed = 0.02104302 #um/sec
Longest_tumbling = function(Traj){
  Intervs = TrajSpeedIntervals(Traj,slowerThan = Max_tumbling_speed, fasterThan =
NULL)
  #returns time of longest interval or 0 if there is no intervals lower than
threshold
  max(c(0, Intervs$duration))}

mean_tumbling = function(Traj){
  Intervs = TrajSpeedIntervals(Traj,slowerThan = Max_tumbling_speed, fasterThan =
NULL)
  #returns the average length of the intervals
  mean(Intervs$duration)}


#if running this again remember to create a "Traj" object
```

```
#Make a function to analyze trajectories
batch_fx = function(Traj){
  derivs = TrajDerivatives(Traj)  #this outputs 4 vectors -> $speed, $speedTimes,
$acceleration and $accelerationTimes
  #a list for all single value outputs:
  Steps = TrajStepLengths(Traj)
  list(
    TrajVelocity = TrajLength(Traj)/TrajDuration(Traj),
    Mean_Vel = TrajMeanVelocity(Traj),
    Longest_tumbling = Longest_tumbling(Traj), #output: duration in sec
    Mean_tumbling = mean_tumbling(Traj),
    Mean_speed = mean(derivs$speed),           #output: speed in um/sec
    sd_speed = sd(derivs$speed),
    Min_speed = min(derivs$speed),
    Max_speed = max(derivs$speed),
    var_speed = var(derivs$speed),
    Length = TrajLength(Traj), #outputs sum of all distances in every step ()
    Step= mean(Steps),
    var_step = var(Steps),
    Mean_acce =  mean(derivs$acceleration),
    var_acce = var(derivs$acceleration),
    sin = TrajSinuosity(Traj),                #this requires a constant step
length
    sin2 = TrajSinuosity2(Traj),
    straightness = TrajStraightness(Traj),     #value between 0 (infinitely
tortuous) to 1 (a straight line)
    #should only be used to compare the tortuosity of random walks consisting of
a similar number of steps
    DC_mean = mean(TrajDirectionalChange(Traj)),
    DC_sd = sd(TrajDirectionalChange(Traj))   #the angular change (in degrees)
between any two points in the trajectory, divided by the time difference between
the two points.DC mean and standard deviation of trajectories can be used as
index values of non linearity and irregularity respectively )}

#Make a data frame with all the stats
#call TrajsMergeStats, which returns a data frame that contains a row for each
trajectory and a column for each index.
summ_indices_NS = TrajsMergeStats(Traj_NS, batch_fx)
summ_indices_92 = TrajsMergeStats(Traj_92, batch_fx)

#give IDs to the data to merge it
summ_indices_NS = summ_indices_NS %>% mutate(ID = "NS")
summ_indices_92 = summ_indices_92 %>% mutate(ID = "KD")

#merge the data
ALL_Traj = bind_rows(summ_indices_NS, summ_indices_92)

#REEPLACE the NaN values by 0, NaN resulted in the trajectories that didnt have
any tumbling intervals
ALL_Traj$Mean_tumbling = replace(ALL_Traj$Mean_tumbling, ALL_Traj$Mean_tumbling
== "NaN",0)
#Drop the NAs
ALL_Traj = ALL_Traj %>% drop_na
#END OF SCRIPT
```

B.7. R script for section 2.12.2 Fluorescence Recovery After Photobleaching (FRAP).
This script was used to do the FRAP analysis. Only the ruffle analysis is shown below but the same procedure was used to analyze stress fibres.

```
#install.packages("frapplot")
library(frapplot)
#install.packages("xts") #THIS TO HANDLE TIME DATASETS
library(xts)
library(tidyverse)
library(ggpubr)
library(reshape2)
library(ggthemes)
Modifications of formula
##############################################################################
#     MAKE A FEW CHANGES IN FORMULA
##############################################################################

frapprocess2 <- function(ds, time_points) {

  # validate input
  if(!is.list(ds) || is.null(names(ds))) {
    stop("Dataset should be a list of matrices containing data of each group.
         Each item in the list has a name that identifies the group.")
  }
  else {
    len.x <- length(time_points)
    for (i in 1: length(ds)) {
      name <- names(ds)[i]
      len <- length(ds[[i]])

      if(!is.matrix(ds[[i]])) {
        stop(sprintf("Each item in the list is a matrix.
            Each column contains data from one cell/sample.
            The %dth item of the list named %s is not a matrix.", i, name))
      }
      else if(len %% (len.x+1) != 0) {
        stop(sprintf("The number of rows in the %dth item of the list named %s
            does not match the length of the time_points provided.
            The matrix needs %d rows which is 1 + length(time_points).", i, name,
len.x+1))
      }
    }
  }

  group_names <- names(ds)
  num <- length(group_names)

  # normalize data
  for (i in 1: num) {
    cur <- ds[[i]]
    normalized <- t(t(cur)/cur[1,])
    ds[[i]] <- normalized[-1,]   #NORMALIZED DATA FRAME
  }
```

```
# calculate sample mean and standard deviation
sample_means <- matrix(0, nrow = length(time_points), ncol = num)
sample_sd <- matrix(0, nrow = length(time_points), ncol = num)

for (i in 1 : num){
  sample_means[, i] <- rowMeans(ds[[i]])
  for (j in 1 : length(time_points)){
    sample_sd[j, i] <- sd(ds[[i]][j, ]) }}

# non-linear curve fitting
result <- data.frame(group_names = group_names,
                     ymax = rep(0, num),
                     ymin = rep(0, num),
                     k = rep(0, num),
                     halftime = rep(0, num),
                     tau = rep(0, num),
                     total_recovery = rep(0, num),
                     total_recovery_sd = rep(0, num))

mod <- vector("list", num)
parameter <- vector("list", num)
details <- vector("list", num)

for (i in 1 : num){
  cur_dataframe <- data.frame(time = time_points, FR = sample_means[, i])

  c.0 <- max(cur_dataframe$FR) * 1.1
  model.0 <- lm(log(c.0 - FR) ~ time, data = cur_dataframe)
  start <- list(a = exp(coef(model.0)[1]), b=coef(model.0)[2], c=c.0)

  mod[[i]] <- nls(FR ~ c - a * exp(b * time),
                  data = cur_dataframe, start = start)
  details[[i]] <- summary(mod[[i]])

  # calculate ymax, ymin, k, tau
  # convert to formula: y = ymax+ (ymin-ymax) * exp(-k * t)
  ymax <- coef(mod[[i]])[3]
  ymin <- coef(mod[[i]])[3] - coef(mod[[i]])[1]
  k <- coef(mod[[i]])[2] * (-1)

  halftime <- 1 / k * log(2)
  tau <- 1 / halftime

  total_recovery <- (ymax - ymin) / (1 - ymin)

  a.sd <- details[[i]]$coefficients[1, 2]
  b.sd <- details[[i]]$coefficients[1, 2] + details[[i]]$coefficients[3, 2]

  sdtemp <- sqrt((a.sd / (ymax - ymin))^2
                 + (b.sd / (1 - ymin))^2
                 - 2 * a.sd * b.sd / (ymax - ymin) / (1 - ymin))
  total_recovery_sd <- total_recovery * sdtemp
```

```
    # copy the results
    result[i, "ymax"] <- ymax
    result[i, "ymin"] <- ymin
    result[i, "k"] <- k
    result[i, "halftime"] <- halftime
    result[i, "tau"] <- tau
    result[i, "total_recovery"] <- total_recovery
    result[i, "total_recovery_sd"] <- total_recovery_sd
  }

  output <- list(time_points = time_points, summary = result,
                 sample_means = sample_means, sample_sd = sample_sd, model = mod,
details = details, normalized = ds)

  return (output)
}

#frapprocess is the original formula
#frapprocess2 also outputs the corrected curves

##############################################################################################
#                   FRAP Expt 04092021
##############################################################################################
#entering the data from ruffle

setwd("~/Documents/FRAP/EXP3_04092021/ruffle/")
#First KD data
KD_files = list.files(".", pattern= "Results-92*", full.names = F)
KD_files

KD_List = lapply(KD_files, read.csv)
COLNAMES = c(".X", ".Mean.Shape.0.0.", ".Mean5", ".Mean.Shape.0.3.")
KD_List= lapply(KD_List, setNames, COLNAMES)
colnames(KD_List[[2]])

KD_List = lapply(KD_List, function(x)
  x%>% mutate(Rnorm=(.Mean.Shape.0.0.- .Mean.Shape.0.3.)/(.Mean5 -
.Mean.Shape.0.3.))
)
KD_List
KD_Rnorm = lapply(KD_List,
                  function(x){
                    x %>%
                      select(Rnorm) %>% slice(1:62)
                  })
KD_Rnorm = lapply(KD_Rnorm,
                  function(x){
                    x = x[-c(1,2), ]
                  })
length(KD_Rnorm[[1]])
#60 #12 cells
#Make a matrix with the lists
KD_Rnorm = unname(matrix(unlist(KD_Rnorm),ncol = 12, nrow = 60))
```

```
#enter NS data
NS_files = list.files(".", pattern= "Results-NS*", full.names = F)

NS_List = lapply(NS_files, read.csv)
NS_List = lapply(NS_List, setNames, COLNAMES)
COLNAMES = c(".X", ".Mean.Shape.0.0.", ".Mean5", ".Mean.Shape.0.3.")
colnames(NS_List[[2]])

NS_List = lapply(NS_List, function(x)
  x%>% mutate(Rnorm=(.Mean.Shape.0.0.- .Mean.Shape.0.3.)/(.Mean5 - .Mean.Shape.0.3.)
  ))

NS_Rnorm = lapply(NS_List,
                  function(x){
                    x %>%
                      select(Rnorm)%>%
                      slice(1:62)
                  })

NS_Rnorm = lapply(NS_Rnorm,
                  function(x){
                    x = x[-c(1,2), ]
                  })

length(NS_Rnorm[[1]])
#60
#make matrix
NS_Rnorm = unname(matrix(unlist(NS_Rnorm),ncol = 13, nrow = 60))

#JOIN THE NS and KD MATRICES
Rnorm_all = list(NS = NS_Rnorm, KD = KD_Rnorm)

#eliminate some cells because the data is not good
Rnorm_all = exclude(Rnorm_all, group = "KD", cols = 9)

#make time points column
(60-2)*2
time_points = seq(0,116, 2)
time_points
length(time_points) #59

#run the FRAPPROCESS function
Results <- frapprocess(Rnorm_all, time_points) #vector of time or create a sequence
with seq()
#view the results
Results$summary
Results$details
Results

x=seq(0,58,1)
DF = as.data.frame( Results$sample_means )
ggplot(DF, aes(x)) +
  geom_line(aes(y = V1, colour = "NS")) +
  geom_line(aes(y = V2, colour = "KD"))
```

```
#DO STATS
DF_stats = data.frame(as.data.frame(Results$sample_means),
                        as.data.frame(Results$sample_sd),
                        time=c(time_points))
colnames(DF_stats) = c("NS_m","KD_m","NS_sd","KD_sd", "time")

n_NS = length(Rnorm_all[["NS"]][1,])
n_KD = length(Rnorm_all[["KD"]][1,])

pvalue = NULL
for(i in 1:nrow(DF_stats)) {
  row <- rownames(DF_stats[i,])
  # do stuff with row
  stats = t.test2(DF_stats[i,1], DF_stats[i,2], DF_stats[i,3], DF_stats[i,4], n_NS,
n_KD)
  print(stats)
  pvalue = as.data.frame(rbind(pvalue,stats))
}
colnames(pvalue) <- c("Difference of means", "Std Error", "t", "pvalue")

pvalue = pvalue %>% mutate(signif = ifelse(pvalue <= 0.0001, "****",
                                           ifelse(pvalue <= 0.001, "***",
                                                  ifelse(pvalue <= 0.01, "**",
                                                         ifelse(pvalue <= 0.05,
"**","ns")))))

#################################################################################
#use the output of frapprocess2 to make data frames with the normalized data
#---------------------- RUFFLE-----------------
Results_2 <- frapprocess2(Rnorm_all, time_points)
Results_2$summary

NS_norm = as.data.frame(Results_2[["normalized"]]$NS)
NS_norm = NS_norm%>% mutate(time=time_points)
NS_norm_lg =  melt(NS_norm, id.vars = "time" )
ggplot(data = NS_norm_lg, aes(x=time, y=value)) + geom_line(aes(colour=variable))

#create line plot for each column in data frame
#create line plot for each column in data frame
ggplot(NS_norm_lg, aes(time, value)) +
  geom_line() +
  facet_wrap(vars(variable), ncol = 3)

KD_norm = as.data.frame(Results_2[["normalized"]]$KD)
KD_norm = KD_norm%>% mutate(time=time_points)
KD_norm_lg =  melt(KD_norm, id.vars = "time" )
ggplot(data = KD_norm_lg, aes(x=time, y=value)) + geom_line(aes(colour=variable))

#create line plot for each column in data frame
ggplot(KD_norm_lg, aes(time, value)) +
  geom_line() +
  facet_wrap(vars(variable), ncol = 3)
```

```
#-------------------FINAL PLOT----------------------
#RUFFLE
DF_stats
time_points
Results$summary
Results$model

FITTED_NS_ruffle = nls( DF_stats$NS_m ~ c - a * exp(b * DF_stats$time), start =
list(a=max(DF_stats$NS_m)-min(DF_stats$NS_m), b=-0.06469 , c = max(DF_stats$NS_m)),
data=DF_stats)
plot(DF_stats$NS_m)
lines(predict(FITTED_NS_ruffle))
model_mean_NS_ruff = predict(FITTED_NS_ruffle)

FITTED_KD_ruffle = nls( DF_stats$KD_m ~ c - a * exp(b * DF_stats$time), start =
list(a=max(DF_stats$KD_m)-min(DF_stats$KD_m), b=-0.02236 , c = max(DF_stats$KD_m)),
data=DF_stats)
plot(DF_stats$KD_m)
lines(predict(FITTED_KD_ruffle))
model_mean_KD_ruff = predict(FITTED_KD_ruffle)

#use either means or fitted_m as y to get the plots
ggplot(data=plot_df_ruffle,
       aes(x=time, y=fited_m)) +
       geom_line(aes(color = factor(ID)), size=1) +
       geom_ribbon(aes(ymin=means-SD, ymax=means+SD, fill=factor(ID)),
                   alpha=0.2,size=0.1)+
       scale_color_manual(breaks=c("NS_m","KD_m"),
                          labels=c("NS", "KD-92"),
                           values=c("#F8766D","#00BFC4"))+
       scale_fill_manual(breaks=c("NS_m","KD_m"),
                          labels=c("NS", "KD-92"),
                          values=c("#F8766D","#00BFC4"))+
       #scale_x_continuous(breaks=seq(0, 125, 20))+
       xlim(0,118)+
       ggtitle(label="Ruffle")+
       labs( x = "Time (sec)", y = "Normalized intensity")+
       theme_classic()+
       theme(
            plot.title = element_text(size=25, face="bold", hjust = 0.5),
            axis.title.y=element_text(size=23, face="bold", margin = margin(r = 10,
l = 0)),
            axis.text.y = element_text(size = 20, colour = "black"),
            axis.title.x=element_text(size=23, face="bold", margin = margin(r = 10,
l = 0)),
            axis.text.x = element_text(size = 20, colour = "black",margin = margin(t
= 10)),
            axis.line = element_line(size = 1),
            axis.ticks = element_line(size = 1),
            legend.position="top",
            legend.title=element_blank(),
            legend.text = element_text(size = 18,face = "bold"))
```

```
######-----PLOT HALFTIME-------#####
#use the normalized data to obtain the half time
#---RUFFLE

NS_norm[,1]
Results$model

#do some testing
FITTED = nls( NS_norm$V1 ~ c - a * exp(b * NS_norm$time), start =
list(a=max(NS_norm$V1)-min(NS_norm$V1), b=-0.06469, c = max(NS_norm$V1)),
data=NS_norm)
plot( NS_norm$V1)
lines(predict(FITTED))
out = data.frame( coef = coef(FITTED), )
FITTED

NS_norm[,1]

#make a fx to calculate the half times of each curve
coefs= NULL
batch_fx = function(df,b){
  time= df$time
  df = select(df, -time)
  for(i in 1:ncol(df)) {
    #mean <- mean(df[,i])
    results = nls( df[,i] ~ c - a * exp(b * time),
                   start = list(a=max(df[,i])-min(df[,i]), b=b, c = max(df[,i])))
    #coefs = coef(results[[i]])[2] * (-1)))
    abc <- coef(results)#[2] * (-1)
    #print(k)
    coefs = as.data.frame(rbind(coefs,abc))
    k = coefs$b * (-1)
    halftime = 1 / k * log(2)
  }
   return(halftime)
}

#get the value of b from the model made with the average curve
Results$model #for NS ruffle b = -0.06469, for KD b = -0.02236
halftime_NS =  batch_fx(NS_norm,-0.06469 )
halftime_KD =  batch_fx(KD_norm,-0.02236)

KD_norm
t.test(halftime_NS,halftime_KD)
```

```
#make the ½ time plots
#----RUFFLE -1/2 time
length(halftime_NS)#13
length(halftime_KD)#11

half_time_ruffle = data.frame(
              ID = c(rep("NS",13), rep("KD",11)),
              half_time = c(halftime_NS,halftime_KD))

half_time_ruffle%>% filter(half_time <80)%>%
  group_by(ID)%>%
  dplyr::summarise(
    N = n(),
    MEAN = mean(half_time),
    SD = sd(half_time)
  )

stat.test <- compare_means(
  half_time ~ ID, data = half_time_ruffle%>% filter(half_time <80),
  ref.group = "NS",
  method = "t.test",
  paired = F
)
stat.test = stat.test %>% mutate(y.position = 45)

ggboxplot(data= half_time_ruffle%>% filter(half_time <80), #get rid of outlayer
          x= "ID", y="half_time",
          color  = "ID",
          add = "jitter",
          add.params = list(jitter = 0.2, size = 4, alpha = 0.5),
          width = 0.5,
          size = 1.2,
          order = c("NS", "KD"),
          bxp.errorbar = F)+
  ggtitle(label="Ruffle")+
  ylab("FI half recovery time (sec)")+
  scale_x_discrete(labels=c("NS"="NS", "KD"="KD-92"))+
  annotate( "text",
            x = c("NS","KD"),
            y = 2,
            label = c(13,11),
            size = 6, color = "#575757", fontface =2)+
  theme(
    plot.title = element_text(size=25, face="bold", hjust = 0.5),
    axis.title.y=element_text(size=23, face="bold", margin = margin(r = 10, l = 0)),
    axis.text.y = element_text(size = 20, colour = "black"),
    axis.title.x=element_blank(),
    axis.text.x = element_text(size = 24, face="bold", colour = "black",margin =
margin(t = 10)),
    axis.line = element_line(size = 1),
    axis.ticks = element_line(size = 1),
    legend.position="none")+
  stat_pvalue_manual(stat.test, label = "p.signif", tip.length = 0, size = 8,
bracket.size =0.8)
#END OF SCRIPT
```

APPENDIX C SUPPLEMENTARY FIGURES

Supplementary Figure 1. RACK1 silencing inhibits *Shigella* growth in HeLa cells. A-C. Growth curves determined by gentamycin protection assay. RACK1-KD and control (NS) cells were infected with WT *Shigella* (MOI 10), treated with gentamycin (100 µg/mL) and lysed at various time points to quantify intracellular bacteria. Colony-forming units (CFU) were divided by total protein concentration to normalize differences in cell number. The growth curves shown are from three separate infection experiments.

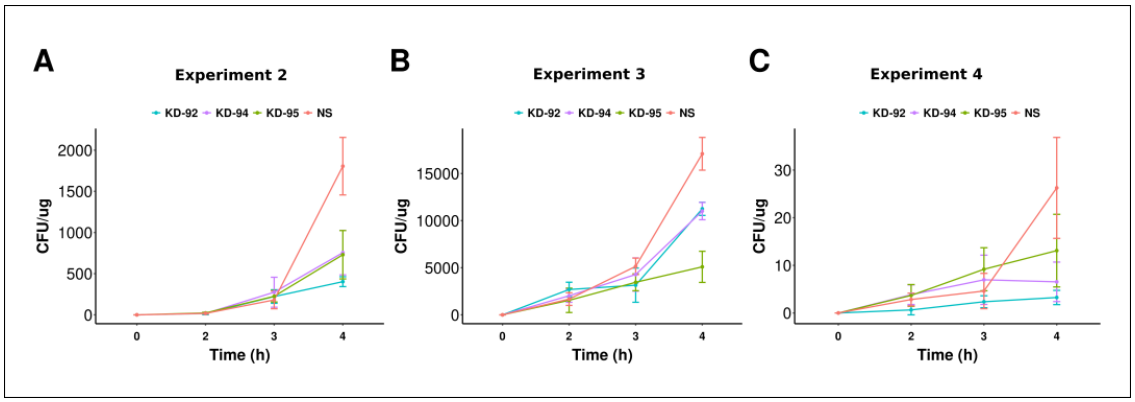

Supplementary Figure 2. RACK1 silencing increases entry foci duration but does not affect foci area or fluorescence intensity. NS and KD-92 cells expressing F-tractin-GFP and infected with dsRED-WT *Shigella* (MOI 10) were imaged every 2 min with a 63X objective on a Zeiss spinning disk microscope. Entry foci were identified by the profuse enrichment of F-actin to the site of bacterial entry. Two independent experiments are shown in **A** and **B**. From left to right: entry foci dynamics were assessed by measuring foci area, average fluorescence intensity (FI), foci duration, FI change over time and actin polymerization rate (see methods section 2.11.3 for details). Dots in the boxplots represent separate entry foci. a.u. = arbitrary units. Statistical differences were calculated by Wilcoxon-test; ns = not significant p>0.05, * p < 0.05, ** p < 0.01, ***p < 0.001

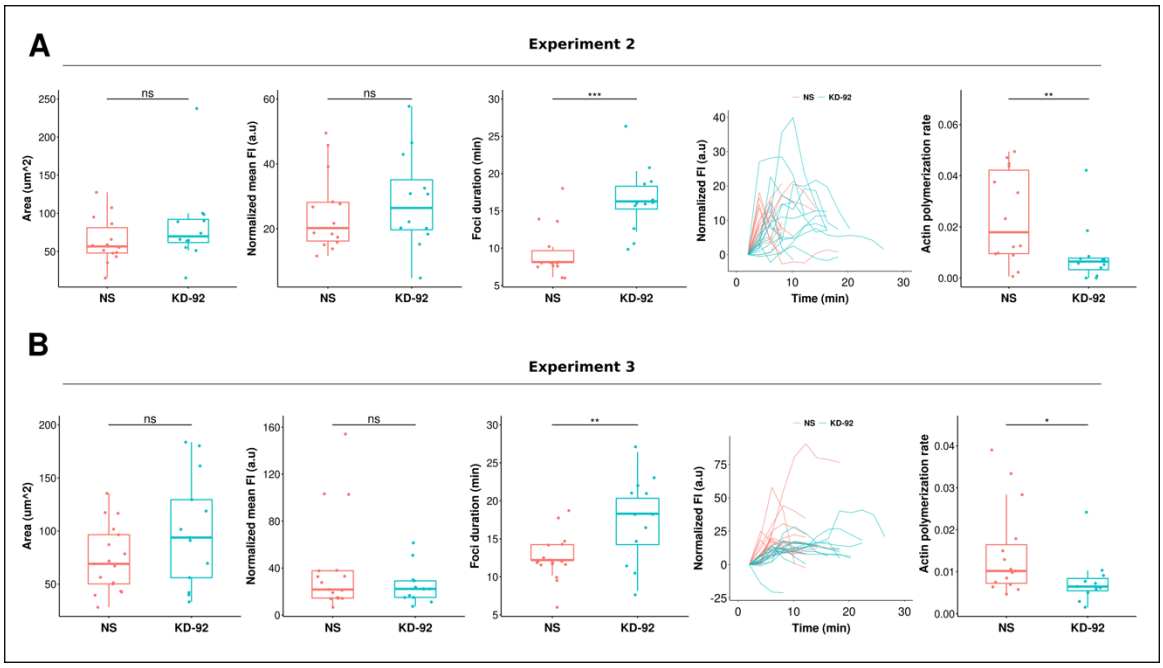

Supplementary Figure 3. RACK1 silencing reduces the plaque areas formed by *Shigella* in HeLa and CaCo-2 cells. Bacterial spreading was analyzed using the modified plaque assay. HeLa cells expressing F-tractin-GFP and CaCo-2 expressing GFP alone were infected with dsRED-WT *Shigella* and overlaid with 0.4% Methocel. The cells were imaged 10 (HeLa) or 15 (CaCo-2) hours post-infection on a widefield Zeiss Z1 with 10X magnification. **A.** Boxplots showing the area of plaques formed in HeLa in two experiments. **B**. Boxplots showing the area of plaques formed in CaCo-2 cells in two experiments. *Shigella*'s plaque boundaries were identified by automatic segmentation using Fiji. Numbers under the boxplots show plaque number. Wilcoxon-test; ns=not significant, * $p < 0.05$, ** $p < 0.01$.

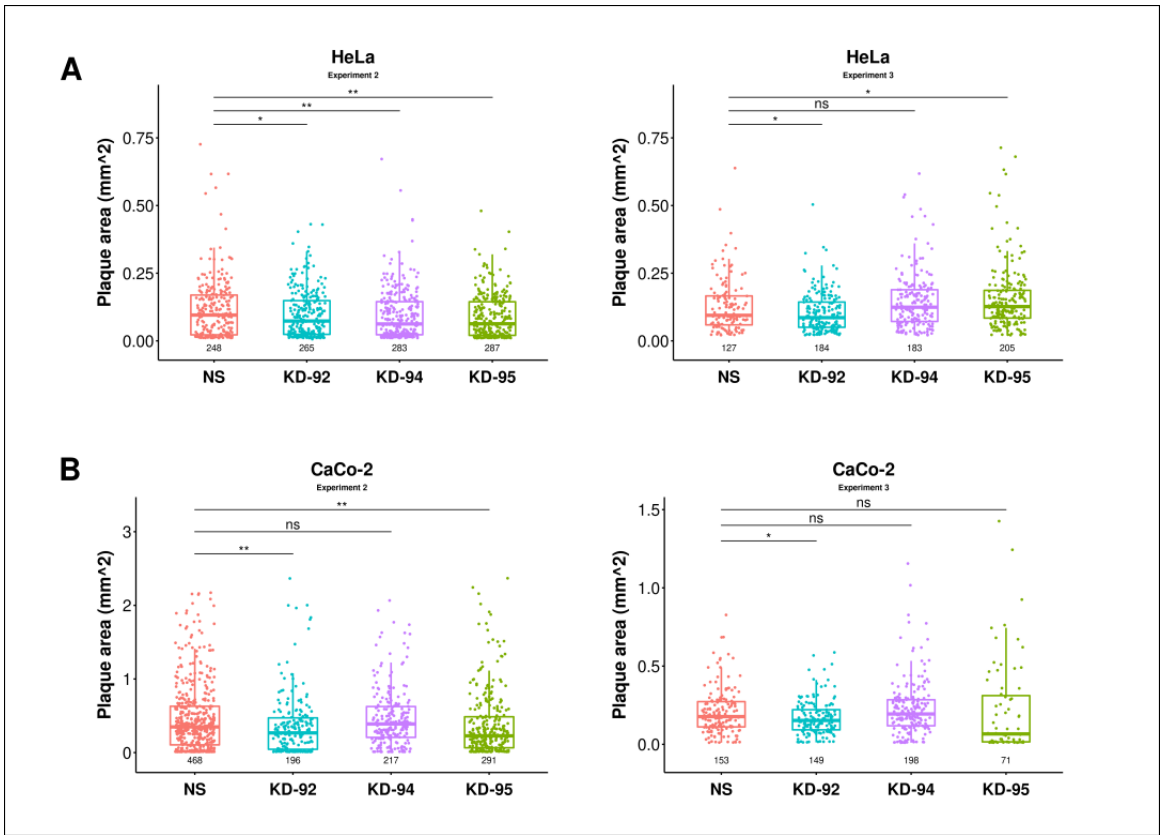

BIBLIOGRAPHY

1. Schroeder, G. N. & Hilbi, H. Molecular Pathogenesis of *Shigella* spp.: Controlling Host Cell Signaling, Invasion, and Death by Type III Secretion. *Clin Microbiol Rev* **21**, 134–156 (2008).
2. de Souza Santos, M. & Orth, K. Subversion of the cytoskeleton by intracellular bacteria: lessons from *Listeria*, *Salmonella* and *Vibrio*. *Cell Microbiol* **17**, 164–173 (2015).
3. Bajunaid, W. *et al.* The T3SS of *Shigella*: Expression, Structure, Function, and Role in Vacuole Escape. *Microorganisms* **8**, 1933 (2020).
4. Choe, J. E. & Welch, M. D. Actin-based motility of bacterial pathogens: mechanistic diversity and its impact on virulence. *Pathog Dis* **74**, ftw099 (2016).
5. Adams, D. R., Ron, D. & Kiely, P. A. RACK1, A multifaceted scaffolding protein: Structure and function. *Cell Commun Signal* **9**, 22 (2011).
6. Lee, J. S. *et al.* RACK1 mediates rewiring of intracellular networks induced by hepatitis C virus infection. *PLOS Pathogens* **15**, e1008021 (2019).
7. Thorslund, S. E. *et al.* The RACK1 Signaling Scaffold Protein Selectively Interacts with Yersinia pseudotuberculosis Virulence Function. *PLOS ONE* **6**, e16784 (2011).
8. Qu, Z. *et al.* Mycobacterial EST12 activates a RACK1–NLRP3–gasdermin D pyroptosis–IL-1β immune pathway. *Science Advances* **6**, eaba4733 (2020).
9. Hennig, E. E., Butruk, E. & Ostrowski, J. RACK1 Protein Interacts with *Helicobacter pylori* VacA Cytotoxin: The Yeast Two-Hybrid Approach. *Biochemical and Biophysical Research Communications* **289**, 103–110 (2001).
10. Marudhupandiyan, S., Prithika, U., Balasubramaniam, B. & Balamurugan, K. RACK-1, a multifaceted regulator is required for *C. elegans* innate immunity against S. flexneri M9OT infection. *Dev Comp Immunol* **74**, 227–236 (2017).
11. Kotloff, K. L., Riddle, M. S., Platts-Mills, J. A., Pavlinac, P. & Zaidi, A. K. M. Shigellosis. *The Lancet* **391**, 801–812 (2018).
12. Hale, T. L. & Keusch, G. T. *Shigella*. in *Medical Microbiology* (ed. Baron, S.) (University of Texas Medical Branch at Galveston, 1996).
13. Khalil, I. A. *et al.* Morbidity and mortality due to *shigella* and enterotoxigenic Escherichia coli diarrhoea: the Global Burden of Disease Study 1990–2016. *The Lancet Infectious Diseases* **18**, 1229–1240 (2018).
14. Aragón, T. J. *et al.* Case-control study of shigellosis in San Francisco: the role of sexual transmission and HIV infection. *Clin Infect Dis* **44**, 327–334 (2007).
15. Marcus, U. *et al.* Shigellosis - a re-emerging sexually transmitted infection: outbreak in men having sex with men in Berlin. *Int J STD AIDS* **15**, 533–537 (2004).
16. Toro, C. *et al.* Shigellosis in Subjects with Traveler's Diarrhea versus Domestically Acquired Diarrhea: Implications for Antimicrobial Therapy and Human Immunodeficiency Virus Surveillance. *Am J Trop Med Hyg* **93**, 491–496 (2015).

17. Nygren, B. L. *et al.* Foodborne outbreaks of shigellosis in the USA, 1998–2008. *Epidemiol Infect* **141**, 233–241 (2013).

18. Kothary, M. H. & Babu, U. S. Infective Dose of Foodborne Pathogens in Volunteers: A Review. *Journal of Food Safety* **21**, 49–68 (2001).

19. Edward, S., Mureithi, E. & Shaban, N. Shigellosis Dynamics: Modelling the Effects of Treatment, Sanitation, and Education in the Presence of Carriers. *International Journal of Mathematics and Mathematical Sciences* **2020**, e3476458 (2020).

20. Guerrero, L. *et al.* Asymptomatic *Shigella* infections in a cohort of Mexican children younger than two years of age. *Pediatr Infect Dis J* **13**, 597–602 (1994).

21. Muthuirulandi Sethuvel, D. p., Devanga Ragupathi, N. k., Anandan, S. & Veeraraghavan, B. Update on: *Shigella* new serogroups/serotypes and their antimicrobial resistance. *Letters in Applied Microbiology* **64**, 8–18 (2017).

22. Thompson, C. N., Duy, P. T. & Baker, S. The Rising Dominance of *Shigella sonnei*: An Intercontinental Shift in the Etiology of Bacillary Dysentery. *PLOS Neglected Tropical Diseases* **9**, e0003708 (2015).

23. Kotloff, K. L. *et al.* Global burden of *Shigella* infections: implications for vaccine development and implementation of control strategies. *Bull World Health Organ* **77**, 651–666 (1999).

24. Livio, S. *et al. Shigella* Isolates From the Global Enteric Multicenter Study Inform Vaccine Development. *Clin Infect Dis* **59**, 933–941 (2014).

25. Guerin, P. J. *et al.* Case management of a multidrug-resistant *Shigella dysenteriae* serotype 1 outbreak in a crisis context in Sierra Leone, 1999–2000. *Transactions of The Royal Society of Tropical Medicine and Hygiene* **98**, 635–643 (2004).

26. Kernéis, S., Guerin, P. J., Seidlein, L. von, Legros, D. & Grais, R. F. A Look Back at an Ongoing Problem: *Shigella dysenteriae* Type 1 Epidemics in Refugee Settings in Central Africa (1993–1995). *PLOS ONE* **4**, e4494 (2009).

27. O'Loughlin, E. V. & Robins-Browne, R. M. Effect of Shiga toxin and Shiga-like toxins on eukaryotic cells. *Microbes and Infection* **3**, 493–507 (2001).

28. Butler, T. Haemolytic uraemic syndrome during shigellosis. *Transactions of The Royal Society of Tropical Medicine and Hygiene* **106**, 395–399 (2012).

29. Gaston, J. Shigella induced reactive arthritis. *Ann Rheum Dis* **64**, 517–518 (2005).

30. Hannu, T., Mattila, L., Siitonen, A. & Leirisalo-Repo, M. Reactive arthritis attributable to *Shigella* infection: a clinical and epidemiological nationwide study. *Annals of the Rheumatic Diseases* **64**, 594–598 (2005).

31. Williams, P. C. M. & Berkley, J. A. Guidelines for the treatment of dysentery (shigellosis): a systematic review of the evidence. *Paediatr Int Child Health* **38**, S50–S65 (2018).

32. Rashid, H. & Rahman, M. Possible transfer of plasmid mediated third generation cephalosporin resistance between Escherichia coli and *Shigella sonnei* in the human gut. *Infect Genet Evol* **30**, 15–18 (2015).

33. Chang, C.-Y. *et al.* Integron types, gene cassettes, antimicrobial resistance genes and plasmids of *Shigella sonnei* isolates from outbreaks and sporadic cases in Taiwan. *J Med Microbiol* **60**, 197–204 (2011).

34. Holt, K. E. *et al.* Tracking the establishment of local endemic populations of an emergent enteric pathogen. *Proc Natl Acad Sci U S A* **110**, 17522–17527 (2013).

35. Mani, S., Wierzba, T. & Walker, R. I. Status of vaccine research and development for *Shigella*. *Vaccine* **34**, 2887–2894 (2016).

36. Flexner, S. The Etiology Of Tropical Dysentery. *The British Medical Journal* **2**, 917–920 (1900).

37. Small, P., Blankenhorn, D., Welty, D., Zinser, E. & Slonczewski, J. L. Acid and base resistance in *Escherichia coli* and *Shigella flexneri*: role of rpoS and growth pH. *J Bacteriol* **176**, 1729–1737 (1994).

38. Calcuttawala, F., Hariharan, C., Pazhani, G. P., Ghosh, S. & Ramamurthy, T. Activity spectrum of colicins produced by *Shigella sonnei* and genetic mechanism of colicin resistance in conspecific *S. sonnei* strains and Escherichia coli. *Antimicrob Agents Chemother* **59**, 152–158 (2015).

39. Haider, K. *et al.* Production of mucinase and neuraminidase and binding of *Shigella* to intestinal mucin. *J Diarrhoeal Dis Res* **11**, 88–92 (1993).

40. Gebert, A., Rothkötter, H. J. & Pabst, R. M cells in Peyer's patches of the intestine. *Int Rev Cytol* **167**, 91–159 (1996).

41. Wassef, J. S., Keren, D. F. & Mailloux, J. L. Role of M cells in initial antigen uptake and in ulcer formation in the rabbit intestinal loop model of shigellosis. *Infection and Immunity* (1989).

42. Mounier, J., Vasselon, T., Hellio, R., Lesourd, M. & Sansonetti, P. J. *Shigella flexneri* enters human colonic Caco-2 epithelial cells through the basolateral pole. *Infect Immun* **60**, 237–248 (1992).

43. Perdomo, O. J. *et al.* Acute inflammation causes epithelial invasion and mucosal destruction in experimental shigellosis. *Journal of Experimental Medicine* **180**, 1307–1319 (1994).

44. Rey, C. *et al.* Transcytosis subversion by M cell-to-enterocyte spread promotes *Shigella flexneri* and *Listeria monocytogenes* intracellular bacterial dissemination. *PLOS Pathogens* **16**, e1008446 (2020).

45. Fernandez-Prada, C. M. *et al. Shigella flexneri* IpaH(7.8) facilitates escape of virulent bacteria from the endocytic vacuoles of mouse and human macrophages. *Infect Immun* **68**, 3608–3619 (2000).

46. Zychlinsky, A., Prevost, M. C. & Sansonetti, P. J. *Shigella flexneri* induces apoptosis in infected macrophages. *Nature* **358**, 167–169 (1992).

47. Hilbi, H. *et al. Shigella*-induced Apoptosis Is Dependent on Caspase-1 Which Binds to IpaB *. *Journal of Biological Chemistry* **273**, 32895–32900 (1998).

48. Frank, D. & Vince, J. E. Pyroptosis versus necroptosis: similarities, differences, and crosstalk. *Cell Death Differ* **26**, 99–114 (2019).

49. Man, S. M. & Kanneganti, T.-D. Converging roles of caspases in inflammasome activation, cell death and innate immunity. *Nat Rev Immunol* **16**, 7–21 (2016).

50. Suzuki, S. *et al.* Shigella IpaH7.8 E3 ubiquitin ligase targets glomulin and activates inflammasomes to demolish macrophages. *PNAS* **111**, E4254–E4263 (2014).

51. Miao, E. A. *et al.* Innate immune detection of the type III secretion apparatus through the NLRC4 inflammasome. *PNAS* **107**, 3076–3080 (2010).

52. Suzuki, T. *et al.* Differential Regulation of Caspase-1 Activation, Pyroptosis, and Autophagy via Ipaf and ASC in Shigella-Infected Macrophages. *PLOS Pathogens* **3**, e111 (2007).

53. GSDMD membrane pore formation constitutes the mechanism of pyroptotic cell death. *The EMBO Journal* **35**, 1766–1778 (2016).

54. Sansonetti, P. J. *et al.* Caspase-1 activation of IL-1beta and IL-18 are essential for *Shigella flexneri*-induced inflammation. *Immunity* **12**, 581–590 (2000).

55. Sansonetti, P. J., Arondel, J., Cavaillon, J. M. & Huerre, M. Role of interleukin-1 in the pathogenesis of experimental shigellosis. *J Clin Invest* **96**, 884–892 (1995).

56. Way, S. S., Borczuk, A. C., Dominitz, R. & Goldberg, M. B. An Essential Role for Gamma Interferon in Innate Resistance to *Shigella flexneri* Infection. *Infect Immun* **66**, 1342–1348 (1998).

57. Mathan, M. M. & Mathan, V. I. Morphology of Rectal Mucosa of Patients with Shigellosis. *Reviews of Infectious Diseases* **13**, S314–S318 (1991).

58. Philpott, D. J., Edgeworth, J. D. & Sansonetti, P. J. The pathogenesis of *Shigella flexneri* infection: lessons from in vitro and in vivo studies. *Philosophical Transactions of the Royal Society of London B: Biological Sciences* **355**, 575–586 (2000).

59. Singer, M. & Sansonetti, P. J. IL-8 Is a Key Chemokine Regulating Neutrophil Recruitment in a New Mouse Model of *Shigella*-Induced Colitis. *The Journal of Immunology* **173**, 4197–4206 (2004).

60. Borregaard, N. Neutrophils, from marrow to microbes. *Immunity* **33**, 657–670 (2010).

61. Segal, A. W. How Neutrophils Kill Microbes. *Annu Rev Immunol* **23**, 197–223 (2005).

62. Mandic-Mulec, I., Weiss, J. & Zychlinsky, A. *Shigella flexneri* is trapped in polymorphonuclear leukocyte vacuoles and efficiently killed. *Infect Immun* **65**, 110–115 (1997).

63. Perdomo, J. J., Gounon, P. & Sansonetti, P. J. Polymorphonuclear leukocyte transmigration promotes invasion of colonic epithelial monolayer by *Shigella* flexneri. *J Clin Invest* **93**, 633–643 (1994).

64. Aratani, Y. Myeloperoxidase: Its role for host defense, inflammation, and neutrophil function. *Arch Biochem Biophys* **640**, 47–52 (2018).

65. Meza-Segura, M. *et al.* SepA Enhances *Shigella* Invasion of Epithelial Cells by Degrading Alpha-1 Antitrypsin and Producing a Neutrophil Chemoattractant. *mBio* **12**, e02833-21.

66. Zurawski, D. V., Mumy, K. L., Faherty, C. S., McCormick, B. A. & Maurelli, A. T. Shigella flexneri type III secretion system effectors OspB and OspF target the nucleus to downregulate the host inflammatory response via interactions with retinoblastoma protein. *Molecular Microbiology* **71**, 350–368 (2009).

67. Zurawski, D. V. *et al.* The NleE/OspZ Family of Effector Proteins Is Required for Polymorphonuclear Transepithelial Migration, a Characteristic Shared by Enteropathogenic Escherichia coli and *Shigella flexneri* Infections. *Infection and Immunity* (2008).

68. Zurawski, D. V., Mitsuhata, C., Mumy, K. L., McCormick, B. A. & Maurelli, A. T. OspF and OspC1 are *Shigella flexneri* type III secretion system effectors that are required for postinvasion aspects of virulence. *Infect Immun* **74**, 5964–5976 (2006).

69. Arbibe, L. *et al.* An injected bacterial effector targets chromatin access for transcription factor NF-kappaB to alter transcription of host genes involved in immune responses. *Nat Immunol* **8**, 47–56 (2007).

70. Zhang, Z., Jin, L., Champion, G., Seydel, K. B. & Stanley, S. L. *Shigella* infection in a SCID mouse-human intestinal xenograft model: role for neutrophils in containing bacterial dissemination in human intestine. *Infect Immun* **69**, 3240–3247 (2001).

71. Lan, R. & Reeves, P. R. *Escherichia* coli in disguise: molecular origins of *Shigella*. *Microbes and Infection* **4**, 1125–1132 (2002).

72. The, H. C., Thanh, D. P., Holt, K. E., Thomson, N. R. & Baker, S. The genomic signatures of *Shigella* evolution, adaptation and geographical spread. *Nat Rev Microbiol* **14**, 235–250 (2016).

73. Pupo, G. M., Lan, R. & Reeves, P. R. Multiple independent origins of *Shigella* clones of *Escherichia coli* and convergent evolution of many of their characteristics. *Proc Natl Acad Sci U S A* **97**, 10567–10572 (2000).

74. Holt, K. E. *et al. Shigella sonnei* genome sequencing and phylogenetic analysis indicate recent global dissemination from Europe. *Nat Genet* **44**, 1056–1059 (2012).

75. Hawkey, J., Monk, J. M., Billman-Jacobe, H., Palsson, B. & Holt, K. E. Impact of insertion sequences on convergent evolution of *Shigella* species. *PLOS Genetics* **16**, e1008931 (2020).

76. Ochman, H., Lawrence, J. G. & Groisman, E. A. Lateral gene transfer and the nature of bacterial innovation. *Nature* **405**, 299–304 (2000).

77. Nakata, N. *et al.* The absence of a surface protease, OmpT, determines the intercellular spreading ability of *Shigella*: the relationship between the ompT and kcpA loci. *Molecular Microbiology* **9**, 459–468 (1993).

78. Maurelli, A. T., Fernández, R. E., Bloch, C. A., Rode, C. K. & Fasano, A. “Black holes” and bacterial pathogenicity: A large genomic deletion that enhances the virulence of *Shigella* spp. and enteroinvasive *Escherichia coli*. *Proc Natl Acad Sci U S A* **95**, 3943–3948 (1998).

79. Sansonetti, P. J., Kopecko, D. J. & Formal, S. B. Involvement of a plasmid in the invasive ability of *Shigella flexneri*. *Infect Immun* **35**, 852–860 (1982).

80. Sansonetti, P. J. *et al.* Alterations in the pathogenicity of *Escherichia* coli K-12 after transfer of plasmid and chromosomal genes from *Shigella flexneri*. *Infect Immun* **39**, 1392–1402 (1983).

81. Buchrieser, C. *et al.* The virulence plasmid pWR100 and the repertoire of proteins secreted by the type III secretion apparatus of *Shigella flexneri*. *Molecular Microbiology* **38**, 760–771 (2000).

82. Sasakawa, C. *et al.* Molecular alteration of the 140-megadalton plasmid associated with loss of virulence and Congo red binding activity in *Shigella flexneri*. *Infect Immun* **51**, 470–475 (1986).

83. Büttner, D. Protein export according to schedule: architecture, assembly, and regulation of type III secretion systems from plant- and animal-pathogenic bacteria. *Microbiol Mol Biol Rev* **76**, 262–310 (2012).

84. Venkatesan, M. M., Buysse, J. M. & Oaks, E. V. Surface presentation of *Shigella flexneri* invasion plasmid antigens requires the products of the spa locus. *J Bacteriol* **174**, 1990–2001 (1992).

85. Hromockyj, A. E. & Maurelli, A. T. Identification of *Shigella* invasion genes by isolation of temperature-regulated inv::lacZ operon fusions. *Infect Immun* **57**, 2963–2970 (1989).

86. Gall, T. L. *et al.* Analysis of virulence plasmid gene expression defines three classes of effectors in the type III secretion system of *Shigella flexneri*. *Microbiology (Reading)* **151**, 951–962 (2005).

87. Buysse, J. M., Stover, C. K., Oaks, E. V., Venkatesan, M. & Kopecko, D. J. Molecular cloning of invasion plasmid antigen (ipa) genes from *Shigella flexneri*: analysis of ipa gene products and genetic mapping. *J Bacteriol* **169**, 2561–2569 (1987).

88. Maurelli, A. T. & Sansonetti, P. J. Identification of a chromosomal gene controlling temperature-regulated expression of *Shigella virulence*. *Proc Natl Acad Sci U S A* **85**, 2820–2824 (1988).

89. Muthuramalingam, M., Whittier, S. K., Picking, W. L. & Picking, W. D. The *Shigella* Type III Secretion System: An Overview from Top to Bottom. *Microorganisms* **9**, 451 (2021).

90. Roehrich, A. D., Guillossou, E., Blocker, A. J. & Martinez-Argudo, I. *Shigella* IpaD has a dual role: signal transduction from the type III secretion system needle tip and intracellular secretion regulation. *Mol Microbiol* **87**, 690–706 (2013).

91. Cheung, M. *et al.* Three-dimensional electron microscopy reconstruction and cysteine-mediated crosslinking provide a model of the type III secretion system needle tip complex. *Mol Microbiol* **95**, 31–50 (2015).

92. Blocker, A. *et al.* The Tripartite Type III Secreton of *Shigella flexneri* Inserts Ipab and Ipac into Host Membranes. *J Cell Biol* **147**, 683–693 (1999).

93. Ménard, R., Sansonetti, P. & Parsot, C. The secretion of the *Shigella flexneri* Ipa invasins is activated by epithelial cells and controlled by IpaB and IpaD. *EMBO J* **13**, 5293–5302 (1994).

94. Veenendaal, A. K. J. *et al.* The type III secretion system needle tip complex mediates host cell sensing and translocon insertion. *Mol Microbiol* **63**, 1719–1730 (2007).

95. Mattock, E. & Blocker, A. J. How Do the Virulence Factors of *Shigella* Work Together to Cause Disease? *Frontiers in Cellular and Infection Microbiology* **7**, (2017).

96. Pinaud, L. *et al.* Identification of novel substrates of *Shigella* T3SA through analysis of its virulence plasmid-encoded secretome. *PLoS One* **12**, e0186920 (2017).

97. Campbell-Valois, F.-X. *et al.* A Fluorescent Reporter Reveals On/Off Regulation of the *Shigella* Type III Secretion Apparatus during Entry and Cell-to-Cell Spread. *Cell Host & Microbe* **15**, 177–189 (2014).

98. Wei, J. *et al.* Complete Genome Sequence and Comparative Genomics of *Shigella flexneri* Serotype 2a Strain 2457T. *Infection and Immunity* (2003).

99. Pope, L. M., Reed, K. E. & Payne, S. M. Increased protein secretion and adherence to HeLa cells by *Shigella* spp. following growth in the presence of bile salts. *Infect Immun* **63**, 3642–3648 (1995).

100. Bernardini, M. L., Mounier, J., d'Hauteville, H., Coquis-Rondon, M. & Sansonetti, P. J. Identification of icsA, a plasmid locus of *Shigella flexneri* that governs bacterial intra- and intercellular spread through interaction with F-actin. *Proc Natl Acad Sci U S A* **86**, 3867–3871 (1989).

101. Brotcke Zumsteg, A., Goosmann, C., Brinkmann, V., Morona, R. & Zychlinsky, A. IcsA is a *Shigella flexneri* adhesin regulated by the type III secretion system and required for pathogenesis. *Cell Host Microbe* **15**, 435–445 (2014).

102. Qin, J., Doyle, M. T., Tran, E. N. H. & Morona, R. The virulence domain of *Shigella* IcsA contains a subregion with specific host cell adhesion function. *PLOS ONE* **15**, e0227425 (2020).

103. Lafont, F., Tran Van Nhieu, G., Hanada, K., Sansonetti, P. & van der Goot, F. G. Initial steps of *Shigella* infection depend on the cholesterol/sphingolipid raft-mediated CD44-IpaB interaction. *EMBO J* **21**, 4449–4457 (2002).

104. Watarai, M., Funato, S. & Sasakawa, C. Interaction of Ipa proteins of *Shigella flexneri* with alpha5beta1 integrin promotes entry of the bacteria into mammalian cells. *J Exp Med* **183**, 991–999 (1996).

105. Skoudy, A. *et al.* CD44 binds to the *Shigella* IpaB protein and participates in bacterial invasion of epithelial cells. *Cell Microbiol* **2**, 19–33 (2000).

106. Parsot, C., Ménard, R., Gounon, P. & Sansonetti, P. J. Enhanced secretion through the *Shigella flexneri* Mxi-Spa translocon leads to assembly of extracellular proteins into macromolecular structures. *Mol Microbiol* **16**, 291–300 (1995).

107. López-Montero, N. & Enninga, J. Diverted recycling—*Shigella* subversion of Rabs. *Small GTPases* **9**, 365–374 (2016).

108. Valencia-Gallardo, C. M., Carayol, N. & Tran Van Nhieu, G. Cytoskeletal mechanics during *Shigella* invasion and dissemination in epithelial cells. *Cell Microbiol* **17**, 174–182 (2015).

109. Lee, J. H., Park, H. & Park, Y. H. Molecular Mechanisms of Host Cytoskeletal Rearrangements by *Shigella* Invasins. *Int J Mol Sci* **15**, 18253–18266 (2014).

110. Bos, J. L., Rehmann, H. & Wittinghofer, A. GEFs and GAPs: Critical Elements in the Control of Small G Proteins. *Cell* **129**, 865–877 (2007).

111. Spiering, D. & Hodgson, L. Dynamics of the Rho-family small GTPases in actin regulation and motility. *Cell Adh Migr* **5**, 170–180 (2011).

112. Tran Van Nhieu, G., Caron, E., Hall, A. & Sansonetti, P. J. IpaC induces actin polymerization and filopodia formation during *Shigella* entry into epithelial cells. *EMBO J* **18**, 3249–3262 (1999).

113. Mounier, J. *et al.* Rho family GTPases control entry of *Shigella flexneri* into epithelial cells but not intracellular motility. *J Cell Sci* **112 (Pt 13)**, 2069–2080 (1999).

114. Terry, C. M. *et al.* The C-terminus of IpaC is required for effector activities related to *Shigella* invasion of host cells. *Microbial Pathogenesis* **45**, 282–289 (2008).

115. Bougnères, L. *et al.* Cortactin and Crk cooperate to trigger actin polymerization during *Shigella* invasion of epithelial cells. *J Cell Biol* **166**, 225–235 (2004).

116. Mounier, J. *et al.* The IpaC Carboxyterminal Effector Domain Mediates Src-Dependent Actin Polymerization during *Shigella* Invasion of Epithelial Cells. *PLOS Pathogens* **5**, e1000271 (2009).

117. Goley, E. D. & Welch, M. D. The ARP2/3 complex: an actin nucleator comes of age. *Nat Rev Mol Cell Biol* **7**, 713–726 (2006).

118. Burton, E. A., Plattner, R. & Pendergast, A. M. Abl tyrosine kinases are required for infection by *Shigella flexneri*. *EMBO J* **22**, 5471–5479 (2003).

119. Ohya, K., Handa, Y., Ogawa, M., Suzuki, M. & Sasakawa, C. IpgB1 is a novel *Shigella* effector protein involved in bacterial invasion of host cells. Its activity to promote membrane ruffling via Rac1 and Cdc42 activation. *J Biol Chem* **280**, 24022–24034 (2005).

120. Hachani, A. *et al.* IpgB1 and IpgB2, two homologous effectors secreted via the Mxi-Spa type III secretion apparatus, cooperate to mediate polarized cell invasion and inflammatory potential of *Shigella flexenri*. *Microbes Infect* **10**, 260–268 (2008).

121. Klink, B. U. *et al.* Structure of *Shigella* IpgB2 in complex with human RhoA: implications for the mechanism of bacterial guanine nucleotide exchange factor mimicry. *J Biol Chem* **285**, 17197–17208 (2010).

122. Uchiya, K. *et al.* Identification of a novel virulence gene, virA, on the large plasmid of *Shigella*, involved in invasion and intercellular spreading. *Mol Microbiol* **17**, 241–250 (1995).

123. Yoshida, S. *et al.* Microtubule-severing activity of *Shigella* is pivotal for intercellular spreading. *Science* **314**, 985–989 (2006).

124. Yoshida, S. *et al.* Shigella deliver an effector protein to trigger host microtubule destabilization, which promotes Rac1 activity and efficient bacterial internalization. *EMBO J* **21**, 2923–2935 (2002).

125. Davis, J. *et al.* Novel fold of VirA, a type III secretion system effector protein from *Shigella flexneri*. *Protein Sci* **17**, 2167–2173 (2008).

126. Germane, K. L., Ohi, R., Goldberg, M. B. & Spiller, B. W. Structural and Functional Studies Indicate That *Shigella* VirA Is Not a Protease and Does Not Directly Destabilize Microtubules. *Biochemistry* **47**, 10241–10243 (2008).

127. Dong, N. *et al.* Structurally distinct bacterial TBC-like GAPs link Arf GTPase to Rab1 inactivation to counteract host defenses. *Cell* **150**, 1029–1041 (2012).

128. Niebuhr, K. *et al.* IpgD, a protein secreted by the type III secretion machinery of *Shigella flexneri*, is chaperoned by IpgE and implicated in entry focus formation. *Molecular Microbiology* **38**, 8–19 (2000).

129. Niebuhr, K. *et al.* Conversion of PtdIns(4,5)P2 into PtdIns(5)P by the *S.flexneri* effector IpgD reorganizes host cell morphology. *EMBO J* **21**, 5069–5078 (2002).

130. Saarikangas, J., Zhao, H. & Lappalainen, P. Regulation of the actin cytoskeleton-plasma membrane interplay by phosphoinositides. *Physiol Rev* **90**, 259–289 (2010).

131. Bonnet, M. & Tran Van Nhieu, G. How *Shigella* Utilizes Ca2+ Jagged Edge Signals during Invasion of Epithelial Cells. *Frontiers in Cellular and Infection Microbiology* **6**, (2016).

132. Sun, C. H. *et al.* The *Shigella* type III effector IpgD recodes Ca2+ signals during invasion of epithelial cells. *EMBO J* **36**, 2567–2580 (2017).

133. Berridge, M. J. Inositol trisphosphate and calcium signalling. *Nature* **361**, 315–325 (1993).

134. Tran Van Nhieu, G. *et al.* Actin-based confinement of calcium responses during *Shigella* invasion. *Nat Commun* **4**, 1567 (2013).

135. Bergounioux, J. *et al.* Calpain Activation by the *Shigella flexneri* Effector VirA Regulates Key Steps in the Formation and Life of the Bacterium's Epithelial Niche. *Cell Host & Microbe* **11**, 240–252 (2012).

136. Carlsson, A. E. Actin Dynamics: From Nanoscale to Microscale. *Annu Rev Biophys* **39**, 91–110 (2010).

137. Tran Van Nhieu, G., Ben-Ze'ev, A. & Sansonetti, P. J. Modulation of bacterial entry into epithelial cells by association between vinculin and the *Shigella* IpaA invasin. *EMBO J* **16**, 2717–2729 (1997).

138. Izard, T., Tran Van Nhieu, G. & Bois, P. R. J. *Shigella* applies molecular mimicry to subvert vinculin and invade host cells. *J Cell Biol* **175**, 465–475 (2006).

139. Le Clainche, C., Dwivedi, S. P., Didry, D. & Carlier, M.-F. Vinculin Is a Dually Regulated Actin Filament Barbed End-capping and Side-binding Protein. *J Biol Chem* **285**, 23420–23432 (2010).

140. Bourdet-Sicard, R. *et al.* Binding of the *Shigella* protein IpaA to vinculin induces F-actin depolymerization. *EMBO J* **18**, 5853–5862 (1999).

141. Park, H., Valencia-Gallardo, C., Sharff, A., Tran Van Nhieu, G. & Izard, T. Novel vinculin binding site of the IpaA invasin of *Shigella*. *J Biol Chem* **286**, 23214–23221 (2011).

142. Ramarao, N. *et al.* Capping of actin filaments by vinculin activated by the *Shigella* IpaA carboxyl-terminal domain. *FEBS Lett* **581**, 853–857 (2007).

143. Demali, K. A., Jue, A. L. & Burridge, K. IpaA targets beta1 integrins and rho to promote actin cytoskeleton rearrangements necessary for *Shigella* entry. *J Biol Chem* **281**, 39534–39541 (2006).

144. Chinthalapudi, K., Rangarajan, E. S. & Izard, T. The interaction of talin with the cell membrane is essential for integrin activation and focal adhesion formation. *PNAS* **115**, 10339–10344 (2018).

145. Valencia-Gallardo, C. *et al. Shigella* IpaA Binding to Talin Stimulates Filopodial Capture and Cell Adhesion. *Cell Rep* **26**, 921-932.e6 (2019).

146. Romero, S. *et al.* ATP-mediated Erk1/2 activation stimulates bacterial capture by filopodia, which precedes Shigella invasion of epithelial cells. *Cell Host Microbe* **9**, 508–519 (2011).

147. Ray, K. *et al.* Tracking the dynamic interplay between bacterial and host factors during pathogen-induced vacuole rupture in real time. *Cell. Microbiol.* **12**, 545–556 (2010).

148. De Geyter, C. *et al.* Purification of IpaC, a protein involved in entry of *Shigella* flexneri into epithelial cells and characterization of its interaction with lipid membranes. *FEBS Lett* **400**, 149–154 (1997).

149. De Geyter, C. *et al.* Characterization of the interaction of IpaB and IpaD, proteins required for entry of *Shigella flexneri* into epithelial cells, with a lipid membrane. *Eur J Biochem* **267**, 5769–5776 (2000).

150. Osiecki, J. C. *et al.* IpaC from Shigella and SipC from Salmonella possess similar biochemical properties but are functionally distinct. *Mol Microbiol* **42**, 469–481 (2001).

151. High, N., Mounier, J., Prévost, M. C. & Sansonetti, P. J. IpaB of *Shigella flexneri* causes entry into epithelial cells and escape from the phagocytic vacuole. *EMBO J* **11**, 1991–1999 (1992).

152. Kuwae, A. *et al. Shigella* invasion of macrophage requires the insertion of IpaC into the host plasma membrane. Functional analysis of IpaC. *J Biol Chem* **276**, 32230–32239 (2001).

153. Schnupf, P. & Sansonetti, P. J. *Shigella* Pathogenesis: New Insights through Advanced Methodologies. *Microbiol Spectr* **7**, (2019).

154. Mellouk, N. *et al. Shigella* Subverts the Host Recycling Compartment to Rupture Its Vacuole. *Cell Host & Microbe* **16**, 517–530 (2014).

155. Stenmark, H. Rab GTPases as coordinators of vesicle traffic. *Nat Rev Mol Cell Biol* **10**, 513–525 (2009).

156. Campa, C. C. *et al.* Rab11 activity and PtdIns(3)P turnover removes recycling cargo from endosomes. *Nat Chem Biol* **14**, 801–810 (2018).

157. Paz, I. *et al.* Galectin-3, a marker for vacuole lysis by invasive pathogens. *Cellular Microbiology* **12**, 530–544 (2010).

158. Ehsani, S. *et al.* Hierarchies of host factor dynamics at the entry site of *Shigella flexneri* during host cell invasion. *Infect Immun* **80**, 2548–2557 (2012).

159. Hong, M.-H., Weng, I.-C., Li, F.-Y., Lin, W.-H. & Liu, F.-T. Intracellular galectins sense cytosolically exposed glycans as danger and mediate cellular responses. *Journal of Biomedical Science* **28**, 16 (2021).

160. Chang, Y.-Y. *et al. Shigella* hijacks the exocyst to cluster macropinosomes for efficient vacuolar escape. *PLoS Pathog* **16**, e1008822 (2020).

161. Campa, C. C. & Hirsch, E. Rab11 and phosphoinositides: A synergy of signal transducers in the control of vesicular trafficking. *Adv Biol Regul* **63**, 132–139 (2017).

162. Weiner, A. *et al.* Macropinosomes are Key Players in Early *Shigella* Invasion and Vacuolar Escape in Epithelial Cells. *PLoS Pathog* **12**, (2016).

163. Mei, K. & Guo, W. The exocyst complex. *Curr Biol* **28**, R922–R925 (2018).

164. Kühn, S. *et al.* Actin Assembly around the *Shigella*-Containing Vacuole Promotes Successful Infection. *Cell Rep* **31**, 107638 (2020).

165. Liu, W. *et al.* Nε-fatty acylation of multiple membrane-associated proteins by *Shigella* IcsB effector to modulate host function. *Nat Microbiol* **3**, 996–1009 (2018).

166. Ramel, D. *et al. Shigella flexneri* infection generates the lipid PI5P to alter endocytosis and prevent termination of EGFR signaling. *Sci Signal* **4**, ra61 (2011).

167. Ogawa, M. *et al.* Escape of intracellular *Shigella* from autophagy. *Science* **307**, 727–731 (2005).

168. Dupont, N. *et al. Shigella* Phagocytic Vacuolar Membrane Remnants Participate in the Cellular Response to Pathogen Invasion and Are Regulated by Autophagy. *Cell Host & Microbe* **6**, 137–149 (2009).

169. Wang, Z. & Li, C. Xenophagy in innate immunity: A battle between host and pathogen. *Dev Comp Immunol* **109**, 103693 (2020).

170. Huett, A. *et al.* The LRR and RING Domain Protein LRSAM1 Is an E3 Ligase Crucial for Ubiquitin-Dependent Autophagy of Intracellular *Salmonella* Typhimurium. *Cell Host Microbe* **12**, 778–790 (2012).

171. Mostowy, S. *et al.* p62 and NDP52 proteins target intracytosolic *Shigella* and *Listeria* to different autophagy pathways. *J Biol Chem* **286**, 26987–26995 (2011).

172. Campbell-Valois, F.-X., Sachse, M., Sansonetti, P. J. & Parsot, C. Escape of Actively Secreting *Shigella flexneri* from ATG8/LC3-Positive Vacuoles Formed during Cell-To-Cell Spread Is Facilitated by IcsB and VirA. *mBio* **6**, e02567-14 (2015).

173. Thurston, T. L. M., Wandel, M. P., von Muhlinen, N., Foeglein, A. & Randow, F. Galectin 8 targets damaged vesicles for autophagy to defend cells against bacterial invasion. *Nature* **482**, 414–418 (2012).

174. Weng, I.-C. *et al.* Cytosolic galectin-3 and -8 regulate antibacterial autophagy through differential recognition of host glycans on damaged phagosomes. *Glycobiology* **28**, 392–405 (2018).

175. Baxt, L. A. & Goldberg, M. B. Host and Bacterial Proteins That Repress Recruitment of LC3 to *Shigella* Early during Infection. *PLoS One* **9**, e94653 (2014).

176. Maculins, T. *et al.* Multiplexed proteomics of autophagy-deficient murine macrophages reveals enhanced antimicrobial immunity via the oxidative stress response. *eLife* **10**, e62320.

177. Zoppino, F. C. M., Militello, R. D., Slavin, I., Alvarez, C. & Colombo, M. I. Autophagosome formation depends on the small GTPase Rab1 and functional ER exit sites. *Traffic* **11**, 1246–1261 (2010).

178. Ferrari, M. L. *et al. Shigella* promotes major alteration of gut epithelial physiology and tissue invasion by shutting off host intracellular transport. *Proc Natl Acad Sci U S A* **116**, 13582–13591 (2019).

179. Burnaevskiy, N. *et al.* Proteolytic elimination of N-myristoyl modifications by the Shigella virulence factor IpaJ. *Nature* **496**, 106–109 (2013).

180. Burnaevskiy, N., Peng, T., Reddick, L. E., Hang, H. C. & Alto, N. M. Myristoylome profiling reveals a concerted mechanism of ARF GTPase deacylation by the bacterial protease IpaJ. *Mol Cell* **58**, 110–122 (2015).

181. Mostowy, S. *et al.* Entrapment of intracytosolic bacteria by septin cage-like structures. *Cell Host Microbe* **8**, 433–444 (2010).

182. Krokowski, S. *et al.* Septins Recognize and Entrap Dividing Bacterial Cells for Delivery to Lysosomes. *Cell Host Microbe* **24**, 866-874.e4 (2018).

183. Mostowy, S. & Cossart, P. Septins: the fourth component of the cytoskeleton. *Nat Rev Mol Cell Biol* **13**, 183–194 (2012).

184. Lobato-Márquez, D. *et al.* Mechanistic insight into bacterial entrapment by septin cage reconstitution. *Nat Commun* **12**, 4511 (2021).

185. Goldberg, M. B. & Theriot, J. A. *Shigella flexneri* surface protein IcsA is sufficient to direct actin-based motility. *Proc Natl Acad Sci U S A* **92**, 6572–6576 (1995).

186. Mazon-Moya, M. J. *et al.* Septins restrict inflammation and protect zebrafish larvae from *Shigella* infection. *PLoS Pathog* **13**, e1006467 (2017).

187. Lamkanfi, M. & Dixit, V. M. Manipulation of host cell death pathways during microbial infections. *Cell Host Microbe* **8**, 44–54 (2010).

188. Li, P. *et al.* Molecular mechanism and therapeutic targeting of necrosis, apoptosis, pyroptosis, and autophagy in cardiovascular disease. *Chin Med J (Engl)* **134**, 2647–2655 (2021).

189. Fink, S. L. & Cookson, B. T. Apoptosis, Pyroptosis, and Necrosis: Mechanistic Description of Dead and Dying Eukaryotic Cells. *Infect Immun* **73**, 1907–1916 (2005).

190. Elmore, S. Apoptosis: A Review of Programmed Cell Death. *Toxicol Pathol* **35**, 495–516 (2007).

191. Günther, S. D. *et al.* Cytosolic Gram-negative bacteria prevent apoptosis by inhibition of effector caspases through lipopolysaccharide. *Nat Microbiol* **5**, 354–367 (2020).

192. Ashida, H., Sasakawa, C. & Suzuki, T. A unique bacterial tactic to circumvent the cell death crosstalk induced by blockade of caspase-8. *EMBO J* **39**, e104469 (2020).

193. Pendaries, C. *et al.* PtdIns(5)P activates the host cell PI3-kinase/Akt pathway during *Shigella flexneri* infection. *EMBO J* **25**, 1024–1034 (2006).

194. Wang, H. *et al.* Mixed lineage kinase domain-like protein MLKL causes necrotic membrane disruption upon phosphorylation by RIP3. *Mol Cell* **54**, 133–146 (2014).

195. Newton, K. *et al.* Cleavage of RIPK1 by caspase-8 is crucial for limiting apoptosis and necroptosis. *Nature* **574**, 428–431 (2019).

196. Yu, P. *et al.* Pyroptosis: mechanisms and diseases. *Signal Transduct Target Ther* **6**, 128 (2021).

197. Kutsch, M. & Coers, J. Human guanylate binding proteins: nanomachines orchestrating host defense. *FEBS J* **288**, 5826–5849 (2021).

198. Suzuki, S. *et al. Shigella* type III secretion protein MxiI is recognized by Naip2 to induce Nlrc4 inflammasome activation independently of Pkcδ. *PLoS Pathog* **10**, e1003926 (2014).

199. Senerovic, L. *et al.* Spontaneous formation of IpaB ion channels in host cell membranes reveals how *Shigella* induces pyroptosis in macrophages. *Cell Death Dis* **3**, e384 (2012).

200. Kobayashi, T. *et al.* The *Shigella* OspC3 effector inhibits caspase-4, antagonizes inflammatory cell death, and promotes epithelial infection. *Cell Host Microbe* **13**, 570–583 (2013).

201. Wandel, M. P. *et al.* Guanylate-binding proteins convert cytosolic bacteria into caspase-4 signaling platforms. *Nat Immunol* **21**, 880–891 (2020).

202. Li, Z. *et al. Shigella* evades pyroptosis by arginine ADP-riboxanation of caspase-11. *Nature* **599**, 290–295 (2021).

203. Luchetti, G. *et al. Shigella* ubiquitin ligase IpaH7.8 targets gasdermin D for degradation to prevent pyroptosis and enable infection. *Cell Host Microbe* **29**, 1521-1530.e10 (2021).

204. Li, P. *et al.* Ubiquitination and degradation of GBPs by a *Shigella* effector to suppress host defence. *Nature* **551**, 378–383 (2017).

205. Wandel, M. P. *et al.* GBPs Inhibit Motility of *Shigella flexneri* but Are Targeted for Degradation by the Bacterial Ubiquitin Ligase IpaH9.8. *Cell Host Microbe* **22**, 507-518.e5 (2017).

206. Li, H. *et al.* The phosphothreonine lyase activity of a bacterial type III effector family. *Science* **315**, 1000–1003 (2007).

207. de Jong, M. F., Liu, Z., Chen, D. & Alto, N. M. *Shigella flexneri* suppresses NF-kB activation by inhibiting linear ubiquitin chain ligation. *Nat Microbiol* **1**, 16084 (2016).

208. Sanada, T. *et al.* The *Shigella flexneri* effector OspI deamidates UBC13 to dampen the inflammatory response. *Nature* **483**, 623–626 (2012).

209. Newton, H. J. *et al.* The type III effectors NleE and NleB from enteropathogenic E. coli and OspZ from *Shigella* block nuclear translocation of NF-kappaB p65. *PLoS Pathog* **6**, e1000898 (2010).

210. Kim, D. W. *et al.* The *Shigella flexneri* effector OspG interferes with innate immune responses by targeting ubiquitin-conjugating enzymes. *Proc Natl Acad Sci U S A* **102**, 14046–14051 (2005).

211. Grishin, A. M. *et al.* Structural basis for the inhibition of host protein ubiquitination by *Shigella* effector kinase OspG. *Structure* **22**, 878–888 (2014).

212. Goldberg, M. B., Bârzu, O., Parsot, C. & Sansonetti, P. J. Unipolar localization and ATPase activity of IcsA, a Shigella flexneri protein involved in intracellular movement. *Journal of Bacteriology* **175**, 2189–2196 (1993).

213. Suzuki, T. *et al.* Neural Wiskott-Aldrich syndrome protein (N-WASP) is the specific ligand for *Shigella* VirG among the WASP family and determines the host cell type allowing actin-based spreading. *Cell Microbiol* **4**, 223–233 (2002).

214. Kadurugamuwa, J. L., Rohde, M., Wehland, J. & Timmis, K. N. Intercellular spread of *Shigella flexneri* through a monolayer mediated by membranous protrusions and associated with reorganization of the cytoskeletal protein vinculin. *Infect Immun* **59**, 3463–3471 (1991).

215. Fukumatsu, M. *et al. Shigella* Targets Epithelial Tricellular Junctions and Uses a Noncanonical Clathrin-Dependent Endocytic Pathway to Spread Between Cells. *Cell Host & Microbe* **11**, 325–336 (2012).

216. Kuehl, C. J., Dragoi, A.-M. & Agaisse, H. The *Shigella flexneri* type 3 secretion system is required for tyrosine kinase-dependent protrusion resolution, and vacuole escape during bacterial dissemination. *PLoS One* **9**, e112738 (2014).

217. Monack, D. M. & Theriot, J. A. Actin-based motility is sufficient for bacterial membrane protrusion formation and host cell uptake. *Cellular Microbiology* **3**, 633–647 (2001).

218. Ogawa, H., Nakamura, A. & Nakaya, R. Cinemicrographic study of tissue cell cultures infected with *Shigella flexneri*. *Jpn J Med Sci Biol* **21**, 259–273 (1968).

219. Makino, S., Sasakawa, C., Kamata, K., Kurata, T. & Yoshikawa, M. A genetic determinant required for continuous reinfection of adjacent cells on large plasmid in S. flexneri 2a. *Cell* **46**, 551–555 (1986).

220. Suzuki, T., Lett, M. C. & Sasakawa, C. Extracellular transport of VirG protein in Shigella. *J Biol Chem* **270**, 30874–30880 (1995).

221. Brandon, L. D. *et al.* IcsA, a polarly localized autotransporter with an atypical signal peptide, uses the Sec apparatus for secretion, although the Sec apparatus is circumferentially distributed. *Mol Microbiol* **50**, 45–60 (2003).

222. Leupold, S., Büsing, P., Mas, P. J., Hart, D. J. & Scrima, A. Structural insights into the architecture of the *Shigella flexneri* virulence factor IcsA/VirG and motifs involved in polar distribution and secretion. *J Struct Biol* **198**, 19–27 (2017).

223. Egile, C., d'Hauteville, H., Parsot, C. & Sansonetti, P. J. SopA, the outer membrane protease responsible for polar localization of IcsA in *Shigella flexneri*. *Mol Microbiol* **23**, 1063–1073 (1997).

224. d'Hauteville, H., Dufourcq Lagelouse, R., Nato, F. & Sansonetti, P. J. Lack of cleavage of IcsA in *Shigella flexneri* causes aberrant movement and allows demonstration of a cross-reactive eukaryotic protein. *Infect Immun* **64**, 511–517 (1996).

225. Shere, K. D., Sallustio, S., Manessis, A., D'Aversa, T. G. & Goldberg, M. B. Disruption of IcsP, the major *Shigella* protease that cleaves IcsA, accelerates actin-based motility. *Mol Microbiol* **25**, 451–462 (1997).

226. Amann, K. J. & Pollard, T. D. Cellular regulation of actin network assembly. *Curr Biol* **10**, R728-730 (2000).

227. Pollard, T. D. & Borisy, G. G. Cellular motility driven by assembly and disassembly of actin filaments. *Cell* **112**, 453–465 (2003).

228. Didry, D., Carlier, M. F. & Pantaloni, D. Synergy between actin depolymerizing factor/cofilin and profilin in increasing actin filament turnover. *J Biol Chem* **273**, 25602–25611 (1998).

229. Shekhar, S., Pernier, J. & Carlier, M.-F. Regulators of actin filament barbed ends at a glance. *J Cell Sci* **129**, 1085–1091 (2016).

230. Alekhina, O., Burstein, E. & Billadeau, D. D. Cellular functions of WASP family proteins at a glance. *J Cell Sci* **130**, 2235–2241 (2017).

231. Rohatgi, R., Ho, H. Y. & Kirschner, M. W. Mechanism of N-WASP activation by CDC42 and phosphatidylinositol 4, 5-bisphosphate. *J Cell Biol* **150**, 1299–1310 (2000).

232. Loisel, T. P., Boujemaa, R., Pantaloni, D. & Carlier, M. F. Reconstitution of actin-based motility of *Listeria* and *Shigella* using pure proteins. *Nature* **401**, 613–616 (1999).

233. Mauricio, R. P. M., Jeffries, C. M., Svergun, D. I. & Deane, J. E. The *Shigella* Virulence Factor IcsA Relieves N-WASP Autoinhibition by Displacing the Verprolin Homology/Cofilin/Acidic (VCA) Domain. *J Biol Chem* **292**, 134–145 (2017).

234. Egile, C. *et al.* Activation of the Cdc42 Effector N-Wasp by the *Shigella flexneri* Icsa Protein Promotes Actin Nucleation by Arp2/3 Complex and Bacterial Actin-Based Motility. *J Cell Biol* **146**, 1319–1332 (1999).

235. Leung, Y., Ally, S. & Goldberg, M. B. Bacterial Actin Assembly Requires Toca-1 to Relieve N-WASP Autoinhibition. *Cell Host Microbe* **3**, 39–47 (2008).

236. Dragoi, A.-M., Talman, A. M. & Agaisse, H. Bruton's Tyrosine Kinase Regulates *Shigella flexneri* Dissemination in HT-29 Intestinal Cells. *Infect Immun* **81**, 598–607 (2013).

237. Mimuro, H. *et al.* Profilin is required for sustaining efficient intra- and intercellular spreading of *Shigella flexneri*. *J Biol Chem* **275**, 28893–28901 (2000).

238. Agaisse, H. Molecular and Cellular Mechanisms of *Shigella flexneri* Dissemination. *Frontiers in Cellular and Infection Microbiology* **6**, 29 (2016).

239. Heindl, J. E., Saran, I., Yi, C., Lesser, C. F. & Goldberg, M. B. Requirement for formin-induced actin polymerization during spread of *Shigella flexneri*. *Infect Immun* **78**, 193–203 (2010).

240. Wallar, B. J. & Alberts, A. S. The formins: active scaffolds that remodel the cytoskeleton. *Trends Cell Biol* **13**, 435–446 (2003).

241. Yang, C. & Svitkina, T. Filopodia initiation. *Cell Adh Migr* **5**, 402–408 (2011).

242. Bohil, A. B., Robertson, B. W. & Cheney, R. E. Myosin-X is a molecular motor that functions in filopodia formation. *Proc Natl Acad Sci U S A* **103**, 12411–12416 (2006).

243. Bishai, E. A. *et al.* Myosin-X facilitates *Shigella*-induced membrane protrusions and cell-to-cell spread. *Cell Microbiol* **15**, 353–367 (2013).

244. Alieva, N. O. *et al.* Myosin IIA and formin dependent mechanosensitivity of filopodia adhesion. *Nat Commun* **10**, 3593 (2019).

245. Sansonetti, P. J., Mounier, J., Prévost, M. C. & Mège, R. M. Cadherin expression is required for the spread of *Shigella flexneri* between epithelial cells. *Cell* **76**, 829–839 (1994).

246. Tran Van Nhieu, G. *et al.* Connexin-dependent inter-cellular communication increases invasion and dissemination of *Shigella* in epithelial cells. *Nat Cell Biol* **5**, 720–726 (2003).

247. Shaikh, N., Terajima, J. & Watanabe, H. IpaC of *Shigella* binds to the C-terminal domain of beta-catenin. *Microb Pathog* **35**, 107–117 (2003).

248. Duncan-Lowey, J. K., Wiscovitch, A. L., Wood, T. E., Goldberg, M. B. & Russo, B. C. *Shigella flexneri* Disruption of Cellular Tension Promotes Intercellular Spread. *Cell Rep* **33**, 108409 (2020).

249. Dragoi, A.-M. & Agaisse, H. The Serine/Threonine Kinase STK11 Promotes *Shigella flexneri* Dissemination through Establishment of Cell-Cell Contacts Competent for Tyrosine Kinase Signaling. *Infection and Immunity* **82**, 4447–4457 (2014).

250. Dragoi, A.-M. & Agaisse, H. The class II phosphatidylinositol 3-phosphate kinase PIK3C2A promotes *Shigella flexneri* dissemination through formation of vacuole-like protrusions. *Infect Immun* **83**, 1695–1704 (2015).

251. Royle, S. J. The cellular functions of clathrin. *Cell Mol Life Sci* **63**, 1823–1832 (2006).

252. Veiga, E. & Cossart, P. The role of clathrin-dependent endocytosis in bacterial internalization. *Trends Cell Biol* **16**, 499–504 (2006).

253. Lum, M., Attridge, S. R. & Morona, R. Impact of Dynasore an Inhibitor of Dynamin II on *Shigella flexneri* Infection. *PLoS One* **8**, e84975 (2013).

254. Rathman, M. *et al.* The development of a FACS-based strategy for the isolation of *Shigella flexneri* mutants that are deficient in intercellular spread. *Molecular Microbiology* **35**, 974–990 (2000).

255. Weddle, E. & Agaisse, H. Spatial, Temporal, and Functional Assessment of LC3-Dependent Autophagy in *Shigella flexneri* Dissemination. *Infection and Immunity* **86**, (2018).

256. Xu, C. & Min, J. Structure and function of WD40 domain proteins. *Protein Cell* **2**, 202–214 (2011).

257. Steele, M. R. *et al.* Identification of a surface on the beta-propeller protein RACK1 that interacts with the cAMP-specific phosphodiesterase PDE4D5. *Cell Signal* **13**, 507–513 (2001).

258. Carrillo, D. R. *et al.* Structure of human Rack1 protein at a resolution of 2.45 Å. *Acta Crystallographica Section F* **68**, 867–872 (2012).

259. Ron, D. *et al.* Cloning of an intracellular receptor for protein kinase C: a homolog of the beta subunit of G proteins. *Proc Natl Acad Sci U S A* **91**, 839–843 (1994).

260. Ron, D. *et al.* Coordinated movement of RACK1 with activated betaIIPKC. *J Biol Chem* **274**, 27039–27046 (1999).

261. Stebbins, E. G. & Mochly-Rosen, D. Binding specificity for RACK1 resides in the V5 region of beta II protein kinase C. *J Biol Chem* **276**, 29644–29650 (2001).

262. Vomastek, T. *et al.* RACK1 targets the extracellular signal-regulated kinase/mitogen-activated protein kinase pathway to link integrin engagement with focal adhesion disassembly and cell motility. *Mol Cell Biol* **27**, 8296–8305 (2007).

263. Belozerov, V. E., Ratkovic, S., McNeill, H., Hilliker, A. J. & McDermott, J. C. In vivo interaction proteomics reveal a novel p38 mitogen-activated protein kinase/Rack1 pathway regulating proteostasis in Drosophila muscle. *Mol Cell Biol* **34**, 474–484 (2014).

264. López-Bergami, P. *et al.* RACK1 mediates activation of JNK by protein kinase C [corrected]. *Mol Cell* **19**, 309–320 (2005).

265. Cargnello, M. & Roux, P. P. Activation and Function of the MAPKs and Their Substrates, the MAPK-Activated Protein Kinases. *Microbiol Mol Biol Rev* **75**, 50–83 (2011).

266. Kiely, P. A., Leahy, M., O'Gorman, D. & O'Connor, R. RACK1-mediated Integration of Adhesion and Insulin-like Growth Factor I (IGF-I) Signaling and Cell Migration Are Defective in Cells Expressing an IGF-I Receptor Mutated at Tyrosines 1250 and 1251 *. *Journal of Biological Chemistry* **280**, 7624–7633 (2005).

267. Zhang, W. *et al.* RACK1 recruits STAT3 specifically to insulin and insulin-like growth factor 1 receptors for activation, which is important for regulating anchorage-independent growth. *Mol Cell Biol* **26**, 413–424 (2006).

268. Zong, C. S. *et al.* Mechanism of STAT3 activation by insulin-like growth factor I receptor. *J Biol Chem* **275**, 15099–15105 (2000).

269. Liliental, J. & Chang, D. D. Rack1, a receptor for activated protein kinase C, interacts with integrin beta subunit. *J Biol Chem* **273**, 2379–2383 (1998).

270. Hermanto, U., Zong, C. S., Li, W. & Wang, L.-H. RACK1, an insulin-like growth factor I (IGF-I) receptor-interacting protein, modulates IGF-I-dependent integrin signaling and promotes cell spreading and contact with extracellular matrix. *Mol Cell Biol* **22**, 2345–2365 (2002).

271. Kiely, P. A. *et al.* Phosphorylation of RACK1 on tyrosine 52 by c-Abl is required for insulin-like growth factor I-mediated regulation of focal adhesion kinase. *J Biol Chem* **284**, 20263–20274 (2009).

272. Besson, A., Wilson, T. L. & Yong, V. W. The anchoring protein RACK1 links protein kinase Cepsilon to integrin beta chains. Requirements for adhesion and motility. *J Biol Chem* **277**, 22073–22084 (2002).

273. De Toni-Costes, F. *et al.* A New alpha5beta1 integrin-dependent survival pathway through GSK3beta activation in leukemic cells. *PLoS One* **5**, e9807 (2010).

274. Sengupta, J. *et al.* Identification of the versatile scaffold protein RACK1 on the eukaryotic ribosome by cryo-EM. *Nat Struct Mol Biol* **11**, 957–962 (2004).

275. Nielsen, M. H., Flygaard, R. K. & Jenner, L. B. Structural analysis of ribosomal RACK1 and its role in translational control. *Cell Signal* **35**, 272–281 (2017).

276. Gallo, S. & Manfrini, N. Working hard at the nexus between cell signaling and the ribosomal machinery: An insight into the roles of RACK1 in translational regulation. *Translation (Austin)* **3**, e1120382 (2015).

277. Ceci, M. *et al.* Release of eIF6 (p27BBP) from the 60S subunit allows 80S ribosome assembly. *Nature* **426**, 579–584 (2003).

278. Gallo, S. *et al.* RACK1 Specifically Regulates Translation through Its Binding to Ribosomes. *Mol Cell Biol* **38**, e00230-18 (2018).

279. Dobrikov, M. I., Dobrikova, E. Y. & Gromeier, M. Ribosomal RACK1:Protein Kinase C βII Phosphorylates Eukaryotic Initiation Factor 4G1 at S1093 To Modulate Cap-Dependent and -Independent Translation Initiation. *Mol Cell Biol* **38**, e00304-18 (2018).

280. Nilsson, J., Sengupta, J., Frank, J. & Nissen, P. Regulation of eukaryotic translation by the RACK1 protein: a platform for signalling molecules on the ribosome. *EMBO Rep* **5**, 1137–1141 (2004).

281. Kim, H. D., Kong, E., Kim, Y., Chang, J.-S. & Kim, J. RACK1 depletion in the ribosome induces selective translation for non-canonical autophagy. *Cell Death Dis* **8**, e2800 (2017).

282. Yang, Z. & Klionsky, D. J. Mammalian autophagy: core molecular machinery and signaling regulation. *Curr Opin Cell Biol* **22**, 124–131 (2010).

283. Yang, Z. & Klionsky, D. J. An overview of the molecular mechanism of autophagy. *Curr Top Microbiol Immunol* **335**, 1–32 (2009).

284. Volta, V. *et al.* RACK1 depletion in a mouse model causes lethality, pigmentation deficits and reduction in protein synthesis efficiency. *Cell Mol Life Sci* **70**, 1439–1450 (2013).

285. Zhao, Y. *et al.* RACK1 Promotes Autophagy by Enhancing the Atg14L-Beclin 1-Vps34-Vps15 Complex Formation upon Phosphorylation by AMPK. *Cell Rep* **13**, 1407–1417 (2015).

286. Jaber, N. & Zong, W.-X. Class III PI3K Vps34: essential roles in autophagy, endocytosis, and heart and liver function. *Ann N Y Acad Sci* **1280**, 48–51 (2013).

287. Kim, J., Kundu, M., Viollet, B. & Guan, K.-L. AMPK and mTOR regulate autophagy through direct phosphorylation of Ulk1. *Nature Cell Biology* **13**, 132 (2011).

288. Erbil, S. *et al.* RACK1 Is an Interaction Partner of ATG5 and a Novel Regulator of Autophagy. *J. Biol. Chem.* **291**, 16753–16765 (2016).

289. Li, J.-J. & Xie, D. RACK1, a versatile hub in cancer. *Oncogene* **34**, 1890–1898 (2015).

290. White, E., Mehnert, J. M. & Chan, C. S. Autophagy, Metabolism, and Cancer. *Clin Cancer Res* **21**, 5037–5046 (2015).

291. Usman, R. M. *et al.* Role and mechanism of autophagy-regulating factors in tumorigenesis and drug resistance. *Asia Pac J Clin Oncol* **17**, 193–208 (2021).

292. Mamidipudi, V. & Cartwright, C. A. A novel pro-apoptotic function of RACK1: suppression of Src activity in the intrinsic and Akt pathways. *Oncogene* **28**, 4421–4433 (2009).

293. Garrido, C. *et al.* Mechanisms of cytochrome c release from mitochondria. *Cell Death Differ* **13**, 1423–1433 (2006).

294. Wu, Y. *et al.* RACK1 promotes Bax oligomerization and dissociates the interaction of Bax and Bcl-XL. *Cell Signal* **22**, 1495–1501 (2010).

295. Al-Reefy, S., Osman, H., Jiang, W. & Mokbel, K. Evidence for a pro-apoptotic function of RACK1 in human breast cancer. *Oncogene* **29**, 5651; author reply 5652 (2010).

296. Cheng, Z.-F., Pai, R. K. & Cartwright, C. A. Rack1 function in intestinal epithelia: regulating crypt cell proliferation and regeneration and promoting differentiation and apoptosis. *Am J Physiol Gastrointest Liver Physiol* **314**, G1–G13 (2018).

297. Zhang, W. *et al.* RACK1 and CIS mediate the degradation of BimEL in cancer cells. *J Biol Chem* **283**, 16416–16426 (2008).

298. Subauste, M. C. *et al.* RACK1 downregulates levels of the pro-apoptotic protein Fem1b in apoptosis-resistant colon cancer cells. *Cancer Biol Ther* **8**, 2297–2305 (2009).

299. Subauste, M. C. *et al.* Fem1b, a proapoptotic protein, mediates proteasome inhibitor-induced apoptosis of human colon cancer cells. *Mol Carcinog* **49**, 105–113 (2010).

300. Sang, N. *et al.* RACK1 interacts with E1A and rescues E1A-induced yeast growth inhibition and mammalian cell apoptosis. *J Biol Chem* **276**, 27026–27033 (2001).

301. Qian, L. *et al.* Downregulation of RACK1 is associated with cardiomyocyte apoptosis after myocardial ischemia/reperfusion injury in adult rats. *In Vitro Cell Dev Biol Anim* **52**, 305–313 (2016).

302. Zou, Y.-H., Li, X.-D., Zhang, Q.-H. & Liu, D.-Z. RACK1 Silencing Induces Cell Apoptosis and Inhibits Cell Proliferation in Hepatocellular Carcinoma MHCC97-H Cells. *Pathol Oncol Res* **24**, 101–107 (2018).

303. Guo, Y. *et al.* Receptor for activated C kinase 1 promotes hepatocellular carcinoma growth by enhancing mitogen-activated protein kinase kinase 7 activity. *Hepatology* **57**, 140–151 (2013).

304. Ruan, Y. *et al.* Ribosomal RACK1 promotes chemoresistance and growth in human hepatocellular carcinoma. *J Clin Invest* **122**, 2554–2566 (2012).

305. Zhang, D. *et al.* RACK1 promotes the proliferation of THP1 acute myeloid leukemia cells. *Mol Cell Biochem* **384**, 197–202 (2013).

306. Zhang, L., Xu, Y., Wang, L. & Liu, H. Role of RACK1 on cell proliferation, adhesion, and bortezomib-induced apoptosis in multiple myeloma. *Int J Biol Macromol* **121**, 1077–1085 (2019).

307. Parsons, J. T., Horwitz, A. R. & Schwartz, M. A. Cell adhesion: integrating cytoskeletal dynamics and cellular tension. *Nat Rev Mol Cell Biol* **11**, 633–643 (2010).

308. Nagano, M., Hoshino, D., Koshikawa, N., Akizawa, T. & Seiki, M. Turnover of focal adhesions and cancer cell migration. *Int J Cell Biol* **2012**, 310616 (2012).

309. Humphries, J. D. *et al.* Vinculin controls focal adhesion formation by direct interactions with talin and actin. *J Cell Biol* **179**, 1043–1057 (2007).

310. Sjöblom, B., Salmazo, A. & Djinović-Carugo, K. Alpha-actinin structure and regulation. *Cell Mol Life Sci* **65**, 2688–2701 (2008).

311. Webb, D. J. *et al.* FAK-Src signalling through paxillin, ERK and MLCK regulates adhesion disassembly. *Nat Cell Biol* **6**, 154–161 (2004).

312. Mitra, S. K. & Schlaepfer, D. D. Integrin-regulated FAK-Src signaling in normal and cancer cells. *Curr Opin Cell Biol* **18**, 516–523 (2006).

313. Nobes, C. D. & Hall, A. Rho, rac, and cdc42 GTPases regulate the assembly of multimolecular focal complexes associated with actin stress fibers, lamellipodia, and filopodia. *Cell* **81**, 53–62 (1995).

314. Lin, H. *et al.* CPNE3 promotes migration and invasion in non-small cell lung cancer by interacting with RACK1 via FAK signaling activation. *J Cancer* **9**, 4215–4222 (2018).

315. Serrels, B. *et al.* A complex between FAK, RACK1, and PDE4D5 controls spreading initiation and cancer cell polarity. *Curr Biol* **20**, 1086–1092 (2010).

316. Yarwood, S. J., Parnell, E. & Bird, R. J. The cyclic AMP phosphodiesterase 4D5 (PDE4D5)/receptor for activated C-kinase 1 (RACK1) signalling complex as a sensor of the extracellular nano-environment. *Cell Signal* **35**, 282–289 (2017).

317. Serrels, B., Sandilands, E. & Frame, M. C. Signaling of the direction-sensing FAK/RACK1/PDE4D5 complex to the small GTPase Rap1. *Small GTPases* **2**, 54–61 (2011).

318. Dave, J. M., Kang, H., Abbey, C. A., Maxwell, S. A. & Bayless, K. J. Proteomic profiling of endothelial invasion revealed receptor for activated C kinase 1 (RACK1) complexed with vimentin to regulate focal adhesion kinase (FAK). *J Biol Chem* **288**, 30720–30733 (2013).

319. Strouhalova, K. *et al.* Vimentin Intermediate Filaments as Potential Target for Cancer Treatment. *Cancers (Basel)* **12**, E184 (2020).

320. Havel, L. S., Kline, E. R., Salgueiro, A. M. & Marcus, A. I. Vimentin regulates lung cancer cell adhesion through a VAV2–Rac1 pathway to control focal adhesion kinase activity. *Oncogene* **34**, 1979–1990 (2015).

321. Mamidipudi, V., Chang, B. Y., Harte, R. A., Lee, K. C. & Cartwright, C. A. RACK1 inhibits the serum- and anchorage-independent growth of v-Src transformed cells. *FEBS Lett* **567**, 321–326 (2004).

322. Yaka, R. *et al.* NMDA receptor function is regulated by the inhibitory scaffolding protein, RACK1. *Proc Natl Acad Sci U S A* **99**, 5710–5715 (2002).

323. Yaka, R., He, D.-Y., Phamluong, K. & Ron, D. Pituitary adenylate cyclase-activating polypeptide (PACAP(1-38)) enhances N-methyl-D-aspartate receptor function and brain-derived neurotrophic factor expression via RACK1. *J Biol Chem* **278**, 9630–9638 (2003).

324. Seddas, P. *et al.* Rack-1, GAPDH3, and actin: proteins of Myzus persicae potentially involved in the transcytosis of beet western yellows virus particles in the aphid. *Virology* **325**, 399–412 (2004).

325. Kuhn, L. *et al.* Definition of a RACK1 Interaction Network in *Drosophila melanogaster* Using SWATH-MS. *G3 (Bethesda)* **7**, 2249–2258 (2017).

326. Filho, E. G. F. *et al.* RACK1 plays a critical role in mast cell secretion and Ca2+ mobilization by modulating F-actin dynamics. *J Cell Sci* **134**, jcs252585 (2021).

327. Buensuceso, C. S., Woodside, D., Huff, J. L., Plopper, G. E. & O'Toole, T. E. The WD protein Rack1 mediates protein kinase C and integrin-dependent cell migration. *J. Cell. Sci.* **114**, 1691–1698 (2001).

328. Cox, E. A., Bennin, D., Doan, A. T., O'Toole, T. & Huttenlocher, A. RACK1 Regulates Integrin-mediated Adhesion, Protrusion, and Chemotactic Cell Migration via Its Src-binding Site. *Mol Biol Cell* **14**, 658–669 (2003).

329. Park, J. H. *et al.* RACK1 interaction with c-Src is essential for osteoclast function. *Exp Mol Med* **51**, 1–9 (2019).

330. Ballek, O. *et al.* TCR Triggering Induces the Formation of Lck-RACK1-Actinin-1 Multiprotein Network Affecting Lck Redistribution. *Front Immunol* **7**, 449 (2016).

331. Kershner, L. & Welshhans, K. RACK1 is necessary for the formation of point contacts and regulates axon growth. *Dev Neurobiol* **77**, 1038–1056 (2017).

332. Feng, C. *et al.* Kindlin-3 Mediates Integrin αLβ2 Outside-in Signaling, and It Interacts with Scaffold Protein Receptor for Activated-C Kinase 1 (RACK1). *J Biol Chem* **287**, 10714–10726 (2012).

333. Osmanagic-Myers, S. & Wiche, G. Plectin-RACK1 (receptor for activated C kinase 1) scaffolding: a novel mechanism to regulate protein kinase C activity. *J Biol Chem* **279**, 18701–18710 (2004).

334. Bachmann, M., Kukkurainen, S., Hytönen, V. P. & Wehrle-Haller, B. Cell Adhesion by Integrins. *Physiol Rev* **99**, 1655–1699 (2019).

335. Kim, S. W., Joo, Y. J. & Kim, J. Asc1p, a ribosomal protein, plays a pivotal role in cellular adhesion and virulence in Candida albicans. *J Microbiol* **48**, 842–848 (2010).

336. Liu, X., Nie, X., Ding, Y. & Chen, J. Asc1, a WD-repeat protein, is required for hyphal development and virulence in Candida albicans. *Acta Biochim Biophys Sin (Shanghai)* **42**, 793–800 (2010).

337. Palmer, D. A., Thompson, J. K., Li, L., Prat, A. & Wang, P. Gib2, a novel Gbeta-like/RACK1 homolog, functions as a Gbeta subunit in cAMP signaling and is essential in *Cryptococcus neoformans*. *J Biol Chem* **281**, 32596–32605 (2006).

338. Wang, Y. *et al.* Noncanonical Gβ Gib2 is a scaffolding protein promoting cAMP signaling through functions of Ras1 and Cac1 proteins in *Cryptococcus neoformans*. *J Biol Chem* **289**, 12202–12216 (2014).

339. Pukkila-Worley, R. *et al.* Transcriptional network of multiple capsule and melanin genes governed by the *Cryptococcus neoformans* cyclic AMP cascade. *Eukaryot Cell* **4**, 190–201 (2005).

340. Blomqvist, K., DiPetrillo, C., Streva, V. A., Pine, S. & Dvorin, J. D. Receptor for Activated C-Kinase 1 (PfRACK1) is required for Plasmodium falciparum intra-erythrocytic proliferation. *Mol Biochem Parasitol* **211**, 62–66 (2017).

341. Sartorello, R., Amaya, M. J., Nathanson, M. H. & Garcia, C. R. S. The Plasmodium Receptor for Activated C Kinase Protein Inhibits Ca2+ Signaling in Mammalian Cells. *Biochem Biophys Res Commun* **389**, 586–592 (2009).

342. Arredondo, S. A., Schepis, A., Reynolds, L. & Kappe, S. H. I. Secretory Organelle Function in the *Plasmodium* Sporozoite. *Trends Parasitol* **37**, 651–663 (2021).

343. Kelly, B. L., Stetson, D. B. & Locksley, R. M. *Leishmania* major LACK antigen is required for efficient vertebrate parasitization. *J Exp Med* **198**, 1689–1698 (2003).

344. Cardenas, D. *et al.* LACK, a RACK1 ortholog, facilitates cytochrome c oxidase subunit expression to promote *Leishmania* major fitness. *Molecular Microbiology* **96**, 95–109 (2015).

345. Fernández, L. *et al.* Antigenicity of Leishmania-Activated C-Kinase Antigen (LACK) in Human Peripheral Blood Mononuclear Cells, and Protective Effect of Prime-Boost Vaccination With pCI-neo-LACK Plus Attenuated LACK-Expressing Vaccinia Viruses in Hamsters. *Front Immunol* **9**, 843 (2018).

346. LaFontaine, E., Miller, C. M., Permaul, N., Martin, E. T. & Fuchs, G. Ribosomal protein RACK1 enhances translation of poliovirus and other viral IRESs. *Virology* **545**, 53–62 (2020).

347. Lee, K.-M., Chen, C.-J. & Shih, S.-R. Regulation Mechanisms of Viral IRES-Driven Translation. *Trends Microbiol* **25**, 546–561 (2017).

348. Majzoub, K. *et al.* RACK1 controls IRES-mediated translation of viruses. *Cell* **159**, 1086–1095 (2014).

349. Dhungel, P., Cao, S. & Yang, Z. The 5'-poly(A) leader of poxvirus mRNA confers a translational advantage that can be achieved in cells with impaired cap-dependent translation. *PLoS Pathog* **13**, e1006602 (2017).

350. Jha, S. *et al.* Trans-kingdom mimicry underlies ribosome customization by a poxvirus kinase. *Nature* **546**, 651–655 (2017).

351. Reinhardt, J. & Wolff, T. The influenza A virus M1 protein interacts with the cellular receptor of activated C kinase (RACK) 1 and can be phosphorylated by protein kinase C. *Vet Microbiol* **74**, 87–100 (2000).

352. Hilsch, M. *et al.* Influenza A Matrix Protein M1 Multimerizes upon Binding to Lipid Membranes. *Biophys J* **107**, 912–923 (2014).

353. Demirov, D., Gabriel, G., Schneider, C., Hohenberg, H. & Ludwig, S. Interaction of influenza A virus matrix protein with RACK1 is required for virus release. *Cell Microbiol* **14**, 774–789 (2012).

354. Shue, B. *et al.* Genome-Wide CRISPR Screen Identifies RACK1 as a Critical Host Factor for Flavivirus Replication. *J Virol* **95**, e0059621 (2021).

355. Hafirassou, M. L. *et al.* A Global Interactome Map of the Dengue Virus NS1 Identifies Virus Restriction and Dependency Host Factors. *Cell Rep* **21**, 3900–3913 (2017).

356. Ci, Y. *et al.* Zika NS1-induced ER remodeling is essential for viral replication. *J Cell Biol* **219**, e201903062 (2020).

357. Fällman, M., Deleuil, F. & McGee, K. Resistance to phagocytosis by *Yersinia*. *Int J Med Microbiol* **291**, 501–509 (2002).

358. Dewoody, R. S., Merritt, P. M. & Marketon, M. M. Regulation of the *Yersinia* type III secretion system: traffic control. *Front Cell Infect Microbiol* **3**, 4 (2013).

359. Foegeding, N. J., Caston, R. R., McClain, M. S., Ohi, M. D. & Cover, T. L. An Overview of Helicobacter pylori VacA Toxin Biology. *Toxins (Basel)* **8**, 173 (2016).

360. Hu, Y. *et al.* Downregulation of tumor suppressor RACK1 by *Helicobacter pylori* infection promotes gastric carcinogenesis through the integrin β-1/NF-κB signaling pathway. *Cancer Lett* **450**, 144–154 (2019).

361. Duan, Y. *et al.* RACK1 Mediates NLRP3 Inflammasome Activation by Promoting NLRP3 Active Conformation and Inflammasome Assembly. *Cell Rep* **33**, 108405 (2020).

362. Kesika, P., Karutha Pandian, S. & Balamurugan, K. Analysis of *Shigella flexneri*-mediated infections in model organism Caenorhabditis elegans. *Scand J Infect Dis* **43**, 286–295 (2011).

363. Cheng, Z. *et al.* Pathogen-secreted proteases activate a novel plant immune pathway. *Nature* **521**, 213–216 (2015).

364. Temple, B. R. S. & Jones, A. M. The plant heterotrimeric G-protein complex. *Annu Rev Plant Biol* **58**, 249–266 (2007).

365. Nakashima, A. *et al.* RACK1 functions in rice innate immunity by interacting with the Rac1 immune complex. *Plant Cell* **20**, 2265–2279 (2008).

366. Wang, B., Yu, J., Zhu, D., Chang, Y. & Zhao, Q. Maize ZmRACK1 is involved in the plant response to fungal phytopathogens. *Int J Mol Sci* **15**, 9343–9359 (2014).

367. Onodera, N. T. *et al.* Genome Sequence of *Shigella flexneri* Serotype 5a Strain M90T Sm. *J Bacteriol* **194**, 3022 (2012).

368. Labigne-Roussel, A. F., Lark, D., Schoolnik, G. & Falkow, S. Cloning and expression of an afimbrial adhesin (AFA-I) responsible for P blood group-independent, mannose-resistant hemagglutination from a pyelonephritic Escherichia coli strain. *Infect Immun* **46**, 251–259 (1984).

369. Rutten, P. *et al.* Calibration Protocol - Conversion of OD_{600} to Colony Forming Units (CFUs). *protocols.io* (2019).

370. Sidik, S. *et al.* A *Shigella flexneri* virulence plasmid encoded factor controls production of outer membrane vesicles. *G3 (Bethesda)* **4**, 2493–2503 (2014).

371. Chen, J., Li, Y., Zhang, K. & Wang, H. Whole-Genome Sequence of Phage-Resistant Strain *Escherichia coli* DH5α. *Genome Announc* **6**, e00097-18 (2018).

372. Schindelin, J. *et al.* Fiji: an open-source platform for biological-image analysis. *Nat Methods* **9**, 676–682 (2012).

373. Livak, K. J. & Schmittgen, T. D. Analysis of relative gene expression data using real-time quantitative PCR and the 2(-Delta Delta C(T)) Method. *Methods* **25**, 402–408 (2001).

374. McLean, D. J. & Skowron Volponi, M. A. trajr: An R package for characterisation of animal trajectories. *Ethology* **124**, 440–448 (2018).

375. Oaks, E. V., Wingfield, M. E. & Formal, S. B. Plaque formation by virulent *Shigella flexneri*. *Infect Immun* **48**, 124–129 (1985).

376. Sharma, A. & Puhar, A. Plaque Assay to Determine Invasion and Intercellular Dissemination of Shigella flexneri in TC7 Human Intestinal Epithelial Cells. *Bio Protoc* **9**, e3293 (2019).

377. Bubb, M. R., Senderowicz, A. M., Sausville, E. A., Duncan, K. L. & Korn, E. D. Jasplakinolide, a cytotoxic natural product, induces actin polymerization and competitively inhibits the binding of phalloidin to F-actin. *J Biol Chem* **269**, 14869–14871 (1994).

378. Wakatsuki, T., Schwab, B., Thompson, N. C. & Elson, E. L. Effects of cytochalasin D and latrunculin B on mechanical properties of cells. *J Cell Sci* **114**, 1025–1036 (2001).

379. Carisey, A., Stroud, M., Tsang, R. & Ballestrem, C. Fluorescence Recovery After Photobleaching. in *Cell Migration: Developmental Methods and Protocols* (eds. Wells, C. M. & Parsons, M.) 387–402 (Humana Press, 2011).

380. Kim, Y.-J., Yeo, S.-G., Park, J.-H. & Ko, H.-J. *Shigella* vaccine development: prospective animal models and current status. *Curr Pharm Biotechnol* **14**, 903–912 (2013).

381. Liévin-Le Moal, V. & Servin, A. L. Pathogenesis of Human Enterovirulent Bacteria: Lessons from Cultured, Fully Differentiated Human Colon Cancer Cell Lines. *Microbiol Mol Biol Rev* **77**, 380–439 (2013).

382. Sansonetti, P. J., Ryter, A., Clerc, P., Maurelli, A. T. & Mounier, J. Multiplication of *Shigella flexneri* within HeLa cells: lysis of the phagocytic vacuole and plasmid-mediated contact hemolysis. *Infect Immun* **51**, 461–469 (1986).

383. Urlinger, S. *et al.* Exploring the sequence space for tetracycline-dependent transcriptional activators: Novel mutations yield expanded range and sensitivity. *PNAS* **97**, 7963–7968 (2000).

384. Liu, Y. *et al.* Multi-omic measurements of heterogeneity in HeLa cells across laboratories. *Nat Biotechnol* **37**, 314–322 (2019).

385. Schnupf, P. & Sansonetti, P. J. Shigella Pathogenesis. in *Bacteria and Intracellularity* 15–39 (John Wiley & Sons, Ltd, 2019).

386. Brandt, S. M. *et al.* Secreted Bacterial Effectors and Host-Produced Eiger/TNF Drive Death in a Salmonella-Infected Fruit Fly. *PLoS Biol* **2**, e418 (2004).

387. Fast, D., Kostiuk, B., Foley, E. & Pukatzki, S. Commensal pathogen competition impacts host viability. *Proc Natl Acad Sci USA* **115**, 7099–7104 (2018).

388. Capo, F., Wilson, A. & Di Cara, F. The Intestine of *Drosophila melanogaster*: An Emerging Versatile Model System to Study Intestinal Epithelial Homeostasis and Host-Microbial Interactions in Humans. *Microorganisms* **7**, 336 (2019).

389. Apidianakis, Y. & Rahme, L. G. *Drosophila melanogaster* as a model for human intestinal infection and pathology. *Dis Model Mech* **4**, 21–30 (2011).

390. Kadrmas, J. L., Smith, M. A., Pronovost, S. M. & Beckerle, M. C. Characterization of RACK1 function in *Drosophila* development. *Dev Dyn* **236**, 2207–2215 (2007).

391. Apidianakis, Y., Pitsouli, C., Perrimon, N. & Rahme, L. Synergy between bacterial infection and genetic predisposition in intestinal dysplasia. *Proc Natl Acad Sci U S A* **106**, 20883–20888 (2009).

392. Carayol, N. & Tran Van Nhieu, G. The inside story of Shigella invasion of intestinal epithelial cells. *Cold Spring Harb Perspect Med* **3**, a016717 (2013).

393. Schell, M. J., Erneux, C. & Irvine, R. F. Inositol 1,4,5-trisphosphate 3-kinase A associates with F-actin and dendritic spines via its N terminus. *J Biol Chem* **276**, 37537–37546 (2001).

394. Kentner, D. *et al. Shigella* reroutes host cell central metabolism to obtain high-flux nutrient supply for vigorous intracellular growth. *Proc Natl Acad Sci U S A* **111**, 9929–9934 (2014).

395. Labbé, K. & Saleh, M. Cell death in the host response to infection. *Cell Death Differ* **15**, 1339–1349 (2008).

396. Ashida, H., Suzuki, T. & Sasakawa, C. *Shigella* infection and host cell death: a double-edged sword for the host and pathogen survival. *Current Opinion in Microbiology* **59**, 1–7 (2021).

397. Park, Y.-J. *et al.* Stress Granule Formation Attenuates RACK1-Mediated Apoptotic Cell Death Induced by Morusin. *Int J Mol Sci* **21**, E5360 (2020).

398. Benhamou, S. How to reliably estimate the tortuosity of an animal's path: straightness, sinuosity, or fractal dimension? *J Theor Biol* **229**, 209–220 (2004).

399. Berg, H. C. & Brown, D. A. Chemotaxis in *Escherichia coli* analysed by Three-dimensional Tracking. *Nature* **239**, 500–504 (1972).

400. Taute, K. M., Gude, S., Tans, S. J. & Shimizu, T. S. High-throughput 3D tracking of bacteria on a standard phase contrast microscope. *Nat Commun* **6**, 8776 (2015).

401. Nasatto, P. L. *et al.* Methylcellulose, a Cellulose Derivative with Original Physical Properties and Extended Applications. *Polymers* **7**, 777–803 (2015).

402. Russo, B. C. *et al.* Intermediate filaments enable pathogen docking to trigger type 3 effector translocation. *Nat Microbiol* **1**, 16025 (2016).

403. Lum, M. & Morona, R. Myosin IIA is essential for *Shigella flexneri* cell-to-cell spread. *Pathog Dis* **72**, 174–187 (2014).

404. Suzuki, T. & Sasakawa, C. Molecular basis of the intracellular spreading of *Shigella*. *Infect Immun* **69**, 5959–5966 (2001).

405. Wang, S. *et al.* Actin stabilizing compounds show specific biological effects due to their binding mode. *Sci Rep* **9**, 9731 (2019).

406. Cooper, J. A. Effects of cytochalasin and phalloidin on actin. *J Cell Biol* **105**, 1473–1478 (1987).

407. Lázaro-Diéguez, F. *et al.* Dynamics of an F-actin aggresome generated by the actin-stabilizing toxin jasplakinolide. *Journal of Cell Science* **121**, 1415–1425 (2008).

408. Hardy, L. R. Fluorescence recovery after photobleaching (FRAP) with a focus on F-actin. *Curr Protoc Neurosci* **Chapter 2**, Unit 2.17 (2012).

409. Chou, Y. C. *et al.* Structure and genomic organization of porcine RACK1 gene. *Biochim Biophys Acta* **1489**, 315–322 (1999).

410. Skop, A. R., Liu, H., Yates, J., Meyer, B. J. & Heald, R. Dissection of the Mammalian Midbody Proteome Reveals Conserved Cytokinesis Mechanisms. *Science* **305**, 61–66 (2004).

411. Cao, X.-X. *et al.* RACK1 promotes breast carcinoma proliferation and invasion/metastasis in vitro and in vivo. *Breast Cancer Res Treat* **123**, 375–386 (2010).

412. Shen, F., Yan, C., Liu, M., Feng, Y. & Chen, Y. RACK1 promotes prostate cancer cell proliferation, invasion and metastasis. *Mol Med Rep* **8**, 999–1004 (2013).

413. Wang, X. *et al.* The Shigella Type III Secretion Effector IpaH4.5 Targets NLRP3 to Activate Inflammasome Signaling. *Front Cell Infect Microbiol* **10**, 511798 (2020).

414. Yang, J., Zhao, Y., Shi, J. & Shao, F. Human NAIP and mouse NAIP1 recognize bacterial type III secretion needle protein for inflammasome activation. *Proc Natl Acad Sci U S A* **110**, 14408–14413 (2013).

415. Myllymäki, H., Valanne, S. & Rämet, M. The *Drosophila* imd signaling pathway. *J Immunol* **192**, 3455–3462 (2014).

416. Ragab, A. *et al. Drosophila* Ras/MAPK signalling regulates innate immune responses in immune and intestinal stem cells. *EMBO J* **30**, 1123–1136 (2011).

417. Burton, E. A., Pendergast, A. M. & Aballay, A. The *Caenorhabditis elegans* ABL-1 tyrosine kinase is required for *Shigella flexneri* pathogenesis. *Appl Environ Microbiol* **72**, 5043–5051 (2006).

418. Bonfini, A., Liu, X. & Buchon, N. From pathogens to microbiota: How *Drosophila* intestinal stem cells react to gut microbes. *Dev Comp Immunol* **64**, 22–38 (2016).

419. Yokota, S. *et al.* Measles virus suppresses interferon-alpha signaling pathway: suppression of Jak1 phosphorylation and association of viral accessory proteins, C and V, with interferon-alpha receptor complex. *Virology* **306**, 135–146 (2003).

420. Cancer Genome Atlas Network. Comprehensive molecular characterization of human colon and rectal cancer. *Nature* **487**, 330–337 (2012).

421. Deng, Y.-Z. *et al.* RACK1 suppresses gastric tumorigenesis by stabilizing the β-catenin destruction complex. *Gastroenterology* **142**, 812-823.e15 (2012).

422. Yu, Z. *et al.* A novel UBE2T inhibitor suppresses Wnt/β-catenin signaling hyperactivation and gastric cancer progression by blocking RACK1 ubiquitination. *Oncogene* **40**, 1027–1042 (2021).

423. Duggan, G. M. & Mostowy, S. Use of zebrafish to study *Shigella* infection. *Dis Model Mech* **11**, dmm032151 (2018).

424. Lieschke, G. J. & Currie, P. D. Animal models of human disease: zebrafish swim into view. *Nat Rev Genet* **8**, 353–367 (2007).

425. Dehio, C., Prévost, M. C. & Sansonetti, P. J. Invasion of epithelial cells by *Shigella flexneri* induces tyrosine phosphorylation of cortactin by a pp60c-src-mediated signalling pathway. *EMBO J* **14**, 2471–2482 (1995).

426. Hernández, A. J. A., Reyes, V. L., Albores-García, D., Gómez, R. & Calderón-Aranda, E. S. MeHg affects the activation of FAK, Src, Rac1 and Cdc42, critical proteins for cell movement in PDGF-stimulated SH-SY5Y neuroblastoma cells. *Toxicology* **394**, 35–44 (2018).

427. Lehto, T., Miaczynska, M., Zerial, M., Müller, D. J. & Severin, F. Observing the growth of individual actin filaments in cell extracts by time-lapse atomic force microscopy. *FEBS Lett* **551**, 25–28 (2003).

428. Doolittle, L. K., Rosen, M. K. & Padrick, S. B. Measurement and Analysis of in vitro Actin Polymerization. *Methods Mol Biol* **1046**, 273–293 (2013).

429. Dewoody, R., Merritt, P. M. & Marketon, M. M. YopK controls both rate and fidelity of Yop translocation. *Mol Microbiol* **87**, 301–317 (2013).

430. Schroeder, G. N. & Hilbi, H. Cholesterol is required to trigger caspase-1 activation and macrophage apoptosis after phagosomal escape of *Shigella*. *Cell Microbiol* **9**, 265–278 (2007).

431. Schroeder, G. N., Jann, N. J. & Hilbi, H. Intracellular type III secretion by cytoplasmic *Shigella flexneri* promotes caspase-1-dependent macrophage cell death. *Microbiology (Reading)* **153**, 2862–2876 (2007).

432. Li, S. *et al.* Multi-omics analysis of glucose-mediated signaling by a moonlighting Gβ protein Asc1/RACK1. *PLoS Genet* **17**, e1009640 (2021).

433. Malik-Kale, P., Winfree, S. & Steele-Mortimer, O. The bimodal lifestyle of intracellular *Salmonella* in epithelial cells: replication in the cytosol obscures defects in vacuolar replication. *PLoS ONE* **7**, e38732 (2012).

434. Miller, A. H., Vayttaden, S. J., Al-Khodor, S. & Fraser, I. D. C. Assay Development for Image-Based Quantification of Intracellular Bacterial Replication and Analysis of the Innate Immune Response to Infection. *Assay Drug Dev Technol* **13**, 515–528 (2015).

435. Birmingham, C. L. *et al.* Listeriolysin O allows *Listeria monocytogenes* replication in macrophage vacuoles. *Nature* **451**, 350–354 (2008).

436. Mou, X., Souter, S., Du, J., Reeves, A. Z. & Lesser, C. F. Synthetic bottom-up approach reveals the complex interplay of *Shigella* effectors in regulation of epithelial cell death. *Proc Natl Acad Sci U S A* **115**, 6452–6457 (2018).

437. Piro, A. S. *et al.* Detection of Cytosolic *Shigella flexneri* via a C-Terminal Triple-Arginine Motif of GBP1 Inhibits Actin-Based Motility. *mBio* **8**, e01979-17 (2017).

438. Padrick, S. B. & Rosen, M. K. Physical Mechanisms of Signal Integration by WASP Family Proteins. *Annu Rev Biochem* **79**, 707–735 (2010).

439. Ho, H.-Y. H. *et al.* Toca-1 mediates Cdc42-dependent actin nucleation by activating the N-WASP-WIP complex. *Cell* **118**, 203–216 (2004).

440. Burton, E. A., Oliver, T. N. & Pendergast, A. M. Abl kinases regulate actin comet tail elongation via an N-WASP-dependent pathway. *Mol Cell Biol* **25**, 8834–8843 (2005).

441. Gouin, E. *et al.* A comparative study of the actin-based motilities of the pathogenic bacteria *Listeria monocytogenes*, *Shigella flexneri* and *Rickettsia conorii*. *Journal of cell science* **112 (Pt 11)**, 1697–708 (1999).

442. Frischknecht, F. *et al.* Tyrosine phosphorylation is required for actin-based motility of vaccinia but not Listeria or Shigella. *Curr Biol* **9**, 89–92 (1999).

443. Grognot, M. & Taute, K. M. More than propellers: how flagella shape bacterial motility behaviors. *Curr Opin Microbiol* **61**, 73–81 (2021).

444. Kühn, S. & Enninga, J. The actin comet guides the way: How *Listeria* actin subversion has impacted cell biology, infection biology and structural biology. *Cell Microbiol* **22**, e13190 (2020).

445. Magdalena, J. & Goldberg, M. B. Quantification of *Shigella* IcsA required for bacterial actin polymerization. *Cell Motil Cytoskeleton* **51**, 187–196 (2002).

446. Zeile, W. L., Purich, D. L. & Southwick, F. S. Recognition of two classes of oligoproline sequences in profilin-mediated acceleration of actin-based *Shigella* motility. *J Cell Biol* **133**, 49–59 (1996).

447. McGrath, J. L. *et al.* The force-velocity relationship for the actin-based motility of *Listeria monocytogenes*. *Curr Biol* **13**, 329–332 (2003).

448. Lacayo, C. I. & Theriot, J. A. *Listeria monocytogenes* Actin-based Motility Varies Depending on Subcellular Location: A Kinematic Probe for Cytoarchitecture. *Mol Biol Cell* **15**, 2164–2175 (2004).

449. Soo, F. S. & Theriot, J. A. Large-Scale Quantitative Analysis of Sources of Variation in the Actin Polymerization-Based Movement of *Listeria monocytogenes*. *Biophys J* **89**, 703–723 (2005).

450. Kuehl, C. J., Dragoi, A.-M., Talman, A. & Agaisse, H. Bacterial spread from cell to cell: beyond actin-based motility. *Trends in Microbiology* **23**, 558–566 (2015).

451. Carpenter, C. D. *et al.* The Vps/VacJ ABC transporter is required for intercellular spread of *Shigella flexneri*. *Infect Immun* **82**, 660–669 (2014).

452. Koestler, B. J., Fisher, C. R. & Payne, S. M. Formate Promotes *Shigella* Intercellular Spread and Virulence Gene Expression. *mBio* **9**, e01777-18 (2018).

453. Ortega, F. E., Koslover, E. F. & Theriot, J. A. *Listeria monocytogenes* cell-to-cell spread in epithelia is heterogeneous and dominated by rare pioneer bacteria. *Elife* **8**, e40032 (2019).

454. Davidson, A. J. & Wood, W. Unravelling the Actin Cytoskeleton: A New Competitive Edge? *Trends Cell Biol* **26**, 569–576 (2016).

455. Gross, S. R. Actin binding proteins. *Cell Adh Migr* **7**, 199–213 (2013).

456. Krishnan, K. & Moens, P. D. J. Structure and functions of profilins. *Biophys Rev* **1**, 71–81 (2009).

457. Edwards, M. *et al.* Capping protein regulators fine-tune actin assembly dynamics. *Nat Rev Mol Cell Biol* **15**, 677–689 (2014).

458. Narita, A. ADF/cofilin regulation from a structural viewpoint. *J Muscle Res Cell Motil* **41**, 141–151 (2020).

459. Jokhadar, Š. Z., Iturri, J., Toca-Herrera, J. L. & Derganc, J. Cell stiffness under small and large deformations measured by optical tweezers and atomic force microscopy: effects of actin disruptors CK-869 and jasplakinolide. *J. Phys. D: Appl. Phys.* **54**, 124001 (2021).

460. Bubb, M. R., Spector, I., Beyer, B. B. & Fosen, K. M. Effects of jasplakinolide on the kinetics of actin polymerization. An explanation for certain in vivo observations. *J Biol Chem* **275**, 5163–5170 (2000).

461. Kim, M., Song, K., Jin, E.-J. & Sonn, J. Staurosporine and cytochalasin D induce chondrogenesis by regulation of actin dynamics in different way. *Exp Mol Med* **44**, 521–528 (2012).

462. Gao, M. *et al.* The influence of actin depolymerization induced by Cytochalasin D and mechanical stretch on interleukin-8 expression and JNK phosphorylation levels in human retinal pigment epithelial cells. *BMC Ophthalmol* **17**, 43 (2017).

463. Albiges-Rizo, C., Destaing, O., Fourcade, B., Planus, E. & Block, M. R. Actin machinery and mechanosensitivity in invadopodia, podosomes and focal adhesions. *J Cell Sci* **122**, 3037–3049 (2009).

464. Dimchev, G. & Rottner, K. Micromanipulation Techniques Allowing Analysis of Morphogenetic Dynamics and Turnover of Cytoskeletal Regulators. *J Vis Exp* (2018).

465. Lachowski, D. *et al.* G Protein-Coupled Estrogen Receptor Regulates Actin Cytoskeleton Dynamics to Impair Cell Polarization. *Front Cell Dev Biol* **8**, 592628 (2020).

466. Leung, T., Chen, X. Q., Manser, E. & Lim, L. The p160 RhoA-binding kinase ROK alpha is a member of a kinase family and is involved in the reorganization of the cytoskeleton. *Mol Cell Biol* **16**, 5313–5327 (1996).

467. Hotulainen, P. & Lappalainen, P. Stress fibers are generated by two distinct actin assembly mechanisms in motile cells. *J Cell Biol* **173**, 383–394 (2006).

468. Maekawa, M. *et al.* Signaling from Rho to the actin cytoskeleton through protein kinases ROCK and LIM-kinase. *Science* **285**, 895–898 (1999).

469. Cao, X.-X. *et al.* RACK1 promotes breast carcinoma migration/metastasis via activation of the RhoA/Rho kinase pathway. *Breast Cancer Res Treat* **126**, 555–563 (2011).

470. Srinivasan, D. & Plattner, R. Activation of Abl tyrosine kinases promotes invasion of aggressive breast cancer cells. *Cancer Res* **66**, 5648–5655 (2006).

471. Kabrawala, S., Zimmer, M. D. & Campellone, K. G. WHIMP links the actin nucleation machinery to Src-family kinase signaling during protrusion and motility. *PLoS Genet* **16**, e1008694 (2020).

472. Yamada, H. *et al.* Dynamic interaction of amphiphysin with N-WASP regulates actin assembly. *J Biol Chem* **284**, 34244–34256 (2009).

473. Chang, Betty Y., Harte, Rachel A., & Cartwright, Christine A. RACK1: a novel substrate for the Src protein-tyrosine kinase. **21**, (2002).

474. Miller, L. D., Lee, K. C., Mochly-Rosen, D. & Cartwright, C. A. RACK1 regulates Src-mediated Sam68 and p190RhoGAP signaling. *Oncogene* **23**, 5682–5686 (2004).